

1225-0767(ISSN Print)  
2287-6715(ISSN Online)  
한국연구재단 우수등재학술지

# Journal of Ocean Engineering and Technology

Vol. 35, No. 2 (Serial Number 159)

April 2021

## 한국해양공학회지



[www.joet.org](http://www.joet.org)



The Korean Society of Ocean Engineers

## Editorial Board

### ■ Editor-in-Chief

Joonmo Choung Inha University, Korea

### ■ Manuscript Editors

Hyeongsik Choi Korea Maritime and Ocean University, Korea

Joon-Young Kim Korea Maritime and Ocean University, Korea

Seokhwan Ahn Jungwon University, Korea

Sungwon Shin

Hanyang University, Korea

Woo Dong Lee

Gyeongsang National University, Korea

### ■ Editorial Board Members

Ahmet Ergin Istanbul Technical University, Turkey

Atila Incecik University of Strathclyde, UK

Beom-Seon Jang Seoul National University, Korea

Bo Woo Nam Seoul National University, Korea

Chang Yong Song Mokpo National University, Korea

Chong Hyun Lee Jeju National University, Korea

Do Kyun Kim Newcastle University, UK

Dongho Jung Korea Research Institute of Ships & Ocean Engineering, Korea

Erkan Oterkus University of Strathclyde, UK

Geoffrey Lyons BPP-TECH, UK

Gökhan Tansel Tayyar Istanbul Technical University, Turkey

Gyusung Cho Tongmyong University, Korea

Hee Jin Kang Korea Research Institute of Ships & Ocean Engineering, Korea

Hooi-Siang Kang Universiti Teknologi Malaysia, Malaysia

Hyeon Kyu Yoon Changwon National University, Korea

Hyun-Sik Kim Tongmyong University, Korea

Jinwhan Kim Korea Advanced Institute of Science and Technology, Korea

Jong Chun Park Pusan National University, Korea

Kangsu Lee Korea Research Institute of Ships & Ocean Engineering, Korea

Kookhyun Kim Tongmyong University, Korea

Kwang-Jun Paik

Inha University, Korea

Masashi Kashiwagi

Osaka University, Japan

Moo Hyun Kim

Texas A&M University, USA

Narakorn Srin

Newcastle University, UK

Norimi Mizutani

Nagoya University, Japan

Se-Min Jeong

Chosun University, Korea

Seongim Choi

Virginia Tech, USA

Seung Min Park

Hyein Engineering & Construction, Co., Ltd., Korea

Soonchul Kwon

Pusan National University, Korea

Sungnam Hong

Gyeongsang National University, Korea

Sung-Woong Choi

Gyeongsang National University, Korea

Taemin Ha

Kangwon National University, Korea

TaeSeong Kim

Loughborough University, UK

TaeSoon Kang

GeoSystem Research Corp., Korea

Tak Kee Lee

Gyeongsang National University, Korea

Weoncheol Koo

Inha University, Korea

Yeon-Joong Kim

Inje University, Korea

Yong Uk Ryu

Chonnam National University, Korea

Younghun Kim

Kyungnam University, Korea

Youngsub Lim

Seoul National University, Korea

## Research Ethics Board

### ■ Chief

Sung-Bu Suh Dongeui University, Korea

### ■ Research Ethics Board Members

Han Koo Jeong Kunsan National University, Korea

Jinwhan Kim Korea Advanced Institute of Science and Technology, Korea

Yong Uk Ryu

Chonnam National University, Korea

Published on April 30, 2021

Published by The Korean Society of Ocean Engineers (KSOE)

Room 1302, 13, Jungang-daero 180beon-gil, Dong-gu, Busan, 48821, Korea

TEL: +82-51-759-0656 FAX: +82-51-759-0657 E-mail: ksoehj@ksoe.or.kr URL: http://www.ksoe.or.kr

Printed by Hanrimwon Co., Ltd., Seoul, Korea E-mail: hanrim@hanrimwon.co.kr

ISSN(print) 1225-0767 ISSN(online) 2287-6715

This journal was supported by the Korean Federation of Science and Technology Societies (KOFST) grant funded by the Korean government.

© 2021 by The Korean Society of Ocean Engineers (KSOE)

This is an open access article distributed under the terms of the creative commons attribution non-commercial license (<http://creativecommons.org/licenses/by-nc/4.0>) which permits unrestricted non-commercial use, distribution, and reproduction in any medium, provided the original work is properly cited.

# Journal of Ocean Engineering and Technology

한국해양공학회지

## CONTENTS

Volume 35, Number 2

April, 2021

---

### <Original Research Articles>

- Simulation-Based Prediction of Steady Turning Ability of a Symmetrical Underwater Vehicle Considering Interactions Between Yaw Rate and Drift/Rudder Angle  
Jeong-Hoon Park, Myung-Sub Shin, Yun-Ho Jeon and Yeon-Gyu Kim ..... 99
- An Experimental Study on Wave Absorber Performance of Combined Punching Plate in a Two-Dimensional Mini Wave Tank  
Hyen-Cheol Jung and Weoncheol Koo ..... 113
- CFD Simulation of Multiphase Flow by Mud Agitator in Drilling Mud Mixing System  
Tae-Young Kim, Gyu-Mok Jeon and Jong-Chun Park ..... 121
- Surrogate Model Based Approximate Optimization of Passive Type Deck Support Frame for Offshore Plant Float-over Installation  
Dong Jun Lee, Chang Yong Song and Kangsu Lee ..... 131
- Evaluation on Sensitivity and Approximate Modeling of Fire-Resistance Performance for A60 Class Deck Penetration Piece Using Heat-Transfer Analysis and Fire Test  
Woo Chang Park and Chang Yong Song ..... 141

### <Technical Article>

- Current Measurement and Velocity Spatial Distribution of Deep Ocean Engineering Basin  
Sung-Jun Jung, Jae-Sang Jung, Yong-Guk Lee, Byeong-Won Park, Sung-Chul Hwang, In-Bo Park, Jin-Ha Kim and Il-Ryong Park ..... 150

### <Review Article>

- Comparison of Fatigue Provisions in Various Codes and Standards-Part 1: Basic Design S-N Curves of Non-Tubular Steel Members  
Sungwoo Im and Joonmo Choung ..... 161

## GENERAL INFORMATION

“Journal of Ocean Engineering and Technology” is the official journal published by “The Korean Society of Ocean Engineers (KSOE)”. The ISO abbreviation is “J. Ocean Eng. Technol.” and acronym is “**JOET**”. It was launched in 1987. It is published bimonthly in February, April, June, August, October, and December each year. Supplement numbers are published at times.

Journal of Ocean Engineering and Technology (JOET) is a medium for the publication of original research and development work in the field of ocean engineering. JOET covers the entire range of issues and technologies related to the following topics:

**Ships and offshore platforms:** Design of marine structures; Resistance and propulsion; Seakeeping and maneuvering; Experimental and computational fluid dynamics; Ocean wave mechanics; Fatigue strength; Plasticity; Optimization and reliability; Arctic technology and extreme mechanics; Noise, vibration, and acoustics; Concrete engineering; Thermodynamics and heat transfer; Hydraulics and pneumatics;  
**Coastal civil engineering:** Coastal structures; Port and harbor structures; Soil mechanics; Drilling and exploration; Hydraulics of estuary; Seismic engineering; Coastal disaster prevention engineering;  
**Ocean renewable energy platforms:** Offshore wind turbines; Wave energy platforms; Tidal current energy platforms; Floating photovoltaic energy platforms;  
**Marine robots:** Robot sensor system; Autonomous navigation; Robot equipments; Spatial information and communications; Underwater network; Design of underwater vehicles;  
**Multidisciplinary areas:** Design for safety; IT-based design; IT-based production engineering; Welding mechanics; Control engineering; GPS and GIS; Inspection and sensor; Port and logistics; Leisure boat and deep sea water; Offshore process systems engineering; Marine metallic materials; Marine organic materials; Marine Composite materials; Materials properties; Corrosion and Anti-corrosion; Tribology;

It contains original research articles, case reports, brief communications and reviews on technical issues. Conference papers, research papers, diploma papers and academic articles can be submitted.

All of the manuscripts are peer-reviewed. **JOET** has a system where two or more peer reviewers must review each submitted paper and it is operated very strictly.

**JOET** is an open access journal distributed under the terms of the creative commons attribution non-commercial license (<http://creativecommons.org/licenses/by-nc/4.0>). Therefore, all ocean engineers and researchers around the world can easily access all journal articles via the journal homepage (<http://www.joet.org>) and download the PDF-based original texts or view the web-based XML texts for free.

**JOET** is being indexed in some prominent database such as Korean Citation Index (KCI), Google Scholar, Science Central, Korea Science and Directory of Open Access Journals (DOAJ).

For correspondences concerning business matters, author needs to contact KSOE Secretariat by email or phone (e-mail: [ksoehj@ksoe.or.kr](mailto:ksoehj@ksoe.or.kr) or Tel: +82 51 759 0656). Correspondences for publication matters can be asked via email to the Editor-in-Chief (email: [heroeswise2@gmail.com](mailto:heroeswise2@gmail.com)).



# Simulation-Based Prediction of Steady Turning Ability of a Symmetrical Underwater Vehicle Considering Interactions Between Yaw Rate and Drift/Rudder Angle

Jeong-Hoon Park<sup>1</sup>, Myung-Sub Shin<sup>2</sup>, Yun-Ho Jeon<sup>2</sup> and Yeon-Gyu Kim<sup>3</sup>

<sup>1</sup>Chief Research Engineer, Mechanical R&D Center, LIG Nex1, Seongnam, Korea

<sup>2</sup>Research Engineer, Mechanical R&D Center, LIG Nex1, Seongnam, Korea

<sup>3</sup>Principal Researcher, Offshore Platform Research Division, KRISO, Daejeon, Korea

**KEY WORDS:** Turning ability, Symmetrical underwater vehicle, Computational fluid dynamics (CFD), Interactions between Yaw rate and drift/Rudder angle, Coupled hydrodynamic force and moment, Turning motion simulation

**ABSTRACT:** The prediction of maneuverability is very important in the design process of an underwater vehicle. In this study, we predicted the steady turning ability of a symmetrical underwater vehicle while considering interactions between the yaw rate and drift/rudder angle through a simulation-based methodology. First, the hydrodynamic force and moment, including coupled derivatives, were obtained by computational fluid dynamics (CFD) simulations. The feasibility of CFD results were verified by comparing static drift/rudder simulations to vertical planar motion mechanism (VPMM) tests. Turning motion simulations were then performed by solving 2-degree-of-freedom (DOF) equations with CFD data. The turning radius, drift angle, advance, and tactical diameter were calculated. The results show good agreement with sea trial data and the effects on the turning characteristics of coupled interaction terms, especially between the yaw rate and drift angle.

## Nomenclature

$\rho$	Density (kg/m <sup>3</sup> )
$m$	Mass of Underwater Vehicle (kg)
$I$	Moment of Inertia (kg-m <sup>2</sup> )
$X_0$	X Position in Earth-Fixed Frame (m)
$Y_0$	Y Position in Earth-Fixed Frame (m)
$\psi$	Yaw Angle in Earth-Fixed Frame (rad)
$u$	Surge Velocity in Body-Fixed Frame (m/s)
$v$	Sway Velocity in Body-Fixed Frame (m/s)
$U$	Overall Speed (m/s)
$r$	Yaw Rate in Body-Fixed Frame (rad/s)
$\beta$	Drift Angle (rad)
$\delta$	Rudder Deflection Angle (rad)
$X$	Surge Force in Body-Fixed Frame (N)
$Y$	Sway Force in Body-Fixed Frame (N)
$N$	Yaw Moment in Body-Fixed Frame (N-m)
$L$	Length of Underwater Vehicle Body (m)
$x_g$	X coordinate of Center of Gravity (m)
$y_g$	Y coordinate of Center of Gravity (m)

## 1. Introduction

Many kinds of underwater vehicles have been developed for military, commercial, and scientific purposes, such as submarines, torpedoes, autonomous underwater vehicles (AUVs), remotely operated vehicles (ROVs), underwater gliders, etc. Underwater vehicles need to have various types of performance depending on their operating concept and tasks. For example, maneuverability, course-keeping ability, turning ability, and course-changing ability are the most fundamental elements, so their prediction is very important work in the design process of underwater vehicles.

The process of predicting maneuverability consists of constructing equations of motion, obtaining hydrodynamic derivatives, and performing flight simulation. Most equations of motion of an underwater vehicle are based on the submarine dynamic model by Gertler and Hagen (1967). Feldman (1979) proposed a modified dynamic model to describe extreme turning and a high angle of attack accurately based on the model of Gertler and Hagen. Healey and Lienard (1993) proposed a dynamic model for a large AUV for low-speed flight. Many another researchers have also carried out research on equations of motion (Bae et al., 2009; Park et al., 2015).

Received 15 November 2020, revised 7 March 2021, accepted 9 March 2021

Corresponding author Jeong-Hoon Park: +82-31-8026-4881, jeonghoon.park@lignex1.com

© 2021, The Korean Society of Ocean Engineers

This is an open access article distributed under the terms of the creative commons attribution non-commercial license (<http://creativecommons.org/licenses/by-nc/4.0>) which permits unrestricted non-commercial use, distribution, and reproduction in any medium, provided the original work is properly cited.

There are mainly two ways to obtain hydrodynamic derivatives of an underwater vehicle during the design stage. One is by experiments, and the other is by computational fluid dynamics (CFD) simulations. Kim et al. (2012) estimated hydrodynamic derivatives of an underwater vehicle from a captive model test using a computerized planar motion carriage (CPMC). Park et al. (2015) conducted coning motion tests and derived hydrodynamic coefficients for roll motion.

Jeong et al. (2016) predicted hydrodynamic derivatives of a submarine after performing rotating arm tests. Nguyen et al. (2018) estimated hydrodynamic derivatives of a submarine by CFD analysis using a full-scale Reynolds-Averaged Navier-Stokes (RANS) solver. De Barros and Dantas (2012) numerically predicted the effects of a duct on the maneuverability. Kim et al. (2015) estimated the roll derivatives of an underwater vehicle, and Cheon et al. (2018) carried out virtual dynamic tests on an X-form configuration submarine using dynamic mesh methods.

After obtaining hydrodynamic derivatives, equations of motion are generally solved to analyze maneuverability. Bae et al. (2009) performed a simulation of the emergency rising, depth change, and floating of a manta-type AUV. Wang and Liang (2019) performed a maneuverability analysis of a modular underwater vehicle that has four tail thrusters and two tunnel thrusters. Go et al. (2017) conducted a 6-degree-of-freedom (DOF) motion analysis of a tow-fish-type underwater vehicle using hydrodynamic derivatives based on CFD.

Turning ability is also significant and critical to the maneuverability of an underwater vehicle, and many researchers have been trying to predict it in the design phase before sea trials. Seol et al. (2005) performed a simulation of turning and zigzag motion of an underwater vehicle using experiment data from a horizontal planar motion mechanism (HPMM). Jeon et al. (2018) did a sensitivity analysis for the parametric optimization of a hull form by the calculating turning and course changing ability based on a 3-DOF dynamic model. Dubbioso et al. (2017) compared the turning ability of cruciform and X-rudder submarines using unsteady free-running maneuvering simulations.

To predict the maneuverability accurately, research about dynamic model using coupled hydrodynamic effects has been conducted actively. Park et al. (2016) verified the interactions between the angle of attack and elevator angle of underwater vehicles that have fixed fins and movable fins. Dantas and de Barros (2013) numerically analyzed the coupled effects of the control surface deflection and angle of attack in an AUV that has only movable fins. Jeong et al. (2016) carried out a rotating arm test of a submarine for coupled motion, and Nguyen et al. (2018) performed a CFD analysis of a submarine for coupled motion. Thus, we can assume that there is some significant coupling of hydrodynamic derivatives in the turning phase of an underwater vehicle because there is large rudder deflection in turning motion, and most underwater vehicles turn with a drift angle.

In this study, we predicted the steady turning ability of an underwater vehicle while considering interactions between the yaw rate and drift/rudder angle. We did this by applying the hydrodynamic

force and moment derived by CFD. In order to find the derivatives by experimental methods, we normally have to perform both vertical planar motion mechanism (VPMM) and rotating arm tests. The reason is that the rotary derivatives obtained by rotating arm tests are more accurate than those from pure yaw in VPMM tests. Performing two tests requires much money and time. Therefore, we carried out only VPMM tests, and rotating arm tests were replaced by numerical simulations.

Static derivatives and control derivatives of fins from CFD were compared to the results of VPMM tests and verified. Based on CFD data, motion simulation of a turning circle test was conducted by solving dynamic equations in a horizontal plane. The turning radius, drift angle, advance, and tactical diameter were calculated and compared to sea trial data.

## 2. Configuration and Specifications of Underwater Vehicle

The underwater vehicle configuration is shown in Fig. 1. The vehicle is symmetrical in the vertical and lateral directions. There are four fixed fins and movable fins with 90-degree intervals, and the fixed fins are located in front of the movable fins. The four movable fins consist of two elevators that control the attitude and depth in the vertical plane and two rudders that control the attitude and trajectory in the horizontal plane. There is a ducted propeller behind the body. Table 1 shows the specifications of the underwater vehicle in this study.

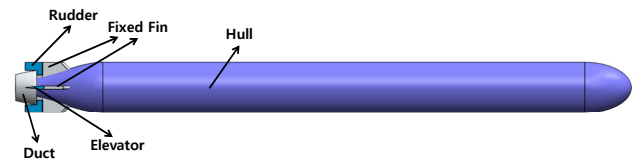


Fig. 1 Configuration of symmetrical underwater vehicle

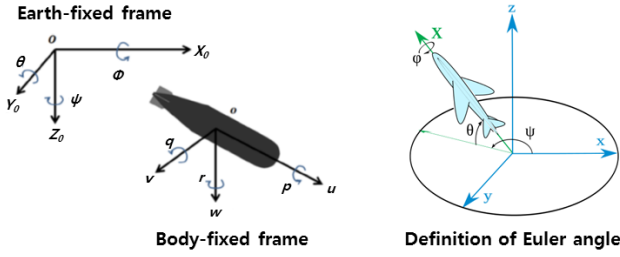
Table 1 Specifications of underwater vehicle in this study

Item	Value
Length (m)	6.6
Diameter of body (m)	0.53
Wing span of fins (m)	0.53
X position of $C_B$ (center of buoyancy) from nose (m)	3.14

## 3. Equations of Motion

### 3.1 Coordinates

In order to analyze the motion of the underwater vehicle, two coordinate systems were adopted. One is an earth-fixed frame, and the other is a body-fixed frame. The earth-fixed frame can be transformed to the body-fixed frame by the Euler angles, and reverse transformation is also possible. The definition of each coordinate and Euler angle is



**Fig. 2** Definition of coordinates (left) and Euler angles (right) (Park et al., 2015)

shown in Fig. 2. In this study, the origin point of the body-fixed frame was set to be the center of buoyancy.

The equations of motion of the underwater vehicle are generally represented by the body-fixed frame because it is easy to express the hydrodynamic force and moment acting on body. The position and attitude of the body are calculated in the earth-fixed frame, and the translational velocity and angular rate are transformed from the body-fixed frame to the earth-fixed frame using Eq. (1).

$$\begin{bmatrix} \dot{X}_0 \\ \dot{Y}_0 \\ \dot{Z}_0 \end{bmatrix} = \begin{bmatrix} \cos\psi\cos\phi & \cos\psi\sin\phi\sin\theta & -\sin\psi\cos\phi & \cos\psi\sin\phi\cos\theta & \sin\psi\sin\phi \\ \sin\psi\cos\phi & \sin\psi\sin\phi\sin\theta & \cos\psi\cos\phi & \sin\psi\sin\phi\cos\theta & \cos\psi\sin\phi \\ -\sin\theta & \cos\theta\sin\psi & & & -\cos\psi\sin\phi \end{bmatrix} \begin{bmatrix} u \\ v \\ w \end{bmatrix}$$

$$\begin{bmatrix} \dot{\phi} \\ \dot{\theta} \\ \dot{\psi} \end{bmatrix} = \begin{bmatrix} 1 & \sin\phi\tan\theta & \cos\phi\tan\theta \\ 0 & \cos\phi & -\sin\phi \\ 0 & \sin\phi\sec\theta & \cos\phi\sec\theta \end{bmatrix} \begin{bmatrix} p \\ q \\ r \end{bmatrix} \quad (1)$$

Since only horizontal motion is considered in this study, Eq. (1) can be rewritten in the horizontal plane as follows:

$$\begin{bmatrix} \dot{X}_0 \\ \dot{Y}_0 \end{bmatrix} = \begin{bmatrix} \cos\psi & -\sin\psi \\ \sin\psi & \cos\psi \end{bmatrix} \begin{bmatrix} u \\ v \end{bmatrix}$$

$$\dot{\psi} = r \quad (2)$$

### 3.2 Equations of Motion in Horizontal Plane

The equations of motion of the underwater vehicle to describe steady turning motion are as follows:

$$m[\dot{u} - vr + wq - x_g(\dot{q}^2 + r^2) + y_g(pq - \dot{r}) + z_g(pr + \dot{q})] = X$$

$$m[\dot{v} - wp + ur - y_g(r^2 + p^2) + z_g(qr - \dot{p}) + x_g(qp + \dot{r})] = Y \quad (3)$$

$$I_{zz}\dot{r} + (I_{yy} - I_{xx})pq - (\dot{q} + rp)I_{yz} + (\dot{q}^2 - p^2)I_{xy} + (rq - \dot{p})I_{xy} + m[x_g(\dot{v} - wp + ur) - y_g(\dot{u} - vr + wq)] = N$$

$X$ ,  $Y$ , and  $N$  are the external force and moment on the underwater vehicle, including hydrodynamic, hydrostatic (gravity and buoyancy), and thrust terms. Roll motion can be neglected because there is little snap roll angle when the vehicle turns steadily. The roll angle is controlled by the elevators. In addition, a surge equation is not included since it can be considered as constant, and the speed of the vehicle is uniformly controlled in the sea trial of this study when the

vehicle goes straight or turns.

Hydrostatic terms can be removed because the roll ( $\phi$ ) and pitch angle ( $\theta$ ) are not considered in horizontal plane motion. Hydrodynamic terms ( $Y_H$  and  $N_H$ ) including the interactions between the yaw rate and drift/rudder angle can be expressed as follows:

$$Y_H = Y_v\dot{v} + Y_vv + Y_{v|v}|v| + Y_r\dot{r} + Y_rr + Y_{r|r}|r| + Y_\delta\dot{\delta} + Y_{coup}(r, v) + Y_{coup}(r, \delta)$$

$$N_H = N_v\dot{v} + N_vv + N_{v|v}|v| + N_r\dot{r} + N_rr + N_{r|r}|r| + N_\delta\dot{\delta} + N_{coup}(r, v) + N_{coup}(r, \delta) \quad (4)$$

In Eq. (4),  $v$  is the sway velocity,  $r$  is the yaw rate, and  $\delta$  is the rudder angle.  $\dot{r}$  is the yaw acceleration,  $\dot{v}$  and  $\dot{r}$  is the yaw acceleration. The subscript “coup” means coupled derivatives.  $i$  and  $\dot{r}$  are not important in steady motion, so  $Y_v, Y_r$  and  $N_v, N_r$  can be neglected. In order to solve the equations for steady turning motion, we have to obtain the damping derivatives of the sway and yaw motion, the control derivatives of the rudder, and coupled interaction terms.

## 4. CFD Analysis

### 4.1 Simulation Method

In order to obtain the hydrodynamic data for steady turning motion by CFD, we have to perform static drift/rudder and rotating arm simulations. Static drift/rudder simulations calculate the force and moment with respect to the drift/rudder angle when the vehicle goes straight at constant speed (Figs. 3–4). Rotating arm simulations calculate the force and moment with respect to the yaw rate when the vehicle turns just like a circle. Rotating arm simulations can also calculate the interaction terms by combining with the static drift/rudder angle (Fig. 5).

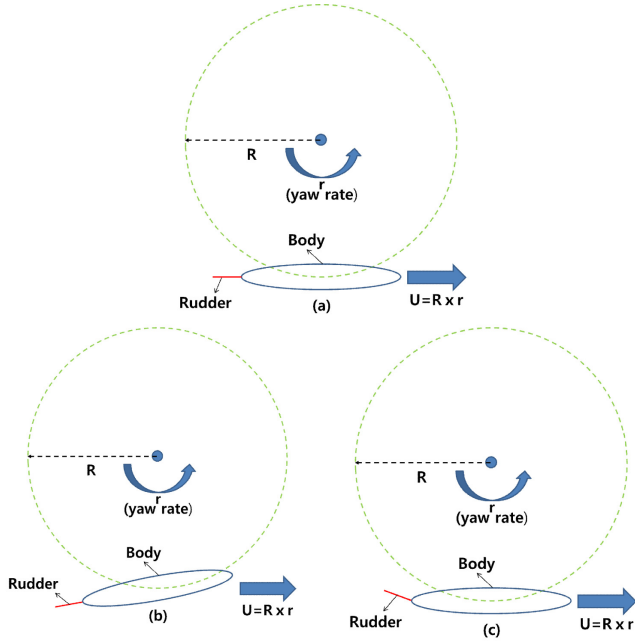
In static drift/rudder simulations, a rectangular domain was adopted, a velocity inlet condition was set at one end, and a pressure outlet condition was set at the other end. This is a very classical method to solve external flow problems. In rotating arm simulations, a cylindrical domain shaped like a donut was used, and the rotation of the vehicle was described by a moving reference frame method (Ansys Inc., 2018; Nguyen et al., 2018). The relative velocity in the moving reference



**Fig. 3** Static drift simulations



**Fig. 4** Static rudder simulations



**Fig. 5** Rotating arm simulations (a) without drift and rudder angle (b) with drift angle (c) with rudder angle

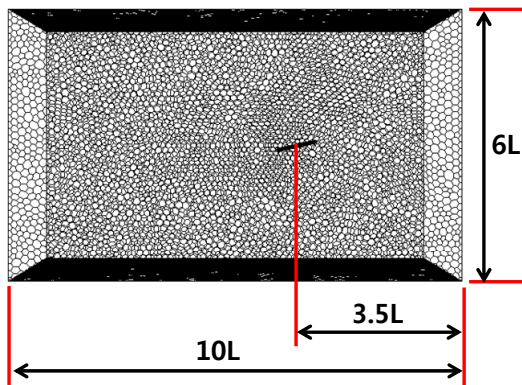
frame is expressed as follows:

$$\begin{aligned} \vec{v}_r &= \vec{v} - \vec{u}_r \\ \vec{u}_r &= \vec{v}_t + \vec{\omega} \times \vec{r} \end{aligned} \quad (5)$$

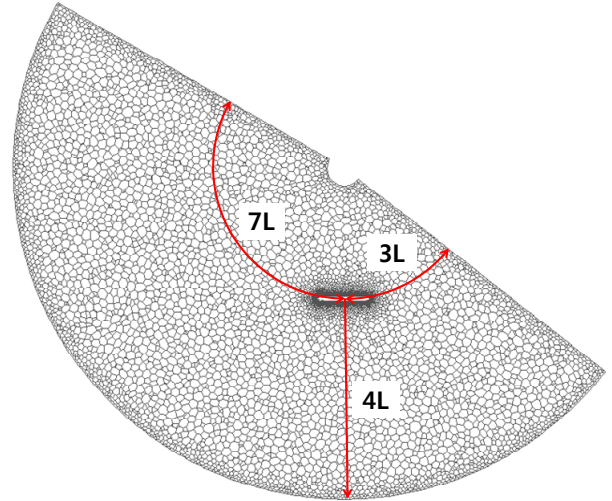
$\vec{v}_r$  is the relative velocity in the moving frame,  $\vec{v}$  is the absolute velocity in the stationary frame,  $\vec{u}_r$  is the velocity of the moving frame in the stationary frame,  $\vec{v}_t$  is the translational frame velocity, and  $\vec{\omega}$  is the angular frame velocity.

The domain size is large enough to avoid a blockage effect. A polyhedral mesh based on a tetrahedral mesh was basically adopted, and a prism layer was produced on the surface of the underwater vehicle body to solve the boundary layer flow (Ansys Inc., 2018). The shapes of the domain and mesh are shown in Figs. 6–7.

The propeller thrust affects the hydrodynamic characteristics of the underwater vehicle and changes the flow around it. However, if the



**Fig. 6** Domain and mesh shape of static drift and rudder simulations

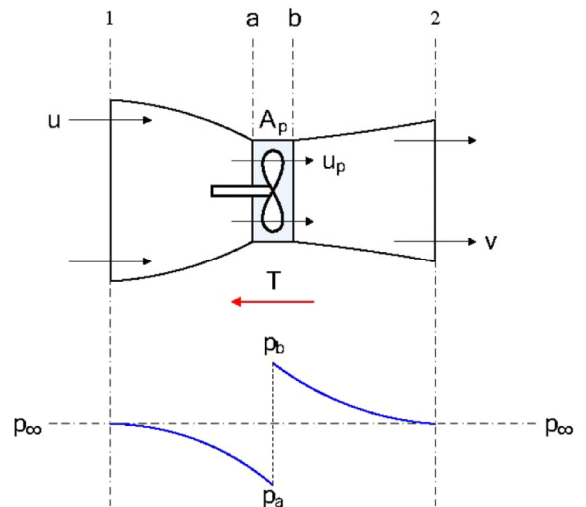


**Fig. 7** Domain and mesh shape of rotating arm simulations

detailed propeller configuration is described in the CFD model, the number of mesh elements increases greatly due to the complex geometry. This causes an increase of the computing resources and solution time. Therefore, we adopted the actuator disk theory to simulate propeller thrust. Actuator disk theory represents the thrust force by a pressure jump through a 2D membrane. The pressure jump can be calculated as follows:

$$\Delta p = \frac{T}{A} \quad (6)$$

$T$  is the thrust, and  $A$  is the area of the disk (propeller surface), as shown in Fig. 8. In this study, the input value of thrust is defined as the propeller force in self-propulsion conditions of the vehicle speed and was obtained by self-propulsion tests in the towing tank of the Korea Research Institute of the Ship and Ocean Engineering (KRISO).



**Fig. 8** Pressure distribution around propeller and relation between thrust and pressure jump (Kim and Chung, 2007)



#### 4.2 Governing Equations and Solver Setting

The governing equations of fluid mechanics are the continuity equation and momentum equations called the Navier-Stokes equations. The equations in the moving reference frame are as follows:

$$\begin{aligned} \frac{\partial \rho}{\partial t} + \nabla \cdot \rho \vec{v}_r &= 0 \\ \frac{\partial}{\partial t} \rho \vec{v} + \nabla \cdot (\rho \vec{v}_r \vec{v}) + \rho [\vec{\omega} \times (\vec{v} - \vec{v}_r)] &= -\nabla p + \nabla \cdot \vec{\tau} + \vec{F} \end{aligned} \quad (7)$$

In the case of the stationary frame,  $\omega$  and  $v_r$  are 0 and  $v_r$  equals  $v$ .

The  $k-\omega$  SST turbulence model was applied, and the Semi-Implicit Method for Pressure Linked Equations – Consistent (SIMPLEC) was used as a pressure-velocity coupling scheme. The operating fluid is sea water, of which the density is 1025.87 kg/m<sup>3</sup>, and the viscosity is 0.00122 kg/m·s. Sea water is considered as an incompressible fluid. All CFD simulations in this study were performed in Ansys Fluent, which is well known and verified commercial CFD software.

#### 4.3 Simulation Conditions

The hydrodynamic derivatives of the underwater vehicle are generally expressed in dimensionless forms. Eq. (4) with non-dimensional coefficients is as follows:

$$\begin{aligned} Y_H &= \left( Y_v' v' + Y_{v|v}|v'| + Y_r' r' + Y_{r|r}|r'| + \right) \times (0.5 \rho U^2 L^2) \\ N_H &= \left( N_v' v' + N_{v|v}|v'| + N_r' r' + N_{r|r}|r'| + \right) \times (0.5 \rho U^2 L^3) \end{aligned} \quad (8)$$

$$\begin{aligned} Y' &= \frac{Y}{0.5 \rho U^2 L^2}, \quad N' = \frac{N}{0.5 \rho U^2 L^3} \\ v' &= \frac{v}{U} = \frac{-U \sin \beta}{U} = -\sin \beta, \quad r' = \frac{rL}{U} \end{aligned} \quad (9)$$

$$U = \sqrt{u^2 + v^2}$$

As examples of the notation, the non-dimensional derivative  $Y_v'$  means  $\partial Y' / \partial v'$ , and  $N_{r|r}'$  means  $\partial N' / \partial (r' |r'|)$ .

In this study, the ranges of the yaw rate, drift angle, and rudder angle were determined by considering the operating concept and mission of the underwater vehicle, as shown in Table 2.  $U$  is the overall speed of the underwater vehicle and is set to 10 kn ( $\approx 5.1$  m/s). In the case of the rotating arm simulations, the turning radius changes as the yaw rate changes, and the overall speed is constant.

**Table 2** Ranges of yaw rate, drift angle and rudder angle

Item	Non-dimensional value	Note
Yaw rate	-0.4–+0.4	Turning radius 16.5–66 (m)
Drift angle	-0.2079–+0.2079	-12–+12 (deg)
Rudder angle	-0.3491–+0.3491 (rad)	-20–+20 (deg)

### 5. Results of the CFD Simulations

#### 5.1 Results of the Static Drift/Rudder Simulations

First of the all, static drift and rudder simulations were performed to obtain hydrodynamic data when the vehicle goes straight ( $r' = 0$ ). Since the vehicle is symmetrical, simulations for only positive  $v'$  and  $\delta$  were conducted, and then the simulation results were compared to VPMM test results from the towing tank of KRISO.

Fig. 9 shows the facilities at KRISO and the VPMM tests of the underwater vehicle used in this study. Static rudder simulations and experiments were performed in conditions where two rudders are all actuated with the same value. The towing speed was 2.29 m/s, which is lower than the CFD simulations because a free surface effect can occur at high speed in VPMM tests.

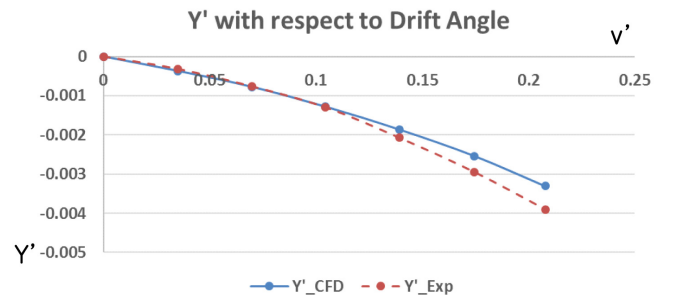


**Fig. 9** Towing tank and carriage at KRISO (left) and VPMM tests of underwater vehicle in this study (right)

The hydrodynamic force and moment with respect to the drift angle and rudder angle are presented in Figs. 10–13. Although there are some errors at high drift angle (large  $v'$ ), the simulation results follow the tendency of the experiments well and have feasibility for predicting to the hydrodynamic derivatives of the underwater vehicle. According to the operating concept of the underwater vehicle, it is very rare that the drift angle is larger than 10 degrees ( $v' = 0.1736$ ) during all flight times.

It is still difficult to predict the wake flow characteristics past a body with a high angle of attack using the RANS method. In addition, the gap between the top of the vehicle and free surface is narrow at high drift angle. When the drift angle is 0 degrees, the depth of the vehicle is 2.2 m. As the drift angle changes to 12 degrees, the minimum gap between the vehicle and free surface is reduced to 1.3 m. This may have a slight effect on the results.

Fig. 14 shows the flow vector field and pressure distribution around



**Fig. 10** Non-dimensional force  $Y'$  with respect to drift angle

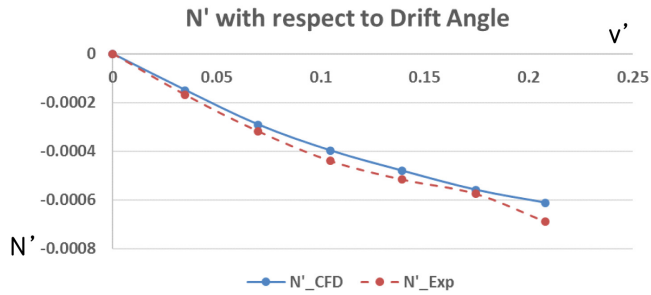


Fig. 11 Non-dimensional moment  $N'$  with respect to drift angle

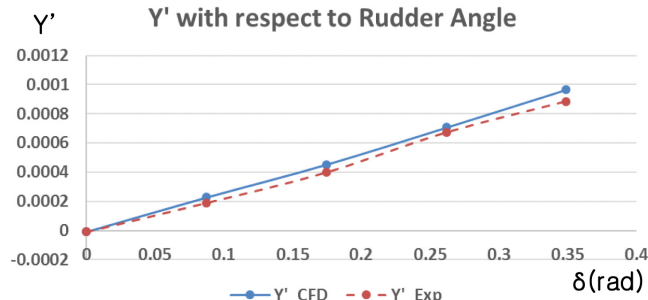


Fig. 12 Non-dimensional force  $Y'$  with respect to rudder angle

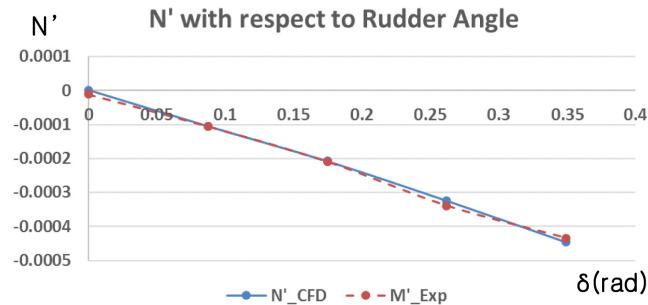


Fig. 13 Non-dimensional moment  $N'$  with respect to rudder angle

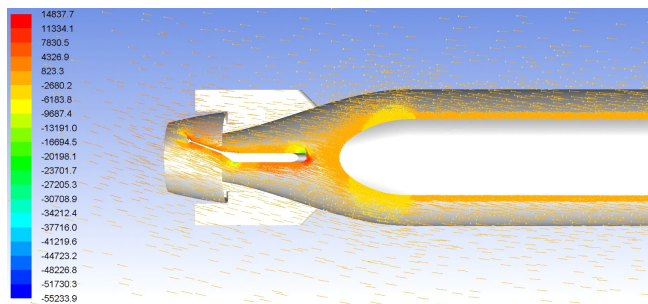


Fig. 14 Flow vector field and pressure distribution around stern body of underwater vehicle in case of static rudder simulations

the stern body of the underwater vehicle in the case of the static rudder simulations. The change of velocity due to the fin angle makes a pressure distribution on the fin surface, and the pressure distribution makes a force and moment that act on the vehicle (Huang et al., 2015).

## 5.2 Results of Rotating Arm Simulations with Drift/Rudder Angle

Rotating arm simulations with the drift angle and rudder angle were

carried out to estimate the rotary derivatives and coupled hydrodynamic terms. The simulations for only positive  $r'$  and the whole range of  $v'$  and  $\delta$  were conducted because the vehicle is symmetrical, but the relative direction between yaw rate and drift/rudder angle can affect the tendency of the interactions. Figs. 15–16 show the total non-dimensional force  $Y'$  and moment  $N'$  for the yaw rate and drift angle, and Figs. 17–18 show the results for the yaw rate and rudder angle.

The results when  $r' = 0$  are the same as in the static drift and rudder simulations, and rotary derivatives for the yaw rate can be estimated from the results when  $v' = 0$  and  $\delta = 0$ . If there is no interaction between them, the shape of the force and moment graphs will coincide regardless of the yaw rate. However, the shape of the graphs changes according to the yaw rate.

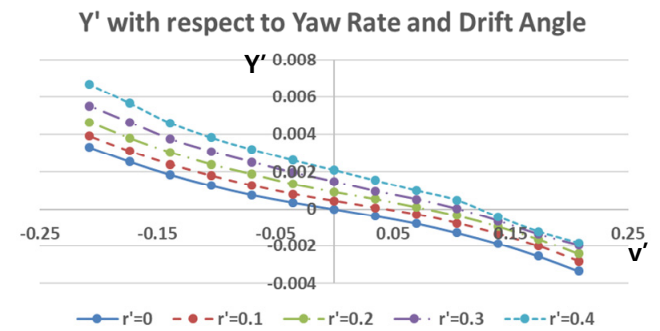


Fig. 15 Total non-dimensional force  $Y'$  with respect to yaw rate and drift angle

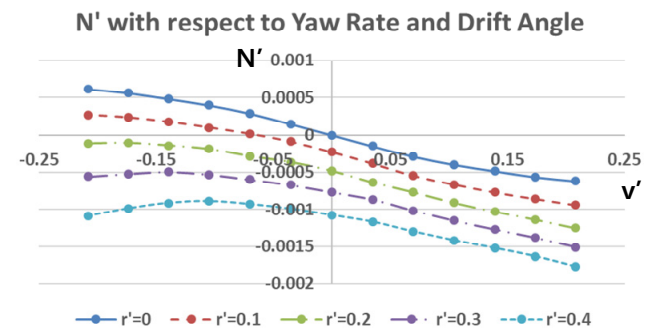


Fig. 16 Total non-dimensional moment  $N'$  with respect to yaw rate and drift angle

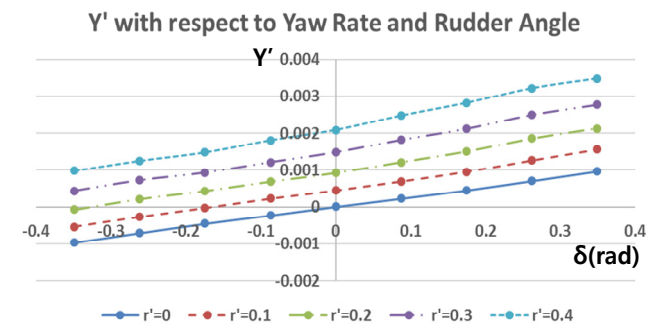


Fig. 17 Total non-dimensional force  $Y'$  with respect to yaw rate and rudder angle

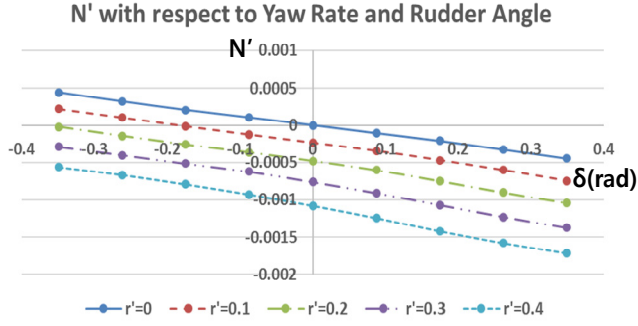


Fig. 18 Total non-dimensional moment  $N'$  with respect to yaw rate and rudder angle

In order to analyze the interactions between the yaw rate and drift/rudder angle, coupled terms were separated from the total force and moment. The total force and moment consist of terms for the yaw rate, drift angle, rudder angle, and coupled terms. The terms of the yaw rate are obtained from rotating arm simulations without the drift and rudder angle, those of the drift angle are obtained from static drift simulations, and those of the rudder angle are obtained from static rudder simulations. The coupled terms can be calculated as follows:

$$Y_{couple}'(r', v') = Y' - Y'(r') - Y'(v')$$

$$N_{couple}'(r', v') = N' - N'(r') - N'(v') \quad (10)$$

$$Y_{couple}'(r', \delta) = Y' - Y'(r') - Y'(\delta)$$

$$N_{couple}'(r', \delta) = N' - N'(r') - N'(\delta)$$

The coupled terms have different tendencies with respect to the relative direction between the yaw rate and drift/rudder angle, as shown in Figs. 19–22. We predicted that these tendencies would be caused by the change of the flow's incidence angle and tangential velocity of the partial vehicle body. When the yaw rate ( $r'$ ) is positive and the drift angle ( $v'$ ) is negative (in other words, the bow of the vehicle is heading for the inside of the turning circle), the tangential velocity of the bow becomes slower, and that of the stern becomes faster because the partial turning radius changes. In addition, the flow

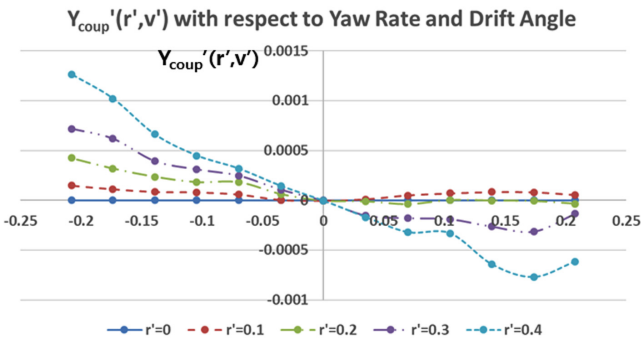


Fig. 19 Coupled non-dimensional force  $Y_{couple}'(r', v')$  with respect to yaw rate and drift angle

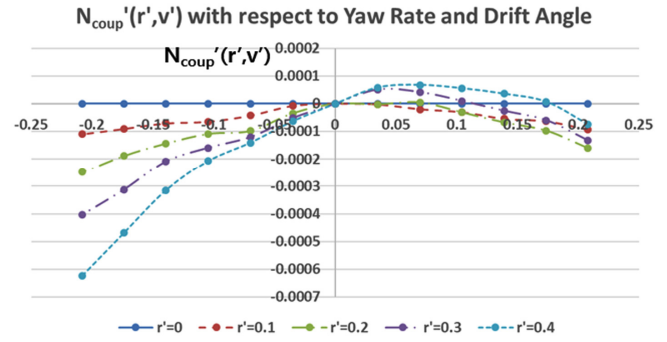


Fig. 20 Coupled non-dimensional moment  $N_{couple}'(r', v')$  with respect to yaw rate and drift angle

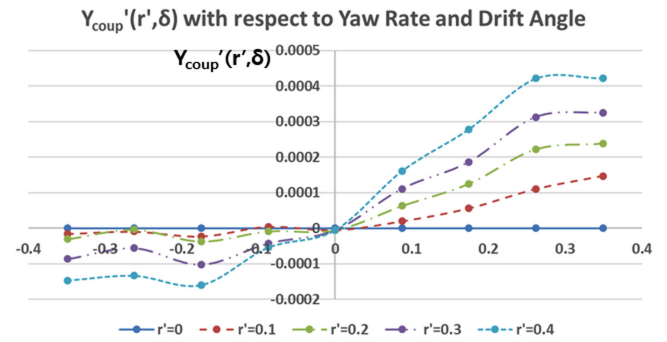


Fig. 21 Coupled non-dimensional force  $Y_{couple}'(r', \delta)$  with respect to yaw rate and rudder angle

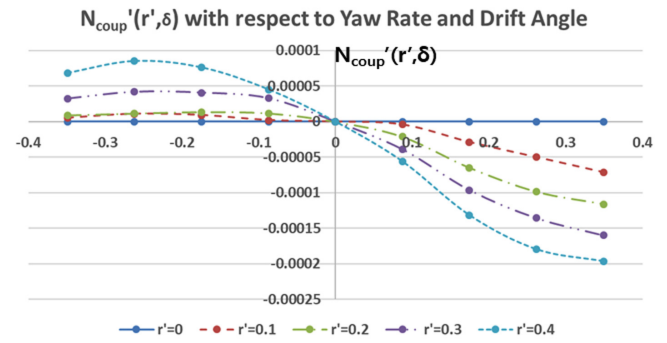
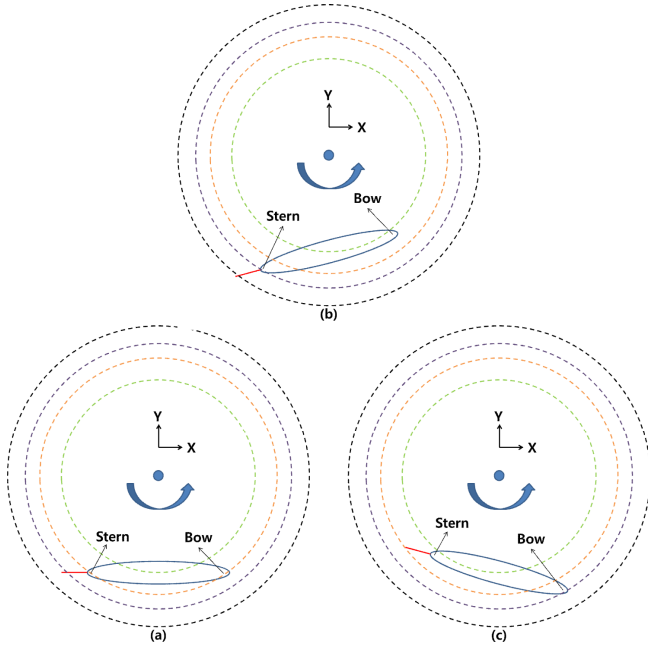


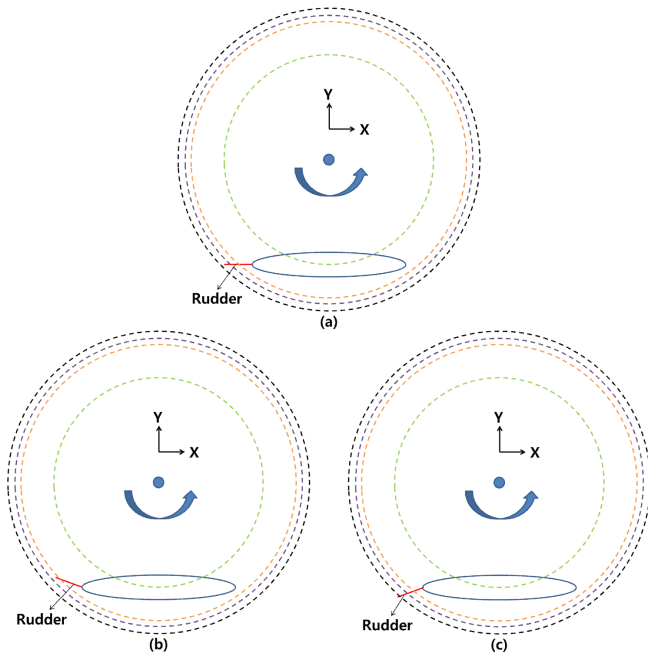
Fig. 22 Coupled non-dimensional moment  $N_{couple}'(r', \delta)$  with respect to yaw rate and rudder angle

incidence angle of the bow becomes smaller, and that of the stern becomes bigger, as shown in Fig. 23(b). These phenomena become stronger as the yaw rate increases.

In contrast, when the yaw rate ( $r'$ ) and drift angle ( $v'$ ) are both positive (in other words, the bow of the vehicle is heading for the outside of the turning circle), the tangential velocity of the bow becomes faster, that of the stern becomes slower, the flow incidence angle of the bow becomes bigger, and that of the stern becomes smaller, as shown in Fig. 23(c). However, in this direction, the interaction force and moments are weak compared to the opposite direction.

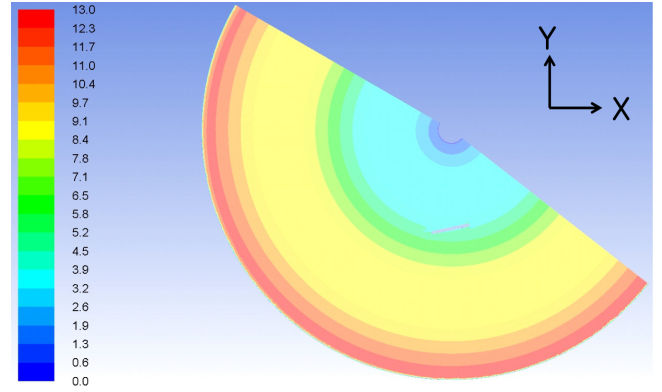


**Fig. 23** The change of the turning radius and flow incidence angle of the partial vehicle body in turning motion (a) without drift angle (b) when yaw rate is positive and drift angle are negative (c) when yaw rate and drift angle are both positive



**Fig. 24** Change of turning radius and flow incidence angle of partial vehicle body at turning motion (a) without rudder angle (b) when yaw rate is positive and rudder angle are negative (c) when yaw rate and rudder angle are both positive

In the case of the simulations with a coupled yaw rate and rudder angle, the same analysis can be applied. When the yaw rate ( $r'$ ) is positive and the rudder angle ( $\delta$ ) is negative, the tangential velocity of



**Fig. 25** Velocity distribution in case of rotating arm simulations

the rudder becomes slower, and flow's incidence angle becomes smaller, as shown in Fig. 24(b). Therefore, reduction of the sway force and yaw moment increases as the yaw rate increases. In contrast, When the yaw rate ( $r'$ ) and rudder angle ( $\delta$ ) are both positive, the tangential velocity of the rudder becomes faster, and flow's incidence angle becomes bigger, as shown in Fig. 24(c). Therefore, the additional sway force and yaw moment increase as the yaw rate increases. Fig. 25 shows the velocity distribution of the whole domain in the case of the rotating arm simulations.

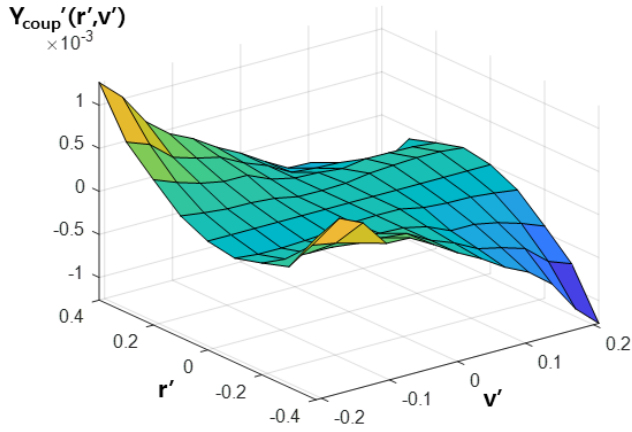
### 5.3 Estimation of Hydrodynamic Derivatives

The static coefficients for the drift and rudder angle were obtained from static drift and rudder simulations, and the rotary coefficients for the yaw rate were obtained from rotating arm simulations without the drift and rudder angle. The derivatives were calculated by the least-squares method, as shown in Table 3. Interaction terms are too difficult to define as coefficients because they have strong non-linearities. Therefore, the coupled hydrodynamic force and moment are functions of the yaw rate and drift angle/rudder angle and are calculated by an interpolation method from the data shown in Tables 4–7. These coupled terms are applied to simulate the turning motion of the underwater vehicle. Figs. 26–29 show 3D contours of the coupled hydrodynamic force and moment from Tables 4–7.

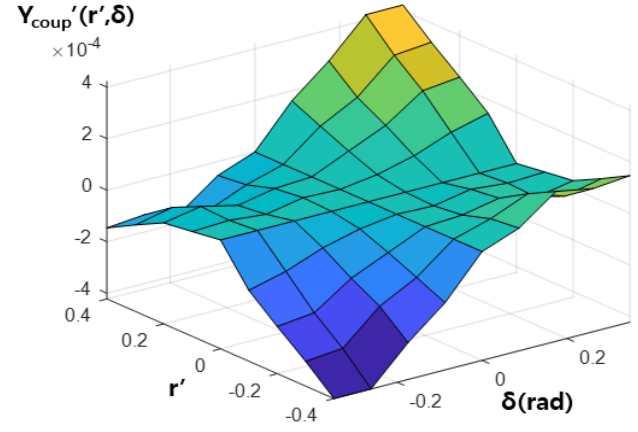
**Table 3** Hydrodynamic derivatives in this study

	Item	Non-dimensional value
Drift angle	$Y_v'$	-8.6468E-03
	$Y_{v v} '$	-3.4639E-02
	$N_v'$	-4.6481E-03
	$N_{v v} '$	8.2357E-03
Rudder angle	$Y_\delta'$	2.7162E-03
	$N_\delta'$	-1.2529E-03
	$Y_r'$	4.1112E-03
Yaw rate	$Y_{r r} '$	2.7877E-03
	$N_v'$	-2.1336E-03
	$N_{v v} '$	-1.3915E-03

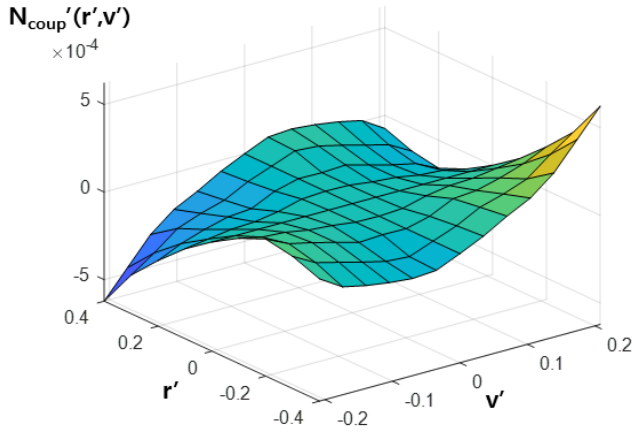




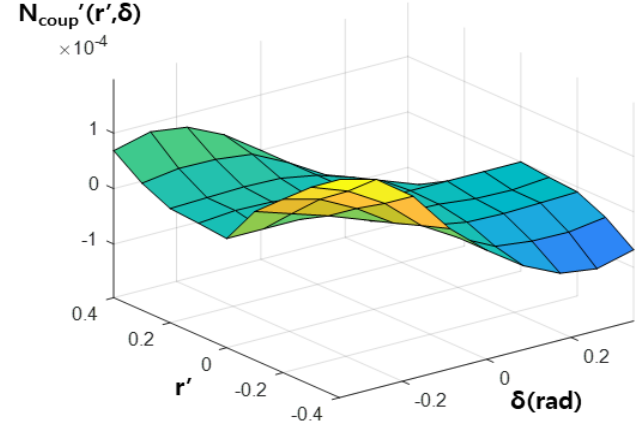
**Fig. 26** 3D contour of coupled non-dimensional force  $Y_{coup}'(r', v')$  with respect to yaw rate and drift angle



**Fig. 28** 3D contour of coupled non-dimensional force  $Y_{coup}'(r', \delta)$  with respect to yaw rate and rudder angle



**Fig. 27** 3D contour of coupled non-dimensional moment  $N_{coup}'(r', v')$  with respect to yaw rate and drift angle



**Fig. 29** 3D contour of coupled non-dimensional moment  $N_{coup}'(r', \delta)$  with respect to yaw rate and rudder angle

**Table 4** Coupled non-dimensional force  $Y_{coup}'(r', v')$  with respect to yaw rate and drift angle

$r' \backslash v'$	-0.2079	-0.1736	-0.1392	-0.1045	-0.0698	-0.0349	0.0000	0.0349	0.0698	0.1045	0.1392	0.1736	0.2079
-0.4001	6.1497E-04	7.7087E-04	6.4444E-04	3.3128E-04	3.2153E-04	1.6937E-04	0.0000E+00	-1.4237E-04	-3.1695E-04	-4.4827E-04	-6.6151E-04	-1.0208E-03	-1.2630E-03
-0.3000	1.3557E-04	3.1364E-04	2.6363E-04	1.8984E-04	1.7871E-04	1.5263E-04	0.0000E+00	-1.0550E-04	-2.4639E-04	-3.0944E-04	-3.9312E-04	-6.1641E-04	-7.1614E-04
-0.2000	3.4696E-05	7.8682E-06	3.0706E-06	-1.1219E-06	3.9708E-05	1.1340E-05	0.0000E+00	-6.1355E-05	-1.8201E-04	-1.8271E-04	-2.3648E-04	-3.1965E-04	-4.2384E-04
-0.0999	-5.3242E-05	-8.1058E-05	-8.3033E-05	-6.9284E-05	-4.9907E-05	-9.3416E-06	0.0000E+00	-2.5361E-06	-5.7996E-05	-8.0089E-05	-8.4197E-05	-1.1209E-04	-1.4858E-04
0.0000	0.0000E+00	0.0000E+00	0.0000E+00	0.0000E+00	0.0000E+00	0.0000E+00	0.0000E+00	0.0000E+00	0.0000E+00	0.0000E+00	0.0000E+00	0.0000E+00	0.0000E+00
0.0999	1.4858E-04	1.1209E-04	8.4197E-05	8.0089E-05	5.7996E-05	2.5361E-06	0.0000E+00	9.3416E-06	4.9907E-05	6.9284E-05	8.3033E-05	8.1058E-05	5.3242E-05
0.2000	4.2384E-04	3.1965E-04	2.3648E-04	1.8271E-04	1.8201E-04	6.1355E-05	0.0000E+00	-1.1340E-05	-3.9708E-05	1.1219E-06	-3.0706E-06	-7.8682E-06	-3.4696E-05
0.3000	7.1614E-04	6.1641E-04	3.9312E-04	3.0944E-04	2.4639E-04	1.0550E-04	0.0000E+00	-1.5263E-04	-1.7871E-04	-1.8984E-04	-2.6363E-04	-3.1364E-04	-1.3557E-04
0.4001	1.2630E-03	1.0208E-03	6.6151E-04	4.4827E-04	3.1695E-04	1.4237E-04	0.0000E+00	-1.6937E-04	-3.2153E-04	-3.3128E-04	-6.4444E-04	-7.7087E-04	-6.1497E-04

**Table 5** Coupled non-dimensional force  $N_{coup}'(r', v')$  with respect to yaw rate and drift angle

$r' \backslash v'$	-0.2079	-0.1736	-0.1392	-0.1045	-0.0698	-0.0349	0.0000	0.0349	0.0698	0.1045	0.1392	0.1736	0.2079
-0.4001	7.4834E-05	-6.9004E-06	-3.5817E-05	-5.5624E-05	-6.7992E-05	-5.8538E-05	0.0000E+00	6.3072E-05	1.4061E-04	2.0734E-04	3.1433E-04	4.6798E-04	6.2255E-04
-0.3000	1.3229E-04	5.9630E-05	2.5779E-05	-9.8648E-06	-4.1839E-05	-5.1254E-05	0.0000E+00	5.1434E-05	1.2023E-04	1.5915E-04	2.0885E-04	3.1186E-04	4.0267E-04
-0.2000	1.5937E-04	9.6579E-05	6.7199E-05	3.1432E-05	-4.9397E-06	2.0174E-06	0.0000E+00	3.4131E-05	9.7470E-05	1.0845E-04	1.4318E-04	1.8756E-04	2.4816E-04
-0.0999	9.2874E-05	6.3237E-05	5.4371E-05	3.0718E-05	1.9978E-05	2.5101E-06	0.0000E+00	7.9577E-06	4.2802E-05	6.4631E-05	7.0833E-05	9.0230E-05	1.0952E-04
0.0000	0.0000E+00	0.0000E+00	0.0000E+00	0.0000E+00	0.0000E+00	0.0000E+00	0.0000E+00	0.0000E+00	0.0000E+00	0.0000E+00	0.0000E+00	0.0000E+00	0.0000E+00
0.0999	-1.0952E-04	-9.0230E-05	-7.0833E-05	-6.4631E-05	-4.2802E-05	-7.9577E-06	0.0000E+00	-2.5101E-06	-1.9978E-05	-3.0718E-05	-5.4371E-05	-6.3237E-05	-9.2874E-05
0.2000	-2.4816E-04	-1.8756E-04	-1.4318E-04	-1.0845E-04	-9.7470E-05	-3.4131E-05	0.0000E+00	-2.0174E-06	-4.9397E-05	-3.1432E-05	-6.7199E-05	-9.6579E-05	-1.5937E-04
0.3000	-4.0267E-04	-3.1186E-04	-2.0885E-04	-1.5915E-04	-1.2023E-04	-5.1434E-05	0.0000E+00	5.1254E-05	4.1839E-05	9.8648E-06	-2.5779E-05	-5.9630E-05	-1.3229E-04
0.4001	-6.2255E-04	-4.6798E-04	-3.1433E-04	-2.0734E-04	-1.4061E-04	-6.3072E-05	0.0000E+00	5.8538E-05	6.7992E-05	5.5624E-05	3.5817E-05	6.9004E-06	-7.4834E-05

**Table 6** Coupled non-dimensional force  $Y_{coup}'(r', \delta)$  with respect to yaw rate and rudder angle

$r' \backslash \delta$	-0.3491	-0.2618	-0.1745	-0.0873	0.0000	0.0873	0.1745	0.2618	0.3491
-0.4001	-4.2212E-04	-4.2142E-04	-2.7900E-04	-1.6135E-04	0.0000E+00	5.3939E-05	1.5945E-04	1.3306E-04	1.4649E-04
-0.3000	-3.2579E-04	-3.1258E-04	-1.8642E-04	-1.1136E-04	0.0000E+00	4.2042E-05	1.0176E-04	5.5598E-05	8.6339E-05
-0.2000	-2.3897E-04	-2.2288E-04	-1.2582E-04	-6.3218E-05	0.0000E+00	8.1034E-06	3.6522E-05	3.5266E-06	3.0353E-05
-0.0999	-1.4705E-04	-1.1034E-04	-5.6058E-05	-2.0011E-05	0.0000E+00	-4.6288E-06	2.2573E-05	9.1181E-06	1.5477E-05
0.0000	0.0000E+00	0.0000E+00	0.0000E+00	0.0000E+00	0.0000E+00	0.0000E+00	0.0000E+00	0.0000E+00	0.0000E+00
0.0999	-1.5477E-05	-9.1181E-06	-2.2573E-05	4.6288E-06	0.0000E+00	2.0011E-05	5.6058E-05	1.1034E-04	1.4705E-04
0.2000	-3.0353E-05	-3.5266E-06	-3.6522E-05	-8.1034E-06	0.0000E+00	6.3218E-05	1.2582E-04	2.2288E-04	2.3897E-04
0.3000	-8.6339E-05	-5.5598E-05	-1.0176E-04	-4.2042E-05	0.0000E+00	1.1136E-04	1.8642E-04	3.1258E-04	3.2579E-04
0.4001	-1.4649E-04	-1.3306E-04	-1.5945E-04	-5.3939E-05	0.0000E+00	1.6135E-04	2.7900E-04	4.2142E-04	4.2212E-04

**Table 7** Coupled non-dimensional force  $N_{coup}'(r', \delta)$  with respect to yaw rate and rudder angle

$r' \backslash \delta$	-0.3491	-0.2618	-0.1745	-0.0873	0.0000	0.0873	0.1745	0.2618	0.3491
-0.4001	1.9664E-04	1.7975E-04	1.3176E-04	5.6064E-05	0.0000E+00	-4.5222E-05	-7.6196E-05	-8.5088E-05	-6.8309E-05
-0.3000	1.6013E-04	1.3581E-04	9.6289E-05	3.9105E-05	0.0000E+00	-3.2789E-05	-4.0580E-05	-4.1706E-05	-3.2202E-05
-0.2000	1.1606E-04	9.8663E-05	6.4774E-05	2.1217E-05	0.0000E+00	-1.1807E-05	-1.3636E-05	-1.1556E-05	-9.0645E-06
-0.0999	7.1287E-05	5.0039E-05	2.8824E-05	4.2862E-06	0.0000E+00	-1.9530E-06	-9.0946E-06	-1.0856E-05	-5.1526E-06
0.0000	0.0000E+00	0.0000E+00	0.0000E+00	0.0000E+00	0.0000E+00	0.0000E+00	0.0000E+00	0.0000E+00	0.0000E+00
0.0999	5.1526E-06	1.0856E-05	9.0946E-06	1.9530E-06	0.0000E+00	-4.2862E-06	-2.8824E-05	-5.0039E-05	-7.1287E-05
0.2000	9.0645E-06	1.1556E-05	1.3636E-05	1.1807E-05	0.0000E+00	-2.1217E-05	-6.4774E-05	-9.8663E-05	-1.1606E-04
0.3000	3.2202E-05	4.1706E-05	4.0580E-05	3.2789E-05	0.0000E+00	-3.9105E-05	-9.6289E-05	-1.3581E-04	-1.6013E-04
0.4001	6.8309E-05	8.5088E-05	7.6196E-05	4.5222E-05	0.0000E+00	-5.6064E-05	-1.3176E-04	-1.7975E-04	-1.9664E-04

## 6. Results of Turning Motion Simulations and Sea Trial of Underwater Vehicle

Based on hydrodynamic force and moment data from CFD, motion simulations were performed. Combining Eqs. (3), (4), (8), and (9) and removing high-order terms, 2-DOF equations of motion for the sway and yaw were constructed as follows:

$$\begin{aligned} m[\dot{v} + ur + x_g \dot{r}] &= \left( Y_v' v' + Y_{v|v}|v'| + Y_r' r' + Y_{r|r}|r'| + \right) \times (0.5\rho U^2 L^2) \\ &\quad \left( Y_{\delta}' \delta + Y_{coup}'(r', v') + Y_{coup}'(r', \delta) \right) \\ I_{zz} \dot{r} + m[x_g(\dot{v} + ur) + y_g vr] &= \left( N_v' v' + N_{v|v}|v'| + N_r' r' + N_{r|r}|r'| + \right) \times (0.5\rho U^2 L^3) \\ &\quad \left( N_{\delta}' \delta + N_{coup}'(r', v') + N_{coup}'(r', \delta) \right) \end{aligned} \quad (11)$$

The sway velocity ( $v$ ) and yaw rate ( $r$ ) in the body-fixed frame were calculated by solving these equations. The surge velocity ( $u$ ) was considered as constant. The values in the body-fixed frame were then transformed to the earth-fixed frame using Eq. (3), and the turning radius and drift angle were obtained by deriving the trajectory and attitude of the vehicle. The simulations were carried out using MATLAB.

Three kinds of simulations were performed. In one of them, coupled hydrodynamic forces and moments are not applied (Case A). In another, only coupled terms between the yaw rate and drift angle ( $Y_{coup}'(r', v')$  and  $N_{coup}'(r', v')$ ) are applied (Case B). In the third one, all coupled terms ( $Y_{coup}'(r', v')$ ,  $N_{coup}'(r', v')$ ,  $Y_{coup}'(r', \delta)$  and  $N_{coup}'(r', \delta)$ ) are applied (Case C). The initial velocity is 4.15 m/s because this it makes it easy to compare the results with sea trial data. The rudder angle was set to  $-20$  degrees to turn with a positive yaw rate.

Next, we performed a sea trial with a vehicle that has the same geometry as in the simulations. After level flight via way-points, the underwater vehicle steadily turned for 3 minutes with a rudder angle of  $-20$  degrees. An inertial measurement unit (IMU) measured the translational acceleration and angular rate of the underwater vehicle, and a guidance and control unit (GCU) calculated and recorded flight data such as the velocity and Euler angles in the earth-fixed frame and the yaw rate in the body-fixed frame. During the sea trial, the speed and depth of the underwater vehicle were constantly controlled. Fig. 30 shows the scenario of the sea trial in this study.

Through the simulation and sea trial, we can obtain the turning

performance, turning radius, drift angle, advance, and tactical diameter. These are defined in Fig. 31. In the case of the sea trial, the turning radius can be calculated with the yaw rate and overall speed ( $R = U/r$ ), and the drift angle can be calculated with the difference between the Euler angle and the flow's incidence angle from the X velocity and Y velocity in the earth-fixed frame. The advance and tactical diameter are estimated with the Euler angle, X velocity, and Y velocity in the earth-fixed frame.

The simulation and sea trial results of the turning motion are shown in Table 8. These values are the average of the steady turning period of the underwater vehicle for 3 minutes. The non-dimensional yaw rates ( $r' = rL/U$ ) are 0.289–0.377, which is in the range of the CFD analysis (0–0.4). When coupled terms are not included, the turning radius, advance, and tactical diameter are smaller, and the drift angle is bigger than the sea trial data.

When coupled terms between the yaw rate and drift angle ( $Y_{coup}'(r', v')$  and  $N_{coup}'(r', v')$ ) are included, the turning radius, advance, and tactical diameter become bigger, and the drift angle becomes smaller because additional force and moment opposite to the rotational direction are produced by the interaction. When coupled terms between the yaw rate and rudder angle ( $Y_{coup}'(r', \delta)$  and  $N_{coup}'(r', \delta)$ ) are included, the turning radius, advance, and tactical diameter become smaller, and the drift angle becomes bigger because additional force and moment in the rotational direction are produced by the interaction.

The additional force and moment from the coupled terms of the simulation (Case C) are shown in Figs. 32–33. The simulation results considering the coupled hydrodynamic force and moment terms agree well with the sea trial results, and the interactions between the yaw rate and drift/rudder angle affect the turning performance of the underwater vehicle. In particular, the effects of the coupled terms for the yaw rate and drift angle are critical. Based on the difference between the results of the simulations and sea trial, it is estimated that the additional force and moment terms due to the combination of the yaw rate and drift angle are bigger in the real flow.

The non-dimensional yaw rate, drift angle, and overall speed are shown in Figs. 34–36. The turning motion starts at 0 s, and the underwater vehicle turns steadily for 3 minutes from 10 s to 190 s. Fig. 37 shows the trajectory of the underwater vehicle. Because there are some disturbances in the sea, the sea trial data have fluctuation, and the trajectory is slightly biased relative to the simulation results.

**Table 8** Turning performance of underwater vehicle by simulations and sea trial

Item		Turning radius (m)	Drift angle (deg)	Advance (m)	Tactical diameter (m)	Non-dimensional yaw rate
Simulations (Case A)	Not including coupled terms	17.5	9.2	27.5	36.4	0.377
Simulations (Case B)	Including only $Y_{coup}'(r', v')$ and $N_{coup}'(r', v')$	22.8	7.4	31.2	46.2	0.289
Simulations (Case C)	Including $Y_{coup}'(r', v')$ , $N_{coup}'(r', v')$ , $Y_{coup}'(r', \delta)$ and $N_{coup}'(r', \delta)$	21.9	7.7	30.6	44.6	0.301
	Sea trial	22.8	7.7	31.1	45.0	0.289

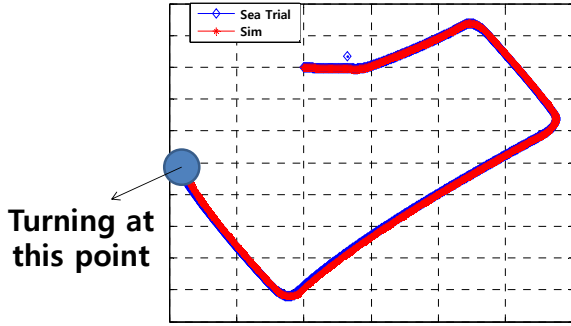


Fig. 30 The scenario of the sea trial

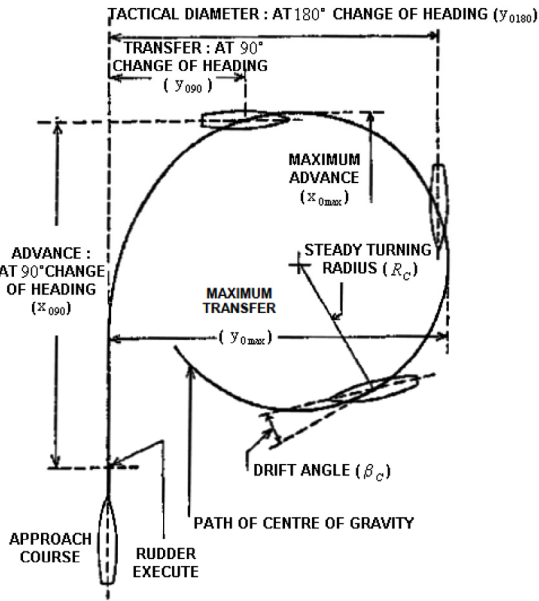


Fig. 31 Definition of turning radius, drift angle, advance and tactical diameter in turning circle motion

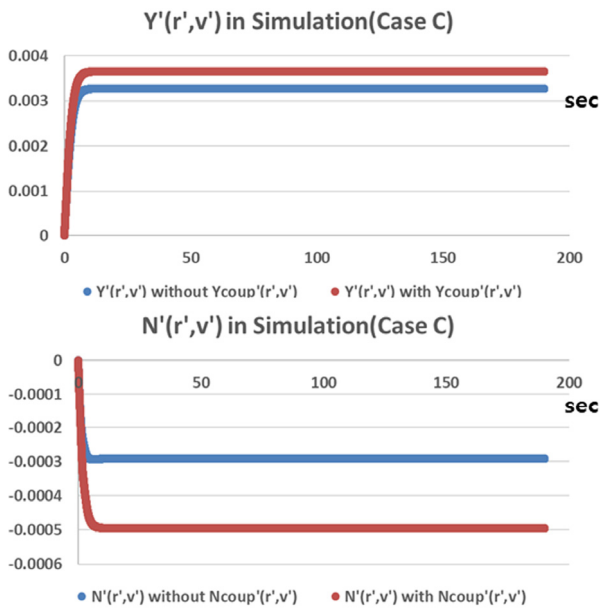


Fig. 32 Additional force and moment due to interaction between yaw rate and drift angle in turning motion simulation (Case C)

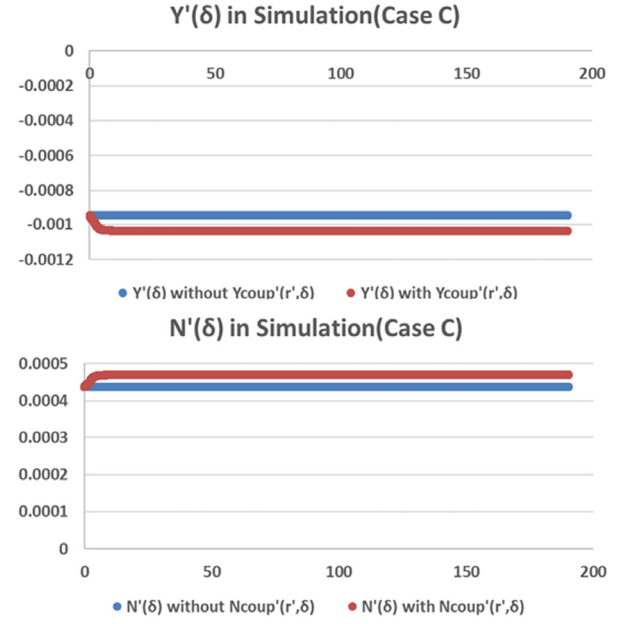


Fig. 33 Additional force and moment due to interaction between yaw rate and rudder angle in turning motion simulation (Case C)

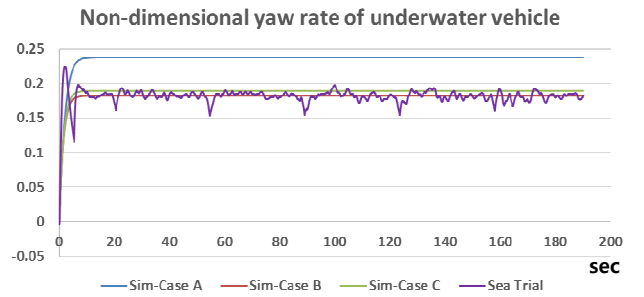


Fig. 34 Non-dimensional yaw rate of underwater vehicle during turning motion

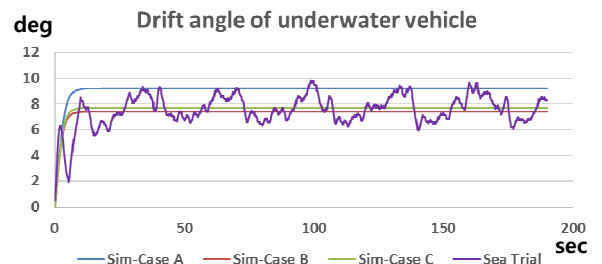


Fig. 35 Drift angle of underwater vehicle during turning motion

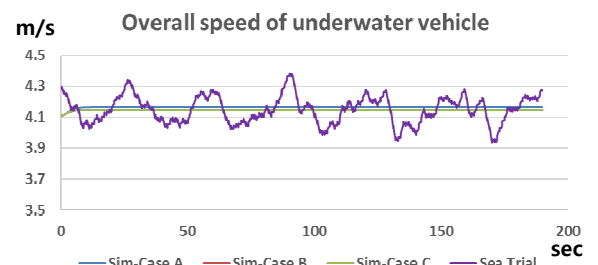
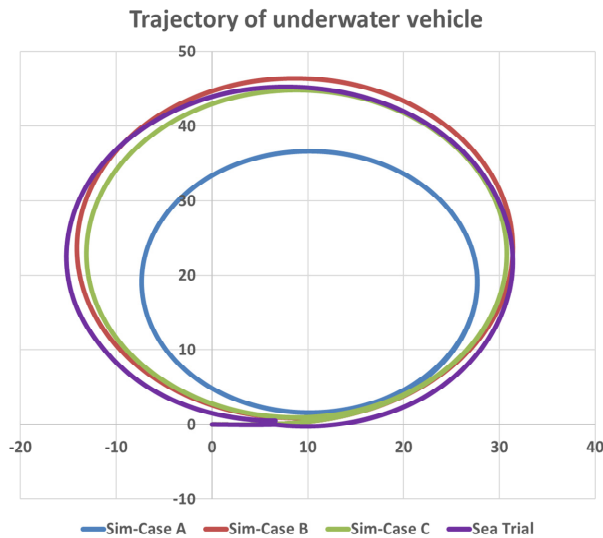


Fig. 36 Overall speed of underwater vehicle during turning motion



**Fig. 37** Trajectory of underwater vehicle during turning motion

## 7. Conclusion

In this study, we predicted the steady turning ability of a symmetrical underwater vehicle while considering interactions between yaw rate and drift/rudder angle through a simulation-based methodology. As a result, we came to the following conclusions:

- (1) The feasibility of the hydrodynamic force and moment from the CFD was verified by comparing the results of the static drift/rudder simulations to those of the VPMM tests.
- (2) Rotating arm simulations with the drift and rudder angle were performed, and we confirmed the existence of interactions. Coupled terms from the interactions have strong non-linearities and different tendencies according to the relative direction of the yaw rate and drift/rudder angle.
- (3) Turning motion simulations were carried out by solving 2-DOF equations based on hydrodynamic data from CFD. The coupled interaction terms should be considered to estimate the turning performance of the underwater vehicle more accurately.

In the future, we will research a transient and detailed analysis of the turning ability of the underwater vehicle by solving full 6-DOF equations that include all hydrodynamic, hydrostatic, added mass, and thrust terms. In addition, other types of maneuverability will be analyzed, such as depth changing and course-changing ability.

## References

- Ansys Inc. (2018). *Fluent Theory Guide 19.2*.
- Bae, J.Y., Sohn, K.H., & Kim, J. (2009). A Study on Manoeuvring Motion of Manta-Type Unmanned Undersea Vehicle. *Journal of the Society of Naval Architecture of Korea*, 46(2), 114–126. <https://doi.org/10.3744/STAK.2010.47.3.328>
- de Barros, E.A., & Dantas, J.L.D. (2012). Effect of a Propeller Duct on AUV Maneuverability. *Ocean Engineering*, 42, 61–70. <https://doi.org/10.1016/j.oceaneng.2012.01.014>
- Cheon, K.H., Seok, W.C., Park, J.Y., Seo, J.H., & Rhee, S.H. (2018). Virtual Captive Model Tests of Submarine with X-Form Configuration Using Dynamic Mesh Methods. *Journal of Computational Fluids Engineering*, 23(2), 86–93. <https://doi.org/10.6112/kscfe.2018.23.2.086>
- Dantas, J.L.D., & de Barros, E.A. (2013). Numerical Analysis of Control Surface Effects on AUV Manoeuvrability. *Applied Ocean Research*, 42, 168–181. <https://doi.org/10.1016/j.apor.2013.06.002>
- Dubbioso, G., Broglia, R., & Zaghi, S. (2017). CFD Analysis of Turning Abilities of a Submarine Model. *Ocean Engineering*, 129, 459–479. <https://doi.org/10.1016/j.oceaneng.2016.10.046>
- Feldman, J. (1979). DTNSRDC Revised Standard Submarine Equations of Motion (DTNSRDC SPD-0303-09). David W. Taylor Naval Slu'p Research and Development Center.
- Gertler, M., & Hagen, G.R. (1967). Standard Equations of Motion for Submarine Simulation. NSRDC-Report SR 009 01 01, Task 0102.
- Go, G.S., Ahn, H.T., & Ahn, J.H. (2017). Simulation-Based Determination of Hydrodynamic Derivatives and 6DOF Motion Analysis for Underwater Vehicle. *Journal of Ocean Engineering and Technology*, 31(5), 371–377. <https://doi.org/10.26748/KSOE.2017.10.31.5.371>
- Healey, A.J., & Lienard, D. (1993). Multivariable Sliding-Mode Control for Autonomous Underwater Vehicles. *IEEE Journal of Ocean Engineering*, 18(3), 327–339.
- Huang, H., Zhou, Z., Li, H., Zhou, H., & Xu, Y. (2020). The Effects of the Circulating Water Tunnel Wall and Support Struts on Hydrodynamic Coefficients Estimation for Autonomous Underwater Vehicles. *International Journal of Naval Architecture and Ocean Engineering*, 12, 1–10. <https://doi.org/10.1016/j.ijnaoe.2019.04.008>
- Jeon, M.J., Yoon, H.K., Hwang, J.H., & Cho, H.J. (2018). Analysis of the Dynamic Characteristics for the Change of Design Parameters of an Underwater Vehicle Using Sensitivity Analysis. *International Journal of Naval Architecture and Ocean Engineering*, 10, 508–519. <https://doi.org/10.1016/j.ijnaoe.2017.10.010>
- Jeong, J.H., Han, J.H., Ok, J.H., Kim, H.D., Kim, D.H., Shin, Y.K., & Lee, S.K. (2016). Prediction of Hydrodynamic Coefficients for Underwater Vehicle Using Rotating Arm Test. *Journal of Ocean Engineering and Technology*, 30(1), 25–31. <https://doi.org/10.5574/KSOE.2016.30.1.025>
- Kim, J.H., & Chung, W.K. (2007). Thruster Modeling for Underwater Vehicle with Ambient Flow Velocity and its Incoming Angle. *The Journal Society of Korea Robotics Society*, 2(2), 109–118.
- Kim, T.W., Kang, T.J., Park, W.G., & Jung, C.M. (2015). Estimation

- of Roll Coefficient of Underwater Vehicle Using a Calculation of Hydrodynamic Forces. *Journal of Computational Fluids Engineering*, 20(2), 81–87. <https://doi.org/10.6112/kscfe.2015.20.2.081>
- Kim, Y.G., Yun, G.H., Kim, S.Y., & Kim, D.J. (2012). Captive Model Test of Submerged Body Using CPMC. *Journal of the Society of Naval Architecture of Korea*, 49(4), 296–303. <https://doi.org/10.3744/SNAK.2012.49.4.296>
- Nguyen, T.T., Yoon, H.K., Park, Y.B., & Park, C.J. (2018). Estimation of Hydrodynamic Derivatives of Full-Scale Submarine using RANS Solver. *Journal of Ocean Engineering and Technology*, 32(5), 386–392. <https://doi.org/10.26748/KSOE.2018.6.32.5.386>
- Park, J.H., Shin, M.S., Choi, J.Y., Hwang, J.H., Shin, Y.H., & Kim, Y.G. (2016). An Experimental Study on Effect of Angle of Attack on Elevator Control Force for Underwater Vehicle with Separate Fixed Fins. *Journal of Ocean Engineering and Technology*, 30(4), 243–252. <https://doi.org/10.5574/KSOE.2016.30.4.243>
- Park, J.Y., Kim, N.W., Rhee, K.P., Kim, C.K., Jung, C.M., Ahn, K.S., & Lee, S.K. (2015). Study on Coning Motion Test for Submerged Body. *Journal of Ocean Engineering and Technology*, 29(6), 436–444. <https://doi.org/10.5574/KSOE.2015.29.6.436>
- Seol, D.M., Rhee, K.P., & Yeo, D.J. (2005). An Experimental Study of the Submerged Depth Effect on the Manoeuvrability in a Horizontal Plane of an Underwater Vehicle. *Journal of the Society of Naval Architecture of Korea*, 42(6), 551–558.
- Wang, X., & Liang, S. (2019). Maneuverability Analysis of a Novel Portable Modular AUV. *Hindawi Mathematical Problems in Engineering*, 2019, 1–17. <https://doi.org/10.1155/2019/1631930>

### Author ORCIDs

Author name	ORCID
Park, Jeong-Hoon	0000-0002-4813-6615
Shin, Myung-Sub	0000-0002-5515-9620
Jeon, Yun-Ho	0000-0002-5979-0217
Kim, Yeon-Gyu	0000-0002-0344-5297



# An Experimental Study on Wave Absorber Performance of Combined Punching Plate in a Two-Dimensional Mini Wave Tank

Hyen-Cheol Jung<sup>1</sup> and Weoncheol Koo<sup>2</sup>

<sup>1</sup>Researcher, Department of Naval Architecture and Ocean Engineering, Inha University, Incheon, Korea

<sup>2</sup>Professor, Department of Naval Architecture and Ocean Engineering, Inha University, Incheon, Korea

**KEY WORDS:** Wave absorber, Punching plate, Reflected wave, 2D mini wave tank, Reflection coefficient

**ABSTRACT:** In order to perform a precise wave tank experiment, it is necessary to maintain the incident wave generated by the wavemaker in a steady state and to effectively remove the reflected waves. In this paper, a combined sloping-wall-type punching plate wave absorber was proposed to attenuate reflected waves effectively in a two-dimensional mini wave tank. Using the four-point reflection separation method, the reflected waves were measured to determine the reflection coefficients. Experiments were conducted under various punching plate porosities, sloping plate angles, and incident wave conditions to evaluate the performance of the combined punching plate wave absorber. The most effective wave absorbing performance was achieved when the porosity was 10% and the inclination angle of the punching plate was 18.6° under the present condition. It was also found that the installation of the sloping plate could improve the wave attenuation performance by generating the shoaling effect of the incident wave.

## 1. Introduction

A two-dimensional (2D) wave tank generates water waves and has been used as an experimental device to perform various hydrodynamic analyses; for example, it is used to investigate the wave-wave and wave-body interactions. However, such a wave tank generates unnecessary reflected waves at the end wall of the tank owing to its limited physical size. Therefore, it is crucial to install an efficient wave absorber to continuously measure the waves generated by the wave maker and maximize the observation range.

Jung and Cho (1999) confirmed that when used as a wave absorber, a flat punching plate performs better than conventional wave absorbers. Cho and Hong (2004) confirmed that the porosity of the punching plate should be 10% and its sloping angle should be within 10°–20° to achieve maximum wave absorption performance when an inclined punching plate is used as a wave absorber.

In this paper, we proposed a combined wave absorber by combining a flat punching plate and a sloping punching plate to minimize the reflected waves in a 2D mini wave tank. Additionally, an experimental study was conducted to evaluate the performance of the proposed punching plate. We separated the incident waves and the

reflected waves using the least square method (Mansard and Funke, 1980) to determine the performance of the wave absorber. This method is to minimize the sum of squares of error between the waveform obtained through an equation and the measured waveform. This method usually uses three wave gauges to measure wave elevations. However, in this study, we measured the incident waves and the separated reflected waves by installing four wave gauges for better accuracy.

The sections of the measured waves to be analyzed should be selected appropriately to achieve an accurate separation between the incident waves and reflected waves. The reflected waves were measured in the steady-state section until the incident waves were reflected from the wave absorber at the end of the tank and then reflected again from the wave maker and reached the same wave gauge. The measured waves were separated into incident waves and reflected waves. In this study, we proposed a novel combined punching plate wave absorber that combined a flat punching plate and sloping punching plate. Additionally, we determined the wave absorption performance, and porosity and slope conditions required for the optimal wave absorption performance of the proposed punching plate.

Received 14 February 2021, revised 8 March 2021, accepted 12 March 2021

Corresponding author Weoncheol Koo: +82-32-860-7348, [wckoo@inha.ac.kr](mailto:wckoo@inha.ac.kr)

© 2021, The Korean Society of Ocean Engineers

This is an open access article distributed under the terms of the creative commons attribution non-commercial license (<http://creativecommons.org/licenses/by-nc/4.0>) which permits unrestricted non-commercial use, distribution, and reproduction in any medium, provided the original work is properly cited.

## 2. Separation of Reflected Waves

In this study, we installed four wave gauges at appropriate intervals in the wave tank to separate the incident and reflected waves. We used the reflected wave separation method proposed by Goda and Suzuki (1977) using the measured wave height data, referring to Suh et al. (2001) and Park et al. (1992). When the frequency of the incident wave is  $\omega$ , the incident wave elevation ( $\zeta_I$ ) and the reflected wave elevation ( $\zeta_R$ ) can be expressed using Eqs. (1) and (2), respectively.

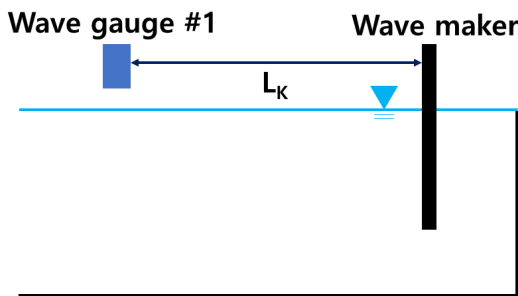
$$\zeta_I = \frac{H_I}{2} \cos(kx - \omega t + \varepsilon_I) \quad (1)$$

$$\zeta_R = \frac{H_R}{2} \cos(kx + \omega t + \varepsilon_R) \quad (2)$$

Here,  $H_I$  and  $H_R$  denote the incident wave height and reflected wave height, respectively,  $\varepsilon_I$  and  $\varepsilon_R$  denote the phase difference of the incident wave and reflected wave, respectively, and  $k$  denotes the wave number. The time series of waves measured at a particular position by the superposition method of the incident and reflected waves can be represented by Eq. (3):

$$\zeta_n(t) = \frac{H_I}{2} \cos(kl_n - \omega t + \varepsilon_I) + \frac{H_R}{2} \cos(kl_n + \omega t + \varepsilon_R) + e_n(t) \quad (3)$$

where  $e_n(t)$  refers to the measurement error for the non-linear interference or noise of waves included in the wave height data measured by the  $n^{\text{th}}$  measurement position ( $n^{\text{th}}$  wave gauge), and  $l_n$  indicates the distance from the reference point to the  $n^{\text{th}}$  measurement position.



**Fig. 1** Distance between the wave maker and the first wave gauge

The reference point was set at a distance of 2 m ( $L_k$ ) from the wave maker to the first wave gauge (Fig. 1). If Eq. (3) was organized using a trigonometric theorem, it can be represented as Eq. (4), and the equation for  $X$  is provided in the appendix.

$$\begin{aligned} \zeta_n(t) = & X_1 \cos(\omega t - kl_n) + X_2 \cos(\omega t + kl_n) \\ & + X_3 \sin(\omega t - kl_n) - X_4 \sin(\omega t + kl_n) + e_n(t) \end{aligned} \quad (4)$$

Meanwhile, the measurement data error for separating the incident and reflected waves can be expressed as the sum of the squares of errors included in the measurement data, as shown in Eq. (5).

$$E = \sum_{n=1}^N \int_0^{T_m} (e_n(t))^2 dt \quad (5)$$

$$\frac{\partial E}{\partial X_j} = 0 \quad (6)$$

Here,  $N$  represents the number of wave gauges, and  $T_m$  represents the measured time. With error ( $E$ ), which is the sum of measurement errors, if the differential value for  $X_j$ , a coefficient related to the wave heights and phases of incident and reflected waves, becomes 0, the error for each coefficient can be minimized. If four  $X_1$ – $X_4$  were calculated using this method, the height and phase of the incident and reflected waves can be obtained. Eq. (7), which is a linear algebraic matrix equation, can be composed using Eq. (6), which can minimize the minimum/maximum of the error ( $E$ ):

$$\begin{pmatrix} c_{11} & c_{12} & c_{13} & c_{14} \\ c_{21} & c_{22} & c_{23} & c_{24} \\ c_{31} & c_{32} & c_{33} & c_{34} \\ c_{41} & c_{42} & c_{43} & c_{44} \end{pmatrix} \begin{pmatrix} X_1 \\ X_2 \\ X_3 \\ X_4 \end{pmatrix} = \begin{pmatrix} F_1 \\ F_2 \\ F_3 \\ F_4 \end{pmatrix} \quad (7)$$

where  $C_{ij}$  expresses the right side of Eq. (4) as a trigonometric function, and  $F_j$  denotes the wave measured at each wave gauge. This equation is provided in detail in the appendix. By calculating Eq. (7), the coefficient  $X_i$  can be obtained. Finally, Eqs. (8)–(11) were applied to calculate the wave height and phase of the incident and reflected waves.

$$\varepsilon_I = \tan^{-1} \frac{X_3}{X_1} \quad (8)$$

$$\varepsilon_R = \tan^{-1} \frac{X_4}{X_2} \quad (9)$$

$$H_I = \frac{2X_1}{\cos(\varepsilon_I)} \quad \text{or} \quad \frac{2X_3}{\sin(\varepsilon_I)} \quad (10)$$

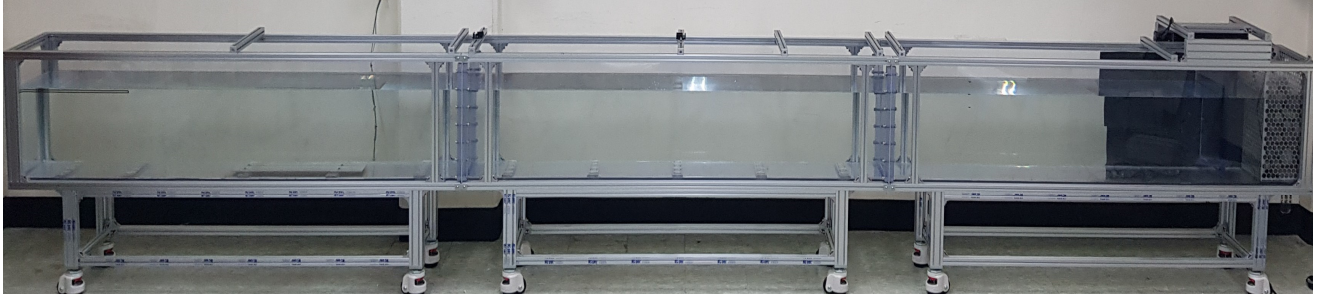
$$H_R = \frac{2X_2}{\cos(\varepsilon_R)} \quad \text{or} \quad \frac{2X_4}{\sin(\varepsilon_R)} \quad (11)$$

## 3. Experimental Equipment and Description

### 3.1 Two-dimensional Wave Tank

In this experimental study, we used the 2D mini wave tank in Inha University. The wave tank was 0.3 m wide, 6 m long, and 0.5 m deep. As the bottom and sides of the tank were made of transparent acrylic material, the waves could be observed from any direction (Fig. 2). The





**Fig. 2** Overview of Two-dimensional mini wave tank

piston-type wave maker was installed in this tank (not an active-damping wave maker). The experiment was conducted by excluding the effect of reflected waves by measuring the wave before the generated wave was re-reflected by the wave maker. A 0.1 s period interval was used in a 0.8–1.2 s range of the incident wave period, and the wavelength was 0.98–1.86 m.

Uniform regular waves were generated at a wave height of 0.5 cm, 1 cm, 2 cm, and 3 cm, respectively. Wave data were collected 20 times per second using wave gauges. Fig. 3 shows the side view and plan view of the overall schematics of the 2D mini wave tank with the punching plates installed. Table 1 shows the experimental conditions for wave length for each wave period.

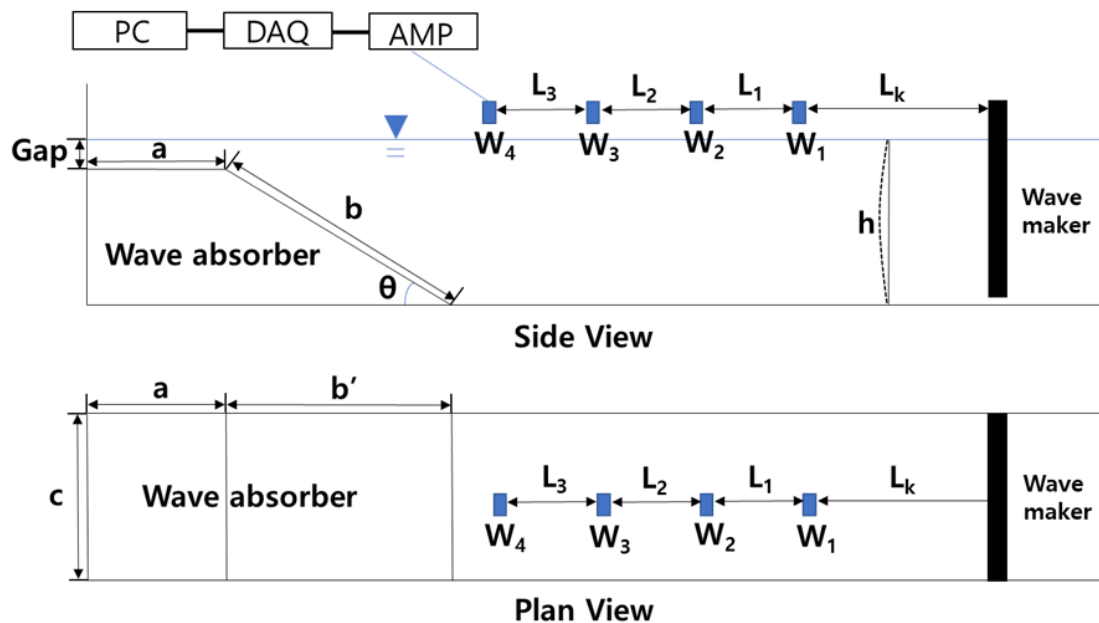
**Table 1** Wave conditions

Wave period	Wave length
0.8 s	0.977 m
0.9 s	1.201 m
1.0 s	1.425 m
1.1 s	1.645 m
1.2 s	1.861 m

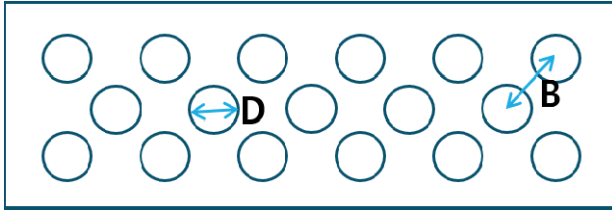
In the side view shown in Fig. 3, the water depth ( $h$ ) was 0.35 m, and the flat punching plate (Position A) was installed such that it was submerged 0.01 m (Gap) from the free surface. The ultrasonic wave gauges were named as wave gauge #1 ( $W_1$ ), #2 ( $W_2$ ), #3 ( $W_3$ ), and #4 ( $W_4$ ), respectively. The spacing between each wave gauge was all set uniformly to 0.3 m, and the spacing ( $L_k$ ) between the wave maker and wave gauge #1 ( $W_1$ ) was set to be 2 m considering the evanescent wave mode. The length ( $a$ ) of the flat punching plate was 0.5 m, and in Case 1, the length ( $b$ ) and angle ( $\theta$ ) of the sloping punching plate were 1 m and  $18.6^\circ$ , respectively. The experiment was conducted on three conditions for the length ( $b$ ) and angle ( $\theta$ ) of the sloping punching plate. In the plan view of Fig. 3, the width of the wave tank ( $c$ ) was 0.3 m, and in Case 1, the projected length ( $b'$ ) of the sloping punching plate was 0.94 m. The signals measured by the ultrasonic wave gauges were amplified using an amplifier (AMP) and sent to a data acquisition device (DAQ). Then, the data were stored and analyzed on a computer.

### 3.2 Punching Plate Wave Absorber

The wave absorber was installed at the end of the mini wave tank by combining a flat punching plate and a sloping punching plate. Fig. 4 shows a schematic diagram of the punching plates used in the wave



**Fig. 3** Overview of an experimental setup

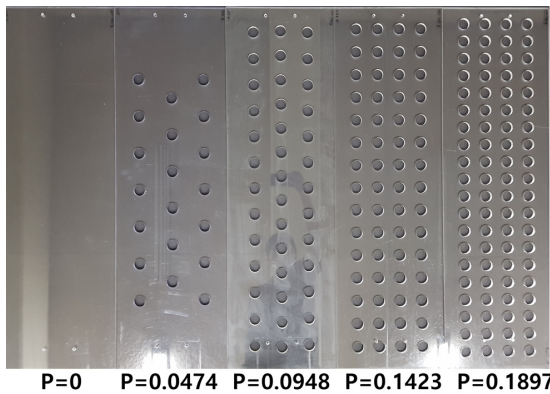


**Fig. 4** Conceptual drawing of a punching plate wave absorber

absorber. Holes of the same diameter ( $D$ ) and spacing ( $B$ ) were drilled onto the plates to maximize the wave absorption effect.  $D$  and  $B$  of all punching plates were identical, and the number of pores (circles) varied depending on the porosity of the punching plate. The punching plates were fabricated using an acrylic material having a thickness of 10 mm.

Fig. 5 shows the punching plate corresponding to the flat plate of the combined wave absorber. The dimension of the flat punching plate was  $500 \times 298$  mm. In this study, porosity ( $P$ ) is given as a ratio of the perforated area to the total area of the plate.

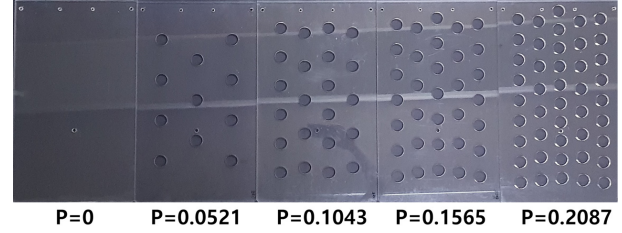
Fig. 6 shows the sloping punching plate with various porosities having the dimension of  $1000 \times 298$  mm, and Table 2 shows the dimension of the flat and sloping punching plates. Each punching plate was fabricated with a porosity of approximately 0%–20% (Table 3). In this study, we conducted the experiment by changing the installation angle and length (Table 2) at a porosity of 0% ( $P = 0$ ) for the sloping punching plate (b).



**Fig. 6** Various porosities of sloping punching plate

**Table 2** Dimension of wave tank with a sloped wave absorber

Parameter	Condition		
	Case 1	Case 2	Case 3
$a$ (Flat plate length)		0.5 m	
$b$ (Sloping plate length)	1 m	0.53 m	0.33 m
$b'$ (Sloping projection length)	0.94 m	0.41 m	0 m
$L$ (Wave gauge interval)		0.3 m	
$L_k$		2 m	
$h$ (Water depth)		0.35 m	
Gap		0.01 m	
$c$ (Tank width)		0.3 m	
$\theta$ (Theta)	18.6°	39.3°	90°



**Fig. 5** Various porosities of flat punching plates

**Table 3** Dimension of punching plates

	Porosity (%)	Number of circles	Diameter of hole ( $D$ ) (mm)
Flat plate	0	-	-
	5.22	11	30
	10.44	22	30
	15.65	33	30
	20.87	44	30
Sloping plate	0	-	-
	4.74	20	30
	9.49	40	30
	14.23	60	30
	18.98	80	30

### 3.3 Ultrasonic Wave Height Gauge

In this experiment, we used Senix TSPC-30S2 ultrasonic wave gauges, whose picture and specifications are shown in Fig. 7 and Table 4. Each ultrasonic wave gauge was installed in the vertical direction on the free surface. This device measures the height of the free surface by measuring the time that the ultrasonic wave generated by the wave gauge is reflected at the free surface. The wave gauges have a built-in temperature compensation circuit because the propagation speed of ultrasonic waves is slower in air than in water. Furthermore, the change in speed of ultrasonic waves due to temperature change cannot be ignored.



**Fig. 7** Ultrasonic wave height gauge (TSPC-30S2)

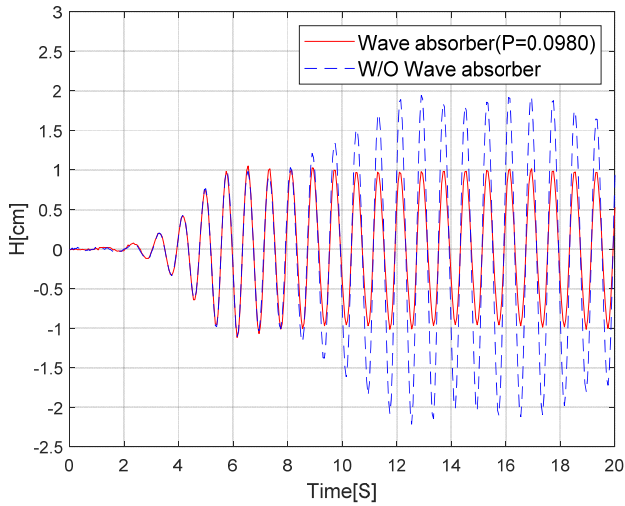
**Table 4** Specifications of TSPC-30S2

Measuring distance	4.4–61 cm (Max. 91 cm)
Resolution	0.086 mm
Sampling rate	20 Hz (50 ms)
Interface	RS-485

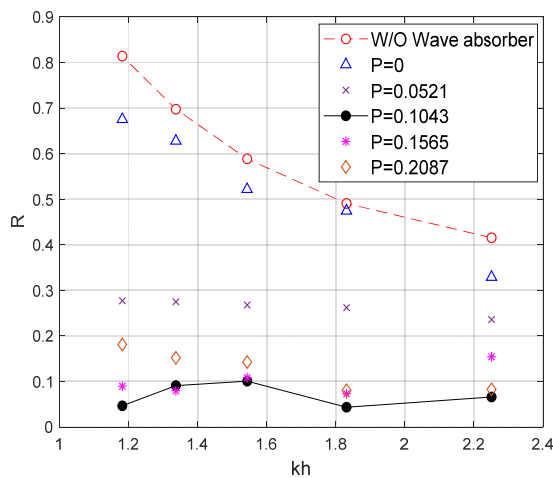
## 4. Results and Analysis of Reflected Wave Separation Experiment

Fig. 8 shows the time-series results comparing the change in the free

surface when the wave absorber was installed and when it was not installed. Here, a combined punching plate with an average porosity of 10% ( $P = 0.0980$ ), which combined a flat punching plate with a porosity of 10% ( $P = 0.1043$ ) and a sloping punching plate with a porosity of 10% ( $P = 0.0948$ ), was installed as the wave absorber, and the time series data measured by the third wave gauge were compared. The wave period of the incident wave was 1.2 s and the wave height was 2 cm. The free surface elevation measured between approximately 6 and 9 s after the generation of an incident wave confirmed that the steady-state was shown irrespective of whether the wave absorber was installed or not. Therefore, it was determined that the reflected waves did not enter the measurement section of the mini wave tank completely. However, after approximately 9 s, when the incident wave was reflected from the end wall of the tank entered the measurement section after being re-reflected by the wave maker plate, the free surface elevation increased by approximately 100% in the case of no wave absorber. On the other hand, when the combined punching plate



**Fig. 8** Time series of measured wave elevations at the 3rd wave gauge ( $T = 0.8$  s,  $H = 2$  cm)



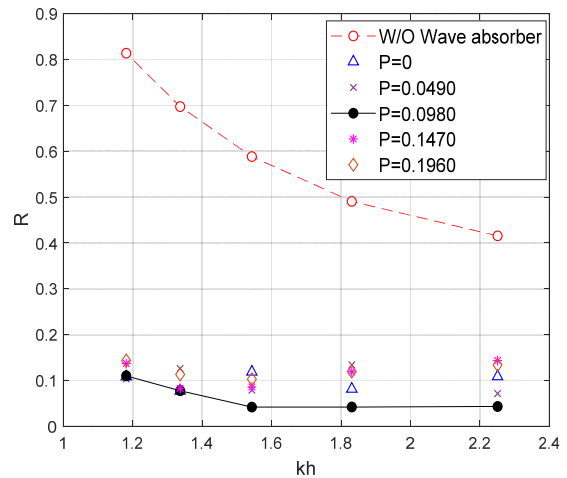
**Fig. 9** Comparison of reflection coefficients on various porosity conditions with a flat punching plate wave absorber ( $H = 2$  cm)

was installed, crest and trough values of the free surface elevations were well maintained in a section of 2 cm, i.e., the incident wave height. This meant that the incident wave was no longer reflected from the wave absorber and most of the energy was dissipated, thereby showing the wave absorption performance of the punching plate.

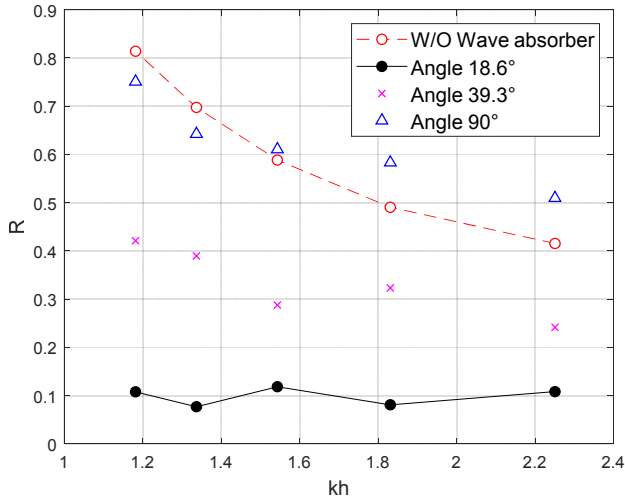
Based on these results, we compared the wave absorption performance of the flat punching plate (Fig. 9) and combined punching plate (Fig. 10) according to the porosity of the punching plate in terms of the reflection coefficient. Here,  $R$  denotes the reflection coefficient,  $k$  denotes the wave number, and  $h$  denotes the water depth. The incident waves were generated at 0.1 s intervals with wave height of 2 cm and wave period of 0.8–1.2 s. The experiment was performed using punching plates with five porosities ( $P = 0$ –0.2087).

Fig. 9 shows that the reflection coefficient is similar for when a flat punching plate with 0% porosity ( $P = 0$ ) is installed and when no punching plate is installed. Furthermore, the reflection coefficient generally increases from the short-wave to the long-wave. This shows that although the flat punching plate (0% porosity,  $P = 0$ ) has been installed, the incident waves are not attenuated by the flat plate alone. However, when the flat plate was porous, considerably superior wave absorption performance was observed, and particularly, good wave absorption performance was confirmed for long-waves. Furthermore, it was confirmed that the deviation of the reflection coefficient according to the wavelength was not very large. When the porosity of the flat punching plate was approximately 5% ( $P = 0.0521$ ), the reflection coefficient was less than or equal to 0.3, but when the porosity was approximately 10% ( $P = 0.1043$ ), the reflection coefficient was less than or equal to 0.1, i.e., it demonstrated the best wave absorption performance. However, for a large porosity of 20% ( $P = 0.2087$ ), the reflection coefficient increased rather slightly in the long-wave region ( $kh = 1.2$ ). In brief, when the porosity was 10% ( $P = 0.1043$ ) on the flat punching plate, the mean reflection coefficient was approximately 0.07, i.e., the best reflection coefficient.

Fig. 10 compares the reflection coefficient of different incident



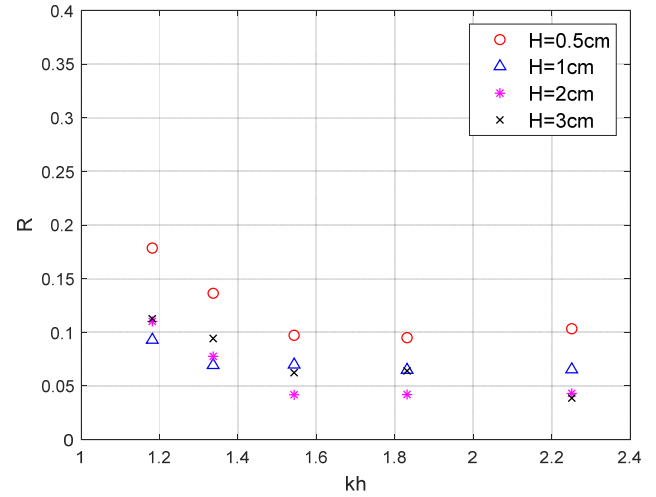
**Fig. 10** Comparison of reflection coefficients on various porosity conditions with a combined punching plate wave absorber ( $H = 2$  cm)



**Fig. 11** Comparison of reflection coefficients on various plate angles with a combined punching plate wave absorber ( $P = 0$ ,  $H = 2$  cm)

wavelengths for the combined punching plate. The porosity was identical between the flat plate and sloping plate in each condition. The combined punching plate was inclined at  $18.6^\circ$ . Compared with the flat punching plate case (Fig. 9), a significantly better wave absorption performance was observed with a reflection coefficient of approximately 0.1 for 0% porosity condition ( $P = 0$ ). Based on this, it was determined that the installation of the sloping plate results in a shoaling effect of incident waves, and the wave energy decreases due to the interaction with the flat plate. Similar to the case of the flat punching plate, it was confirmed that the best wave absorption performance (a low reflection coefficient) was observed for a porosity of 10% ( $P = 0.0980$ ) under the combined punching plate condition. This shows that the optimal porosity was generally approximately 10% irrespective of the incident wavelength. Cho (2013) also obtained similar results. Therefore, it can be expected that the energy loss rate of the incident wave is the largest when the porosity of the punching plate is 10%. As reported by Ko and Cho (2018), the load on the punching plates is expected to decrease if the porosity increases. This is because the pressure difference between the punching plates decreases. Furthermore, for the combined punching plate, the effect of installing the sloping punching plate is greater than the wave absorption performance produced by the porosity change.

Fig. 11 shows the comparison of wave absorption performance between various slope angles of the sloping plate of a combined wave absorber with 0% porosity ( $P = 0$ ). When the installation angle of the sloping plate was  $90^\circ$ , the result was very similar to that of the case where there was no wave absorber. Moreover, the reflection coefficient increased in the short-wave region. When the angle of the sloping plate was  $39.3^\circ$ , the reflection coefficient was approximately 0.3 to 0.4, showing a certain degree of wave absorption performance. However, when the slope angle was  $18.6^\circ$ , the best wave absorption performance was recorded. Therefore, for the given conditions of this experiment (incident wave period: 0.8–1.2 s, water depth: 0.35 m), it



**Fig. 12** Comparison of reflection coefficients on various wave heights with a combined punching plate wave absorber ( $P = 0.098$ , case 1)

was appropriate to maintain the angle of the sloping plate at approximately  $18.6^\circ$  to achieve effective wave absorption performance. Ko and Cho (2018) reported that the optimal angle for the sloping punching plate ranged from  $10^\circ$ – $20^\circ$ . Therefore, we determined the angle that can produce an appropriate shoaling effect when an incident wave enters the punching plate area. In this experiment, no breaking wave occurred on the sloping punching plate. However, some breaking waves occurred on the flat punching plate because the waves that entered the flat plate were reflected at the end wall of the wave tank, resulting in superposed waves.

Fig. 12 shows the comparison of the change in wave absorption performance of the combined punching plate at different incident wave heights. The sloping plate was inclined at  $18.6^\circ$  and the porosity of the combined punching plate was 10% ( $P = 0.098$ ). When the incident wave height was 0.5 cm, the reflection coefficient increased in all wave frequencies. This is because the installation depth of the flat punching plate was 1 cm below the free surface, so when the incident wave height is small, the wave absorption effect of the flat punching plate cannot be expected. When the wave height was greater than 1 cm, the reflection coefficient was less than or equal to 0.1, which showed significantly effective wave absorption performance. Generally, similar wave absorption performance was shown irrespective of the wave height. Furthermore, the reflection coefficient generally increases as the incident wavelength increases (as  $kh$  decreases). This result is similar to the conclusion of a study conducted by Yuan et al. (2013), which states that the reflection rate increases as the wave frequency increases on a sloping punching plate.

Overall, combined punching plates have better wave absorption performance than separated punching plates. As the flat plate is combined with the sloping plate, the incident water particles with a circular or elliptical trajectory produce a shoaling effect with the sloping plate, thereby increasing the wave height. Here, as the water particles near the free surface enter more above the flat plate, the wave



energy is attenuated at the pores of the flat plate, and additional energy is attenuated as the waves reflected from the end wall of the wave tank are superposed, thereby breaking the waves. The energy of wave particles below the free surface is consumed at the pores of the sloping plate. Therefore, it is understood that a significant amount of wave energy is attenuated on the flat punching plate, and additional wave energy is consumed by the sloping punching plate.

## 5. Conclusion

In this study, we proposed a combined wave absorber by combining a flat punching plate and a sloping punching plate. Additionally, the wave absorption performance of the proposed wave absorber was comparatively analyzed according to the porosity of the punching plates, existence/absence of the sloping punching plate, installation angle of the sloping plate, and incident wave height. The punching plate wave absorber was installed in a 2D mini wave tank having a length of 6 m to conduct the experiments. We installed four wave gauges and separated the reflected waves by using a least square method to analyze the reflection coefficient to determine the wave absorption performance.

For installing the punching plate wave absorber, it was confirmed via time series comparisons that the reflected waves were suppressed and incident waves of the steady-state were measured for a long time. When the flat punching plate was installed, the wave absorption performance was excellent at a porosity of 10% ( $P = 0.1043$ ).

When the combined punching plate was installed with a porosity of 10% ( $P = 0.0980$ ) with the punching plate having an installation angle of  $18.6^\circ$ , the reflection coefficient was reduced by up to 95%, thereby showing the most effective wave absorption performance. This means that the combination of a flat punching plate and a sloping punching plate can effectively attenuate the incident wave energy. When the incident wave height was greater than the installation depth of the flat punching plate, the difference in wave absorption performance due to the wave height change was not that large, and all cases showed excellent performance.

The installation angle of the sloping plate produces a shoaling effect when the incident wave enters the plate, thereby increasing the incident wave height. The wave absorption performance can be improved if more water particles enter above the flat punching plate. However, owing to the limitations of the experimental equipment and physical conditions, additional comparisons and a precise analysis of wave absorption performance are required for more segmented slope angles in the future.

## Conflict of interest

No potential conflict of interest relevant to this article was reported.

## Funding

This research was conducted with the support of the Korea Institute

for Advancement of Technology (KIAT) as a source of the “Industry Professional Manpower Competency Reinforcement Project” of the Ministry of Trade, Industry, and Energy. (2020 Future Ocean Plant Global Advanced Professional Training Project, No.: P0012646). In addition, This research is supported by the National Research Foundation of Korea, a basic research project in the field of science and engineering (NRF-2018R1D1A1B07040677).

## References

- Cho, I.H. (2013). Reflection and Transmission Coefficients by a Surface-Mounted Horizontal Porous Plate. *Journal of Korean Society of Coastal and Ocean Engineers*, 25(5), 327–334. <https://doi.org/10.9765/KSCOE.2013.25.5.327>
- Cho, I.H., & Hong, S.W. (2004). Development of a Wave Absorbing System Using an Inclined Punching Plate. *Journal of Ocean Engineering and Technology*, 18(1), 1–6.
- Goda, Y., & Suzuki, Y. (1977). Estimation of Incident and Reflected Waves in Random Wave Experiments. *Proceedings of 15<sup>th</sup> International Coastal Engineering*, Honolulu, Hawaii, United States, 828–845. <https://doi.org/10.1061/9780872620834.048>
- Jung, H.J., & Cho, I.H. (1999). Experimental Study of Wave-Absorbing Performance by Horizontal Punching Plates. *Journal of the Korean Society for Marine Environment & Energy*, 2(1), 40–48.
- Ko, C.H., & Cho, I.H. (2018). Reflection of Porous Wave Absorber Using Quasi-Linear Numerical Model. *Journal of Korean Society of Coastal and Ocean Engineers*, 30(1), 1–9. <https://doi.org/10.9765/KSCOE.2018.30.1.1>
- Mansard, E.P., & Funke, E.R. (1980). The Measurement of Incident and Reflected Spectra Using a Least Squares Method. *Proceedings of 17<sup>th</sup> International Coastal Engineering*, Sydney, Australia, 154–172. <https://doi.org/10.1061/9780872622647.008>
- Park, W.S., Oh, Y.M., & Chun, I.S. (1992). Separation Technique of Incident and Reflected Waves Using Least Squares Method. *Journal of Korean Society of Coastal and Ocean Engineers*, 4, 139–145.
- Suh, K., Park, W.S., & Park, B.S. (2001). Separation of Incident and Reflected Waves in Wave-Current Flumes. *Coastal Engineering*, 43(3–4), 149–159. [https://doi.org/10.1016/S0378-3839\(01\)00011-4](https://doi.org/10.1016/S0378-3839(01)00011-4)
- Yuan, Z.Z., Jung, E.C., & Hee-Chang, L.I.M. (2013). Study of a Sloping-Wall-Type Wave Absorber Placed in Various Sinusoidal Propagate Waves. *Proceedings of Spring Conference of The Korean Society of Mechanical Engineers*, 147–152.

## Author ORCIDs

Author name	ORCID
Jung, Hyen-Cheol	0000-0003-1274-8844
Koo, Weoncheol	0000-0002-4384-0996

## Appendix

The variables of Eq. (4) in the paper are represented by Eqs. (A1)–(A4).

$$X_1 = \frac{H_I}{2} \cos(\varepsilon_I) \quad (\text{A1})$$

$$X_2 = \frac{H_R}{2} \cos(\varepsilon_R) \quad (\text{A2})$$

$$X_3 = \frac{H_I}{2} \sin(\varepsilon_I) \quad (\text{A3})$$

$$X_4 = \frac{H_R}{2} \sin(\varepsilon_R) \quad (\text{A4})$$

The coefficients in Eq. (6) are represented by Eqs. (A5) and (A6).

$$C_{11} = \sum_{k=1}^N \int_0^{T_m} \cos^2(ut - kl_n) dt$$

$$C_{12} = C_{21} = \sum_{k=1}^N \int_0^{T_m} \cos(ut - kl_n) \sin(ut + kl_n) dt$$

$$C_{13} = C_{31} = \sum_{k=1}^N \int_0^{T_m} \cos(ut - kl_n) \sin(ut - kl_n) dt$$

$$C_{14} = C_{41} = \sum_{k=1}^N \int_0^{T_m} -\cos(ut - kl_n) \sin(ut + kl_n) dt$$

$$C_{22} = \sum_{k=1}^N \int_0^{T_m} \cos^2(ut + kl_n) dt$$

$$C_{23} = C_{32} = \sum_{k=1}^N \int_0^{T_m} \cos(ut + kl_n) \sin(ut - kl_n) dt$$

$$C_{24} = C_{42} = \sum_{k=1}^N \int_0^{T_m} -\cos(ut + kl_n) \sin(ut + kl_n) dt$$

$$C_{33} = \sum_{k=1}^N \int_0^{T_m} \sin^2(ut - kl_n) dt$$

$$C_{34} = C_{43} = \sum_{k=1}^N \int_0^{T_m} -\sin(ut - kl_n) \sin(ut + kl_n) dt$$

$$C_{44} = \sum_{k=1}^N \int_0^{T_m} \sin^2(ut + kl_n) dt \quad (\text{A5})$$

$$F_1 = \sum_{k=1}^N \int_0^{T_m} \cos(ut - kl_n) \zeta_n(t) dt$$

$$F_2 = \sum_{k=1}^N \int_0^{T_m} \cos(ut + kl_n) \zeta_n(t) dt$$

$$F_3 = \sum_{k=1}^N \int_0^{T_m} \sin(ut - kl_n) \zeta_n(t) dt$$

$$F_4 = \sum_{k=1}^N \int_0^{T_m} -\sin(ut + kl_n) \zeta_n(t) dt \quad (\text{A6})$$

# CFD Simulation of Multiphase Flow by Mud Agitator in Drilling Mud Mixing System

Tae-Young Kim<sup>1</sup>, Gyu-Mok Jeon<sup>2</sup> and Jong-Chun Park<sup>3</sup>

<sup>1</sup>Senior Technical Engineer, Technical Business Team, FunctionBay, Gyeonggi-do, Korea

<sup>2</sup>Graduate Student, Department of Naval Architecture and Ocean Engineering, Pusan National University, Busan, Korea

<sup>3</sup>Professor, Department of Naval Architecture and Ocean Engineering, Pusan National University, Busan, Korea

**KEY WORDS:** Mud mixing system, Mud agitator, Liquid-solid multi-phase flow, Distribution of bulk particles, Computational fluids dynamics (CFD)

**ABSTRACT:** In this study, a computational fluid dynamics (CFD) simulation based on an Eulerian-Eulerian approach was used to evaluate the mixing performance of a mud agitator through the distribution of bulk particles. Firstly, the commercial CFD software Star-CCM+ was verified by performing numerical simulations of single-phase water mixing problems in an agitator with various turbulence models, and the simulation results were compared with an experiment. The standard model was selected as an appropriate turbulence model, and a grid convergence test was performed. Then, a simulation of the liquid-solid multi-phase mixing in an agitator was simulated with different multi-phase interaction models, and lift and drag models were selected. In the case of the lift model, the results were not significantly affected, but Syamlal and O'Brien's drag model showed more reasonable results with respect to the experiment. Finally, with the properly determined simulation conditions, a multi-phase flow simulation of a mud agitator was performed to predict the mixing time and spatial distribution of solid particles. The applicability of the CFD multi-phase simulation for the practical design of a mud agitator was confirmed.

## 1. Introduction

Offshore drilling refers to a mechanical process of drilling mud to extract petroleum or natural gas through a wellbore in the seabed. The mud is a mixture of oil (or water) and bulk materials (barite, bentonite, polymer, etc.) and it has high viscosity. It can be used to remove cuttings, provide hydrostatic pressure, and cool down or lubricate the drill bit. There are many different types of facilities where offshore drilling operations take place, and the core system is a drilling system that is mainly maintained by mud-handling and bulk-handling systems.

When a drilling operation is being performed, many physical and chemical changes occur in the wellbore. In order to handle many changes in the well conditions and maintain the drilling process, bulk additives are added to drilling mud through a mixing system. Examples of additives include bentonite for increasing the density of the drilling mud, barite for increasing the viscosity, polymer for chemical control, surfactants, etc. In this process, a mud agitator performs the function of mixing both the mud and bulk, which are

pre-mixed in a mud tank, and the homogeneous material properties are maintained using the swirling motion of a mechanical impeller. The achievement of required material properties through the mud agitator is essential to stabilize a drilling system. Thus, it is important to analyze the multi-phase flow and system and guaranteeing safety.

There have been some experimental and numerical investigations for the design of agitators, including fundamental experiments regarding the change geometric shape of the impeller (Nagata et al., 1959), performance of agitation with various sizes of the impeller (Nienow, 1997), and experiments in regard to change torque and position of impeller with 45° pitched blades (Chang and Hur, 2000; Choi et al., 2013). Experimental measurement was done using a laser Doppler velocimeter (LDV), and numerical simulation was done for the flow patterns in an agitator relating to its geometric shape and power of agitation (Kumaresan and Joshi, 2006). Unsteady numerical simulation was done with a free surface in an agitator (Ahn et al., 2006), and a solid-liquid multiphase simulation was done using a granular flow model in the commercial software ANSYS-Fluent for multiphase interaction (Darelius et al., 2008). Numerical simulations

Received 1 February 2021, revised 3 March 2021, accepted 11 March 2021

Corresponding author Jong-Chun Park: +82-51-510-2480, [jcpark@pnu.edu](mailto:jcpark@pnu.edu)

© 2021, The Korean Society of Ocean Engineers

This is an open access article distributed under the terms of the creative commons attribution non-commercial license (<http://creativecommons.org/licenses/by-nc/4.0>) which permits unrestricted non-commercial use, distribution, and reproduction in any medium, provided the original work is properly cited.

were done to predict the solid particle distribution in an agitator using various baffle types (Kim et al., 2009) and various impeller speeds (Wadherkar et al., 2012), and a numerical simulation was done for particle distribution in an agitator using the commercial software STAR-CCM+ (Lo, 2012; Kubicki and Lo, 2012), etc..

In summary, many experimental investigations have been performed to design an agitator and predict the solid particle distribution in a stirred tank using an experiment, and it seems to be difficult to predict the mixing performance and to conduct an experiment directly for high-viscosity fluids. As an alternative way, computational fluid dynamics (CFD) simulations have also been carried out for predicting the performance of an impeller and the distribution of solid particles inside a mixing tank. However, for more practical application of a mud agitator to some equipment in an offshore plant, a multiphase simulation of solid-liquid flow should be performed with high-viscosity mud inside the tank.

In the present study, the numerical simulation of swirling and liquid-solid multiphase flow around a mechanical agitator system was carried out to investigate the distribution of bulk particles in a system using commercial CFD software, STAR CCM+ ver.8.04, based on an Eulerian-Eulerian approach. First, for verifying the CFD tool, water mixing problems for a model-scale agitator were simulated with various turbulence models, and the results of the simulation for the velocity components around the impeller were compared to those of experiments performed by Guida et al. (2009) and Guida (2010). Next, the liquid-solid multiphase flow in a mud agitator was simulated with different multi-phase interaction models, and both the velocity profile and solid concentration were compared with the experiments (Guida et al., 2009) and another numerical simulation (Kubicki and Lo, 2012). Finally, the liquid-solid multiphase flow in a mud agitator was simulated under properly adopted simulation conditions. The prediction of the mixing time and distribution of bulk particles in the mud agitator are discussed.

## 2. Numerical Formulation and Conditions

### 2.1 Governing Equations and Numerical Modeling

The governing equations for an incompressible and viscous flow involving multiple phases are the continuity and Reynolds-averaged Navier-Stokes (RaNS) equations. To solve the liquid-solid multiphase flow, governing equations were modified with the volume fraction of each phase, and momentum transfer and internal force terms were added to the right hand side (RHS) of the RaNS Eq. (2) as follows:

$$\frac{\partial(\alpha_i \rho_i)}{\partial t} + \nabla \cdot (\alpha_i \rho_i \mathbf{u}_i) = 0 \quad (1)$$

$$\begin{aligned} \frac{\partial \alpha_i \rho_i \mathbf{u}_i}{\partial t} + \nabla \cdot \alpha_i \rho_i \mathbf{u}_i \mathbf{u}_i = \\ -\alpha_i \nabla p + \nabla \cdot [\alpha_i (\boldsymbol{\tau}_i + \boldsymbol{\tau}'_i)] + \mathbf{M}_i + (\mathbf{F}_{int})_i + \alpha_i \rho_i \mathbf{g}_i \end{aligned} \quad (2)$$

where  $\alpha$  is the volume fraction,  $\rho$  is the density,  $t$  is time,  $\mathbf{u}$  is the

velocity vector,  $p$  is the pressure,  $\boldsymbol{\tau}$  is the stress,  $\boldsymbol{\tau}'$  is the turbulent stress,  $\mathbf{g}$  is the gravity acceleration,  $\mathbf{M}$  is the momentum transfer term between the different phases,  $\mathbf{F}_{int}$  is the internal forces, and the subscript  $i$  indicates the type of fluid.

Components of multiphase interaction models composed of momentum transfer and internal force terms on the RHS of Eq. (2) were modeled in the same manner as Kim et al. (2017) and CD-Adapco (2014). In order to consider the momentum exchange at the interface, the drag, lift, and turbulent diffusion forces for multiphase flow are introduced in the present study. For the drag force, we used Gidaspow's model (Gidaspow, 1994) and Syamlal and O'Brien's model (Syamlal and O'Brien, 1989), which consider the behavior of solid particles. In the case of Gidaspow's model, the linearized drag coefficient can be obtained by the following equation (3):

$$A_D = \begin{cases} \frac{150\alpha_p^2\mu_c}{\alpha_c l^2} + \frac{1.75\alpha_p\rho_c|u_r|}{l} & \alpha_p \geq 0.2 \\ \frac{3}{4}C_D \frac{\alpha_p\rho_c}{l} |u_r| \alpha_c^{-1.65} & \alpha_p < 0.2 \end{cases} \quad (3)$$

Here,  $\alpha_p$  is the volume fraction for solid phase, which was obtained as 0.2 through an experiment.  $\mu_c$  is the viscosity of the liquid phase,  $\rho_c$  is the density of liquid,  $l$  is the average diameter of particles,  $\alpha_c$  is the volume fraction for liquid, and  $u_r$  is the relative velocity between adjacent phases. The drag coefficient  $C_D$  is corrected by a correlation equation from Schiller and Naumann and is written as Eq. (4):

$$C_D = \begin{cases} \frac{24}{Re_d} (1 + 0.15 Re_d^{0.687}) & 0 < Re_d \leq 1000 \\ 0.44 & Re_d > 1000 \end{cases} \quad (4)$$

where the Reynolds number for the dispersed phase can be expressed in Eq. (5):

$$Re_d = \frac{\rho_c |u_r| l}{\mu_c} \quad (5)$$

Similarly, Syamlal and O'Brien's drag model is obtained from the measured value of the terminal velocity in the bed where solid particles are deposited and is calculated as Eq. (6):

$$A_D = \frac{3}{4} \frac{\alpha_p \alpha_c \rho_c C_D}{l} |u_{mf}| \quad (6)$$

where  $u_{mf}$  is the minimum fluidization velocity, and  $C_D$  is the drag coefficient of the solid particle group, which is presented as Eq. (7):

$$C_D = \frac{C_{Ds}}{V_r^2} \quad (7)$$



Here,  $C_{Ds}$  is the drag coefficient of a single solid particle and is given in Eq. (8):

$$C_{Ds} = \left( 0.63 + \frac{4.8}{\sqrt{Re_s/V_r}} \right)^2 \quad (8)$$

where  $Re_s$  is the Reynolds number of a single solid particle in Eq. (9), and  $V_r$  is the ratio of the terminal velocity of the single particle in Eq. (10) and the total particles:

$$Re_s = \frac{\rho_p |v_r| l}{\mu_p} \quad (9)$$

$$V_r = \frac{1}{2} \left[ A - 0.06 Re_s + \sqrt{(0.06 Re_s)^2 + 0.12 Re_s (2B - A) + A^2} \right] \quad (10)$$

$$A = \alpha_c^{4.14} \quad (11)$$

$$B = \begin{cases} 0.8 \alpha_c^{1.28} & \alpha_c < 0.85 \\ \alpha_c^{2.65} & \alpha_c \geq 0.85 \end{cases} \quad (12)$$

where  $\mu_p$  is the viscosity coefficient of the solid phase, and  $\rho_p$  is the density of the solid phase.

The lift acts in the direction perpendicular to the relative velocity between solid and fluid particles and can be calculated as Eq. (13) by Auton's formula (Auton, 1987):

$$F_L = C_L \alpha_p \rho_c [u_r \times (\nabla \times u)] \quad (13)$$

where  $u$  is the velocity of fluid, and  $C_L$  is the lift coefficient. In the case of the lift coefficient, the default value is set to 0.25, but in this study, a value of 0.1 was used because it is suitable for small-sized particles according to Ekambara et al. (2009).

Next, the turbulent diffusion force due to the interaction between solid particles and fluid eddy is considered as shown in Eq. (14):

$$F_{td} = \left( A_D \frac{\nu_p^t}{\sigma_p} + A_D \frac{\nu_s^t}{\sigma_s} \right) \left( \frac{\nabla \alpha_s}{\alpha_s} - \frac{\nabla \alpha_p}{\alpha_p} \right) \quad (14)$$

where  $\sigma_p$  and  $\sigma_s$  are the turbulent Prandtl numbers of the solid and fluid, respectively, and both are set to a value of 1. Additionally,  $\nu_p^t$  and  $\nu_s^t$  represent the kinematic viscosity of the solid and fluid due to turbulence, respectively. Inside the solid phase, a pressure force between the solid phases acts when the distribution of the solid reaches the maximum distribution. In order to consider the pressure of the solid, in this study, the granular pressure model was used, as represented by Eq. (15):

$$(F_{int}) = \nabla \cdot \left[ -P_p + \left( \xi_p - \frac{2}{3} \mu_p \right) \nabla \cdot u_p \right] I \quad (15)$$

where  $P_p$  is the solid pressure,  $\mu_p$  is the effective granular viscosity,  $I$  is the isotropic tensor, and  $\xi_p$  is the bulk viscosity.

In the granular pressure model, the interactions between particles are considered by dividing them into several cases. First, in the case of the kinetic regime, the collision between particles is defined by the distribution function  $g_0$  of Ding and Gidaspow (1990) if the particle distribution is lower than the maximum distribution criterion as Eq. (16):

$$g_0 = \frac{3}{5} \left[ 1 - \left( \frac{\alpha_p}{\alpha_{p,max}} \right)^{1/3} \right]^{-1} \quad (16)$$

where  $\alpha_p$  is the particle volume fraction, and  $\alpha_{p,max}$  is the maximum particle volume fraction.

The distribution function  $g_0$  is used to calculate the granular temperature  $\theta_p$ , which determines the effective granular viscosity. The effective granular viscosity is composed of the collisional ( $C$ ) and kinetic ( $K$ ) contributions (Gidaspow, 1994) as given in Eqs. (17)~(19):

$$\mu_p = \mu_p^C + \mu_p^K \quad (17)$$

$$\mu_p^C = \frac{4}{5} \alpha_p^2 \rho_p d_p g_0 (1 + e) \sqrt{\frac{\theta_p}{\pi}} \quad (18)$$

$$\mu_p^K = \frac{10 \rho_p d_p \sqrt{\pi \theta_p}}{96(1 + e) g_0} \left[ 1 + \frac{4}{5} g_0 \alpha_p (1 + e) \right]^2 \quad (19)$$

The formula of Schaeffer (1987) was used for the frictional regime, in which the distribution of solid particles is close to the maximum distribution criterion. In this case, the solid pressure and effective granular viscosity can be written as Eqs. (20)~(21). In this case,  $\phi$  is given as  $25^\circ$  from Schaeffer (1987). In addition, the maximum distribution criterion for rigid spherical solid particles is applied based on the representative value of 0.624 obtained from an experiment.

$$p_p^f = \begin{cases} 10^{25} (\alpha_p - \alpha_{p,max})^{10} & \alpha_p > 0.624 \\ 0 & \alpha_p \leq 0.624 \end{cases} \quad (20)$$

$$\mu_p^f = \begin{cases} \min \left( \frac{p_p^f \sin \phi}{\sqrt{4 I_{2D}}}, \mu_p^{f,max} \right) & \alpha_p > 0.624 \\ 0 & \alpha_p \leq 0.624 \end{cases} \quad (21)$$

$p_p^f$  is the frictional solid pressure,  $\mu_p^f$  is the effective granular viscosity,  $\phi$  is the angle of internal friction, and  $I_{2D}$  is the second invariant of deviator of is the strain rate tensor.

## 2.2 Geometric Shape and Grid System

For the verification of the CFD tool, STAR-CCM+, firstly, the single-phase swirling flow in an agitator was simulated and compared with an experiment (Guida et al., 2009). The experiment was conducted in a model-sized cylindrical tank with 4-plate baffles and a 45°-pitch 6-blade impeller, as illustrated in Fig. 1. The connection between the hub and blades of the impeller was referenced from Guida et al. (2009), as shown in Fig. 2. The detailed dimensions of geometric shapes are summarized in Table 1. In the experiments, the rotation of the impeller was set to 360 rpm. Salt water with a density of  $1,150 \text{ kg/m}^3$  and viscosity of  $0.0045 \text{ Pa}\cdot\text{s}$  was used as the working fluid. The Reynolds number was calculated based on the maximum diameter of the impeller as about  $10^6$ .

The grid system shown in Fig. 3 was generated almost automatically by an algorithm in STAR-CCM+. For solving the rotary motion of the impeller, a cylinder-like rotational region including both the impeller

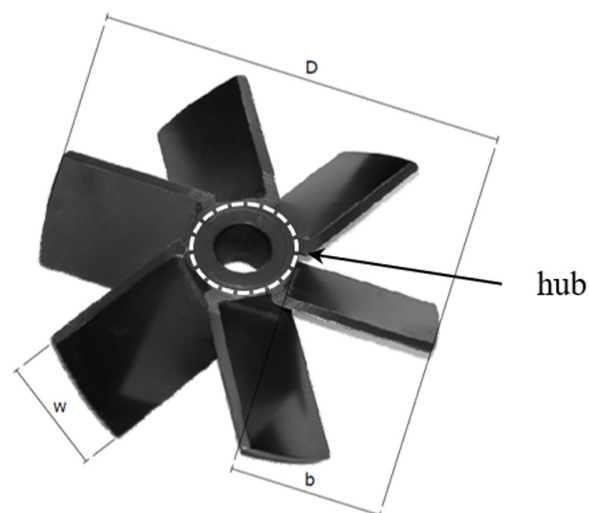


Fig. 2 45°-pitch 6-blade impeller (from Guida et al., 2009)

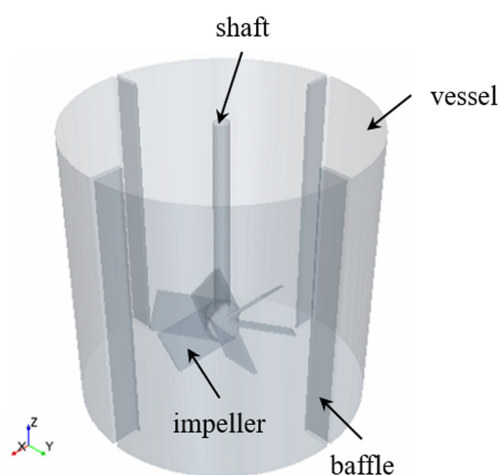


Fig. 1 3D configuration of pitched-blade agitator

Table 1 Details of pitched-blade agitator

	Type	Value (mm)
Vessel	Height	288
	Diameter	288
	Diameter	144
Impeller	Height	28
	Clearance	72
	Thickness	3
Shaft	Diameter	16
Hub	Diameter	28
	Height	30
Baffles	Width	29
	Thickness	5

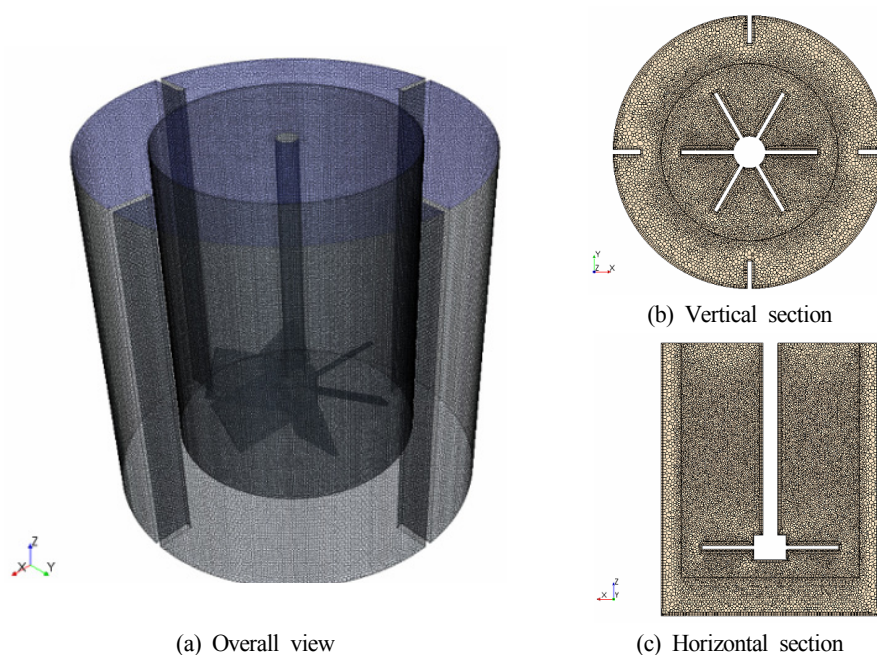


Fig. 3 Grid system used

and its shaft was designated using polyhedral meshes with a prism layer that has a minimum size of  $y^+ \approx 30$ . The total number of grid elements used was about 1.8 million for the turbulence model test, and 5 grid systems in the range of about 800,000–4,800,000 elements were used for the grid convergence test.

### 2.3 Boundary Conditions

The boundary conditions for the simulation are defined in Fig. 4. A symmetry boundary condition was adopted at the top of the tank, assuming that the free-surface motion does not significantly affect the entire flow field. Other wall boundaries including the impeller were given no-slip wall conditions. The rotary motion of the impeller was applied by introducing a rigid body motion (RBM) model that directly rotates the rotational region inside the grid system. The time step in the simulation was set to 0.001 s in consideration of the rpm of the impeller.

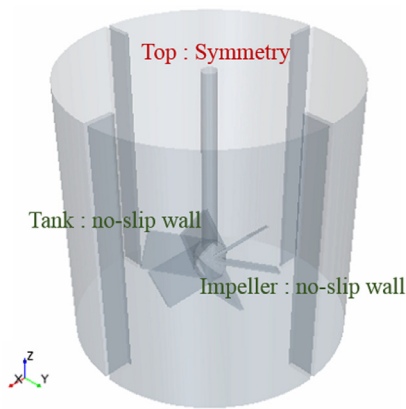


Fig. 4 Boundary conditions for agitator

## 3. Simulation Results

### 3.1 Verification of Single-phase Swirling Flow Around Agitator

Numerical simulations for single-phase water mixing in an agitator were performed with various turbulence models to verify the applicability of the commercial software STAR-CCM+. The software can cope with the turbulent swirling flow generated by the agitator inside a cylindrical tank. The simulation results regarding the velocity components around the impeller were compared to experiments (Guida et al., 2009; Guida, 2010). In the present simulation, as shown in Fig. 5, the time-averaged velocity components were measured along the probe line just below the impeller after the flow field reached quasi-steady state.

First, turbulence models based on 2-equation models were tested: the standard  $k-\epsilon$  (SKE), realizable  $k-\epsilon$  (RKE), and  $k-\omega$  models (KW) models. The initial conditions for turbulence in the flow field for all subsequent cases were turbulence intensity (TI) = 0.01 and turbulent viscosity ratio (TVR) = 10. Fig. 6 shows the time-averaged profiles of the simulated axial and tangential velocities compared to the experiments. Similarly, in both the simulation and experiment, the magnitude of the velocity tends to increase toward the end of the blade

with a radius of 0.072 m and then gradually decreases. However, it was found that the tendency of the velocity profile is slightly different between the simulation results depending on turbulence models employed in the simulation. It seems that all of the turbulence models cannot predict accurately the peak value of a tangential velocity.

In the vector field shown in Fig. 7, it can be seen that the SKE model forms stronger vortices around the wall where the vertical baffles are attached. However, the KW model represents the small and large-scale of eddies in complicated manner in the lower part around the impeller. In the case of the real RKE model, the influence of vortices is somewhat scattered and weakened near the wall, which seems to lead to a decrease in axial velocity, as shown in Fig. 6. In the case of the KW model, small vortices around blades make different patterns of the tangential velocity compared with the experiment.

Next, numerical tests for the Reynolds stress model (RSM) and large eddy simulation (LES) were performed. In this study, the linear pressure strain and Smagorinsky models were used as sub-models of RSM and LES, respectively. The RSM is a higher-level turbulence model, and LES can resolve an ample range of both time- and length-scale eddies. In the LES, about 4.8 million grid elements were used. In Fig. 8, it seems that the results of the axial component from the RSM and LES models look more similar to the experiment at the peak value than the SKE, but the trend of the distribution after the blade ends shows a difference from the experiment.

On the other hand, in the tangential component, especially in the case of the RSM and LES, there are more severe fluctuations toward the wall after the blade end. As shown in the velocity vector field in Fig. 9, it can be considered that the generation and development of more vigorous vortices in the case of RSM and LES are due to the fluctuations in the velocity distribution. As a result, both the RSM and LES models will likely require more test cases for the complemented grid system and solution setup to determine the suitability for agitation simulation. Therefore, we used the SKE, which can capture the overall average behavior of the flow field and has a relatively fast computation time.

Finally, a grid convergence test was performed using SKE and five grid sizes of 0.8–4.8 million. The results of the axial velocity profile from a center position between the hub and tank bottom are shown in Fig. 10. Except for slight differences in the vicinity of the wall baffles, it seems to show a tendency to converge overall.

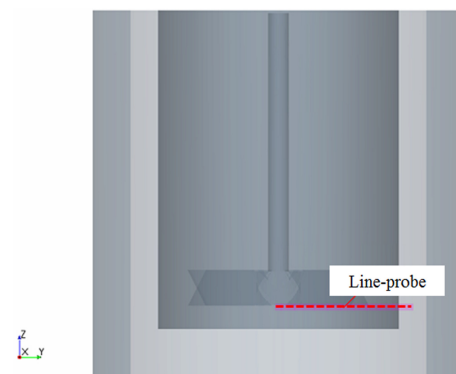
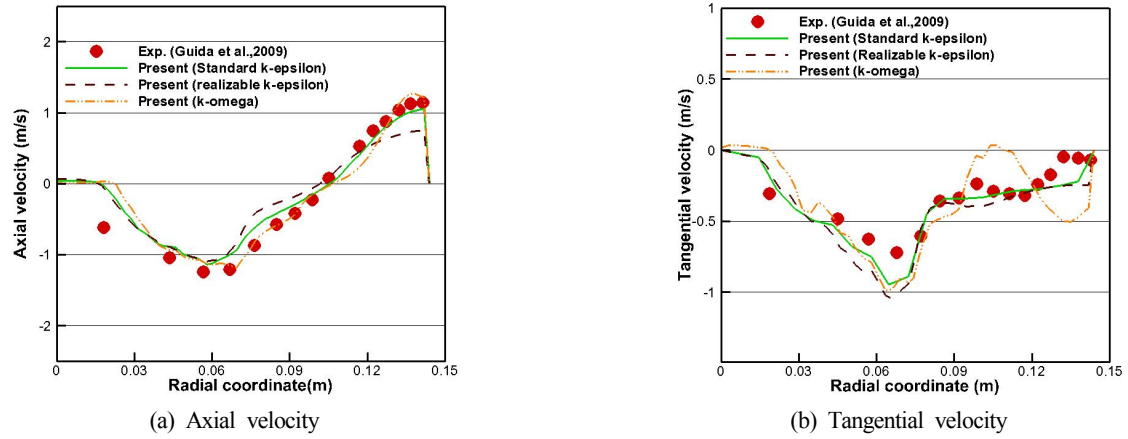
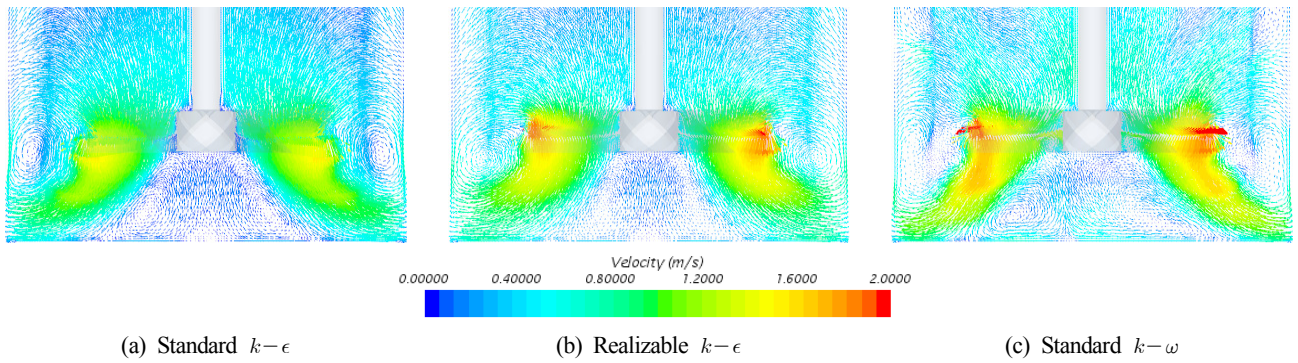


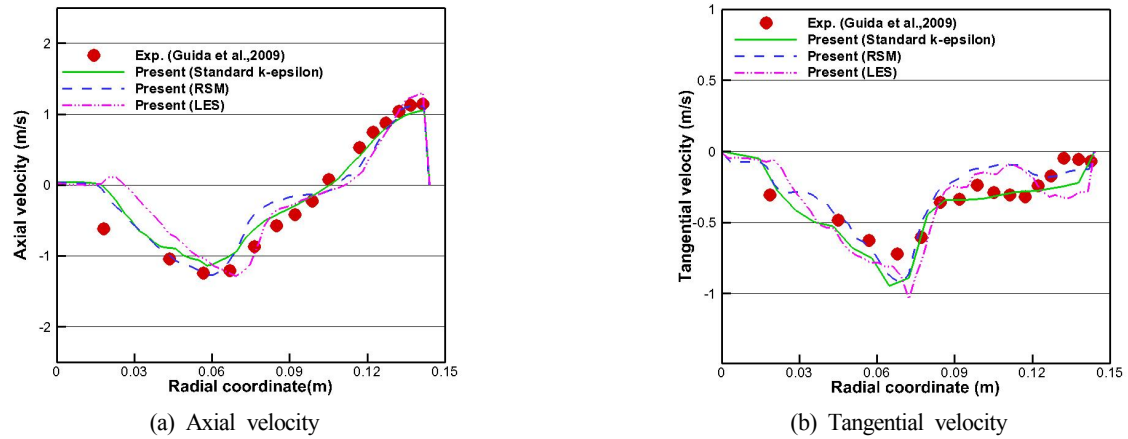
Fig. 5 Definition of probe line located below the impeller



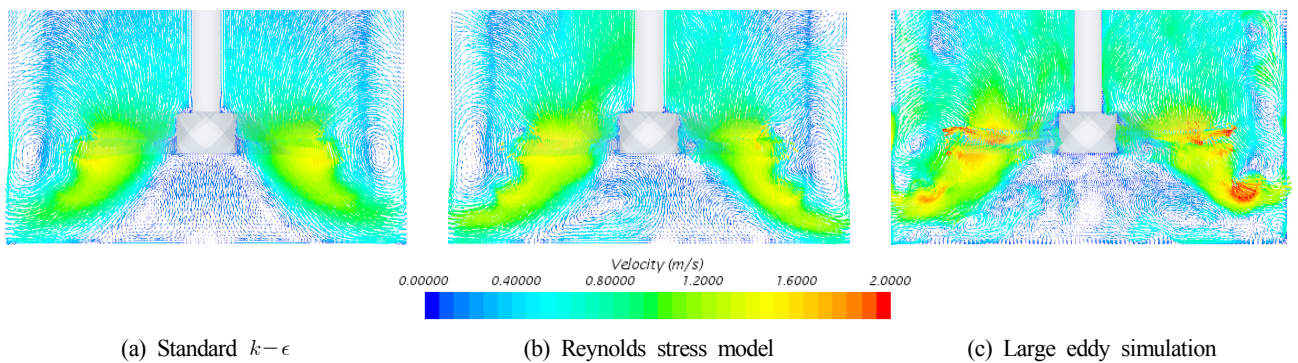
**Fig. 6** Comparison of velocity profiles in case with 2-equation turbulence models for single-phase agitator



**Fig. 7** Instantaneous velocity vectors in case with 2-equation turbulence models for single-phase agitator



**Fig. 8** Comparison of velocity profiles with higher level turbulence models for single-phase agitator



**Fig. 9** Instantaneous velocity vectors with higher-level turbulence models for single-phase agitator



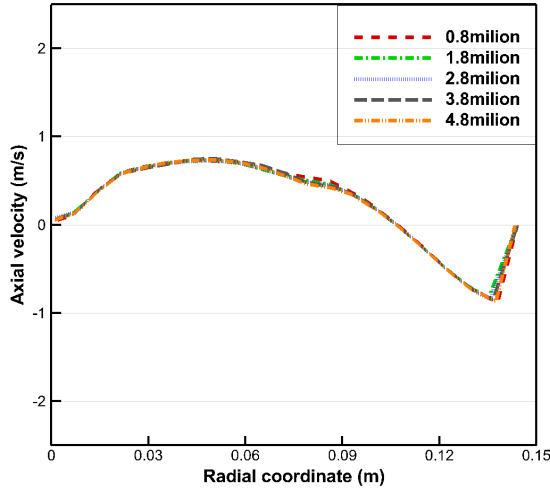


Fig. 10 Numerical results of grid convergence tests

### 3.2 Verification of Liquid-solid Multi-phase Flow Around Agitator

The mixing problem of liquid-solid multi-phase flow was set in the same manner as the experimental conditions of Guida et al (2009). The flat-base cylindrical vessel has a diameter of  $T = 288$  mm and 4 wall baffles. The inner 6-blade  $45^\circ$ -pitch impeller has a diameter of  $0.5T$  and rotates at 360 rpm. The liquid was a suspension of water adjusted

to a density of  $1,150 \text{ kg/m}^3$  by adding NaCl. Spherical glass beads ( $d = 2.85\text{--}3.30 \text{ mm}$ ) with a density of  $2,485 \text{ kg/m}^3$  were used as the solid. Initially, solid particles are evenly distributed in the space and mostly settle down from their own weight for 3 seconds. After 3 seconds, a swirling flow is generated by the rotational motion of the impeller in the agitator, and then the particles slowly start to suspend.

Fig. 11 shows the concentration distribution of the particles at the time when the mixed flow reaches steady state. Here, the concentration of particles refers to the volume fraction of the solid phase in a cell. A stagnation zone with a concentration higher than the average is observed below the hub and bottom corner of the wall baffles, where the flow rate is relatively low.

In order to find the optimal combination of liquid-solid interaction model, a multi-phase flow simulation was performed to decide whether or not to use a lift model and two different drag models (Eqs. (3) and (6)). The plane-averaged concentration according to the height was compared with the experiment by Guida et al. (2009) and the CFD simulation by Kubicki and Lo (2012). The numerical simulation by Kubicki and Lo (2012) was performed in steady state using the same CFD software (STAR-CCM+) as in this study, and the SKE turbulence model was applied. The modeling of the drag force and turbulent dispersion force for interfacial forces is the same as in this study, but

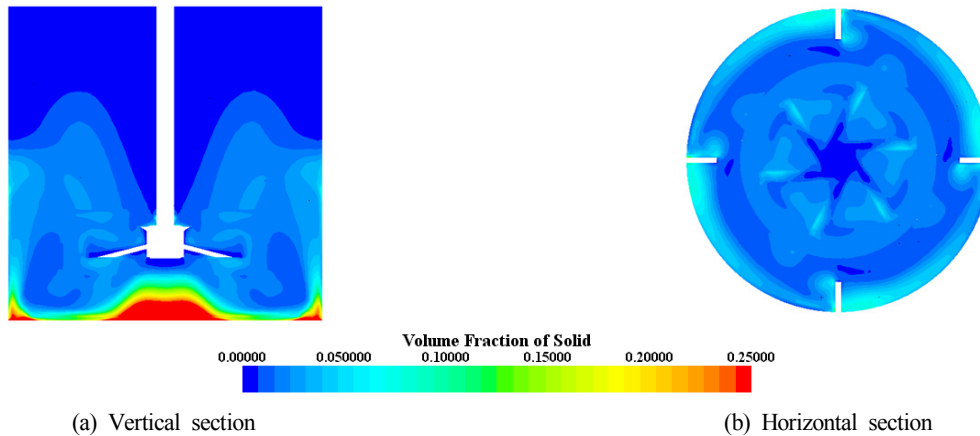


Fig. 11 Concentration distribution of particles at multi-phase agitator

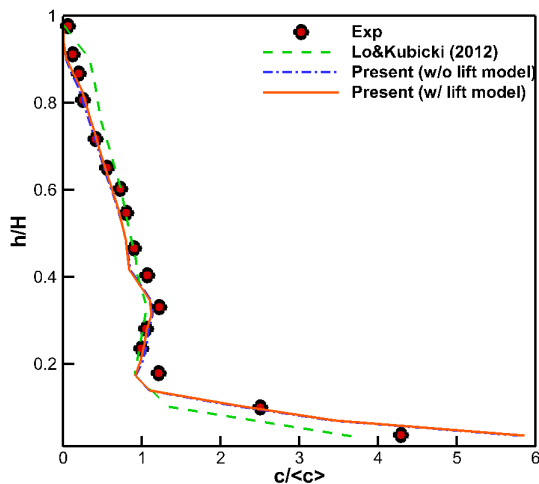


Fig. 12 Concentration with and without lift model

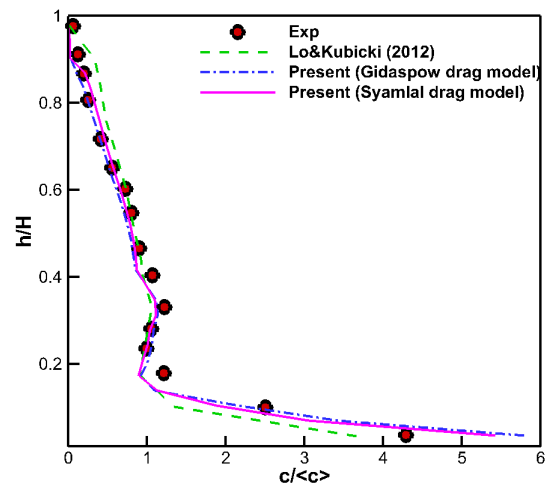
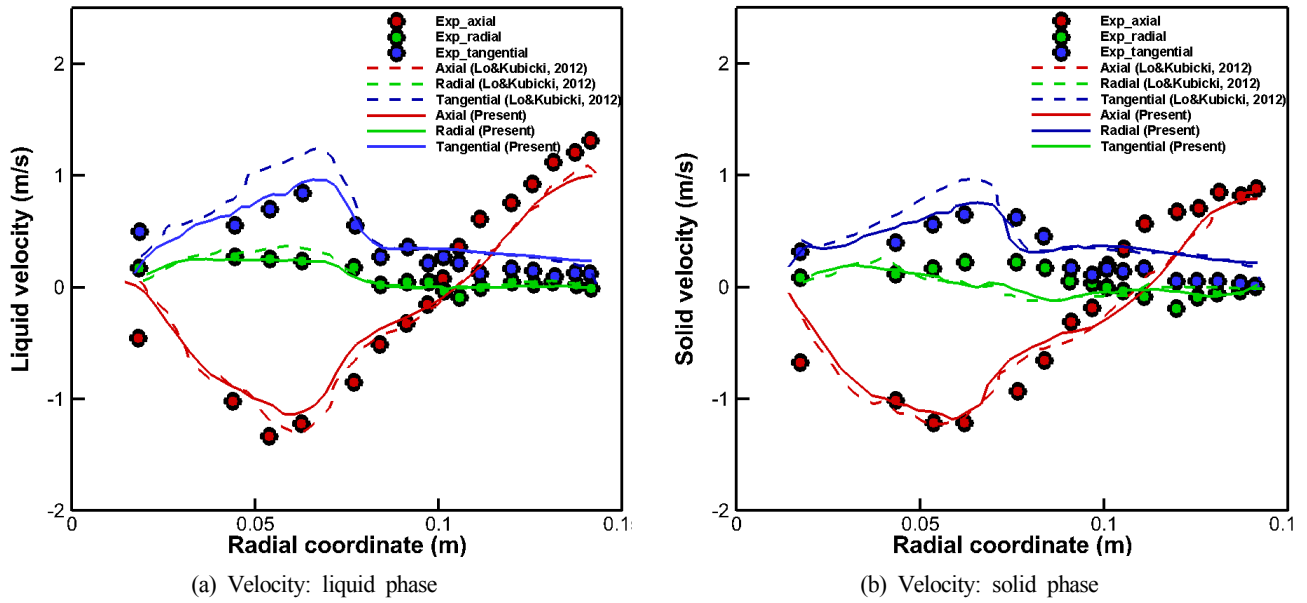


Fig. 13 Concentration with different drag mode



**Fig. 14** Liquid and solid velocity profile for multi-phase agitator

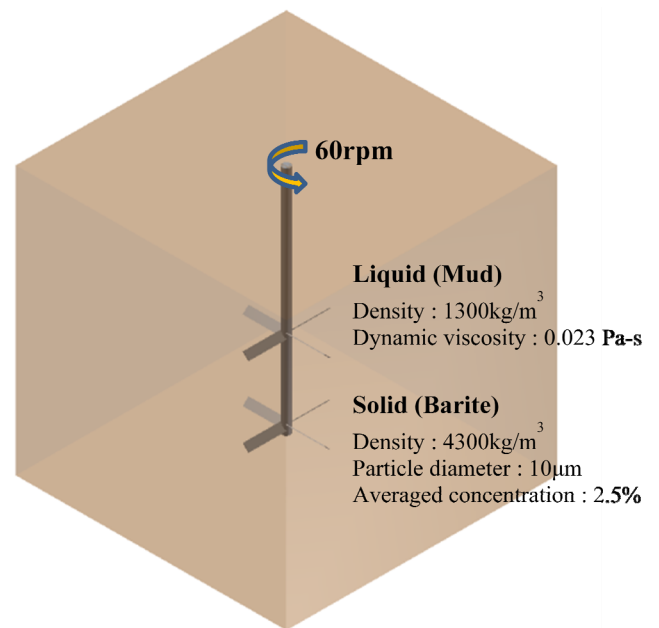
for the solid pressure force, an exponential function was used instead of the granular pressure model used in this study.

Simulation results for the interaction model tests are shown in Figs. 12–13. The results show that the lift model has less effect on the concentration distribution, whereas for the drag model, the concentration distribution with Syamlal and O'Brien's drag model becomes closer to the experiment. This suggests that the drag coefficient calculated directly from flow field of the Syamlal–O'Brien drag model is more suitable for the prediction of concentration. In addition, the simulation results obtained in this study show that the concentration distribution is more similar to that of the experiment compared to the other CFD simulation, especially in the lower part (Kubicki and Lo, 2012).

Finally, based on the Syamlal–O'Brien drag model, the three velocity components of each phase for the liquid and solid were compared with those from the experiments and other CFD simulations, as shown in Fig. 14. The overall trend of the velocity profiles shows that the simulation results and experiments are similar to each other. However, the tangential velocities for both liquid and solid phase have better agreement with the experiment than the other CFD simulation results. From these validation results, the Syamlal–O'Brien drag model was employed to simulate the multi-phase flow of a mud agitator in the next step.

### 3.3 Multi-phase Flow Simulation Around Mud Agitator

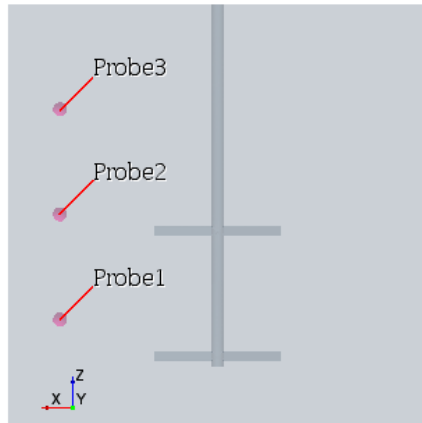
The mud agitator for the CFD simulation is a cube-shaped tank with a side length of 4 m. It contains a double-bladed impeller, which was modeled as shown in Fig. 15. The detailed dimensions of the mud agitator, including the inner 4-blade 45°-pitch impeller, are summarized in Table 2. The boundary conditions and grid system are almost the same as in the previous simulations, and about one million



**Fig. 15** 3D view of modeled mud agitator and operating conditions

**Table 2** Detailed dimensions of mud agitator and impeller

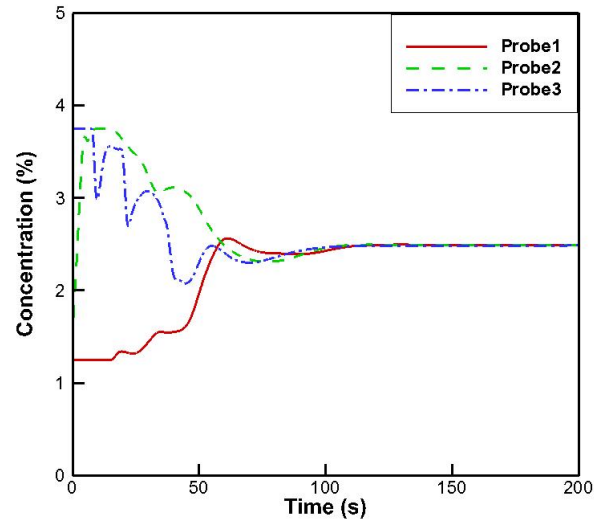
Variable		Value
Vessel	Height (m)	4.00
	Width (m)	4.00
	Diameter (m)	1.20
	Height (m)	0.085
Impeller	Thickness (m)	0.005
	Clearance (m)	1.837 and 0.655 (from flat-base)
	Revolution (rpm)	60
	Diameter (m)	0.12
Shaft		
Diameter (m)		0.12



**Fig. 16** Location of 3 probes for measuring concentration in mud tank

grid points were used. To account for the multi-phase mixing between the liquid mud and bulk (barite) in the mud tank, the liquid mud is assumed to be Newtonian fluid that has constant material properties. The detailed properties for each of the liquid and solid phases are specified in Fig. 15. To check the mixing process of the mud agitator, the concentration inside the mud tank was measured through probes located at three different heights, as shown in Fig. 16.

During actual operation, the role of the mud agitator is to maintain uniform density and viscosity of the pre-mixed mud. In this simulation, however, it is initially set to have a discontinuous concentration distribution as the initial distribution, as shown in in Fig. 16 (0 s). The average concentrations of the solid-phase at the higher and lower parts of the tank are 3.75% and 1.25%, respectively. As time goes by, as shown in Fig. 17, the concentration distribution of the solid phase in the space gradually becomes homogeneous and seems to be almost mixed after 100 s. In Fig. 18, it can be observed quantitatively that the time history of the concentration measured at 3 places converges to a constant value of about 2.5% after 100 s, and the mud becomes well mixed. The total torque acting on the two impellers after thoroughly mixing was calculated to be about 532 N·m, which can be seen to consume about 26.7% more power compared to mixing single-phase water.

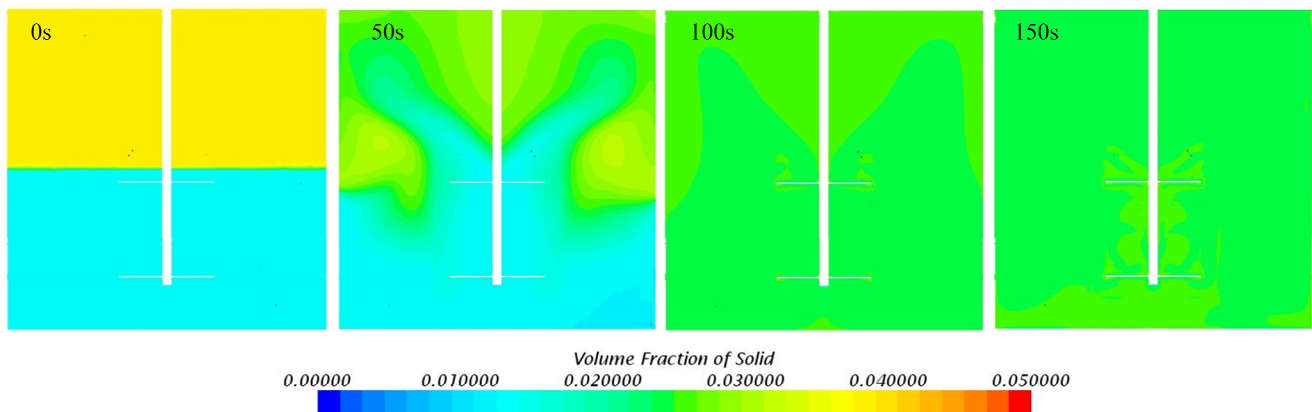


**Fig. 18** Time history of concentration for solid-phase at 3 probes

#### 4. Conclusions

In this study, the mixing performance of a mud agitator for offshore drilling was evaluated through a CFD simulation based on an Eulerian-Eulerian approach. For verification of the CFD tool, the velocity distribution for the vortical flow of single-phase water generated by an impeller inside a model-scale tank was compared with an experiment (Guida et al., 2009; Guida, 2010). Moreover, after alternately employing various turbulence models (STE, RKE, KW, RSM, and LES), the SKE showed more valid results with respect to the experiment and faster in computation. Thus, it was selected through comparison of the average velocity distribution during the mixing process.

Subsequently, a comparison of the multiphase interaction models was performed in the mixing problem for the liquid-solid multiphase flow. As a result, it was found that the Syamlal-O'Brien drag model, which directly calculates the drag coefficient, has better agreement with the experiment (Guida et al., 2009) than other CFD results (Kubicki and Lo, 2012) in the concentration distribution and velocity field during the mixing process. Using the verified simulation



**Fig. 17** Time-sequential distribution of concentration for solid-phase in mud tank

conditions, a liquid-solid multiphase flow simulation was then performed. In the simulation, it was observed that the solid concentration uniformly converged and mixed well in all places measured

## Funding

This work was supported by a 2- year research grant from Pusan National University

## References

- Ahn, I.J., Song, A.K., & Hur, N.K. (2006). Transient Flow Simulation a Mixer with Free Surface. *Journal of Computational Fluids Engineering*, 11(4), 9–13.
- Auton, T.R. (1987). The Lift Force on a Spherical Boddy in Rotational Flow. *Journal of Fluid Mechanics*, 183, 199–218. <https://doi.org/10.1017/S002211208700260X>
- CD-Adapco. (2014). Release 9.02 STAR-CCM+ User Guide Manual.
- Chang, J., & Hur, N. (2000). Flow Simulation of a 45° Pitched Paddle Type Mixer. *Proceedings of Fall Conference of the Korean Society of Computational Fluid Engineering*, 109–114.
- Choi, Y., Choi, J., Kim, D., & Hur, N. (2013). A Numerical Analysis on Mixing Performance for Various Types off Turbine Impeller in a Stirred Vessel. *The KSFM Journal of Fluid Machinery*, 16(1), 47–55. <https://doi.org/10.5293/kfma.2013.16.1.047>
- Darelius, A., Rasmuson, A., van Wachem, B., Björn, I.N., & Folestad, S. (2008). CFD Simulation of the High Shear Mixing Process Using Kinetic Theory of Granular Flow and Frictional Stress Models. *Chemical Engineering Science*, 63(8), 2188–2197. <https://doi.org/10.1016/j.ces.2008.01.018>
- Ding, J., & Gidaspow, G. (1990). A Bubbling Fluidisation Model Using Kinetic Theory of Granular Flow. *AIChE Journal*, 36(4), 523–538. <https://doi.org/10.1002/aic.690360404>
- Ekambara, K., Sanders, R.S., Nandakumar, K., & Masliyah, J.H. (2009). Hydrodynamic Simulation of Horizontal Slurry Pipeline Flow Using ANSYS-CFX. *Industrial & Engineering Chemistry Research*, 48(17), 8159–8171. <https://doi.org/10.1021/ie801505z>
- Gidaspow, D. (1994). *Multiphase Flow and Fluidization - Continuum and Kinetic Theory Descriptions*. Academic Press.
- Guida, A. (2010). *Positron Emixxion Particle Tracking Applied to Solid-Liquid Mixing in Mechanically Agitated Vessels* (Ph.D. Thesis). University of Birmingham. <http://etheses.bham.ac.uk/id/eprint/935>
- Guida, A., Fan, X., Parker, D.J., Nienow, A.W., & Barugou, M. (2009). Positron Emission Particle Tracking in a Mechanically Agitated Solid-Liquid Suspension of Coarse Particles. *Chemical Engineering Research and Design*, 87(4), 421–429. <https://doi.org/10.1016/j.cherd.2008.12.001>
- Kim, C.G., Lee, S.J., Won, C.S., & Hur, N.K. (2009). Transient Simulation of Solid Particle Distribution with Various Design Parameters of the Baffle in a Stirred Tank. *Journal of Computational Fluids Engineering*, 14(4), 1–6.
- Kim, T.Y., Jeon, G.M., Ock, D.K., & Park, J.C. (2017). Simulation-Based Design of Shear Mixer for Improving Mixing Performance. *Journal of Korean Society of Marine Environment & Energy*, 20(2), 107–116. <https://doi.org/10.7846/JKOSMEE.2017.20.2.107>
- Kubicki, D., & Lo, S. (2012). CFD Predictions of Solids Distribution in Stirred Vessel. In *Ninth International Conference on CFD in the Minerals and Process Industries*, Melbourne, Australia.
- Kumaresan, T., & Joshi, J.B. (2006). Effect of Impeller Design on the Flow Pattern and Mixing in Stirred Tanks. *Chemical Engineering Journal*, 155(3), 173–193. <https://doi.org/10.1016/j.cej.2005.10.002>
- Lo, S. (2012). Multiphase Flow Models in STAR-CCM+. In *STAR Japanese Conference 2012*, Tokyo, Japan.
- Nagata, S., Yamamoto, K., & Ujihara, M. (1959). Flow Patterns of Liquid in a Cylindrical Mixing Vessel Without Baffles. *Chemical Engineering*, 23(3), 130–137. <https://doi.org/10.1252/kakoronbunshu1953.23.130>
- Nienow, A.W. (1997). On Impeller Circulation and Mixing Effectiveness in the Turbulent Flow Regime. *Chemical Engineering Science*, 52, 2557–2565. [https://doi.org/10.1016/S0009-2509\(97\)00072-9](https://doi.org/10.1016/S0009-2509(97)00072-9)
- Schaeffer, D.G. (1987). Instability in the Evolution Equations Describing Incompressible Granular Flows. *Journal of Differential Equations*, 66, 19–50.
- Syamlal, M., & O'Brien, T.J. (1989). Computer Simulation of Bubbles in a Fluidized Bed. *AIChE Symp. Ser.*, 85(270), 22–31.
- Wadnerkar, D., Utikar, R.P., Tade, M.O., & Pareek, V.K. (2012). CFD Simulation of Solid-Liquid Stirred Tanks. *Advanced Powder Technology*, 23(4), 445–453. <https://doi.org/10.1016/j.appt.2012.03.007>

## Author ORCIDs

Author name	ORCID
Kim, Tae-Young	0000-0002-2586-2112
Jeon, Gyu-Mok	0000-0002-6194-8474
Park, Jong-Chun	0000-0002-3168-2054



# Surrogate Model Based Approximate Optimization of Passive Type Deck Support Frame for Offshore Plant Float-over Installation

Dong Jun Lee<sup>1</sup>, Chang Yong Song<sup>2</sup> and Kangsu Lee<sup>3</sup>

<sup>1</sup>Graduate Student, Department of Naval Architecture & Ocean Engineering, Mokpo National University, Jeonnam, Korea

<sup>2</sup>Professor, Department of Naval Architecture & Ocean Engineering, Mokpo National University, Jeonnam, Korea

<sup>3</sup>Principal Researcher, Korea Research Institute of Ships & Ocean Engineering (KRISO), Daejeon, Korea

**KEY WORDS:** Passive type deck support frame, Float-over installation, Approximate optimization, Design of experiment, Surrogate model

**ABSTRACT:** The paper deals with comparative study of various surrogate models based approximate optimization in the structural design of the passive type deck support frame under design load conditions. The passive type deck support frame was devised to facilitate both transportation and installation of 20,000 ton class topside. Structural analysis was performed using the finite element method to evaluate the strength performance of the passive type deck support frame in its initial design stage. In the structural analysis, the strength performances were evaluated for various design load conditions. The optimum design problem based on surrogate model was formulated such that thickness sizing variables of main structure members were determined by minimizing the weight of the passive type deck support frame subject to the strength performance constraints. The surrogate models used in the approximate optimization were response surface method, Kriging model, and Chebyshev orthogonal polynomials. In the context of numerical performances, the solution results from approximate optimization were compared to actual non-approximate optimization. The response surface method among the surrogate models used in the approximate optimization showed the most appropriate optimum design results for the structure design of the passive type deck support frame.

## 1. Introduction

The importance of developing float-over installation technology and additional-structure designing technology for the safe installation of topside has increased in recent years owing to the increase in the size and weight of offshore plants. Float-over installation is one of marine construction methods used to load a completely constructed topside weighing tens of thousands of tons on an installation ship at a quay wall or pier, and then safely transport and install it on an offshore platform, to which the topside will be connected. Among the additional structures applied in the float-over installation method, a deck support frame (DSF), which can safely support a heavy topside, should be designed by applying classification rules considering actual operating conditions. For a DSF developed in a new format, weight-reduction design is crucial for ensuring the buoyancy and motion performance of offshore installation ships to which the DSF is applied, as well as for ensuring the safety of the structural design. This requires a design optimization that can satisfy the structural design safety of DSFs and secure a minimal weight simultaneously.

Studies that investigate the optimum design for offshore structures or related equipment have been conducted in a limited scope hitherto. Song et al. (2011) conducted a reliability-based design optimization using a constraint-feasible moving least-squares method, which is a conservative approximation model, to minimize the design risk of floating production storage and offloading (FPSO) riser support. Jung et al. (2009) investigated the impact load that can occur on a topside and an offshore structure's platform during float-over installation. Park et al. (2019) used design of experiments (DOE) to devise an optimum design method that can solve the resonance problem of radar mast occurring from the conventional operating area of the main engine of a large ship. Park et al. (2011) conducted an optimum design using an evolution algorithm to minimize the design weight of support while satisfying the strength constraints provided in pipeline design regulations for FPSO flare systems. Ji et al. (2015) used a genetic algorithm to develop an optimal arrangement design that can satisfy the stress and dynamic characteristics of resilient mounts installed for vessels.

In this study, structural analysis was performed using finite element

Received 4 January 2021, revised 28 January 2021, accepted 1 February 2021

Corresponding author Chang Yong Song: +82-61-450-2732, [cysong@mokpo.ac.kr](mailto:cysong@mokpo.ac.kr)

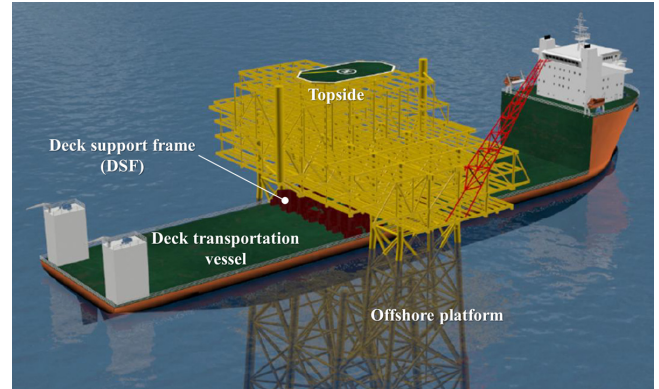
© 2021, The Korean Society of Ocean Engineers

This is an open access article distributed under the terms of the creative commons attribution non-commercial license (<http://creativecommons.org/licenses/by-nc/4.0>) which permits unrestricted non-commercial use, distribution, and reproduction in any medium, provided the original work is properly cited.

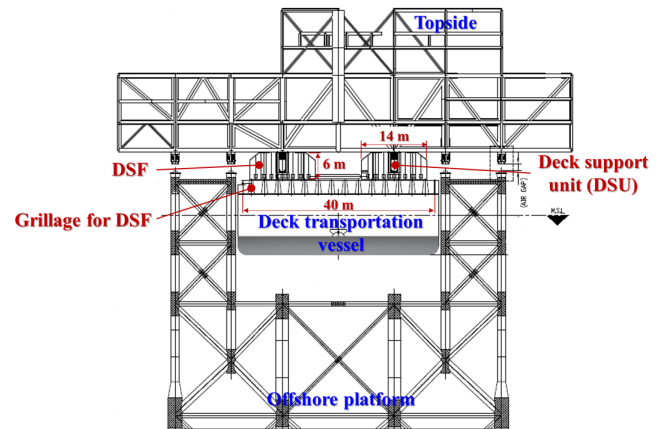
method (FEM) to review the initial design of structural safety of passive type DSF, and an approximate optimization was performed using various surrogate models to obtain the most efficient optimum design results for the structural design of passive-type DSFs. Because newly developed offshore plant equipment such as passive-type DSF lack design information or validation data, surrogate-model-based approximate optimization results may not satisfy the constraint feasibility based on the characteristics of design problems. Therefore, it must be reviewed using various surrogate models. The approximate optimization method is often applied to multidisciplinary optimization and stochastic optimization, which require involved numerical calculations. If an appropriate surrogate model is selected based on a deterministic approximate optimization, then the efficiency of performing deterministic optimization such as reliability-based optimization can be increased. To evaluate the structural safety for the initial design of passive-type DSFs, design load conditions reflecting the classification rules were selected, and a three-dimensional (3D) structural analysis model was created using FEM to evaluate the strength performance for each design load condition. The optimum design problem was formulated to determine the thickness dimension variables of primary structural members that can minimize the total structure weight while satisfying all constraints of strength performance for each design load condition. For an approximate optimization, three surrogate models, i.e., the response surface method (RSM), Chebyshev orthogonal polynomials (COP), and Kriging model were applied to investigate the optimization design results, and the optimization results were compared based on the surrogate model characteristics. The results of approximate optimization methods by surrogate model characteristics were compared with the results of actual non-approximate optimization. Moreover, considering the optimum design characteristics and numerical calculation cost, the study was conducted to identify the most appropriate approximate optimization method for the structural design of passive-type DSFs. Among the surrogate models applied in this study, the approximate optimization method based on the RSM yielded the most efficient optimum design results for the structural design. Herein, Section 2 presents an FEM-based strength performance evaluation for each design load condition with respect to the initial structural design of passive-type DSFs. Section 3 provides a brief review of the surrogate model theory and summarizes the results of approximate optimization based on approximate model characteristics. Finally, the conclusions are presented.

## 2. Safety Evaluation of Initial Design Structure

A DSF is an offshore equipment mounted on a deck transportation vessel (DTV) for offshore plant installation to transport and install a constructed topside. It can be classified into truss-type, independent-structure-type, and beam-structure-type DSFs. As shown in Fig. 1, the passive-type DSF considered in this study was developed to transport and install a 20,000-ton class topside; it was designed to accommodate



(a) ISO view



(b) Front view

**Fig. 1** Topside mating procedure via float-over installation with passive type DSF

a deck support unit (DSU) to finely adjust the height during topside installation at the center of the DSF. In the float-over method, the topside is loaded onto the passive-type DSF connected to the center of gravity of the DTV. Hence, the topside was connected to the offshore platform, which was installed in advance at the offshore field, as shown in Fig. 1(a). As illustrated in Fig. 1(b), the passive-type DSF was equipped with a DSU at the center, and it was designed to be 14 m wide and 6 m high. Furthermore, a 40-m-wide grillage was mounted on the DTV to prevent excessive strain on the DTV deck caused by the heavy topside, whereas the passive-type of DSF was installed on the upper side of the grillage.

To evaluate the structural safety in the initial design of the DSF, the design load conditions were first determined by applying the classification rules pertaining to the actual operating conditions. For the performance evaluation of the structural design, a 3D structural analysis model was created, and the design load conditions were applied to the structural analysis model to yield structural analysis results. Subsequently, the maximum stress was analyzed at each design load condition.

### 2.1 Design Load Cases

The design load cases for the structural performance evaluation of

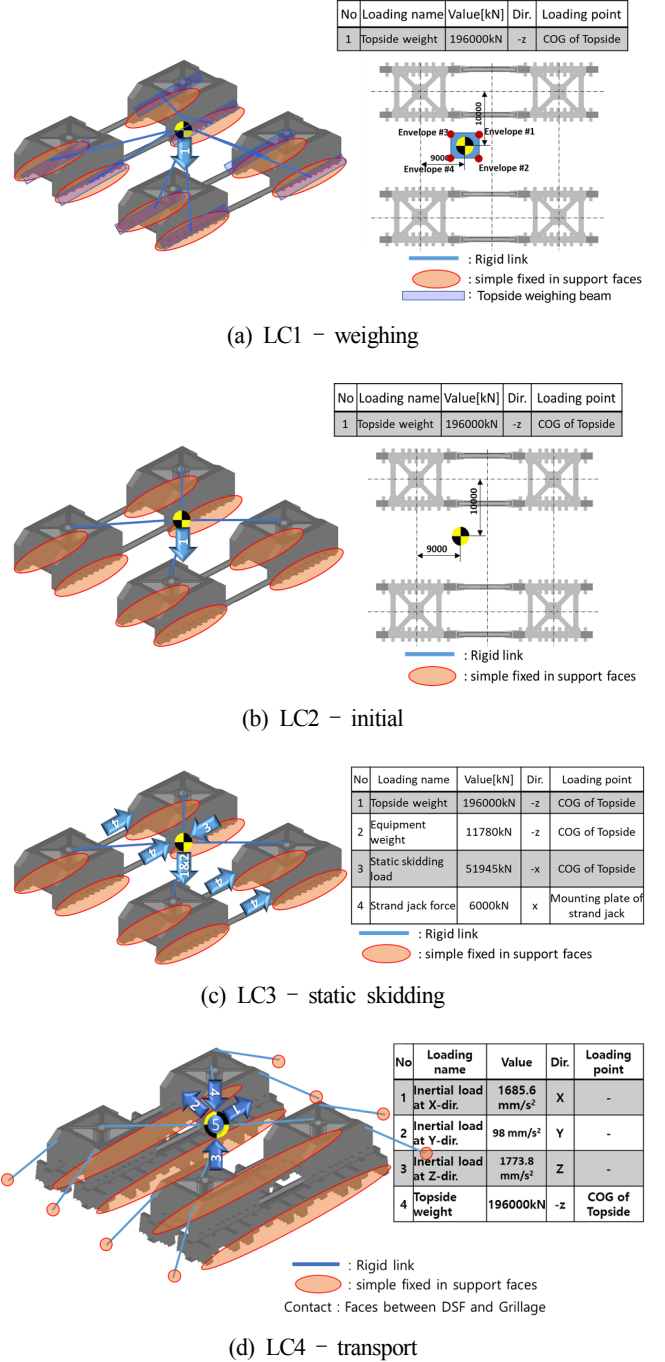
**Table 1** Design load case for structure analysis of passive type DSF

Operation condition	Design load case	Reference to rule & guidance
Load-out	LC1 - weighing	- Guidelines for load-outs - Load transfer operations
	LC2 - initial	
	LC3 - skidding	
Transportation	LC4 - transport	- Guidelines for marine transportations - Offshore installation operations

the passive-type DSF comprised four cases, as shown in Table 1. These cases reflect the classification rules pertaining to the offshore installation operation (DNV-GL, 2012; DNV-GL, 2013, GL, 2015a; GL, 2015b). As shown in Table 1, the design load cases comprised operation conditions for load-out and transportation, separately: the cases for load-out included weighing (LC1), initial (LC2), and skidding (LC3) cases, which reflected the operation conditions of loading a completely constructed topside on the passive-type DSF and shifting it to the DTV; the cases for transportation comprised the transport (LC4) case, which was for shifting the DTV, on which the topside and passive-type DSF were loaded, to the offshore platform. In the case of LC1, the topside weighing beam part was fastened, and the weighing load of the topside was applied to verify whether a heavy topside can be safely loaded onto the passive-type DSF. In LC2, the topside was connected to the passive-type DSF while considering the center of gravity of the topside after completing the weighing review prior to the load-out operation. In LC3, the topside-connected passive-type DSF was shifted to the DTV. In LC4, the topside-connected passive-type DSF was loaded, fastened, and transported to the grillage of the DTV.

The design load cases shown in Table 1 were used as load conditions for FEM-based structural analysis, and Fig. 2 shows the load and boundary conditions applied to the passive-type DSF in detail.

As shown in Table 1 and Fig. 2, for the load and boundary conditions of LC1, the weight of the topside was converted into a load and then applied in the gravity direction from the center of gravity, and the degree of freedom in the lateral direction on the fastened part of the topside weighing beam was constrained and considered. For the load and boundary conditions of LC2, the load of the topside weight was applied in the gravity direction from the center of gravity, and the degree of freedom in the lateral direction on the surface of lower part of the passive-type DSF was constrained and considered. For the load conditions of LC3, the weights of the topside and load-out equipment were applied in the gravity direction from the center of gravity, and the hydraulic operating force of a strand jack was applied in the load-out direction. Furthermore, as shown in the following equation specified in the classification rules, a static skidding force ( $F_s$ ) was applied in the opposite direction of the load-out direction (DNV-GL, 2012; GL, 2015a).

**Fig. 2** Load and boundary conditions for structure analysis of DSF

$$F_s = \mu_{ud,s} (W + W_{eq}) + P_s \quad (1)$$

where

$\mu_{ud,s}$ : static upper bound design friction coefficient (0.3)

$W$ : topside weight

$W_{eq}$ : loadout equipment weight

$P_s$ : inertial load or environmental load occurring during break-out

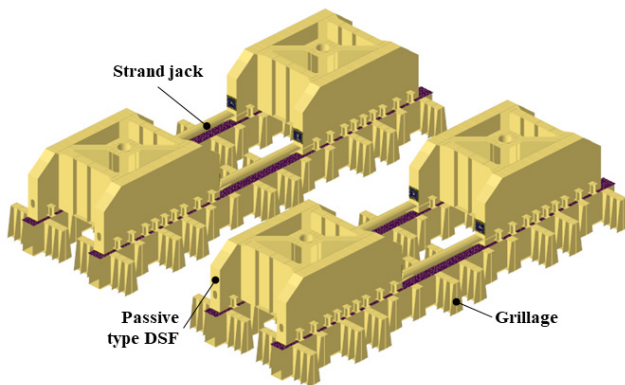
For the boundary conditions of LC3, the degree of freedom in the lateral direction on the surface of the lower part of the passive-type DSF was constrained and considered. For the load conditions of LC4,

the load of the topside weight was applied in the gravity direction from the center of gravity, and the motion acceleration for each direction calculated through the motion analysis of DTV (Kim et al., 2017) was considered and applied as an inertia load. In the boundary conditions of LC4, a contact condition was applied to the part where the passive-type DSF and the grillage coincided to consider the condition of the passive-type DSF loaded onto the DTV. In addition, eight steel tension wires that fastened the passive-type DSF on the DTV deck were idealized as 1-D rigid link elements, and the degree of freedom in the lateral direction was constrained. As for the allowable stress in the structural performance evaluation, the working stress design method (DNV-GL, 2015) used in offshore structure designs was applied, where 85% of the material yield strength was considered.

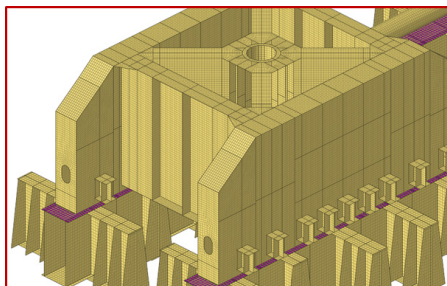
## 2.2 Structure Analysis Results

FEM-based structure analysis was performed to evaluate the structural performance of the passive-type DSF designed for the installation of a 20,000-ton class topside on an offshore platform using the float-over method. The geometry used in the FEM modeling for the structure analysis is shown in Fig. 3

As shown in Fig. 3, the structure analysis model of the passive-type DSF was created using 717,452 elements and 654,452 nodes, including the DSF and the grillage based on the LC4 case provided in Fig. 2. In addition, shell elements were applied for the primary structural members; meanwhile, the steel tension wires for fastening and the load-applied part were modeled using a rigid link. Among the structural members of the passive-type DSF, the API-5L-X52 material



(a) Overall view



(b) Detail view

**Fig. 3** FEM model of passive type DSF

was used for the tube-shaped member, whereas the SM490YB material was used for the other members. The properties of these materials are summarized in Table 2.

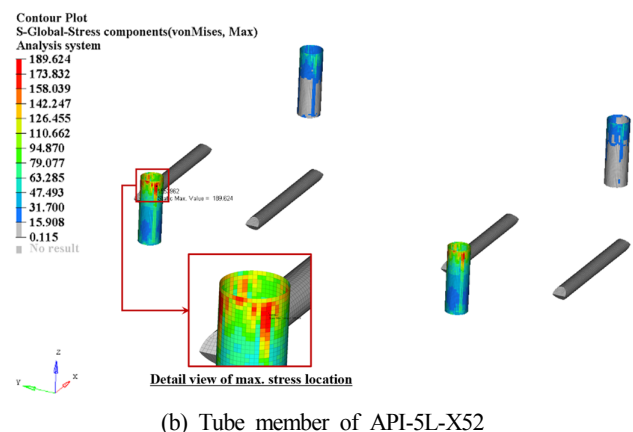
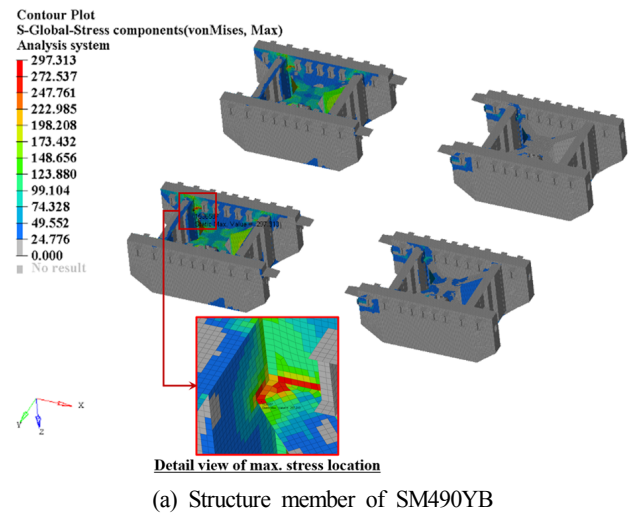
Based on the 85% yield strength of the classification rules, the estimated allowable stresses were 301.75 and 318.75 MPa for the SM490YB and API-5L-X52 materials, respectively. The structure

**Table 2** Material properties

Material property	SM490YB	API-5L-X52
Elastic modulus (N/mm <sup>2</sup> )	206,000	208,000
Poisson's ratio	0.3	0.3
Density (N-s <sup>2</sup> /mm <sup>4</sup> )	7.85E-9	7.85E-9
Yield strength (MPa)	355	375

**Table 3** Structure analysis results of passive type DSF

Design load case	Max. stress (MPa)		Structure safety
	SM490YB	API5LX52	
LC1	244.023	0.952	OK
LC2	194.926	120.139	OK
LC3	297.313	189.624	OK
LC4	153.521	103.403	OK



**Fig. 4** Stress contour results of LC3



analysis was performed using ABAQUS/Implicit (Simulia, 2018), a general-purpose finite element analysis software. The results from the structure analysis are summarized in Table 3 based on the von-Mises stress.

As shown in Table 3, the maximum stress of the passive-type DSF satisfies the allowable stress of the classification rules for all design load conditions. Furthermore, the structural member of the SM490YB material indicated a higher stress level than the structural member of the API-5L-X52 material. In the case of LC3, the maximum stress level of the passive-type DSF was 297.3 MPa, which was similar to the limit of the allowable stress, indicating that this design load case requires precaution during design. Fig. 4 shows the stress distribution of LC3 as a representative case.

In the conditions for LC3, as shown in Fig. 4, the maximum stress of the passive-type DSF occurred at the internal connecting member of the lower part among the structural members of SM490YB material. Meanwhile, the structural member of API-5L-X52 material shows that the maximum stress occurred at the tube member connected to the position where the maximum stress occurred in the structural member of SM490YB material. Therefore, the weight must be minimized while the design load conditions of LC3 satisfied for structure optimization to achieve the minimum weight design of passive-type DSFs.

### 3. Approximate Optimization Design of Passive-Type DSF

Surrogate model-based approximate optimization methods were used in this study to derive efficient and optimal weight-reducing design approaches for the structural design of passive-type DSFs. Three surrogate models were used for the approximate optimization: the RSM, Kriging, and COP. The formulation for the optimum design problem was configured to determine the optimal thickness of the primary structural members to minimize the structure weight, while satisfying all the constraints of strength performance below the allowable maximum yield strength for each design load condition. The approximate optimization results were analyzed based on the surrogate model characteristics. Subsequently, by comparing them with the results of actual non-approximate optimization, the most appropriate approximate optimization method for the minimal-weight structural design of passive-type DSFs was identified. For the non-approximate optimization, we used sequential approximate optimization (SAO), which is used for typical constraint optimization problems (Haftka and Gürdal, 1991).

#### 3.1 Surrogate Model Theory

Surrogate models used for approximate optimization were developed to predict the response characteristics of a constraint function and the response characteristics of an objective function with minimal errors within a specified design scope. Furthermore, they are applied during optimization analysis to improve the convergence and numerical calculation speed. Surrogate models are generally developed using a

regressive method of polynomial form or an interpolative method that considers the design area based on a stochastic method. In this study, an approximate optimization was performed using three surrogate models, i.e., the regressive methods of RSM and COP, and the interpolative method of Kriging. In this subsection, the three surrogate models are briefly described.

The RSM is expressed as a regression model of quadratic polynomial form using the least-squares method.

$$g = A_0 + \sum_{i=1}^k A_i Z_i + \sum_{i=1}^k A_{ii} Z_i^2 + \sum_{i < j}^k A_{ij} Z_i Z_j + e \quad (1)$$

If an actual response vector  $g$  and a matrix  $Z$  of  $k$  basic variables are provided from the experimental points calculated using DOE, then the relationship between  $g$  and  $Z$  can be expressed as follow (Song and Lee, 2010):

$$g = ZA_R + e \quad (2)$$

If a least-squares function is applied to calculate the RSM's approximation coefficient of vector  $A_R$  after minimizing the random error vector  $e$ , and the approximation coefficient of the surrogate model is applied, then the regression surrogate model can be obtained.

The Kriging surrogate model is expressed as the sum of a global model exhibiting the global characteristics of the actual design space function to be approximated, and the local model corresponding to the deviation between the actual function and the global model, as follows (Cho et al., 2009):

$$\tilde{g}(x)_K = Z(x)^T A_K + E(x) \quad (3)$$

where  $A_K = \{a_1, a_2, \dots, a_p\}^T$  is a coefficient vector, and  $Z(x) = \{z_1(x), z_2(x), \dots, z_p(x)\}^T$  is a global model vector defined by a design variable  $x \in E^{n_d}$ .  $E(x)$  is assumed to be an independent normal distribution, and the response vector obtained from  $n$  experimental points is defined as follows:

$$g = [g(x^1), g(x^2), \dots, g(x^n)]^T \quad (4)$$

$E(x)$  is defined as Gauss function, i.e., a correlation function. It can be expressed as a spatial correlation of design data, as follows:

$$E(\theta, x^i, x^j) = \exp \left[ - \sum_{k=1}^{n_d} \theta_k (x^i - x^j)^2 \right] \quad (5)$$

where  $\theta, x \in E^{n_d}$ , and the correlation matrix is a positive definite matrix with a diagonal element of 1. The correlation coefficient  $\theta$  can be calculated stochastically as the most likely correlation coefficient using maximum likelihood estimation, which maximizes the likelihood function.



The COP surrogate model for a quadratic polynomial regression model is defined as follows using Chebyshev orthogonal polynomial  $P_n(x)$  (Baek et al., 2011).

$$\begin{aligned} \tilde{g}(x)_C = & b_0 + b_1 p_1(x)^2 + b_2 p_2(x) \\ & + b_3 \left[ p_1(x)^3 - \frac{3a^2 - 7}{20} p_1(x) h^2 \right] + b_n p_n(x) + \dots \end{aligned} \quad (6)$$

where

$$\begin{aligned} p_0(x) &= 1, \quad n=0 \\ p_1(x) &= x - \bar{x}, \quad n=1 \\ p_2(x) &= (x - \bar{x})^2 - \frac{a^2 - 1}{12} h^2, \quad n=2 \\ p_n(x) &= p_{n-1}(x) p_1(x) - (n-1)^2 [a^2 - (n-1)^2] \\ &\quad h^2 p_{n-1}(x) / [4(4(n-1)^2 - 1)], \quad n=3, 4, 5, \dots \end{aligned}$$

where  $\bar{x}$  is the mean of the design variable,  $a$  the number of levels, and  $h$  the level interval coefficient; the degree  $n$  must be smaller than the number of levels  $a$ , and the maximum degree of each design variable becomes  $a-1$ .  $b$  is an approximate coefficient, which is defined by the as follows:

$$\begin{aligned} b_0 &= \bar{g}_C \\ b_n &= \frac{\sum_{k=1}^a p_n(x_k) g_{C_k}}{\sum_{k=1}^a p_n^2(x_k)}, \quad k=1, 2, \dots, a \end{aligned} \quad (7)$$

### 3.2 Formulation of Approximate Optimization Design

Fig. 5 shows the design variables and their range for the structural design optimization of the passive-type DSF considered in this study.

In the design variables, the upper and lower limits were applied to nine primary structural members of different thicknesses within  $\pm 20\%$  of the initial design thickness, as shown in Fig. 5, and they were set considering the range that facilitated actual fabrication and production. The formulation for an optimum design was defined as follows to minimize the weight under the constraints of strength performance:

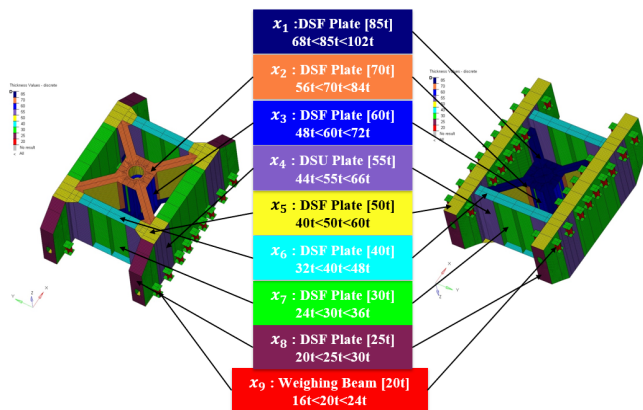


Fig. 5 Design variables and their range for passive type DSF

Minimize

$$W = W(x_1, x_2, x_3, x_4, x_5, x_6, x_7, x_8, x_9) \quad (8)$$

Subject to

$$\begin{aligned} g_1(x_1, x_2, x_3, x_4, x_5, x_6, x_7, x_8, x_9) &= LC1 \text{ stress} \leq 301.75 \text{ MPa} \\ g_2(x_1, x_2, x_3, x_4, x_5, x_6, x_7, x_8, x_9) &= LC2 \text{ stress} \leq 301.75 \text{ MPa} \\ g_3(x_1, x_2, x_3, x_4, x_5, x_6, x_7, x_8, x_9) &= LC3 \text{ stress} \leq 301.75 \text{ MPa} \\ g_4(x_1, x_2, x_3, x_4, x_5, x_6, x_7, x_8, x_9) &= LC4 \text{ stress} \leq 301.75 \text{ MPa} \\ 68.0 \leq x_1 &\leq 102.0 \text{ [mm]} \\ 56.0 \leq x_2 &\leq 84.0 \text{ [mm]} \\ 48.0 \leq x_3 &\leq 72.0 \text{ [mm]} \\ 44.0 \leq x_4 &\leq 66.0 \text{ [mm]} \\ 40.0 \leq x_5 &\leq 60.0 \text{ [mm]} \\ 32.0 \leq x_6 &\leq 48.0 \text{ [mm]} \\ 24.0 \leq x_7 &\leq 36.0 \text{ [mm]} \\ 20.0 \leq x_8 &\leq 30.0 \text{ [mm]} \\ 16.0 \leq x_9 &\leq 24.0 \text{ [mm]} \end{aligned}$$

The upper limit applied to the non-equivalence constraints of Eq. (8) was the design performance reference value for ensuring the structural safety of the passive-type DSF; it was set to less than or equal to 301.75 MPa, i.e., the allowable material yield strength of SM490YB material. Because the maximum stress from the LC3 conditions calculated from the initial values of the design variables (shown in Table 3) was similar to the upper limit of the design, a weight-minimizing design method that satisfies the LC3 conditions must be identified when designing a passive DSF.

### 3.3 Approximate Optimization Process

The following approximate optimization was performed to compare approximate optimization methods based on the surrogate model characteristics for the structural design of passive-type DSFs.

(1) In the DOE for creating a surrogate model, an orthogonal array design (Park, 2012) was used to construct the experimental matrix, and a structure analysis using the FEM was performed to generate experimental data for surrogate modeling.

(2) Experimental data based on a structure analysis using the FEM were used to create surrogate models of RSM, Kriging, and COP for the objective function and constraint functions of Eq. (8).

(3) The optimal solution was obtained by applying the SAO method using each surrogate model.

(4) A structure analysis using the FEM was performed for the converged optimal solution to validate the feasibility of the constraint function of each approximate optimal solution.

(5) Actual non-approximate optimization based on a structure analysis using the FEM was performed, and the approximate optimum design characteristics and numerical calculation costs were compared.

In the orthogonal array design used in the DOE of clause (1), a three-level experimental matrix was applied, and the experimental matrix was constructed for 243 times considering the lower, initial, and upper limits of the design variables shown in Fig. 5. The SAO used in the approximate optimization using the surrogate model of clause (3) is a method of determining whether to perform repetitive

optimization calculation through a sequential determination of the convergence of the optimal solution. This method involves a move limit strategy, which prevents excessive approximation by determining the moving distance (Haftka and Gürdal, 1991). The surrogate model of the RSM developed for the design of the passive-type DSF is expressed as follows:

$$\tilde{W}(x)_{R-mass} = 20040 + 1.69x_1 + 0.97x_2 - 15.8x_3 + 0.67x_4 + 4.86x_5 + 5.7x_6 + 1.19x_7 + 0.97x_8 + 0.54x_9 \quad (9)$$

$$\begin{aligned} & -0.536x_1^2 + 4.938x_2^2 + 3.429x_3^2 - 9.645x_4^2 - 4.321x_5^2 - 2.266x_6^2 \\ & + 1.715x_7^2 - 1.575x_8^2 + 2.350x_9^2 - 6.173x_1x_2 - 3.858x_1x_3 \\ & + 8.681x_1x_4 - 4.630x_1x_5 + 6.457x_1x_6 + 2.572x_1x_7 - 1.360x_1x_8 \\ & + 1.816x_1x_9 - 1.025x_2x_3 - 0.0001x_2x_4 + 1.852x_2x_5 - 3.613x_2x_6 \\ & + 6.173x_2x_7 + 1.764x_2x_8 - 2.905x_2x_9 + 1.929x_3x_4 - 1.543x_3x_5 \\ & - 1.403x_3x_6 - 1.286x_3x_7 + 1.565x_3x_8 + 1.531x_3x_9 + 1.157x_4x_5 \\ & + 4.209x_4x_6 + 9.645x_4x_7 + 1.653x_4x_8 - 6.808x_4x_9 + 8.418x_5x_6 \\ & + 1.543x_5x_7 + 3.307x_5x_8 + 3.268x_5x_9 + 7.422x_6x_9 + 2.572x_7x_8 \end{aligned}$$

$$\begin{aligned} \tilde{g}(x)_{R-LC1} &= 586.4 - 2.7x_1 - 0.9x_2 - 2.4x_3 - 0.36x_4 - 1.91x_5 \\ & - 1.05x_6 + 0.14x_7 - 0.73x_8 - 3.03x_9 + 0.004x_1^2 - 0.017x_2^2 \\ & + 0.014x_3^2 + 0.0003x_4^2 + 0.025x_5^2 + 0.027x_6^2 + 0.0005x_7^2 \\ & + 0.002x_8^2 + 0.026x_9^2 + 0.120x_1x_2 - 0.0001x_1x_3 - 0.0006x_1x_4 \\ & + 0.0004x_1x_5 - 0.010x_1x_6 + 0.002x_1x_7 + 0.009x_1x_8 - 0.008x_1x_9 \\ & - 0.0002x_2x_3 + 0.0004x_2x_4 - 0.0004x_2x_5 - 0.01x_2x_6 - 0.003x_2x_7 \\ & + 0.008x_2x_8 - 0.005x_2x_9 + 0.0075x_3x_4 - 0.0078x_3x_5 + 0.027x_3x_6 \\ & + 0.0015x_3x_7 + 0.0013x_3x_8 - 0.005x_3x_9 + 0.001x_4x_5 + 0.005x_4x_6 \\ & - 2.893x_4x_7 + 0.0004x_4x_8 - 0.003x_4x_9 - 0.027x_5x_6 \end{aligned}$$

$$\begin{aligned} \tilde{g}(x)_{R-LC2} &= 877.58 - 1.09x_1 + 6.66x_2 - 4.33x_3 \\ & - 0.34x_4 - 3.61x_5 + 0.74x_6 - 2.55x_7 - 2.24x_8 \\ & - 5.02x_9 + 0.071x_1^2 - 0.107x_2^2 + 0.040x_3^2 - 0.002x_4^2 + 0.037x_5^2 \\ & + 0.043x_6^2 - 0.003x_7^2 + 0.001x_8^2 + 0.039x_9^2 - 0.013x_1x_2 \\ & - 0.015x_1x_3 - 0.0014x_1x_4 + 0.0039x_1x_5 + 0.066x_1x_6 \\ & - 0.004x_1x_7 - 0.046x_1x_8 + 0.023x_1x_9 - 0.007x_2x_3 \\ & - 0.0001x_2x_4 + 0.007x_2x_5 - 0.066x_2x_6 + 0.051x_2x_7 \\ & + 0.029x_2x_8 - 0.0016x_2x_9 + 0.023x_3x_4 - 0.027x_3x_5 \\ & + 0.032x_3x_6 + 0.004x_3x_7 + 0.008x_3x_8 - 0.007x_3x_9 \\ & - 0.004x_4x_5 + 0.006x_4x_6 - 8.922x_4x_7 + 0.001x_4x_8 \\ & - 0.006x_4x_9 - 0.034x_5x_6 \end{aligned}$$

$$\begin{aligned} \tilde{g}(x)_{R-LC3} &= 421.61 - 0.05x_1 + 3.47x_2 - 1.93x_3 \\ & + 0.05x_4 - 2.09x_5 + 0.98x_6 - 1.36x_7 - 0.82x_8 \\ & - 2.54x_9 + 0.014x_1^2 - 0.057x_2^2 + 0.024x_3^2 - 0.002x_4^2 \\ & + 0.021x_5^2 + 0.018x_6^2 + 0.0001x_7^2 + 0.002x_8^2 + 0.018x_9^2 \\ & - 0.06x_1x_2 - 0.005x_1x_3 + 0.0007x_1x_4 + 0.01x_1x_5 \\ & + 0.042x_1x_6 - 0.004x_1x_7 - 0.04x_1x_8 + 0.017x_1x_9 \\ & - 0.003x_2x_3 + 0.0004x_2x_4 + 0.009x_2x_5 - 0.045x_2x_6 \\ & + 0.026x_2x_7 + 0.01x_2x_8 + 0.006x_2x_9 + 0.009x_3x_4 \\ & - 0.01x_3x_5 + 0.014x_3x_6 + 0.002x_3x_7 + 0.005x_3x_8 \\ & - 0.01x_3x_9 - 0.002x_4x_5 + 0.004x_4x_6 - 0.0008x_4x_7 \\ & + 0.0008x_4x_8 - 0.004x_4x_9 - 0.02x_5x_6 \end{aligned}$$

$$\begin{aligned} \tilde{g}(x)_{R-LC4} &= 735.96 - 35.31x_1 + 0.0023x_2 - 2.31x_3 \\ & - 0.0012x_4 + 0.0064x_5 + 0.12x_6 - 0.09x_7 - 0.00032x_8 \\ & - 0.00071x_9 + 0.639x_1^2 - 7.407x_2^2 + 0.028x_3^2 + 2.604x_4^2 \\ & + 7.963x_5^2 - 0.0007x_6^2 + 0.0005x_7^2 + 2.74x_8^2 - 7.903x_9^2 \\ & - 0.0002x_1x_2 - 0.029x_1x_3 - 3.183x_1x_4 - 0.0003x_1x_5 \\ & - 0.008x_1x_6 + 0.004x_1x_7 - 6.393x_1x_8 - 5.973x_1x_9 \\ & + 3.12x_2x_3 + 3.38x_2x_4 - 6.30x_2x_5 + 3.659x_2x_6 - 3.44x_2x_7 \\ & + 8.113x_2x_8 + 7.117x_2x_9 + 8.68x_3x_4 + 6.821x_3x_5 \\ & + 0.004x_3x_6 - 0.002x_3x_7 - 3.351x_3x_8 + 5.81x_3x_9 \\ & - 7.292x_4x_5 - 1.473x_4x_6 - 2.122x_4x_7 + 1.091x_4x_8 \\ & + 3.949x_4x_9 - 3.064x_5x_6 \end{aligned}$$

**Table 4** Correlation coefficient of Kriging surrogate model

Response	Correlation coefficient								
	$x_1$	$x_2$	$x_3$	$x_4$	$x_5$	$x_6$	$x_7$	$x_8$	$x_9$
$\tilde{W}(x)_{K-mass}$	0.843	0.222	1.386	0.052	0.942	0.834	0.003	0.332	0.101
$\tilde{g}(x)_{K-LC1}$	0.491	0.019	0.682	0.083	0.954	1.134	0.094	0.705	0.349
$\tilde{g}(x)_{K-LC2}$	0.265	0.018	0.671	0.113	1.062	0.859	0.133	0.406	0.853
$\tilde{g}(x)_{K-LC3}$	0.631	0.578	0.760	0.041	0.888	0.457	0.091	0.240	0.658
$\tilde{g}(x)_{K-LC4}$	1.511	0.374	0.757	0.18	0.772	0.005	0.691	0.071	0.198

The correlation coefficients of the Kriging surrogate model obtained for the design of the passive-type DSF are summarized in Table 4.

Furthermore, the COP surrogate model developed for the design of the passive-type DSF is expressed as follows:

$$\tilde{W}(x)_{C-mass} = 2134.1 + 1.68p_1(x) \quad (10)$$

$$\begin{aligned} & -0.00015p_2(x) + 0.97p_3(x) + 0.00005p_4(x) \\ & + 15.8p_5(x) + 0.00003p_6(x) + 0.67p_7(x) \\ & - 0.000009p_8(x) + 4.86p_9(x) - 0.00001p_{10}(x) \\ & + 5.7p_{11}(x) + 0.00001p_{12}(x) - 1.2p_{13}(x) \\ & + 0.0000086p_{14}(x) + 0.98p_{15}(x) - 0.000013p_{16}(x) \\ & + 0.54p_{17}(x) + 0.000017p_{18}(x) \end{aligned}$$

$$\begin{aligned} \tilde{g}(x)_{C-LC1} &= 205.73 - 0.06p_1(x) + 0.004p_2(x) \\ & + 0.03p_3(x) - 0.017p_4(x) - 0.438p_5(x) + 0.014p_6(x) \\ & - 0.019p_7(x) + 0.00029p_8(x) - 0.98p_9(x) + 0.025p_{10}(x) \\ & - 0.97p_{11}(x) + 0.03p_{12}(x) - 0.011p_{13}(x) + 0.00062p_{14}(x) \\ & - 0.19p_{15}(x) + 0.002p_{16}(x) - 0.35p_{17}(x) + 0.026p_{18}(x) \end{aligned}$$

$$\begin{aligned} \tilde{g}(x)_{C-LC2} &= 326.1 + 0.31p_1(x) + 0.07p_2(x) \\ & + 0.15p_3(x) - 0.11p_4(x) - 0.88p_5(x) + 0.04p_6(x) \\ & - 0.069p_7(x) - 0.002p_8(x) - 1.39p_9(x) + 0.037p_{10}(x) \\ & - 0.81p_{11}(x) + 0.051p_{12}(x) - 0.023p_{13}(x) - 0.0134p_{14}(x) \\ & - 0.52p_{15}(x) + 0.015p_{16}(x) - 1.057p_{17}(x) + 0.038p_{18}(x) \end{aligned}$$

$$\begin{aligned} \tilde{g}(x)_{C-LC3} &= 173.33 + 0.28p_1(x) + 0.014p_2(x) \\ & + 0.19p_3(x) - 0.057p_4(x) - 0.435p_5(x) + 0.024p_6(x) \\ & - 0.022p_7(x) - 0.0024p_8(x) - 0.79p_9(x) + 0.021p_{10}(x) \\ & - 0.31p_{11}(x) + 0.02p_{12}(x) - 0.041p_{13}(x) + 0.004p_{14}(x) \\ & - 0.35p_{15}(x) + 0.011p_{16}(x) - 0.57p_{17}(x) + 0.019p_{18}(x) \end{aligned}$$

$$\begin{aligned} \tilde{g}(x)_{C-LC4} &= 230.96 - 10.86p_1(x) + 0.64p_2(x) \\ & + 0.0018p_3(x) - 0.0000074p_4(x) - 0.118p_5(x) + 0.028p_6(x) \\ & + 0.00002p_7(x) + 0.0000026p_8(x) + 0.00056p_9(x) \\ & + 0.0000079p_{10}(x) - 0.0087p_{11}(x) + 0.000062p_{12}(x) \\ & - 0.0082p_{13}(x) + 0.0017p_{14}(x) + 0.00019p_{15}(x) \\ & - 0.000012p_{16}(x) - 0.0002p_{17}(x) + 0.0000034p_{18}(x) \end{aligned}$$

where

$$\begin{aligned} p_1(x) &= x_1 - 20; \quad p_2(x) = (x_1)^2 - 10.67; \quad p_3(x) = x_2 - 25; \\ p_4(x) &= (x_3)^2 - 16.67; \quad p_5(x) = (x_3 - 30); \\ p_6(x) &= (x_5)^2 - 24; \quad p_7(x) = (x_4 - 40); \\ p_8(x) &= (x_7)^2 - 42.67; \quad p_9(x) = (x_5 - 50); \\ p_{10}(x) &= (x_9)^2 - 66.67; \quad p_{11}(x) = (x_6 - 55); \\ p_{12}(x) &= (x_1)^2 - 80.67; \quad p_{13}(x) = (x_7 - 60); \\ p_{14}(x) &= (x_3)^2 - 96; \quad p_{15}(x) = (x_8 - 70); \\ p_{16}(x) &= (x_5)^2 - 130.67; \quad p_{17}(x) = (x_9 - 85); \\ p_{18}(x) &= (x_7)^2 - 192.67; \end{aligned}$$

### 3.4 Approximate Optimization Results

Approximate optimal solutions were obtained by applying the RSM,

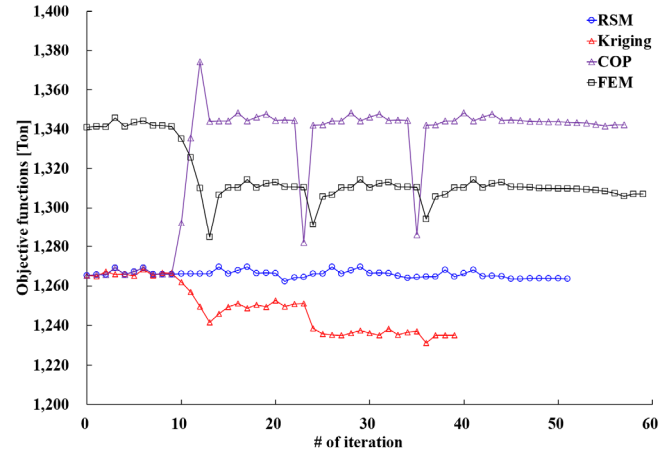
Kriging, and COP surrogate models, separately, in the design range defined during the formulation of an approximate optimum design for the passive-type DSF. To compare the efficiencies of the approximate optimization results based on the surrogate model characteristics, an FEM structure-analysis-based non-approximate optimization was performed, through which the optimal solution was derived and compared with the result of approximate optimization. The convergence result of the approximate optimization was recalculated using the FEM structure analysis to validate the actual value. In Table 5, the optimization results are summarized for the optimal design variable, satisfying the constraint feasibility; weight reduction, which is the objective function; and number of function evaluations (NFE). Fig. 6 illustrates the optimization convergence results of the objective function.

**Table 5** Comparative results of approximate optimization

Method	Optimum (mm)	Objective (t)	Approximate constraint (MPa)	Actual constraint (MPa)	NFE
RSM	$x_1 = 20$	1263.70	$g_1 = 213.24$ $g_2 = 202.28$ $g_3 = 301.75$ $g_4 = 163.73$	$g_1 = 229.08$ $g_2 = 199.88$ $g_3 = 299.34$ $g_4 = 167.54$	260
	$x_2 = 30$				
	$x_3 = 24$				
	$x_4 = 48$				
	$x_5 = 40$				
	$x_6 = 66$				
	$x_7 = 48$				
	$x_8 = 70$				
	$x_9 = 105$				
Kriging	$x_1 = 21$	1235.18	$g_1 = 221.01$ $g_2 = 200.79$ $g_3 = 301.15$ $g_4 = 171.26$	$g_1 = 217.78$ $g_2 = 202.23$ $g_3 = 303.87^{1)}$ $g_4 = 166.16$	200
	$x_2 = 27$				
	$x_3 = 25$				
	$x_4 = 47$				
	$x_5 = 41$				
	$x_6 = 63$				
	$x_7 = 48$				
	$x_8 = 70$				
	$x_8 = 100$				
COP	$x_1 = 19$	1336.80	$g_1 = 237.67$ $g_2 = 195.53$ $g_3 = 301.75$ $g_4 = 162.39$	$g_1 = 238.43$ $g_2 = 192.53$ $g_3 = 289.96$ $g_4 = 152.73$	290
	$x_2 = 33$				
	$x_3 = 27$				
	$x_4 = 48$				
	$x_5 = 46$				
	$x_6 = 65$				
	$x_7 = 47$				
	$x_8 = 70$				
	$x_8 = 100$				
FEM (Non-approximate)	$x_1 = 18$	1,217	-	$g_1 = 269.38$ $g_2 = 200.56$ $g_3 = 301.75^{2)}$ $g_4 = 169.16$	-
	$x_2 = 29$				
	$x_3 = 19$				
	$x_4 = 48$				
	$x_5 = 43$				
	$x_6 = 63$				
	$x_7 = 46$				
	$x_8 = 70$				
	$x_8 = 97$				

<sup>1)</sup> Infeasible constraint

<sup>2)</sup> Active constraint



**Fig. 6** Iteration history of objective functions

As shown in Table 5 and Fig. 6, the approximate optimization result using the Kriging model indicated the most significant weight reduction. However, although the result of LC3 constraints satisfied the upper limit of the constraints in the approximate optimization, the actual constraint evaluation result showed that the feasibility was not satisfied. This is attributable to the design problem and the surrogate model's characteristics; hence, it indicates that an approximate optimal solution may exist outside the feasible area because of the nonlinear characteristics of the constraint function. Therefore, such a Kriging-based approximate optimum design does not satisfy the constraints and hence cannot be used in passive-type DSF designs. The FEM-structure-analysis-based non-approximate optimization shows activated results for the upper limit of LC3 conditions, which is the most critical aspect in the design of passive DSFs. Under the LC3 conditions, the approximate optimization results of the RSM and COP were distributed in approximately 0.7% and 3.9% of the feasible range, respectively, compared with the FEM-structure-analysis-based non-approximate optimization results. These characteristics afforded increased structural safety with respect to uncertainties in design and manufacturing. Except for the Kriging-based approximate optimization, the RMS indicated the most significant weight reduction effect among the approximate optimization methods. Considering the initial design weight, i.e., 1,341 ton, of the passive-type DSF, the RSM-based approximate optimization yielded a 5.8% weight reduction. The convergence was excellent in the case of using Kriging since the NFE was the lowest; however, because the constraints of LC3 were violated, it can be concluded that the RSM-based approximate optimization demonstrated a more appropriate convergence. Based on the convergence results of the objective function and the NFE, it is concluded that the RSM is the most efficient method for the approximate optimization design of passive-type DSFs.

#### 4. Conclusion

In this study, an approximate optimization was performed using various surrogate models to identify the most appropriate optimal design method for the structural design of passive-type DSFs. The

efficiency and feasibility analysis of the approximate optimization was performed based on the characteristics of the surrogate models because a feasibility validation through approximate optimization or reliability analysis is crucial to enable the use of surrogate models in actual design problems. The primary findings of this study are as follows.

(1) To evaluate the structural safety in the initial design of DSFs used to install a 20,000-ton class topside on an offshore platform using the float-over method, we determined the design load conditions by applying classification rules pertaining to actual operating conditions. For the performance evaluation of the structural design, a 3D structure analysis model using the FEM was developed, and the structure analysis results were obtained by applying the design load and boundary conditions to the structure analysis model. Subsequently, the maximum stress was analyzed at each design load condition.

(2) The maximum stress of the passive-type DSF satisfied the allowable stress of classification rules at every design load condition. Furthermore, the structural members of SM490YB material showed a higher overall stress level than those of API-5L-X52 material. The maximum stress level of the passive-type DSF was similar to the allowable stress limit in the case of LC3, indicating that the weight must be minimized while the design load conditions of LC3 satisfied in the structure optimization for a minimum-weight design.

(3) Three surrogate models were applied for the approximate optimization: RSM, Kriging, and COP models. An optimal design problem was formulated to determine the design variable of thickness for the primary structural members to minimize the structure weight while satisfying all the constraints of strength performance, i.e., less than or equal to the allowable maximum yield stress at each design load condition. RSM, Kriging, and COP surrogate models were applied, separately, for the design scope defined during the approximate optimum design formulation to obtain the approximate optimal solutions. To compare the efficiencies of approximate optimization results based on the surrogate model characteristics, an FEM-structure-analysis-based non-approximate optimization was performed to derive optimal solutions, which were compared with the results of approximate optimal solutions.

(4) In the approximate optimum design of passive-type DSFs, the result of approximate optimization using Kriging demonstrated the most significant weight reduction; however, the constraint evaluation indicated poor feasibility. The results of approximate optimization using Kriging showed that the result of LC3 constraints satisfied the upper limit of the constraints in the approximate optimization; however, because the feasibility was poor based on the actual constraint evaluation, we concluded that Kriging cannot be used when designing an actual passive-type DSF. Compared with the initial design weight of the passive-type DSF, the RSM-based approximate optimization indicated a 5.8% weight reduction. Furthermore, based on the convergence results of objective functions and the NFE, it is concluded that the RSM is the most effective method for the approximate optimization design of passive-type DSFs.

Based on the results of this study, we plan to conduct a study pertaining to stochastic optimization, such as robustness and reliability-based optimum designs, in the future.

## Funding

This research was supported by a grant from the National R&D Project of “Development of Core Installation Technologies for Float-over and Dual Crane Methods” funded by Ministry of Oceans and Fisheries, and KIAT grant funded by the Korea government (MOTIE) (P0001968, The competency development program for industry specialist).

## References

- Baek, S.H., Kim, H.S., & Han, D.S. (2011). Structural Optimization of Variable Swash Plate for Automotive Compressor Using Orthogonal Polynomials. *Transactions of the Korean Society of Mechanical Engineers - A*, 35(10), 1273–1279. <https://doi.org/10.3795/KSME-A.2011.35.10.1273>
- Cho, S.K., Byun, H., & Lee, T.H. (2009). Selection Method of Global Model and Correlation Coefficients for Kriging Metamodel. *Transactions of the Korean Society of Mechanical Engineers - A*, 33(3), 813–818. <https://doi.org/10.3795/KSME-A.2009.33.8.813>
- DNV-GL. (2012). Load Transfer Operations. Det Norske Veritas.
- DNV-GL. (2013). Offshore Installation Operations. Det Norske Veritas.
- DNV-GL. (2015). Structural Design of Offshore Units WSD (Working Stress Design) Method. Det Norske Veritas.
- GL. (2015a). Guidelines for Load-outs. GL Noble Denton.
- GL. (2015b). Guidelines for Marine Transportations. GL Noble Denton.
- Haftka, R.T., & Gürdal, Z. (1991). *Elements of Structural Optimization*. Dordrecht, Netherlands: Kluwer Academic Publishers.
- Ji, Y.J., Kwak, J.S., Lee, H.Y., & Kim S.C. (2015). Optimal Arrangement of Resilient Mount installed on Frame Support Structure at Shipboard Equipment under Shock Load. *Journal of the Society of Naval Architects of Korea*, 52(4), 298–304. <https://doi.org/10.3744/STAK.2015.52.4.298>
- Jung, J.J., Lee, W.S., Shin, H.S., & Kim, Y.H. (2009). Evaluating the Impact Load on the Offshore Platform During Float-over Topside Installation. *Proceedings of 9th International Offshore and Polar Engineering Conference*, Osaka, Japan, 205–210.
- Kim, H.S., Kim, B.W., Jung, D., & Sung, H.G. (2017). Numerical Study for Topside Effect on Behavior of Deck Transportation Vessel and Seafastening Structure. *Proceedings of OCEANS 2017, Aberdeen, UK*. <https://doi.org/10.1109/OCEANSE.2017.8084841>
- Park, J.M., Park, C.H., Kim, T.S., & Choi, D.H. (2011). Optimal

- Determination of Pipe Support Types in Flare System for Minimizing Support Cost. *Journal of the Society of Naval Architects of Korea*, 48(4), 325–329. <https://doi.org/10.3744/SNAK.2011.48.4.325>
- Park, J.H., Lee, D., Yang, J.W., & Song, C.Y. (2019). Design Enhancement to Avoid Radar Mast Resonance in Large Ship Using Design of Experiments. *Journal of Ocean Engineering and Technology*, 33(1), 50–60. <https://doi.org/10.26748/KSOE.2018.088>
- Park, S.H. (2012). *Design of Experiments*. Seoul, Korea: Minyoung Publishing.
- Simulia. (2018). *Abaqus User Manual*. Simulia.
- Song, C.Y., Lee, J., & Choung, J. (2011). Reliability-based Design Optimization of an FPSO Riser Support Using Moving Least Squares Response Surface Meta-models. *Ocean Engineering*, 38(1), 304–318. <https://doi.org/10.1016/j.oceaneng.2010.11.001>
- Song, C.Y., & Lee, J. (2010). Comparative Study of Approximate Optimization Techniques in CAE-based Structural Design. *Transactions of the Korean Society of Mechanical Engineers - A*, 34(11), 1603–1611. <https://doi.org/10.3795/KSME-A.2010.34.11.1603>

### Author ORCIDs

Author name	ORCID
Lee, Dong Jun	0000-0002-0610-1756
Song, Chang Yong	0000-0002-1098-4205
Lee, Kangsu	0000-0002-9505-6802



# Evaluation on Sensitivity and Approximate Modeling of Fire-Resistance Performance for A60 Class Deck Penetration Piece Using Heat-Transfer Analysis and Fire Test

Woo Chang Park<sup>1</sup> and Chang Yong Song<sup>2</sup>

<sup>1</sup>Graduate Student, Department of Naval Architecture & Ocean Engineering, Mokpo National University, Jeonnam, Korea

<sup>2</sup>Professor, Department of Naval Architecture & Ocean Engineering, Mokpo National University, Jeonnam, Korea

**KEY WORDS:** A60 class deck penetration piece, Heat transfer analysis, Fire test, Fire resistance sensitivity, Approximate model

**ABSTRACT:** The A60 class deck penetration piece is a fire-resistance apparatus installed on the deck compartment to protect lives and to prevent flame diffusion in the case of a fire accident in a ship or offshore plant. In this study, the sensitivity of the fire-resistance performance and approximation characteristics for the A60 class penetration piece was evaluated by conducting a transient heat-transfer analysis and fire test. The transient heat-transfer analysis was conducted to evaluate the fire-resistance design of the A60 class deck penetration piece, and the analysis results were verified via the fire test. The penetration-piece length, diameter, material type, and insulation density were used as the design factors (DFs), and the output responses were the weight, temperature, cost, and productivity. The quantitative effects of each DF on the output responses were evaluated using the design-of-experiments method. Additionally, an optimum design case was identified to minimize the weight of the A60 class deck penetration piece while satisfying the allowable limits of the output responses. According to the design-of-experiments results, various approximate models, e.g., a Kriging model, the response surface method, and a radial basis function-based neural network (RBFN), were generated. The design-of-experiments results were verified by the approximation results. It was concluded that among the approximate models, the RBFN was able to explore the design space of the A60 class deck penetration piece with the highest accuracy.

## 1. Introduction

A fire that occurs in a ship or offshore plant can result in large-scale structural damage and loss of lives owing to the flame spread. Thus, the International Maritime Organization (IMO) is strengthening the fire-prevention regulations for the major sections of ships and offshore plants. With regard to A60 class fire-prevention equipment, the fire-prevention design regulated by Safety of Life at Sea (SOLAS) should be applied to prevent the flame spread in the section where the corresponding equipment is installed for 60 min (IMO, 2010). The A60 class deck penetration piece (A60 DPP) is fire-prevention equipment applied in the case where the cable for control or communication must penetrate the horizontal structure of the section, introducing a high risk of fire. The IMO requires the verification the fire-prevention performance of the A60 DPP according to the fire test procedure (FTP) regulations (MSC, 2010).

Research on evaluating the fire-prevention performance of ships and

offshore plants has only been partially conducted. Yu et al. (2000) proposed electric arc furnace test and tank test methods for the evaluation of the fire-prevention performance of oil boom material types. Choi et al. (2013) conducted the fire-prevention performance test by adjusting the fireproof material conditions of the fire damper blade and coaming to satisfy the H-120 fire-prevention performance of the H-120 class fire damper. Choi et al. (2014) conducted a fire-prevention test considering the manufacturing conditions of various composite materials to assess the fire-prevention performance for fiberglass-reinforced plastic ship materials. Jang et al. (2014) performed thermal analysis on the fire-prevention design items of the H-120 class fire damper and conducted a fire-prevention test by changing the fire-prevention design conditions. Song and Kim (2020) verified the design items of the A0 class bulkhead penetration pipe applied to vertical structures of a ship through a heat-transfer analysis and fire prevention test.

In this study, the approximation characteristics of the design space

Received 18 February 2021, revised 5 March 2021, accepted 12 March 2021

Corresponding author Chang Yong Song: +82-61-450-2732, [cysong@mokpo.ac.kr](mailto:cysong@mokpo.ac.kr)

© 2021, The Korean Society of Ocean Engineers

This is an open access article distributed under the terms of the creative commons attribution non-commercial license (<http://creativecommons.org/licenses/by-nc/4.0>) which permits unrestricted non-commercial use, distribution, and reproduction in any medium, provided the original work is properly cited.

were evaluated via a sensitivity analysis of the fire-prevention performance of the A60 DPP used for a ship and offshore plant, a fire-prevention design sensitivity analysis based on the design of experiments to minimize the weight, and various approximate models. By applying statistical methods such as design of experiments to the design process of the fire-prevention system, such as the newly developed A60 DPP, the design space was explored effectively, and the optimum design plan was easily deduced. For the evaluation of the fire-prevention performance of the A60 DPP, a transient heat-transfer analysis based on the finite-element method (FEM) was performed by reflecting the specimen specifications and temperature conditions on the FTP regulation code. A fire test was conducted for verifying the transient heat-transfer analysis results, in accordance with the FTP regulation code of the Maritime Safety Committee. The verified finite-element model and transient heat-transfer analysis results were linked with the design of experiments. For the design factors (DFs), the length of the A60 DPP, diameter, material type, and insulation density were used, and for the output responses, the weight, temperature, price, and productivity were individually applied. In the sensitivity analysis, the effect of each DF on the output response was quantitatively assessed using the design-of-experiments results, and the optimum design combinations to minimize the weight while satisfying the tolerance limit of the output response, such as the temperature, price, and productivity, were identified. On the basis of the design-of-experiments results, various approximate models, e.g., a Kriging model, the response surface method (RSM), and a radial basis function-based neural network (RBFN), were produced. The design-of-experiments results were verified by analyzing the accuracy of each approximate model to approximate the design space of the A60 DPP. The results indicated that the RBFN could approximate the A60 DPP design space with the highest accuracy. The design items and fire-prevention performance evaluation regulations of the A60 DPP, transient heat-transfer analysis results, and fire-test verification results are presented in Chapter 2, the design-of-experiments and sensitivity-analysis results are presented in Chapter 3, and the theory for the approximate models and approximation characteristics is reviewed in Chapter 4. The conclusions are presented at the end of the paper.

## 2. Evaluation of Fire-Prevention Performance

### 2.1 Fire-prevention Design and Performance Evaluation Regulations for A60 DPP

The A60 DPP applied to ships and offshore plants is fire-prevention equipment used for the maintenance of confidentiality in the case of a deck fire, along with the safe operation of cables penetrating the deck for control and communication. The objective of this study was to evaluate the fire-prevention performance of the newly developed A60 DPP by reducing the body length and applying insulating refractory materials for improving the productivity and quality. The design configuration of the A60 DPP investigated in this study is presented in Fig. 1.

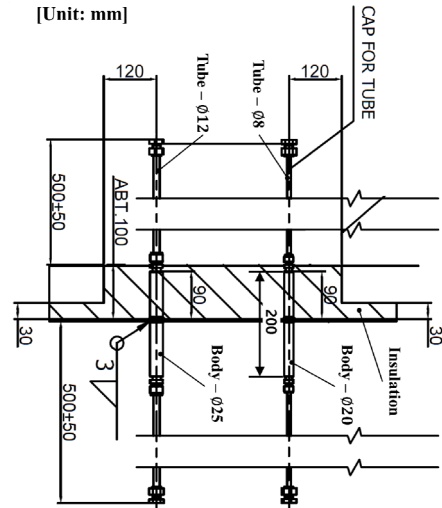


Fig. 1 Design specifications of the A60 DPP

As shown in Fig. 1, the length of the penetration pipe body was designed to be 200 mm, the diameter of the tube was designed to be  $\varnothing 8$  and  $\varnothing 12$  mm, and the diameter of the body was designed to be  $\varnothing 20$  and  $\varnothing 25$  mm. The insulation was attached 90 mm lean to one side from the center of the penetration pipe. Regarding the materials of the penetration pipe, the specifications for the carbon steel for machine structural use (S45C) and austenitic stainless steel (SUS316L) were separately applied.

The A60 DPP should be designed to make the temperature measured at the other side of the inflamed side  $<180^\circ\text{C}$  under the flame heating conditions set for 60 min. Fig. 2 shows the configuration of the specimen for the fire test (structure steel core) based on the FTP code.

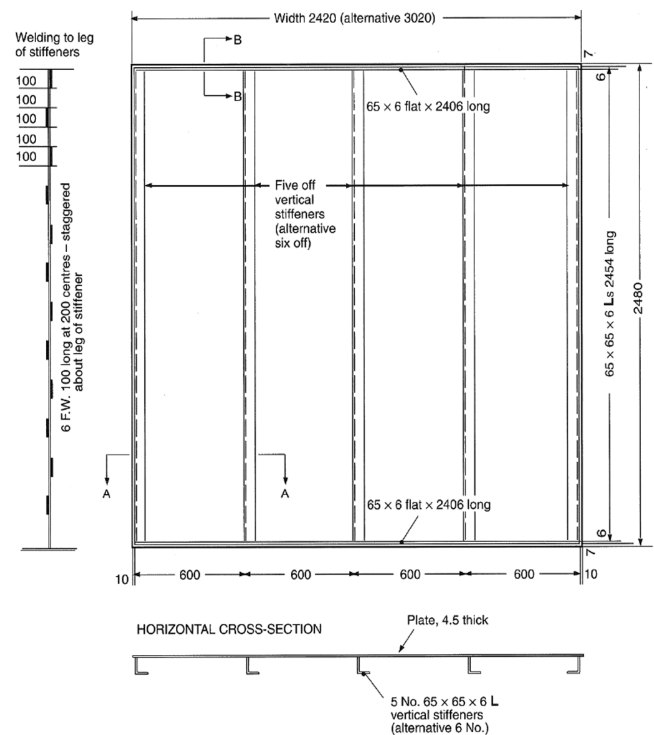


Fig. 2 Configuration of the structure steel core (MSC, 2010)

As shown in Fig. 2, the specimen for the fire test for the A60 DPP must be made of steel, and the L-type reinforcement with dimensions of  $(65 \pm 5) \times (65 \pm 5) \times (6 \pm 1)$  mm should be arranged with intervals of 600 mm on a slab with a width of 2,440 mm, length of 2,500 mm, and depth of  $4.5 \pm 0.5$  mm. The fire-prevention performance of the A60 DPP should be verified through the fire test, where it is attached with insulation between L-type stiffeners of the specimen shown in Fig. 2. For the fire-test specimen with the A60 DPP and insulation attached, the insulation should be placed on the flamed side for the evaluation, identical to the installation status of an actual ship and offshore plant. It should be installed horizontally to the furnace and heated to  $940^\circ\text{C}$  for 60 min.

## 2.2 Transient Heat-Transfer Analysis and Fire Test

A transient heat-transfer analysis was conducted using the general-purpose FEM software ABAQUS/Implicit (Simulia, 2019). The transient heat-transfer analysis model, which was generated on the basis of the A60 DPP design configuration shown in Fig. 1 and the fire-test specimen presented in Fig. 2, is displayed in Fig. 3. The detailed specifications of this analysis model are presented in Table 1. The finite-element model applied to the transient heat-transfer analysis comprised 1,352,236 elements and 323,738 nodal points, and for the finite element, a tetrahedral heat-transfer element (DC3D4) was utilized.

Regarding the thermal conductivity and specific heat characteristics of the material, the characteristics with different temperatures were

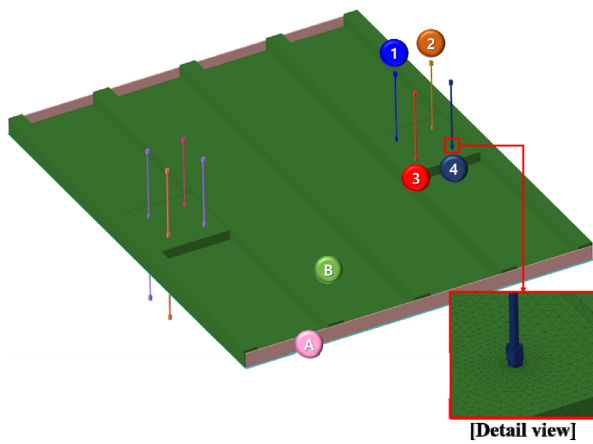


Fig. 3 Transient heat-transfer analysis model

Table 1 Specifications of the analysis model

No.	Part	Dimension (mm) (Tube / Body)	Material type
1	Penetration piece	$\varnothing 8 / \varnothing 20$	SUS316L
2	Penetration piece	$\varnothing 8 / \varnothing 20$	S45C
3	Penetration piece	$\varnothing 12 / \varnothing 25$	SUS316L
4	Penetration piece	$\varnothing 12 / \varnothing 25$	S45C
A	Structure steel core	-	SS400
B	Insulation	-	A60 class

applied by referring to the results of previous research to improve the accuracy of the transient heat-transfer analysis, as shown in Figs. 4–7.

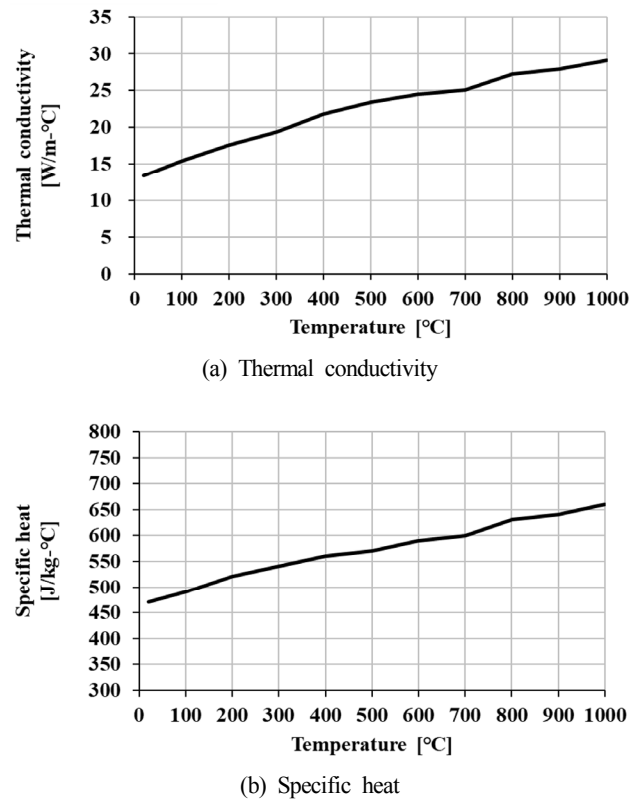


Fig. 4 Material properties of SUS316L (Piscopo et al., 2019)

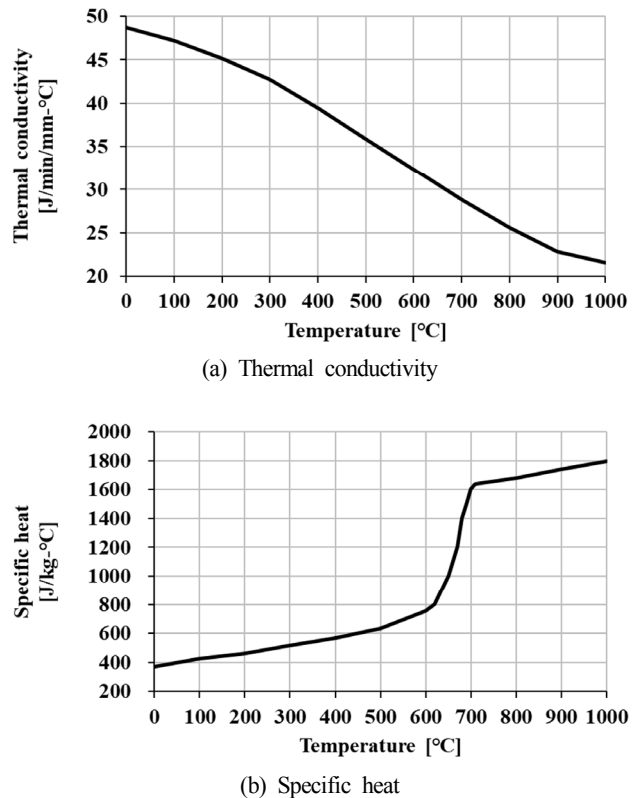
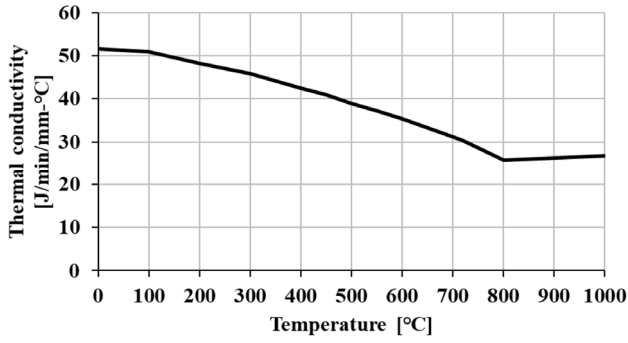
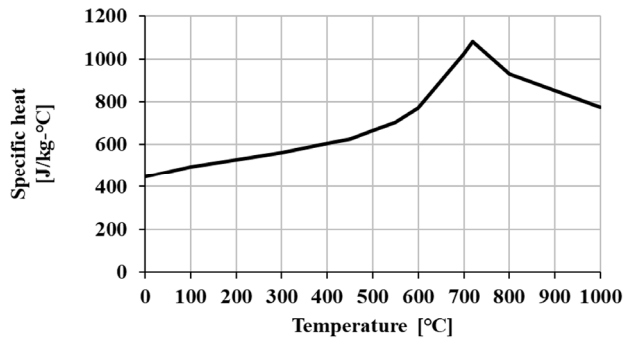


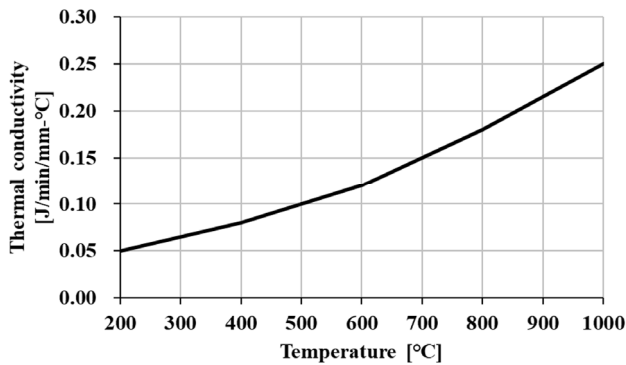
Fig. 5 Material properties of S45C (Magnabosco et al., 2006)



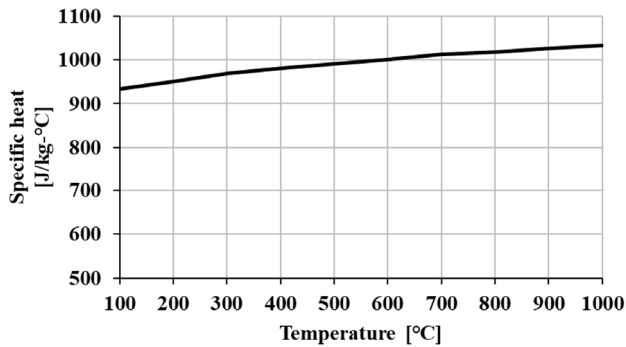
(a) Thermal conductivity



(b) Specific heat

**Fig. 6** Material properties of SS400 (Suman et al., 2016)

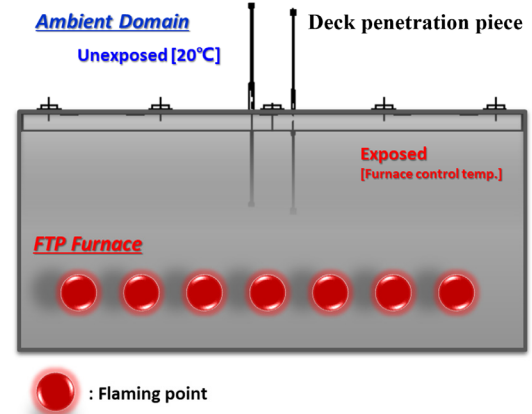
(a) Thermal conductivity



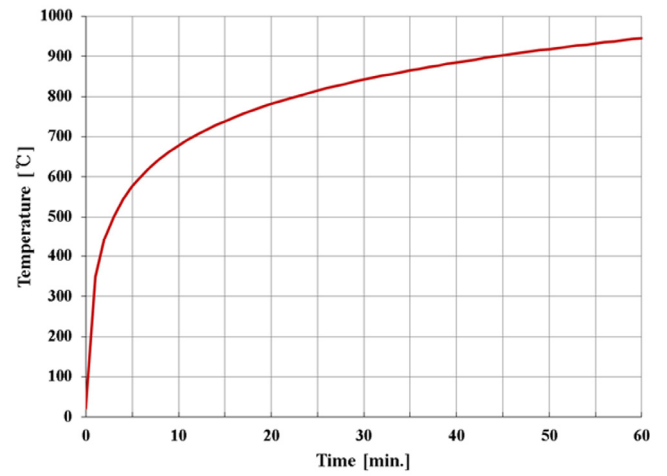
(b) Specific heat

**Fig. 7** Material properties of insulation (Ohmura et al., 2003)

The furnace heating condition regulated by the FTP code was identically applied for the heat input condition of the transient



(a) Furnace condition



(b) Furnace control temperature

**Fig. 8** Furnace flame condition

heat-transfer analysis, as shown in Fig. 8. As indicated by Fig. 8(a), the specimen in which the A60 DPP is embedded at the furnace is installed in a horizontal direction to give the insulation-attached side an internal orientation toward the furnace. The internal temperature of the furnace is increased to 940 °C for 60 min with the flame of flaming point following the furnace control temperature curve presented in Fig. 8(b). The furnace control temperature curve is defined by Eq. (1). (MSC, 2010):

$$T = 340 \log_{10}(8t + 1) + 20 \text{ [}^\circ\text{C]} \quad (1)$$

where  $T$  represents the heating temperature (°C), and  $t$  (min) represents the heating time.

Regarding the temperature measurement, the maximum temperature at the A60 DPP body is measured at the unexposed ambient domain of the furnace. We decided to satisfy the regulations in the case where the temperature deviation is below 180 °C.

Because the furnace heating condition regulated in the FTP code is a method of increasing the atmosphere temperature inside the closed furnace, Eq. (2) for calculating the convection coefficient was utilized in the transient heat-transfer analysis (Yunus and Afshin, 2012):

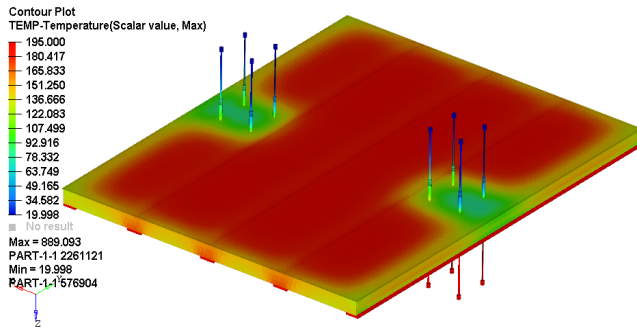


Fig. 9 Temperature distribution contour results for unexposed ambient domain

$$h = \frac{k}{L} Nu \quad [W/m^2 K] \quad (2)$$

$$Nu = 0.27 R_{aL}^{1/4}$$

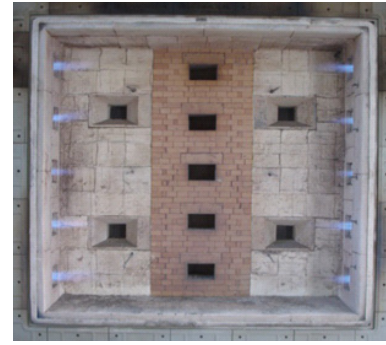
$$R_{aL} = \frac{g\beta(T_s - T_\infty)L^3}{\nu^2} Pr$$

Here,  $Nu$  represents the Nusselt number,  $R_{aL}$  represents the Rayleigh number,  $Pr$  represents the Prandtl number,  $k$  represents the thermal conductivity of the fluid,  $L$  represents the characteristic length,  $\nu$  represents the kinematic viscosity of the fluid,  $g$  represents the gravitational acceleration,  $\beta$  is the cubic expansion coefficient,  $T_s$  represents the surface temperature, and  $T_\infty$  represents the temperature of the fluid far from the surface.

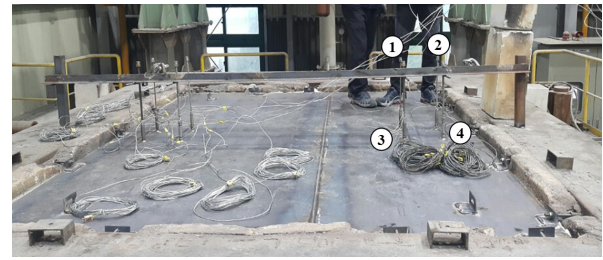
The temperature-distribution results of the transient heat-transfer analysis at the heating time point of 60 min are presented in Fig. 9.

The temperature distribution at the unexposed ambient domain was between 20 and 195 °C, as shown in Fig. 9, and the temperature of the part where the A60 DPP was installed was found to be high. In the transient heat-transfer analysis, the temperatures measured at the A60 DPP body at the unexposed ambient domain at the heating time point of 60 min were 63.7, 84.3, 64.6, and 88.1 °C at points 1, 2, 3, and 4, respectively, which correspond to the numbers in Fig. 3 and Table 1.

For the verification of the transient heat-transfer analysis results, the specimen was manufactured in accordance with the FTP regulation code, similar to the analysis model, and a fire test was performed according to the international standard test method. The horizontal furnace, i.e., fire-testing equipment for the A60 DPP, is an instrument for testing fire-prevention equipment of the A-class horizontal sections used in ships and offshore plants, and it requires an effective heating area of 3,000 mm × 3,000 mm. The internal temperature of the furnace is controlled by following the furnace control temperature curve, as shown in Eq. (1), through the burner installed at the lower part of the side, and the fire test is performed for different durations depending on the fire rating (ISO, 1999). The furnace equipment and the composition of the test setup utilized for the A60 DPP fire test are shown in Fig. 10.



(a) Horizontal furnace



(b) Fire test of the A60 DPP

Fig. 10 Fire-test setup

Table 2 Comparison of the temperature measurement results

No.	Analysis (°C)	Test (°C)	Error (%)
1	63.7	58.6	8.7
2	84.3	95.0	11.3
3	64.6	58.2	11.0
4	88.1	99.7	11.6

As shown in Fig. 10(b), the A60 DPP temperature was measured at the position used for the transient heat-transfer analysis during the fire test, and the measurement results were compared with the analysis results, as shown in Table 2.

As shown in Table 2, the minimum error between the A60 DPP transient heat-transfer analysis and the fire test (8.7%) was obtained for measurement point 1, and the maximum error (11.6%) was obtained for point 4. The average error for all the measurement positions was 10.7%, and the tendency of change in temperature characteristics depending on different design specifications was also found to be similar. Considering that it is the transient heat-transfer analysis for the 60 min-fire test, it was concluded that the accuracy of the analysis results is verified. Therefore, it was confirmed that the fire-prevention design specifications of the A60 DPP considered in this study satisfy the FTP code regulations. Furthermore, because the fire-prevention design and heat-transfer characteristics of the A60 DPP were confirmed to be suitable via the transient heat-transfer analysis, a sensitivity analysis of the fire-prevention performance of the A60 DPP along with an evaluation of the approximation of the design space was conducted using analytical methods.



### 3. Sensitivity Analysis

In the sensitivity analysis of the A60 DPP, the verified finite-element model and transient heat-transfer analysis results were linked with the design of experiments, and the effect of each DF on the output response was quantitatively evaluated. For the DFs of the design of experiments, the length of the A60 DPP, diameter, material type, and insulation density were used. For the output responses, the weight, temperature, price, and productivity were individually applied. According to the design-of-experiments results, the optimum design combinations that can minimize the weight while satisfying the tolerance limit of the output response, such as the temperature, price, and productivity, were identified. In the design of experiments, the DFs and their levels were defined to be three levels for the body length and tube diameter, two levels for the material type of the A60 DPP, and three levels for the insulation type. Details are presented in Table 3.

Among the output responses, the weight of the A60 DPP (excluding the specimen and the insulation connected to the A60 DPP) was considered as the weight, the measurement results from the transient heat-transfer analysis were applied as the temperature, and the price for each material type of the A60 DPP per the unit weight in a unit of

**Table 3** Design factors and their levels

Design factor	Level 1	Level 2	Level 3
DF#1: Length of body (mm)	150	200	250
DF#2: Diameter of tube (mm)	∅6	∅8	∅12
DF#3: Material type of A60 DPP	S45C	SUS316L	-
DF#4: Insulation density (kg/m <sup>3</sup> )	96	128	160

**Table 4** Full-factorial experiment results

Run	Design factor			
	DF#1 (mm)	DF#2 (mm)	DF#3	DF#4 (kg/m <sup>3</sup> )
1	150	6	S45C	96
2	150	6	S45C	128
3	150	6	S45C	160
⋮	⋮	⋮	⋮	⋮
52	250	12	SUS316L	96
53	250	12	SUS316L	128
54	250	12	SUS316L	160

Run	Output response			
	Weight (kg)	Temp. (°C)	Cost (1000×₩)	Productivity
1	0.65	100.05	3.8	12.6
2	0.65	86.17	3.8	12.6
3	0.65	74.15	3.8	12.6
⋮	⋮	⋮	⋮	⋮
52	1.30	71.24	37	12
53	1.30	63.39	37	12
54	1.30	54.21	37	12

**Table 5** Main effect results (unit: %)

Output response	Design factor			
	DF#1	DF#2	DF#3	DF#4
Weight	22.65	40.96	1.52	0.50
Temperature	8.96	4.12	19.95	21.33
Cost	3.73	7.07	20.82	0.02
Productivity	50.01	38.57	0.42	0.00

1,000 KRW was considered as the price. A productivity grade was assigned to each of the following and used as a quantitative index: the A60 DPP length, diameter, and the material type. The minimum weight was set to be preferred, and the tolerance limit of the temperature was defined to be below 180 °C, in accordance with the FTP code regulation. The maximum values for price and productivity calculated in the DF fluctuation level range of Table 3 were 37 and 17, respectively, and the 20% upper limit and lower limit of the maximum value were set as the tolerance limits, respectively. A full-factorial experiment with 54 runs was designed by applying the DF fluctuation level shown in Table 3, and the output-response results with changes in the DFs are presented in the experimental matrix of Table 4.

In the sensitivity analysis, a quantitative main effect analysis of the DFs on each output response was conducted using the experimental matrix of Table 4, and the results are presented in Table 5. The main effect analysis indicates the average change of the output response observed with the fluctuation of DF levels, i.e., the sensitivity, and if the magnitude of the effect calculated from a DF is high, the importance of this factor to the output response is high.

As shown in Table 5, the DFs with the most significant effects on the weight, temperature, price, and productivity were found to be the A60 DPP diameter, insulation density, material type of the A60 DPP, and length of the A60 DPP, respectively. On the basis of the sensitivity-analysis results, the selection of the insulation and A60 DPP material type in the fire-prevention design was found to be highly important. Furthermore, the effects of the A60 DPP length and diameter on the productivity were significant. The optimum design combinations that minimized the A60 DPP weight while satisfying the tolerance limit of the output responses were selected from the results presented in Table 4 and are presented in Table 6.

**Table 6** Optimum design cases for A60 DPP

	Content	Initial design	Optimum design case
	DF#1 (mm)	200	150
Design factors	DF#2 (mm)	8	6
	DF#3	S45C	S45C
	DF#4 (mm)	128	96
Output response	Weight (kg)	0.84	0.65 (↓ 22.6%)
	Temp. (°C)	84.29	100.05 (↑ 18.7%)
	Cost (1000×₩)	5.0	3.8 (↓ 24.0%)
	Productivity	11.6	12.6 (↑ 8.6%)

As shown in Table 6, using the optimum DF combinations, the weight and price were reduced by 22.6% and 24%, respectively, while the productivity was increased by 8.6%. Although the temperature was increased by 18.7%, it sufficiently satisfied the condition of a temperature below 180 °C, which is the FTP code regulation. In summary, useful design information regarding the fire-prevention performance and productivity of the A60 DPP was obtained via the design of experiments and sensitivity analysis.

#### 4. Approximation Modeling

Because an approximate model is generally obtained from the design of experiments, the general suitability of the design of experiments, such as the number of experiments conducted and levels of the DFs, can be verified by reviewing the accuracy of the approximate model (Song and Lee, 2010). Meanwhile, securing an approximate model suitable for the design problem can reduce the numerical cost for optimization analysis, robust analysis, and reliability analysis, which are computationally expensive; thus, the generation of an approximate model with high accuracy is important in design space exploration research. In the approximation modeling evaluation, different approximate models, i.e., Kriging, the RSM, and RBFN, were created according to the design-of-experiments results for the A60 DPP. Moreover, the suitability of the design-of-experiments results was verified by examining the accuracy of the approximation modeling results, and the accuracies of the models for approximating the A60 DPP design space were compared.

The Kriging model is defined as the sum of the whole model of the actual design space function to be approximated and the local model corresponding to the deviation of the actual function and whole model (Cho et al., 2009).

$$\tilde{g}(x)_K = Z(x)^T A_K + E(x) \quad (3)$$

Here,  $A_K$  represents the unknown coefficient vector, and  $Z(x)$  represents the global model vector.  $E(x)$  represents the spatial correlation of design data and is defined as the Gaussian correlation function.

The RSM is expressed as the following second-degree polynomial regression model using the least-squares method (Song and Lee, 2010).

$$g = A_0 + \sum_{i=1}^k A_i Z_i + \sum_{i=1}^k A_{ii} Z_i^2 + \sum_{i < j}^k A_{ij} Z_i Z_j + e \quad (4)$$

When the matrix  $Z$  defined by response vector  $g$  and  $k$  base variables is obtained from  $n$  experimental points, the unknown RSM approximation coefficient vector  $A_R$  is calculated using the following equation, by minimizing the random error vector  $e$  from the relationship between  $g$  and  $Z$ .

$$A_R = (Z^T Z)^{-1} Z^T g \quad (5)$$

By applying the approximation coefficient calculated using Eq. (5), the RSM second-degree regression approximate model can be generated.

The RBFN was developed to approximate the scattered multivariate data with high accuracy (Dyn et al., 1986). The RBFN uses linear combinations of the radial symmetry function utilizing Euclidean distance for the approximation of the output response. When the node-set of the neural network, i.e.,  $x_1, \dots, x_n \in ohm \subset R^n$ , is provided, the basis function of the RBFN is defined as follows:

$$g_j(x) = \phi(\|x - x_j\|) \in R, j = 1, \dots, n \quad (6)$$

where  $\phi$  represents the power spline basis function, and norm  $\|x - x_j\|$  represents the Euclidean distance. Using the Euclidean distance, the input layer data of the neural network is classified into uniform clusters. The power spline basis function is defined as follows:

$$\phi = r^c \quad (7)$$

where  $c$  is a positive constant and a variable of the shape function. When the response data  $x_1, \dots, x_n \in ohm \subset R^n$  to be approximated with the input data  $y_1, \dots, y_n \in ohm \subset R^n$  is provided, the RBFN approximate model is defined as outlined in Eq. (8) after the neural-network learning process, as shown in Fig. 11.

$$\begin{aligned} \tilde{g}_{RBF}(x) &= \sum_{j=1}^n \alpha_j g_j(x) + \alpha_{n+1} \\ \sum_{j=1}^n \alpha_j g_j(x) + \alpha_{n+1} &= y_i, i = 1, \dots, n \end{aligned} \quad (8)$$

Here,  $\alpha_j$  is the unknown approximation coefficient.

The accuracy of the approximate model was determined using the  $R^2$  value, as follows:

$$R^2 = 1 - \frac{\sum (t_i - y_i)^2}{\sum (t_i - \bar{t}_i)^2} \quad (9)$$

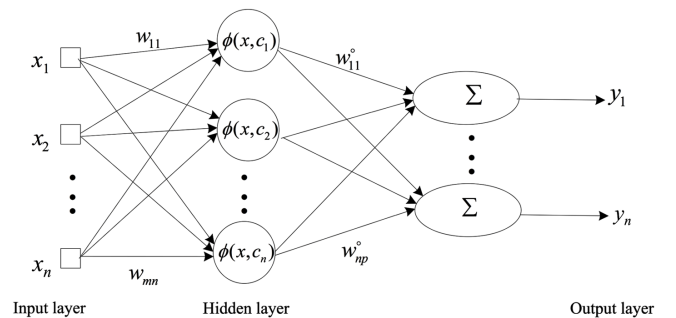


Fig. 11 Learning procedure of the RBFN

**Table 7** Comparison of approximate modeling results

Approximate model	$R^2$ value				
	Weight	Temp.	Cost	Productivity	Avg.
Kriging	0.978	0.947	0.955	0.976	0.964
RSM	0.999	0.987	0.998	1.000	0.996
RBFN	1.000	0.999	1.000	0.999	1.000

where  $t_i$  represents the actual value,  $y_i$  represents the predicted value estimated using the approximate model, and  $\bar{t}_i$  represents the average value of the actual values.  $R^2 = 1.0$  indicates that the predicted value estimated using the approximate model perfectly matches the actual value of the total design space. The accuracy analysis results for each output response of the A60 DPP calculated using each approximate model are presented in Table 7.

As indicated by Table 7, the  $R^2$  values for the output responses of all the approximate models were  $>0.96$  on average, indicating a high accuracy. Among approximate models, the Kriging model exhibited the lowest accuracy overall, while the average  $R^2$  results for the RSM and RBFN were high: 0.996 and 1.000, respectively. For all the approximate models, the accuracy of the temperature response was the lowest, and that of weight response was the highest. This difference in approximation accuracy can be explained by the fact that the weight response is a linear characteristic while the temperature response, which is the result of the transient heat-transfer analysis, has a relatively high nonlinearity. The design-of-experiments method used in this study was verified to be suitable for the design-space analysis of A60 DPP. Among the approximate models used in the full-factorial experiment of this study, the RBFN allowed exploration of A60 DPP design space with the highest accuracy and is expected to be used for optimization analysis, robust analysis, and reliability analysis to improve the efficiency of numerical calculations in the future. The RBFN has a higher accuracy for the exploration of the A60 DPP design space than the RSM and Kriging models because it can effectively approximate the nonlinear response results of the transient heat-transfer analysis through the neural-network learning process.

## 5. Conclusions

The approximation characteristics of the design space for the A60 DPP used for ships and offshore plants were evaluated by performing a sensitivity analysis on the fire-prevention design via the design of experiments and applying various approximate models to a sensitivity analysis on the fire-prevention performance and minimum weight design. To evaluate the fire-prevention performance of the A60 DPP, a transient heat-transfer analysis based on the FEM was conducted after applying the specimen specifications and temperature conditions regulated in the FTP code. According to the transient heat-transfer analysis, the temperature results measured at the A60 DPP body at the unexposed ambient domain at the heating time point of 60 min were found to satisfy the condition of a temperature below 180 °C, which is

the FTP code regulation. A fire test for verification of the transient heat-transfer analysis results was conducted in accordance with the FTP regulation code of the Maritime Safety Committee. The minimum and maximum errors between the transient heat-transfer analysis and fire test were 8.7% and 11.6%. Moreover, the average error for all the total measurement positions was 10.7%, and the tendencies of the changes in the temperature characteristics with different design specifications were similar. The verified finite-element model and transient heat-transfer analysis results were linked with the design of experiments. The length of the A60 DPP, diameter, material type, and insulation density were used as DFs, and the weight, temperature, price, and productivity were individually applied as output responses. In the design of experiments, a total of 54 full-factorial experiments were performed after applying the DF fluctuation level. For the sensitivity analysis, the effect of each DF on the output response was quantitatively assessed using the results of the design of experiments, and the optimum design combinations that minimized the weight while satisfying the tolerance limit of the output responses, such as the temperature, price, and productivity, were identified. On the basis of the sensitivity-analysis results, the DFs with the most significant effects on the weight, temperature, price, and productivity were found to be the A60 DPP diameter, insulation density, A60 DPP material type, and length, respectively. Furthermore, it was found that selecting the proper insulation and A60 DPP material type are highly important in the fire-prevention design, and with regard to productivity, the effects of the A60 DPP length and diameter are significant. According to the results of the optimum DF combinations of the design of experiments, the weight and price were reduced by 22.6% and 24%, respectively, and the productivity was improved by 8.6%. Although the temperature was increased by 18.7%, it was below 180 °C, satisfying the FTP code regulation. Using the results of the design of experiments, various approximate models, i.e., a Kriging model, RSM model, and RBFN, were produced. According to the analysis results for the accuracy of each approximate model for approximating the A60 DPP design space, the approximation accuracies of all the approximate models for the output response were high, confirming that the design-of-experiments method used in this study is suitable for the analysis of the A60 DPP design space. Furthermore, it was found that among the approximate models used in the full-factorial experiment of this study, the RBFN allows the exploration of the A60 DPP design space with the highest accuracy.

## Funding

This work was supported by project for Collabo R&D between Industry, Academy, and Research Institute funded by Korea Ministry of SMEs and Startups (Project No.S2910737) and also supported by “Regional Innovation Strategy (RIS)” through the National Research Foundation of Korea (NRF) funded by the Ministry of Education (MOE).

## References

- Cho, S.K., Byun, H., & Lee, T.H. (2009). Selection Method of Global Model and Correlation Coefficients for Kriging Metamodel. *Transactions of the Korean Society of Mechanical Engineers - A*, 33(3), 813–818. <https://doi.org/10.3795/KSME-A.2009.33.8.813>
- Choi, J.M., Um, H.C., & Jin, Y.H. (2014). Comparison on the Fire Performance of Additional Insulation Materials for Improving the Fire Retardancy in Engine-room of FRP Vessel. *Journal of the Korean Society of Marine Engineering*, 38(9), 1150–1155. <https://doi.org/10.5916/jkosme.2014.38.9.1150>
- Choi, T.J., Kim, J.S., Choi, K.K., Lim, Y.S., & Kim, Y.T. (2013). An Experimental Study on the Fireproof of Fire Damper in Accordance with Insulation Conditions on the Coaming and Blade. *Journal of the Korean Society of Marine Engineering*, 37(4), 431–437. <https://doi.org/10.5916/jkosme.2013.37.4.431>
- Dyn, N., Levin, D., & Rippa, S. (1986). Numerical Procedures for Surface Fitting of Scattered Data by Radial Basis Functions. *SIAM Journal on Scientific and Statistical Computing*, 7(2), 639–659. <https://doi.org/10.1137/0907043>
- International Maritime Organization (IMO). (2010). *International Convention for the Safety of Life at Sea (SOLAS 1999/2000). Amendment*, UK.
- International Organization for Standardization (ISO). (1999). *Fire Resistance Tests - Elements of Building Construction (ISO 834-1)*. Switzerland.
- Jang, C.J., Hur, N.S., & Kim, I.W. (2014). Performance Experiment of H-120 Class Fire Damper for Offshore. *Journal of the Korean Society of Manufacturing Process Engineers*, 13(2), 131–136. <https://doi.org/10.14775/ksmpe.2014.13.2.131>
- Magnabosco, I., Ferro, P., Tiziani, A., & Bonollo, F. (2006). Induction Heat Treatment of a ISO C45 Steel Bar: Experimental and Numerical Analysis. *Computational Materials Science*, 35(2), 98–106. <https://doi.org/10.14775/ksmpe.2014.13.2.131>
- Maritime Safety Committee (MSC). (2010). *Adoption of the International Code for Application of Fire Test Procedures [MSC.307(88)]*. UK.
- Ohmura, T., Tsuboi, M., Onodera, M., & Tomimura, T. (2003). Specific Heat Measurement of High Temperature Thermal Insulations by Drop Calorimeter Method. *International Journal of Thermophysics*, 24(2), 559–575. <https://doi.org/10.1023/A:1022936408676>
- Piscopo, G., Atzeni, E., & Salmi, A. (2019). A Hybrid Modeling of the Physics-Driven Evolution of Material Addition and Track Generation in Laser Powder Directed Energy Deposition. *Materials*, 12(17), 2819. <https://doi.org/10.3390/ma12172819>
- Simulia. (2019). *Abaqus User Manual*. Simulia.
- Song, C.Y., & Kim, Y. (2020). Identification of Fire Resistance Characteristics of Bulkhead Penetration Pieces for A-0 Class Compartment. *Journal of Advanced Marine Engineering and Technology*, 44(6), 414–421. <https://doi.org/10.5916/jamet.2020.44.6.414>
- Song, C.Y., & Lee, J. (2010). Comparative Study of Approximate Optimization Techniques in CAE-based Structural Design. *Transactions of the Korean Society of Mechanical Engineers - A*, 34(11), 1603–1611. <https://doi.org/10.3795/KSME-A.2010.34.11.1603>
- Suman, S., Biswas, P., & Sridhar, P. (2016). Numerical Prediction of Welding Distortion in Submerged Arc Welded Butt and Fillet Joints. *Proceeding of International Conference on Design and Manufacturing, IIITDM, Kanchipuram*.
- Yu, J.S., Sung, H.G., & Oh, J.H. (2000). An Experimental Study on Fire-resistant Boom. *Journal of the Korean Society of Marine Environmental Engineering*, 3(2), 25–32.
- Yunus, A.C., & Afshin, J.G. (2012). *Heat and Mass Transfer: Fundamentals and Applications*, McGraw-Hill.

## Author ORCIDs

Author name	ORCID
Park, Woo Chang	0000-0003-1655-7957
Song, Chang Yong	0000-0002-1098-4205

# Current Measurement and Velocity Spatial Distribution of Deep Ocean Engineering Basin

Sung-Jun Jung<sup>1</sup>, Jae-Sang Jung<sup>2</sup>, Yong-Guk Lee<sup>3</sup>, Byeong-Won Park<sup>1</sup>,  
Sung-Chul Hwang<sup>2</sup>, In-Bo Park<sup>2</sup>, Jin-Ha Kim<sup>4</sup> and Il-Ryong Park<sup>5</sup>

<sup>1</sup>Senior Researcher, Korea Research Institute of Ships and Ocean Engineering, Busan, Korea

<sup>2</sup>Senior Engineer, Korea Research Institute of Ships and Ocean Engineering, Busan, Korea

<sup>3</sup>Engineer, Korea Research Institute of Ships and Ocean Engineering, Busan, Korea

<sup>4</sup>Principal Researcher, Korea Research Institute of Ships and Ocean Engineering, Busan, Korea

<sup>5</sup>Professor, Department of Naval Architecture & Ocean Engineering, Donggeu University, Busan, Korea

**KEY WORDS:** Model test, Current generator, Deep ocean engineering basin, Current velocity, Velocity measurement

**ABSTRACT:** To ensure the international competitiveness of the domestic offshore plant industry, a consensus has been formed regarding the requirement for large offshore basins for performing offshore plant performance verification. Accordingly, the Korea Research Institute of Ships & Ocean Engineering has built the world's largest deep ocean engineering basin (DOEB). The purpose of this study is to evaluate the characteristics of velocity distribution under various conditions of the DOEB. An independent measuring jig is designed and manufactured to measure the current velocities of many locations within a short time. The measurement jig is a 15-m-high triangular-truss structure, and the measurement sensors can move 15 m vertically through an electric motor-wire device. The current speed is measured under various impeller revolutions per minute and locations of the DOEB using the jig. The spatial distribution characteristics of the current velocity in the DOEB and the performance of the current generator are analyzed. The maximum speed is 0.56 m/s in the center of the DOEB water surface, thereby confirming sufficient current velocity distribution uniformity for model testing.

## 1. Introduction

In the past around 2010, the offshore plant construction industry was extremely active, and the demand for model test basins for verifying offshore plant performance increased significantly. However, almost all demand was concentrated in the large European basins; as such, tests could only be performed during available slots. Accordingly, a consensus was formed regarding the requirement for a large ocean engineering basin in Korea to increase its international competitiveness in the offshore plant industry and to verify the front-end engineering design and performance of offshore plants. Consequently, the world's largest deep ocean engineering basin was constructed in Korea.

The deep ocean engineering basin is the world's largest rectangular basin, with an operating area measuring 100 m (length) × 50 m (width). Equipped with a depth control device, it can simulate all depths in the range of 0 to 15 m. The pit in the middle of the basin is 12 m in diameter and 50 m deep based on the waterplane, thereby

enabling the use of prototype models instead of truncated models for model tests of deep-sea risers and tension leg platforms, where the effect of water depth is important. The deep ocean engineering basin is equipped with a wave generating system, wind generator, and current generator to simulate the various environments of the ocean, rendering it an optimal facility for evaluating offshore plants. In this study, the characteristics of currents generated through a current generator, which is one of the environment simulation devices inside the deep ocean engineering basin, were measured and analyzed. The current generating system comprises five impellers and six layers, and it can generate the vertical velocity profile of a current based on requirements imposed.

Yang et al. (2000) measured and analyzed the current characteristics of existing rectangular offshore basins in Korea and derived a relationship correlating the rotational speed of the impeller and the average flow velocity. Oh and Lee (2018) enabled flow rate control by installing a circulation system inside a two-dimensional wave

Received 11 September 2020, revised 4 February 2021, accepted 4 February 2021

Corresponding author Sungjun Jung: +82-51-604-7827, [jungsj@kriso.re.kr](mailto:jungsj@kriso.re.kr)

© 2021, The Korean Society of Ocean Engineers

This is an open access article distributed under the terms of the creative commons attribution non-commercial license (<http://creativecommons.org/licenses/by-nc/4.0>) which permits unrestricted non-commercial use, distribution, and reproduction in any medium, provided the original work is properly cited.



generating basin. However, the only publicly available data pertaining to the current generator of a large offshore basin capable of controlling the vertical velocity profile are those of the ocean engineering basin currently operated by the Maritime Research Institute of Netherlands (MARIN) (Buchner et al., 1999; Buchner et al., 2001; Buchner and de Wilde, 2008). The basin operated by the MARIN measures 46 m (length)  $\times$  36 m (width)  $\times$  10.3 m (depth) and is smaller than a deep ocean engineering basin; nonetheless, it is the most preferred commercial rectangular basin in the world. The MARIN's basin comprises a weight to be fixed to the floor, a wire system, and a lightweight structure that is connected to the wire system and can move along the water depth, allowing the velocity at each depth to be measured.

In this study, the current velocity was measured under various test operating conditions of the deep ocean engineering basin current generator using a custom-developed current measurement jig. Subsequently, the performance of the current generator and the spatial distribution characteristics of the current velocity within the deep ocean engineering basin were analyzed. Based on the results of this study, an optimal current generator operation plan for the performance evaluation of the offshore plant will be derived.

## 2. Method for Measuring Current

### 2.1 Current Generator of Deep Ocean Engineering Basin

The main components of the deep ocean engineering basin current generator are shown in Fig. 1. Flow is generated from the five ducts, composed of pumps and motors, inside the impeller room. The basin comprises six layers of different depths. Because the wave maker is above these layers, the first layer is distant from the water surface. In the fifth and sixth layers, flow is generated by a single impeller. The rotational speed of the impeller in each of the ducts, which are separated by depth, can be controlled independently. However, in the fifth and sixth layers, the flow velocity is controlled only through the fifth impeller at the bottom. Subsequently, the flow passes through a

guide vane and various rectifying devices in the mixing chamber, thereby yielding a uniform current. Similar rectifying devices are installed downstream, and as shown in Fig. 1(b), the flow circulates in the counterclockwise direction. To produce a uniform current, various rectifying devices (net grid, perforated side wall, distributing plate, screen, etc.) were designed for the inlet and outlet based on various computational fluid dynamics (CFD) analyses (Park et al., 2014; Haro et al., 2018).

### 2.2 Design of Jig for Current Velocity Measurement

Similar to a previous study by the MARIN, if the measuring device is fixed to the floor, then the operation of the current pump must be halted, the control device depth increased, and the weight-type fixing device on the floor shifted to change the horizontal position. This necessitates a significant amount of time for current measurement. In this study, a current measurement jig optimized for current measurement and the deep ocean engineering basin environment was designed and assembled.

To obtain the current velocity profile inside the deep ocean engineering basin, many areas must be measured when the current pump is being operated. Considering the length, width, and depth of the basin, it is essential to reduce the measurement time. Therefore, a measurement jig that requires a shorter measurement time is necessitated, and a structure that does not cause deformation, deflection, and vibration due to fluid flow (current) must be designed for a stable current velocity measurement.

To satisfy these conditions, the deep ocean engineering basin measurement jig was installed on the measuring frame of the towing tank to enable movement in the X-Y plane (forward/horizontal movement of the tank), and three current measurement sensors were attached on the measurement jig in equal intervals along the depth direction. If the jig is fixed only onto the measurement frame of the tank, the jig may shake; therefore, the bottom of the jig was reinforced by a rubber support such that it can be supported on the floor. Because the upper and lower ends were strongly fixed, vibration can be

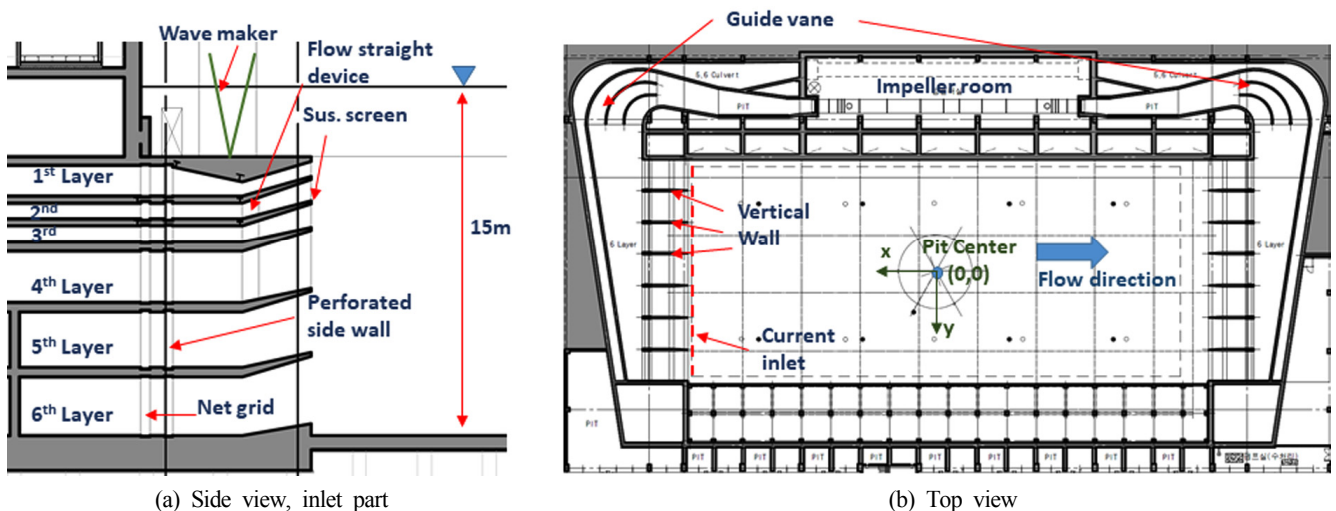


Fig. 1 Current generator system of deep ocean engineering basin

minimized. As confirmed during the actual operation, even when the jig was not fixed to the floor, the vibration of the jig or the measured value was not affected. The initial design features are shown in Fig. 2.

The basic shape of the current measurement jig was based on a vertical triangular-truss structure that allowed movement in all sections of the 15 m depth, and a linear motion guide for the Z-axis (depth direction) movement was placed vertically at the front of the current inlet such that the installation jig for the measurement sensor can move. The measurement sensor installation jig was driven by rotating the electric clutch type winch using an electric motor as well as driving it up and down both ways; meanwhile, the wire cable in the vertical direction was wound up and rotated. Stainless use steel, which can be used underwater, was used as the material for the wire cable, and it was designed to maintain a constant tension to maintain an accurate position. The motion of the sensor bracket was restrained in all directions except the vertical transfer direction.

The basic shape was of a 15-m-long heavy structure, and a primary fluid load analysis was performed on the basic design using StarCCM+(Ver. 11.06) to determine the load value required for structural analysis (Fig. 3(a)). The fluid load analysis was performed using two flow velocities: 0.5 m/s, which is the design value for the deep ocean engineering basin current velocity; and 1 m/s, which is the extreme environmental condition. The current velocity decreased toward the lower part compared with the conditional velocity; however, a uniform flow was assumed for a conservative structural strength calculation. Using this value as the load condition, the primary structural analysis was performed using Ansys (2020 R2), and the structural characteristics, strength, and stress of the current measurement jig structure were analyzed. Based on the result of the structural analysis, a maximum stress of 60.934 MPa was confirmed at the uppermost assembly of the triangular-truss, and a maximum deflection of 15.66 mm at the bottom of the structure. The structural

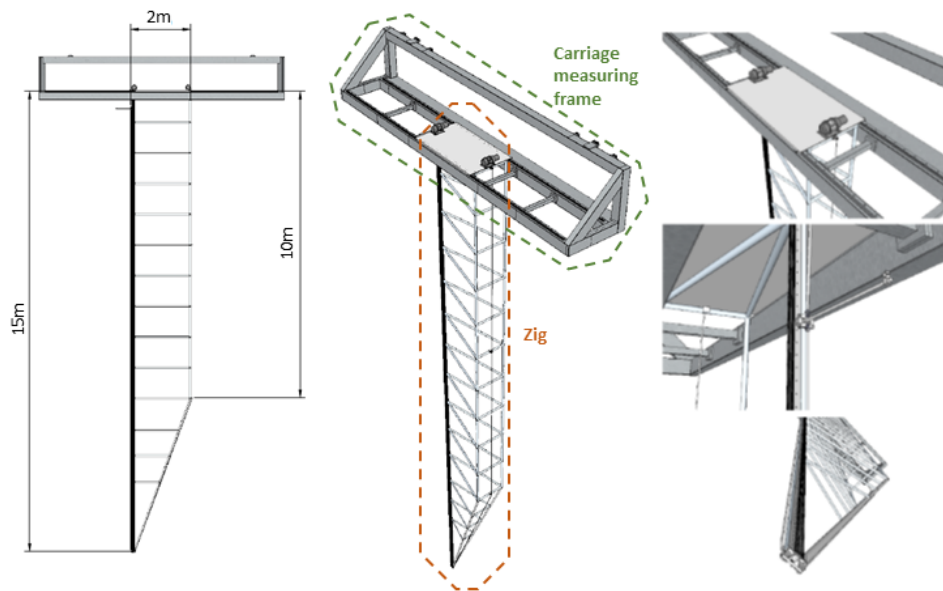
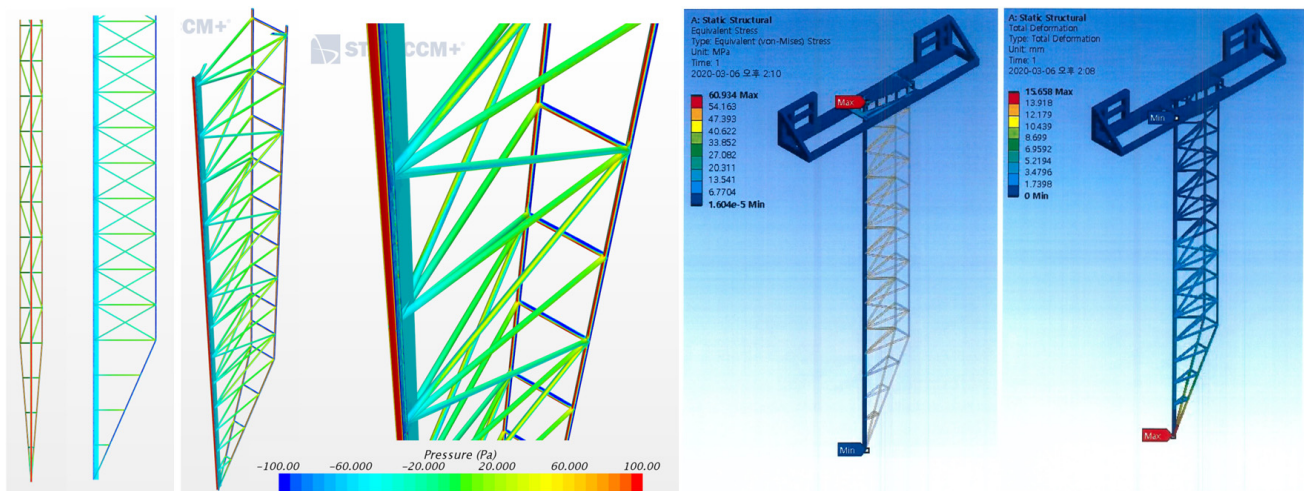


Fig. 2 Modelling of the current measurement jig (initial design)



(a) Surface pressure distribution

(b) Structural deformation and stress distribution

Fig. 3 CFD & structural analysis of the jig

**Table 1** Current load acting on frame based on CFD analysis of frame (detailed design)

Current velocity	Front area of vertical frame (Pa)	Front area of truss frame (Pa)
0.5 m/s	135	130
1.0 m/s	525	515

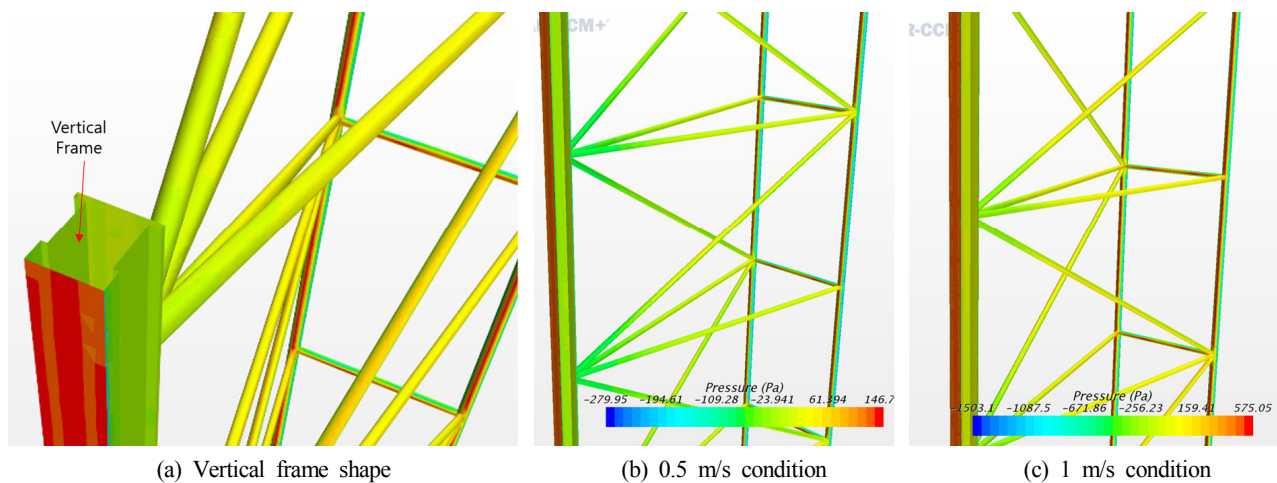
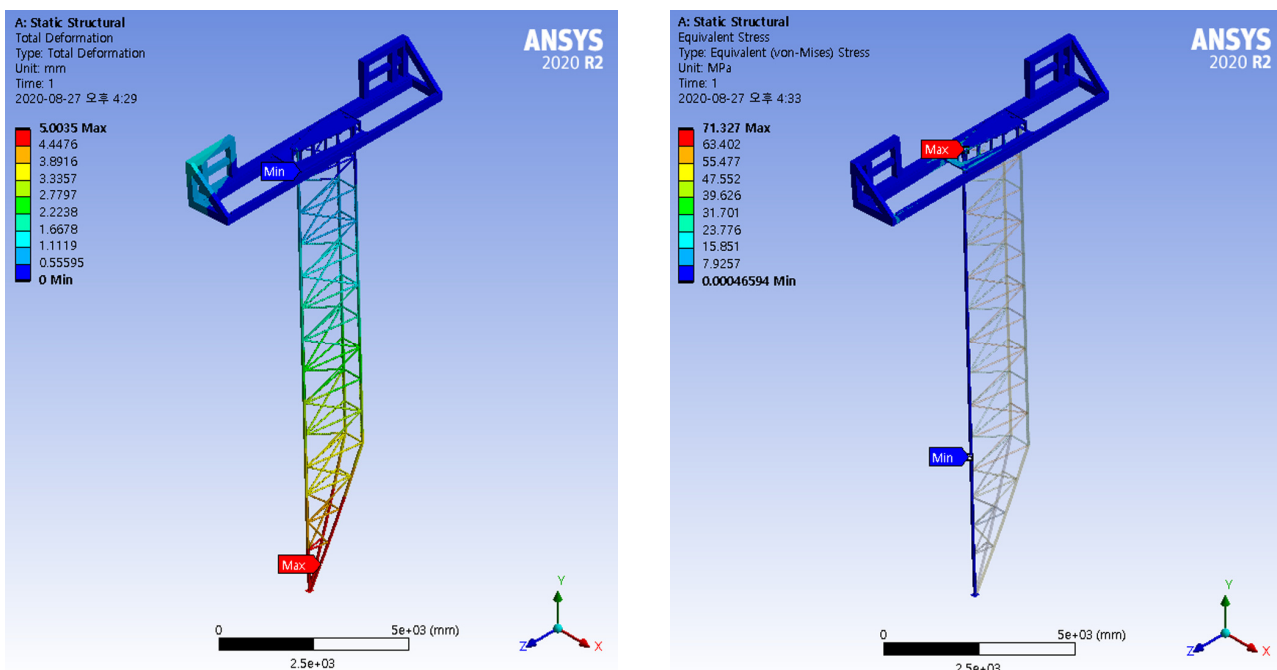
deformation and stress distribution are shown in Fig. 3(b). The maximum stress generated on the structural member was satisfactory. Similarly, the deflection, which was approximately 1/1000 the total height of the structure, was satisfactory. Therefore, the detailed design phase was proceeded in the study.

A detailed design was performed based on the basic design. For it to be operable in shallow water, it was designed such that it can be disassembled in the longitudinal direction. Subsequently, considering

the efficiency in terms of manufacturing/assembly/installation, the vertical frame shape, measurement sensor jig size and shape, pipe diameter, and truss length were slightly modified. A secondary fluid load analysis and a structural analysis were conducted on the modified detailed design structure. The shape was modeled based on a CAD drawing of the detailed design with the mesh generated using approximately 15 million cells, and a steady state numerical analysis in a single phase was performed while disregarding the free surface effect. The results are shown in Table 1 and Fig. 4.

**Table 2** Static structural Analysis of current measurement jig

	Maximum	Average
Total deformation	5.003 mm	0.409 mm
Equivalent stress	71.327 MPa	1.490 MPa

**Fig. 4** Pressure distribution of the jig (detailed design)**Fig. 5** Structural analysis of current measurement jig (deformation and stress distribution)





**Fig. 6** Current measurement jig

Under the 1 m/s condition, the highest pressure of 525 Pa occurred on the front surface center of the vertical frame of the current measurement jig and on both ends owing to flow separation, and a similar level of 515 Pa occurred on the front side of the reinforced truss frame. Based on the pressure distribution obtained from the CFD analysis under the 1 m/s condition, a structural analysis was performed, of which the results are shown in Table 2 and Fig. 5.

Based on the structural analysis, the safety factor was approximately 2.8 times the yield strength (205 MPa) of the STS304 pipe, i.e., a member of the current measurement jig; moreover, the deflection was 5 mm, which was approximately 1/3000 the total frame height. The expected maximum flow velocity with the impeller operating at the maximum rotational speed of 592 revolutions per minute (RPM) was

0.5 m/s in the surface layer, and the velocity decreased rapidly with depth. As the measurement jig was designed to withstand up to 1 m/s of uniform flow velocity, the strength of the jig was considered to be sufficient. In addition, the extremely small deflection of the jig implies that the position change of the measuring sensor will be small. Accordingly, the design structure was confirmed, and the assembled jig is shown in Fig. 6.

### 2.3 Current Measurement Sensor

A number of current sensors for the current measurement have been reviewed; however, ultrasonic waves were used in most current measurement sensors, i.e., a method based on the Doppler effect. Hence, particles must be present inside the fluid to enable

**Table 3** Comparison of current measurement sensors

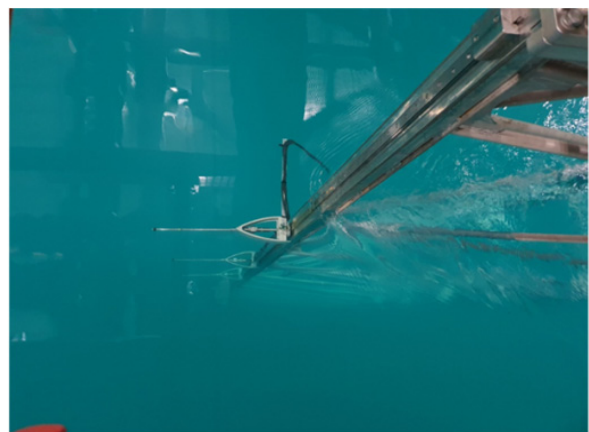
	Kenek VM-1001RS	Nobska MAVS4
Type	Electromagnetic	Differential travel time
MEAS. Axis	3-Axis	3-Axis
Range	0 ~ $\pm 2$ m/s (0.25, 1, 2–3 range switching)	0 ~ $\pm 2$ m/s
Accuracy	0.04 m/s (F.S.)	0.003 m/s (F.S.)
Response time	2 Hz	25 Hz
Depth	20 m	2,000 m or 6,000 m
Dimension	$\Phi 20 \times 335$ (mm)	$\Phi 82.6 \times 914$ (mm)



(a) Sensor



(b) Installed sensor on the jig



(c) Current measurement with the jig

**Fig. 7** Current measurement sensor

measurement. However, the model test basin uses clear water, where particles are almost non-existent; therefore, the current measurement sensors available for this study were limited. Table 3 shows a comparison of two types of current measurement sensors.

The comparison shows that the Nobska MAVS4 model demonstrated better response time and accuracy; however, it was considerably larger than the Kenek VM-1001RS model. The sensor to be installed on the current measurement jig for measurements should be small to reduce fluid load and disturbance on the current flow field; therefore, the Kenek VM-1001RS model was selected. It is a sensor that measures the flow velocity based on the change in the electromagnetic field as well as measures three-dimensional flow directions. Its measurement accuracy is 0.02 m/s within the measurement range of  $\pm 1$  m/s. All signals are in 2 Hz frequency; therefore, the measurements were obtained in 0.5 s intervals. Fig. 7(a) shows the sensor, and Fig. 7(b) shows the sensor attached to a jig that was temporarily laid down. Fig. 7(c) shows the three attached measurement sensors used for actual measurements.

### 3. Analysis of Current Measurement Results

#### 3.1 Vertical Space Distribution Inside Basin

After installing the current measurement jig onto the tank, all the impellers were operated at maximum speed of 592 RPM, and the

current flow velocity was measured at the center of the basin (pit center); the results are shown in Fig. 8. The rotational speed was increased in intervals of 100, 200, 300, 400, 500, 592 RPM. In the initial stage of the graph within 2,000 s, a staircase graph was observed, whereby the fluid velocity remained flat while the rotational speed RPM was maintained at the same level for approximately 5 min. When the RPM of the current impeller was changed, the fluid velocity converged to a new velocity almost instantaneously. The current velocity stabilized in a short duration. This measurement was performed for more than 4 h at the maximum RPM. After 2,000 s, a constant current velocity was maintained without any significant change. At the maximum RPM, the maximum velocity was measured to be approximately 0.56 m/s in the surface layer.

For frequency analysis, Fig. 9 shows the spectrum matching of the velocity time series measured in the maximum RPM test shown Fig. 8 for the 3,000–15,000 s range, where the velocity stabilized and the acceleration and deceleration excluded sufficiently. From each velocity time series, the mean component was removed to conceal the zero-frequency component. In the surface layer (0.1 m), the variation component was small, and a specific frequency component that was relatively larger did not exist. At a depth of 3.1 m, the energy component was large at a frequency of 0.2 rad/s or less. Although no specific resonance frequency existed, a long-cycle vibration component of 30–200 s appeared. This vibration component will not

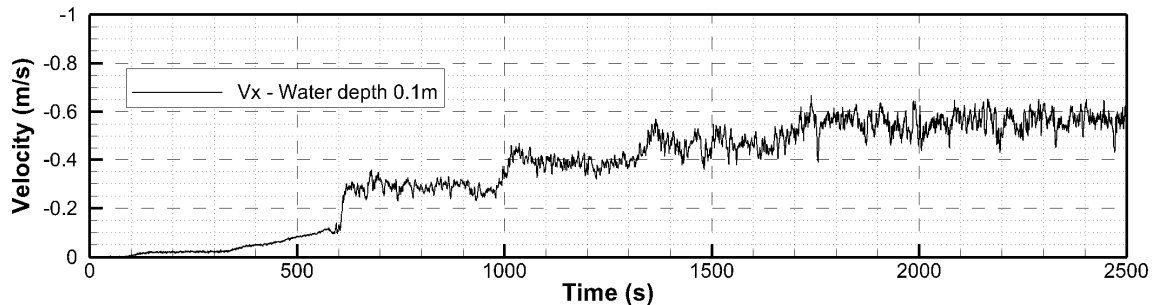


Fig. 8 Current velocity (0 to 592 RPM)

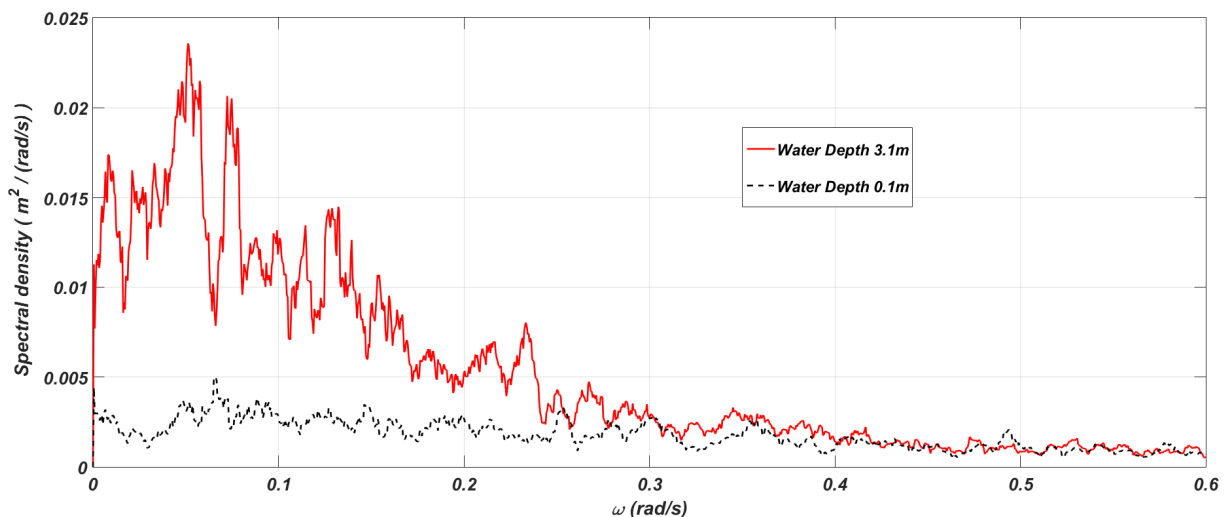
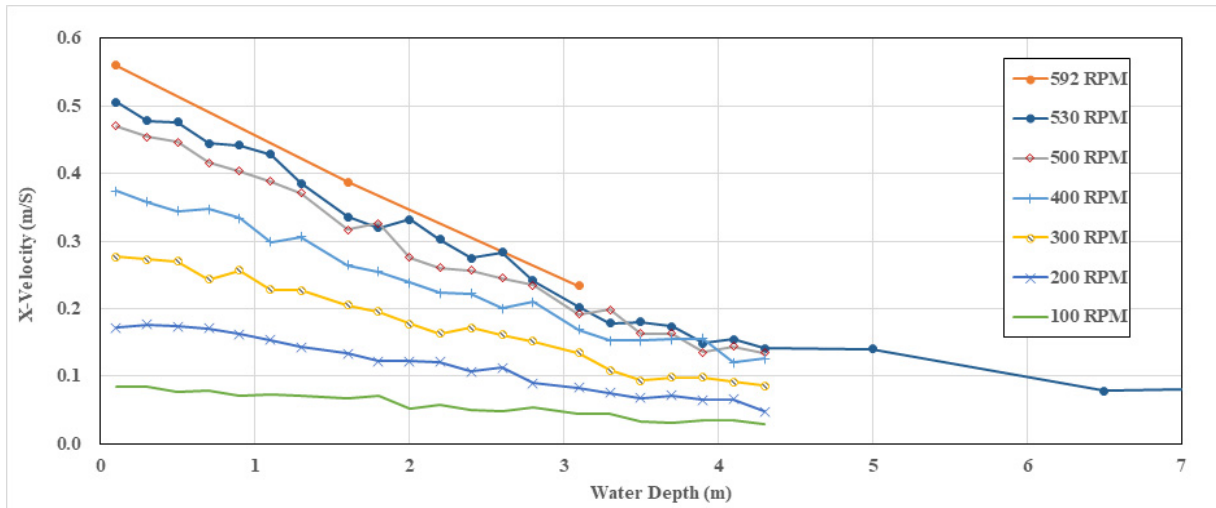
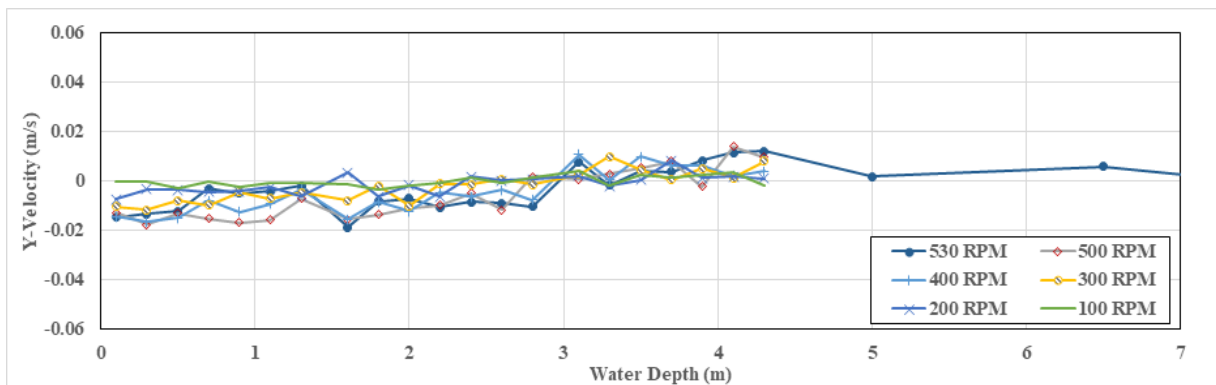


Fig. 9 Energy spectrum of current velocity

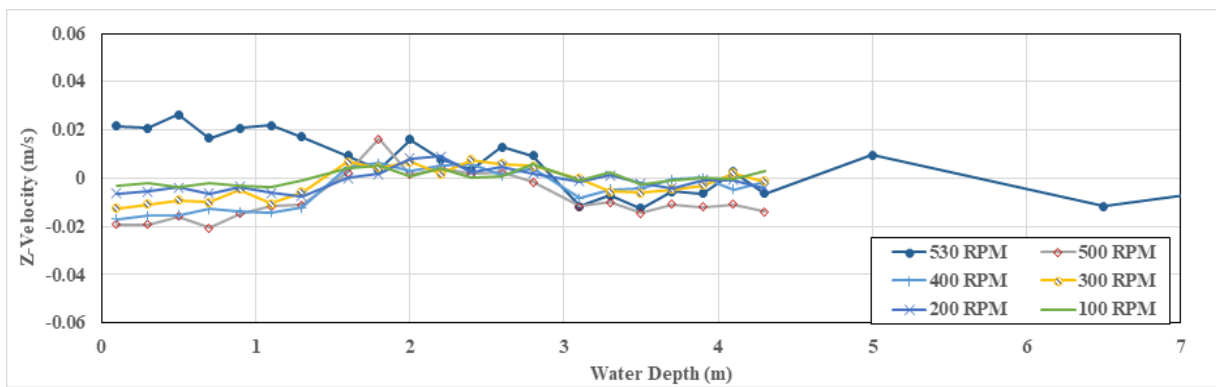




(a) X-velocity



(b) Y-velocity



(c) Z-velocity

Fig. 10 Current velocity profile

affect the ships and offshore plants that are floating on the surface; however, it will affect slender structures such as mooring lines that are located deep in the water. Therefore, further investigations are necessitated.

During low velocity or deceleration, such as from 200 to 100 RPM, a longer time was required to stabilize the current velocity. Nevertheless, in all cases, sufficient current velocity stabilization was achieved, enabling the model test to be performed within 20 min after reaching the target RPM.

Fig. 10 shows the current velocity measurements at the center of the basin for various depths and RPMs. As mentioned earlier, the surface layer (0.1 m) velocity was approximately 0.56 m/s when all the current pumps were operating at a maximum rotational speed of 592 RPM. This exceeded the initial design target velocity of 0.5 m/s of the current generating system, thereby indicating sufficient performance. For example, in a model test of the offshore plant, which is considered to be the most general, if the model ratio is 1/50, then a model speed of 0.5 m/s would translate to an extremely high velocity of approximately 3.5 m/s on an actual ship. Therefore, all current velocities applied to marine structures can be reproduced.

By interpolating the result at 500 RPM and the velocity at 592 RPM, a 0.5 m/s surface layer velocity was expected to be achieved at approximately 530 RPM; therefore, the velocity profile was measured up to a depth of 12.4 m for only 530 RPM. In general, the change in the RPM resulted in a relatively constant change in the velocity. Up to a depth of 4 m, the velocity gradient was almost linear with the depth. The RPM condition was the same for all duct layers; however, a low speed was measured in depths of 5 m and less owing to the large area of the outlet at the fourth, fifth, and sixth layers, i.e., the lower parts of the current generator.

The velocity on the Y- and Z-axes was close to 0, and only

extremely small velocities were measured. This implies that the straightness of the flow was obtained in the targeted direction. Although the velocity was less than 0.002 m/s, i.e., significantly lower than the accuracy of the measurement sensor, the sign trend changed at intervals of approximately 1.5 m. Because the three sensors were installed on the measurement jig in 1.5 m intervals, the abovementioned phenomenon was regarded as a consequence of a minute error in the sensor installation angle, not as an actual flow velocity phenomenon. Considering the mounting angle error and measurement error, the mean velocity component on the Y- and Z-axes was non-existent.

Fig. 11 shows the turbulence intensity by depth. The turbulence intensity,  $TI$ , is expressed as shown in Eq. (1).

$$TI = \sigma / V \quad (1)$$

Here,  $\sigma$  is the standard deviation of the velocity, and  $V$  is the average current velocity. In the surface layer, the turbulence intensity was measured to be 5%–7%. Furthermore, the turbulence intensity increased with a constant slope up to approximately 4 m in depth.

As shown in Fig. 11, the flow was directed upward from the bottom to the surface. In addition, the inlet was segmented into six layers, and the inlet became narrower toward the upper layers, causing the velocity to be highest in the surface layer. As the flow ejected rapidly from the discharge port and coincided with the free water surface, it dissipated and stabilized. Therefore, almost no spatial velocity gradient was observed in the surface layer, resulting in insignificant velocity fluctuations.

For the lower velocity fluctuations (lower turbulence intensity), it will be difficult to reduce the porosity of the already installed perforated side wall; however, it will be relatively easy to install

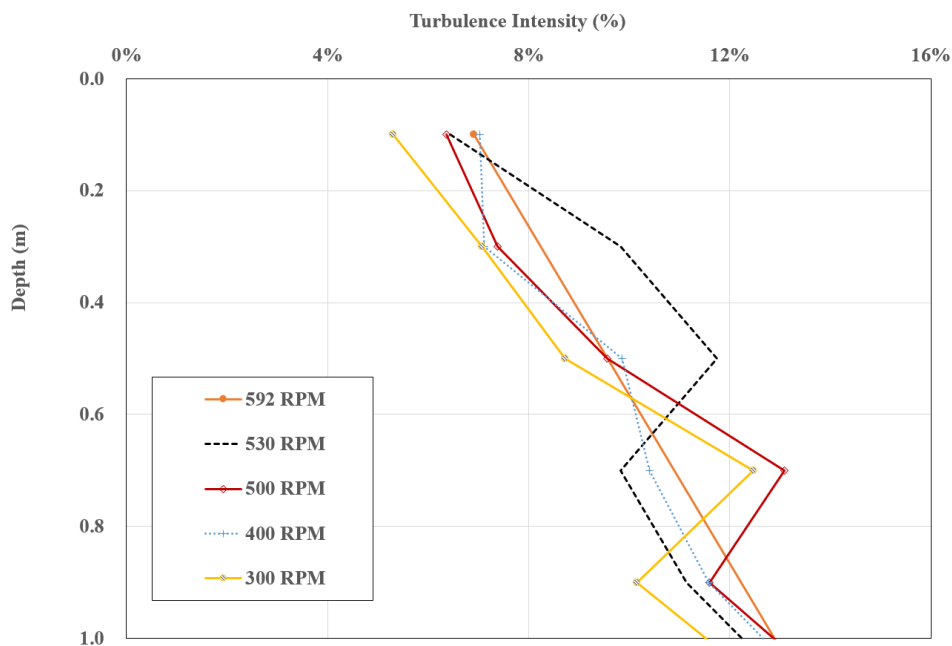


Fig. 11 Turbulence intensity profile

additional rectifying devices such as a screen at the discharge port. This will enable a constant flow velocity, but the velocity performance will decrease due to pressure loss.

### 3.2 Horizontal Spatial Distribution of Current Velocity

As previously mentioned, the initially designed target velocity of 0.5 m/s was expected to be achieved by applying a rotational speed of 530 RPM; therefore, the vicinity of the center of the basin was measured at 2 m intervals. Fig. 12 shows the trend in velocity change as the flow moved from upstream to downstream. In general, a target velocity of approximately 0.5 m/s was measured, with the surface layer velocity being high upstream (near  $x = 5$  m) and decreasing downstream. In the graph, the position of the origin is the center of the pit, and the direction of the axis is shown in Fig. 1(b). It is noteworthy that a different trend was shown in deep water. At a depth of 3.1 m, the velocity increased slightly downstream. This is considered to be due to

the velocity gradient stabilizing as the high velocity flow in the surface layer became mixed downstream.

A peculiar phenomenon was also observed from the Y-axis. As shown in Fig. 13, the velocity increased and decreased at regular intervals. This trend was observed in the preliminary CFD analysis at the designing stage, but the effect was excessive in the actual measurement. It was observed that the velocity increased and decreased in 5 m intervals, which is equivalent to the distance between the vertical walls at the discharge port (Fig. 1(b) shows the vertical wall location). The flow velocity was expected to decrease at the vertical wall due to viscosity; however, a higher velocity was measured. The cause was investigated and shown in Fig. 14. The velocity decreased at the vertical wall near the discharge port, resulting in a velocity gradient. However, the vorticity in the opposite direction (Z-axis vorticity) to offset this velocity gradient occurred from a distance of 10 m or more from the discharge port, and this rotational

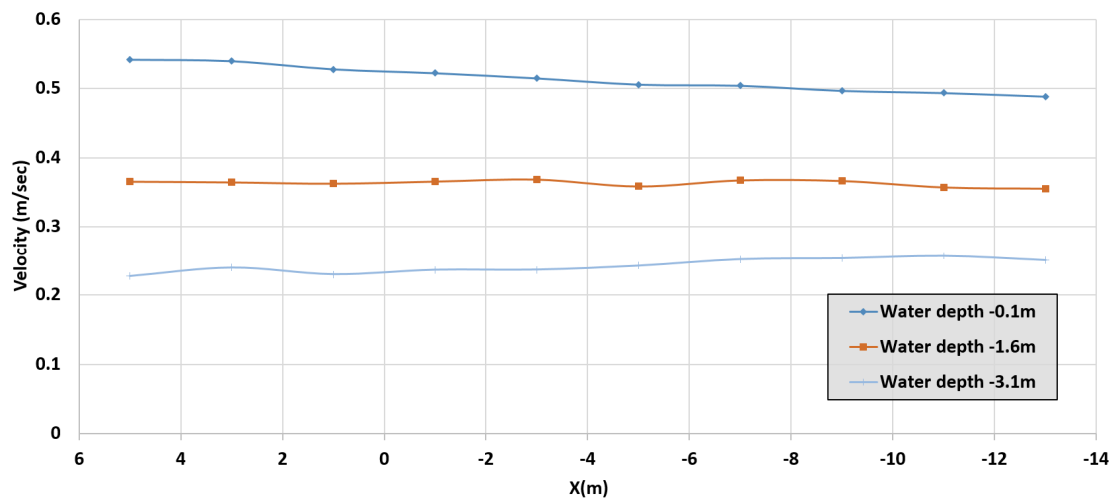


Fig. 12 Current velocity changes from upstream to downstream (530 RPM)

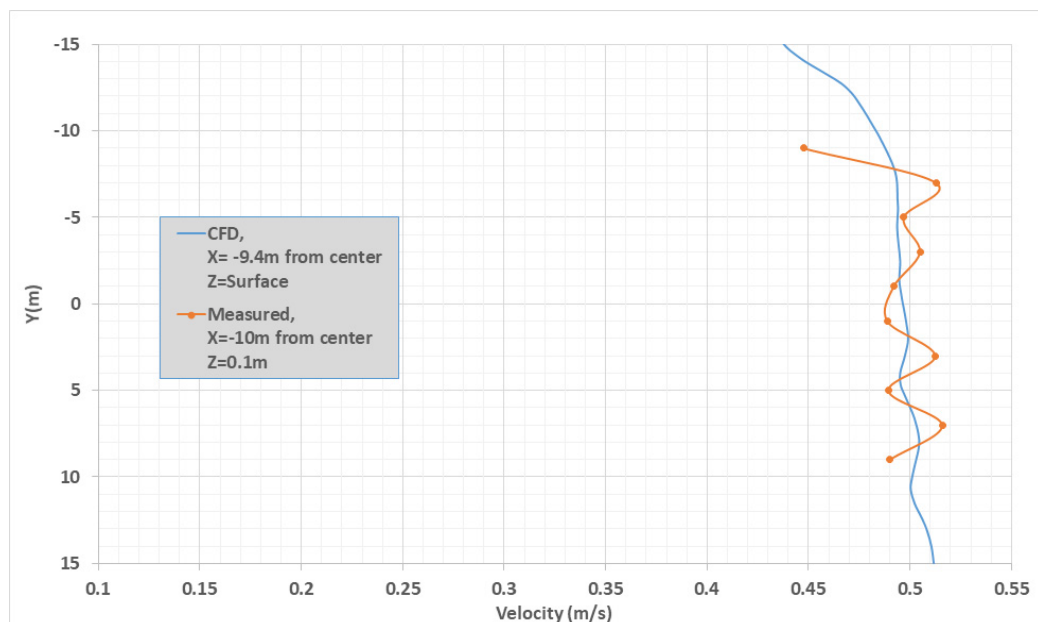


Fig. 13 Current velocity changes based on Y-position (water depth = 0.1 m)

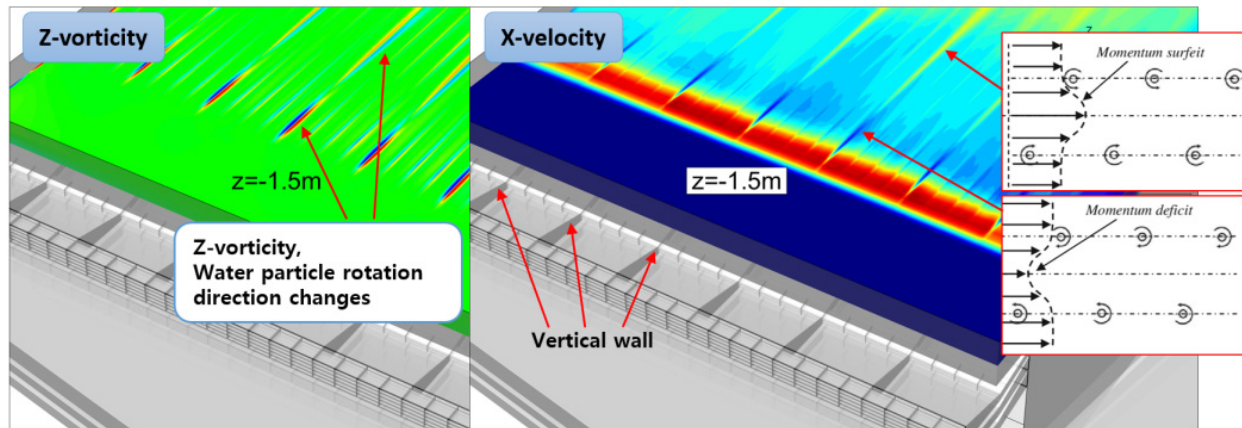


Fig. 14 Z-vorticity effect on X-velocity due to vertical walls (water depth = 1.5 m)

component might have increased the flow velocity (i.e., a momentum surfeit).

Other measurement results confirmed that it is advantageous to perform tests slightly downstream from the center of the basin (or pit center) to obtain a more even distribution of the current velocity. However, for some tests that require the 50 m depth of the pit, those tests can only be conducted at the center. In addition, the quality of the waves is expected to be better at the center rather than downstream. Therefore, the appropriate test location must be determined based on the characteristics and purpose of the offshore plant model test, such as the wave quality, current uniformity, and pit utilization. In this study, we obtained sufficient current distribution results from the model test; however, whether more rectifying devices can be added to the discharge port to achieve a more uniform current distribution should be investigated.

#### 4. Conclusion

In this study, an efficient current velocity measurement jig was designed and assembled to verify the performance of a current generator in a deep ocean engineering basin. The jig was a 15-m-high triangular-truss structure, and the measurement sensor can move along the entire 15 m section through an electric motor-wire device. Fluid load and structural stability analyses were performed, and measurements were performed without significant deflection or deformation even at a current velocity of 1.0 m/s. Using this device, the performance of the current generator of a deep ocean engineering basin was confirmed, and the operation method and limitations of the current generator for future offshore plant performance verification model tests were summarized.

The current velocity was measured in various vertical and horizontal positions. The velocity profile by depth was derived from various rotational speeds including the maximum driving speed of 592 RPM. A maximum velocity of 0.56 m/s was achieved in the surface layer, and all current conditions required for the offshore plant model test within a realistic range were achievable. The variation component of the current velocity over time, which can be represented as an index of

turbulence intensity, was confirmed. A turbulence intensity of 5%–7% for each RPM was confirmed in the surface layer, thereby ensuring sufficient uniformity in the model tests.

An additional turbulence control device can be installed at the discharge port to reduce the variation component over time and to obtain a more homogeneous current. In such a case, a decrease in velocity due to pressure loss is expected; therefore, an optimal turbulence control device must be developed. The variation component by area and the main cause were identified, and it was discovered that the velocity fluctuation occurred primarily around the vertical wall at the discharge port. By further investigating the flow control device at the discharge port, improvements in the spatial distribution and homogeneous currents are expected.

#### Acknowledgments

This study was conducted through the main project of the Korea Research Institute of Ships & Ocean Engineering (KRISO), “Development of the performance evaluation technology for standard offshore structures based on deep ocean engineering basin” (PES3920).

#### References

- Buchner, B., Wichers, J.E.W., & Wilde, J. J. (1999). Features of the State-of-the-art Deepwater Offshore Basin. *Offshore Technology Conference*, Houston, 363-373. <https://doi.org/10.4043/10814-MS>
- Buchner, B., Cozijn, H., van Dijk, R., & Wichers, J. (2001). Important Environmental Modelling Aspects for Ultra Deep Water Model Tests. *Proceedings of Deep Offshore Technology Conference (DOT)*, Rio de Janeiro.
- Buchner, B., & de Wilde, J. (2008). Current Modeling Experience in an Offshore Basing. *Proceedings of the ASME 27th International Conference on Offshore Mechanics and Arctic Engineering (OMAE2008)*, Estoril, Portugal, 417-424. <https://doi.org/10.1115/OMAE2008-57597>
- Haro, M.P.E., Hwang, S.C., Nam, B.W., Cho, S.K., & Sung, H.G.

- (2018). Numerical Simulations for Current Generation of Constant and Variable Velocity Profiles in Deepwater Ocean Engineering Basin of KRISO. Proceedings of the 13<sup>th</sup> (2018) ISOPE Pacific/Asia Offshore Mechanics Symposium. International Society of Offshore and Polar Engineers, Jeju, Korea, 146–154.
- Oh, S.H., & Lee, D.S. (2018). Two-Dimensional Wave Flume with Water Circulating System for Controlling Water Level. Journal of Korean Society of Coastal and Ocean Engineers, 30(6), 337–342. <https://doi.org/10.9765/KSCOE.2018.30.6.337>
- Park, I.R., Kim, J.H., Hong, S.W., & Sung, H.G. (2014). Numerical Investigation of Current Generation Performance in a Large Ocean Engineering Basin (Oral Presentation). Proceedings of the Eleventh Pacific-Asia Offshore Mechanics Symposium PACOMS2014, Shanghai, China.
- Yang, C.K., Choi, H.S., & Hong, S.W. (2000). An Experimental Study on the Characteristics of Current in the Ocean Engineering Basin. Journal of the Society of Naval Architects of Korea, 37(4), 55–65.

### Author ORCIDs

Author name	ORCID
Jung, Sung-Jun	0000-0001-5938-2988
Jung, Jae-Sang	0000-0001-7090-2382
Lee, Yong-Guk	0000-0002-3167-3553
Park, Byeong-Won	0000-0001-8294-1696
Hwang, Sung-Chul	0000-0002-5905-384X
Park, In-Bo	0000-0001-8500-5561
Kim, Jin-Ha	0000-0003-3856-9668
Park, Il-Ryong	0000-0002-6194-5716



# Comparison of Fatigue Provisions in Various Codes and Standards -Part 1: Basic Design S-N Curves of Non-Tubular Steel Members

Sungwoo Im<sup>1</sup> and Joonmo Choung<sup>2</sup>

<sup>1</sup>Research Professor, Department of Naval Architecture and Ocean Engineering, Inha University, Incheon, Korea

<sup>2</sup>Professor, Department of Naval Architecture and Ocean Engineering, Inha University, Incheon, Korea

**KEY WORDS:** Basic design S-N curve, Structural detail category, Nominal stress, Hot spot stress, Effective notch stress, Probability of survival

**ABSTRACT:** For the fatigue design of offshore structures, it is essential to understand and use the S-N curves specified in various industry standards and codes. This study compared the characteristics of the S-N curves for five major codes. The codes reviewed in this paper were DNV Classification Rules (DNV GL, 2016), ABS Classification Rules (ABS, 2003), British Standards (BSI, 2015), International Welding Association Standards (IIW, 2008), and European Standards (BSI, 2005). Types of stress, such as nominal stress, hot-spot stress, and effective notch stress, were analyzed according to the code. The basic shape of the S-N curve for each code was analyzed. A review of the survival probability of the basic design S-N curve for each code was performed. Finally, the impact on the conservatism of the design was analyzed by comparing the S-N curves of three grades D, E, and F by the five codes. The results presented in this paper are considered to be a good guideline for the fatigue design of offshore structures because the S-N curves of the five most-used codes were analyzed in depth.

## 1. Introduction

The largest issues for offshore structures in terms of steels are the development of heavy thick plate and heavy wall thickness pipe, improvement of the corrosion resistance, and the development of high toughness steel at cryogenic temperatures. Improving the fatigue strength of welded joints is an important issue from the viewpoint of the design of offshore structures because the fatigue lives at weld joints can be reduced due to stress concentrations and weld imperfections.

Some S-N curves, also known as Wöhler curves, are necessary to evaluate the fatigue life of offshore structures. Because the formation of S-N curves for real structures has considerable limitations in terms of the size of the test equipment and the experimental budget, it is common to derive the S-N curve through experiments on small specimens instead of the actual structure.

Experiments on the stress ranges of at least three levels are required to produce a single S-N curve, but at least 10 levels or more are required for a reliable S-N curve. On the other hand, small sized-specimens may have different imperfections, such as residual stress and initial deformation, because of the different manufacturing processes. Even if a small specimen is taken from an actual structure,

there are insufficient aspects to simulate real structures accurately due to the release of the residual stress.

When evaluating the fatigue life of an actual structure using the small specimen-based S-N curve, it is essential to recognize the stochastic characteristics of the S-N curve. The S-N curve, including a specified survival or failure probability, is defined as a basic design S-N curve.

The symbols and formulae describing a basic design S-N curve differ according to the fatigue guidelines, recommendations, or codes. Let the guideline, recommendation, and code associated with fatigue denote the fatigue codes. In this paper, the basic design S-N curves of a non-tubular member made of steel and the corresponding material constants by the fatigue codes were analyzed, and the S-N curves were compared according to the codes.

The fatigue codes provide the basic design S-N curves for each structural detail category (SDC). The SDC is also called the classification of details, detail category, classification reference, and joint classification. The SDC is determined by the type of stress, geometry detail, and the direction of stress relative to the potential fatigue crack (normal and shear stresses) (BSI, 2015).

The fatigue codes considered in this study were DNVGL-RP-C203 (DNV GL, 2016), Guide for Fatigue Assessment of Offshore Structures

Received 4 January 2021, revised 28 January 2021, accepted 1 February 2021

Corresponding author Joonmo Choung: +82-32-860-7346, [heroeswise2@gmail.com](mailto:heroeswise2@gmail.com)

© 2021, The Korean Society of Ocean Engineers

This is an open access article distributed under the terms of the creative commons attribution non-commercial license (<http://creativecommons.org/licenses/by-nc/4.0>) which permits unrestricted non-commercial use, distribution, and reproduction in any medium, provided the original work is properly cited.

(ABS, 2003), BS 7608 (BSI, 2015), and IIW-1823 (IIW, 2008), and Eurocode3 (BSI, 2005). In this paper, these codes are termed as DNV GL, ABS, BS, Det Norske Veritas, and EC3, respectively.

## 2. Notations

In this review paper, five codes (DNV GL, ABS, BS, IIW, and EC3) were analyzed intensively. Table 1 lists the symbols used here.

**Table 1** Symbols and abbreviations

Item	DNV GL	ABS	BS	IIW	EC3
Nominal stress	$\sigma_{nominal}$	$S_{nom}$	$S_N$	$\sigma_{nom}$	-
Hot-spot stress	$\sigma_{hotspot}$	$S_{hot}$	$S_H$	$\sigma_{hs}$	-
Stress range	$\Delta\sigma$	$S$	$S_r$	$\Delta\sigma$	$\Delta\sigma_R$
Fatigue strength of the detail in MPa at $2 \times 10^6$ cycles	-	-	-	FAT	$\Delta\sigma_C$
Number of cycles to failure	$N$	$N$	$N$	$N$	$N_R$
Intercept of the design S-N curve with the $\log N$ axis	$\bar{a}$	$A, C$	$C_2$	$C$	-
Intercept of the mean S-N curve with the $\log N$ axis	$a$	$A_1, C_1$	$C_0$	-	-
Negative inverse slope of the S-N curve	$m$	$m, r$	$m$	$m$	$m$
Standard deviation of $\log N$	$s_{\log N}$	$\log \sigma$	$SD$	-	-

Unless stated otherwise, the basic design S-N curves in the five codes are based on the nominal stress, and the different notations for the nominal stress are used for each code. Here, the nominal stress means stress that does not include any form of stress concentration. The extrapolated stress, including the stress concentration factor (SCF) caused by the geometric detail, is called hot-spot stress, and the corresponding notations are used for each code. The basic design S-N curve uses a stress range rather than a stress amplitude, and various stress range notations are shown for each code. Some codes (DNV GL, ABS, and BS) plot the S-N curves with slope and intercept, while others (IIW and EC3) use the fatigue strength (FAT) and slope at 2 million cycles.

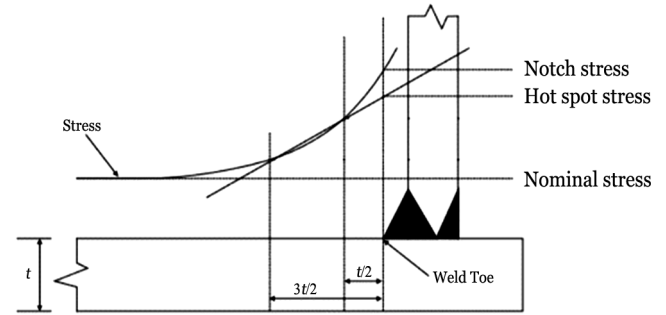
To represent the survival probability applied to the basic design S-N curve, some codes (DNV GL, ABS, and BS) provide the standard deviation of the logarithmic life to failure. Therefore, a mean S-N curve is suggested together. In contrast, IIW and EC3 provide a basic design S-N curve by specifying the 95% survival probability instead of the standard deviation.

## 3. Types of Stresses

The stress range used for the S-N curve is very important. That is, nominal stress, hot-spot stress, and effective notch stress are used mainly in the S-N curve.

### 3.1 Nominal Stress

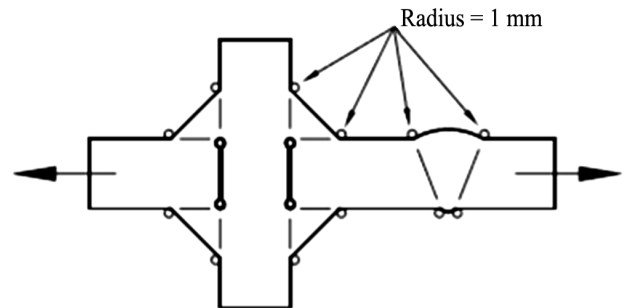
The nominal stress is the stress away from the local stress concentration area, where fatigue cracking can occur. That is, the nominal stress does not include welding residual stresses and SCFs due to the weld geometry. The stress concentration must not be included in the nominal stress (see Fig. 1). Most of the basic design S-N curves in the five codes are based on the nominal stress approach.



**Fig. 1** Schematic stress distributions near a weld

### 3.2 Effective Notch Stress

As shown in Fig. 2, the local stress at a weld toe, which is called the effective notch stress, was calculated by modeling the notch radius of 1 mm. Because the effective notch stress approach assumes a very small notch radius, it cannot be obtained through direct measurements and can only be derived through finite element analysis with a very fine mesh.

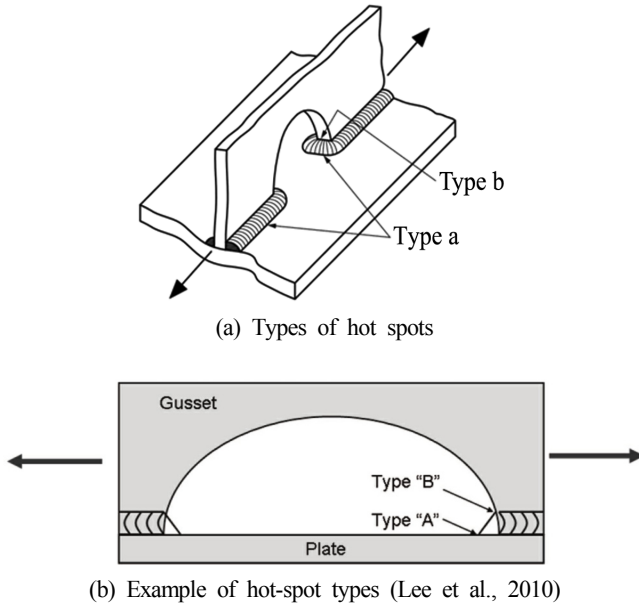


**Fig. 2** Sketch for effective notch stress

The effective notch stress approach is applicable to structures with thicknesses of 5 mm or more. Internal defects or surface roughness cannot be modeled as the effective notch radii. In addition, the effective notch stress approach cannot be applied to cases under the loads parallel to the weld or root gap. DNV GL and IIW support the basic design of S-N curves based on the effective notch stress approach.

### 3.3 Hot-spot Stress

The hot-spot stress is the imaginary stress obtained by extrapolating the surface stresses at the two or three points in front of the weld toe. The hot-spot stress approach is used mainly in the shipbuilding and offshore industries because it can derive the hot-spot stress at a low cost with a relatively coarser mesh. The hot-spot stress can be



**Fig. 3** Schematic stress distributions near a weld

calculated by finite element analysis or measurements using strain gauges.

When applying finite element analysis, the hot-spot stresses can be calculated using either the shell or solid elements. When shell elements are used, there is no need to contain weld beads. It is common to include weld beads for solid elements application.

Weld residual stresses and stress concentrations due to the weld detail and structural geometry should not be included in the hot-spot stress. Alternatively, the SCFs for representative structural details can be obtained from handbooks or other codes.

According to BS and IIW, the hot-spot stress is divided into types a and b. Type a is a case where the hot-spot stress is affected by the base plate thickness, while the base plate thickness varies the hot spot stress in the case of type b (see Fig. 3(a)). In Fig. 3(b), point A is classified as a type a hot spot because it is affected by the base plate thickness, and point B should be classified as a type b hot spot.

### 3.3.1 Type a hot-spot stress

The type a hot-spot stress is obtained by linearly extrapolating the stress either at  $0.4t$  and  $1.0t$  away or  $0.5t$  and  $1.5t$  away from the weld toe (see Eqs. (1) and (2)). This type of hot-spot stress can be determined by quadratic extrapolation of the stresses at  $0.4t$ ,  $0.9t$ , and  $1.4t$  away from the weld toe (see Eq. (3)). Here,  $t$  means the base plate thickness.

According to IIW, the hot-spot stresses should be obtained by the mesh sizes. That is, Eq. (1) or (3) should be applied for a fine mesh model that has an element size less than the base plate thickness, while Eq. (2) is used for a coarse mesh model with an element size equal to the base plate thickness.

According to BS, because there are no special instructions or recommendations for the finite element sizes, Eqs. (1)–(3) can be applied regardless of the element sizes.

$$\sigma_{hs} = 1.67\sigma_{0.4t} - 0.67\sigma_{1.0t} \quad (1)$$

$$\sigma_{hs} = 1.5\sigma_{0.5t} - 0.5\sigma_{1.5t} \quad (2)$$

$$\sigma_{hs} = 2.52\sigma_{0.4t} - 2.24\sigma_{0.9t} + 0.72\sigma_{1.4t} \quad (3)$$

### 3.3.2 Type b hot-spot stress

According to IIW, Eqs. (4) and (5) are applied to the fine and coarse mesh models, respectively. The subscripts in Eqs. (4) and (5) refer to the physical distance from the weld toe.

In the case of BS, there is no special indication or recommendation for the finite element sizes. Provided the surface stresses can be derived at the specified positions, Eqs. (4) and (5) can be applied to both fine and coarse mesh models.

$$\sigma_{hs} = 3\sigma_{4mm} - 3\sigma_{8mm} + \sigma_{12mm} \quad (4)$$

$$\sigma_{hs} = 1.5\sigma_{5mm} - 0.5\sigma_{15mm} \quad (5)$$

Because DNV GL and ABS do not distinguish the hot-spot stress derivation formulas by the hot-spot types, Eq. (2) may be used to determine the type a and type b hot-spot stresses.

## 4. Basic Design S-N Curves

The fatigue lives obtained through fatigue tests inevitably have a scatter that tends to increase for long lives or low stresses. A mean S-N curve is derived by regression analysis for the fatigue lives to failures. To consider this scatter probabilistically, after assuming that the log fatigue lives obey a normal distribution, the S-N curve corresponding to a specific probability of survival can be derived. This S-N curve is defined as the basic design S-N curve.

Among the five codes investigated in this study, DNV GL and ABS define a basic design S-N curve based on the mean minus two standard deviations. This corresponds to a survival probability of 97.7% or a failure probability of 2.3%. On the other hand, BS provides multiplication factors to the standard deviations according to the probability of failure. IIW and EC3 use the basic design S-N curves corresponding to a 95% probability of survival.

### 4.1 Basic Design S-N Curves of DNV GL

DNVGL-RP-C203 (DNV GL, 2016) and DNV Classification Notes No. 30.7 (DNV, 2014) are representative fatigue codes published by DNV GL. After DNV and GL were integrated, Classification Notes No. 30.7 were revised to DNVGL-CG-0129 (DNV GL, 2018). In this process, there were cases, in which some of the basic design S-N curves presented by DNVGL-RP-C203 and DNVGL-CG-0129 conflicted with each other. For example, DNVGL-CG-0129 specifies the B grade S-N curve, while DNVGL-RP-C203 does not. On the other hand, DNVGL-RP-C203 suggests F1 to W3 grades, but DNVGL-CG-0129 does not. In addition, the material constants of the basic

design S-N curves for grades B1 to C2 are different between the two codes. In particular, the S-N curves in DNVGL-RP-C203 were shown using the slope and intercept, whereas those in DNVGL-CG-0129 also included the fatigue strength (FAT) at 2 million cycles as well as the slope and intercept.

In this paper, DNVGL-RP-C203 was judged to be a code commonly applied to offshore structures rather than DNVGL-CG-0129. Thus, the basic design S-N curves were summarized based on DNVGL-RP-C203. Hereinafter, DNV GL refers to DNVGL-RP-C203.

DNV GL defines the basic design S-N curves using the following Eq. (6), where  $s_{\log N}$  is 0.2 for weld joints of non-tubular and tubular members under an in-air environment (IA), a seawater environment with cathodic protection (CP), and a free corrosion environment (FC). In the case of high-strength steel with a yield strength exceeding 500 MPa,  $s_{\log N}$  is 0.162.

$$\log N = \log \bar{a} - m \cdot \log \Delta \sigma = \log a - 2 \cdot s_{\log N} - m \cdot \log \Delta \sigma \quad (6)$$

To select a basic design S-N curve that can be applied to a real offshore structure, the environmental conditions (IA, CP, and FC environments), SDC, type of stress (nominal, hot-spot, and effective notch stresses), and stress component (normal and shear stresses) should be determined. DNV GL provides the basic design S-N curves according to the environmental conditions and SDCs, whereas selection according to the type of stress is unclear. When using hot-spot stress, the D grade curve is recommended, regardless of the SDCs. Therefore, only the D grade curve has been used for hot-spot stress applications.

Tables 2–4 summarize the material constants required in the basic design S-N curves corresponding to the environmental conditions of IA, CP, and FC, respectively. The basic design S-N curves for the IA

**Table 2** Constants of basic design S-N curves in an in-air environment by DNV GL

SDC	$N \leq 10^7$		$N > 10^7$		Fatigue limit at $10^7$ cycles	SCF	$s_{\log N}$
	$m$	$\log \bar{a}$	$m$	$\log \bar{a}$			
B1	4.0	15.117	5.0	17.146	106.97	-	0.2
B2	4.0	14.885	5.0	16.856	93.59	-	0.2
C	3.0	12.592	5.0	16.320	73.10	-	0.2
C1	3.0	12.449	5.0	16.081	65.50	-	0.2
C2	3.0	12.301	5.0	15.835	58.48	-	0.2
D	3.0	12.164	5.0	15.606	52.63	1.00	0.2
E	3.0	12.010	5.0	15.350	46.78	1.13	0.2
F	3.0	11.855	5.0	15.091	41.52	1.27	0.2
F1	3.0	11.699	5.0	14.832	36.84	1.43	0.2
F3	3.0	11.546	5.0	14.576	32.75	1.61	0.2
G	3.0	11.398	5.0	14.330	29.24	1.80	0.2
W1	3.0	11.261	5.0	14.101	26.32	2.00	0.2
W2	3.0	11.107	5.0	13.845	23.39	2.25	0.2
W3	3.0	10.970	5.0	13.617	21.05	2.50	0.2

**Table 3** Constants of basic design S-N curves in seawater environment with cathodic protection by DNV GL

SDC	$N \leq 10^6$		$N > 10^6$		Fatigue limit at $10^7$ cycles	SCF	$s_{\log N}$
	$m$	$\log \bar{a}$	$m$	$\log \bar{a}$			
B1	4.0	14.917	5.0	17.146	106.97	-	0.2
B2	4.0	14.685	5.0	16.856	93.59	-	0.2
C	3.0	12.192	5.0	16.320	73.10	-	0.2
C1	3.0	12.049	5.0	16.081	65.50	-	0.2
C2	3.0	11.901	5.0	15.835	58.48	-	0.2
D	3.0	11.764	5.0	15.606	52.63	1.00	0.2
E	3.0	11.610	5.0	15.350	46.78	1.13	0.2
F	3.0	11.455	5.0	15.091	41.52	1.27	0.2
F1	3.0	11.299	5.0	14.832	36.84	1.43	0.2
F3	3.0	11.146	5.0	14.576	32.75	1.61	0.2
G	3.0	10.998	5.0	14.330	29.24	1.80	0.2
W1	3.0	10.861	5.0	14.101	26.32	2.00	0.2
W2	3.0	10.707	5.0	13.845	23.39	2.25	0.2
W3	3.0	10.570	5.0	13.617	21.05	2.50	0.2

**Table 4** Constants of basic design S-N curves for free corrosion environment by DNV GL

SDC	$m$	$\log \bar{a}$	$s_{\log N}$	SDC	$m$	$\log \bar{a}$	$s_{\log N}$
B1	3.0	12.436	0.2	F	3.0	11.378	0.2
B2	3.0	12.262	0.2	F1	3.0	11.222	0.2
C	3.0	12.115	0.2	F3	3.0	11.068	0.2
C1	3.0	11.972	0.2	G	3.0	10.921	0.2
C2	3.0	11.824	0.2	W1	3.0	10.784	0.2
D	3.0	11.687	0.2	W2	3.0	10.630	0.2
E	3.0	11.533	0.2	W3	3.0	10.493	0.2

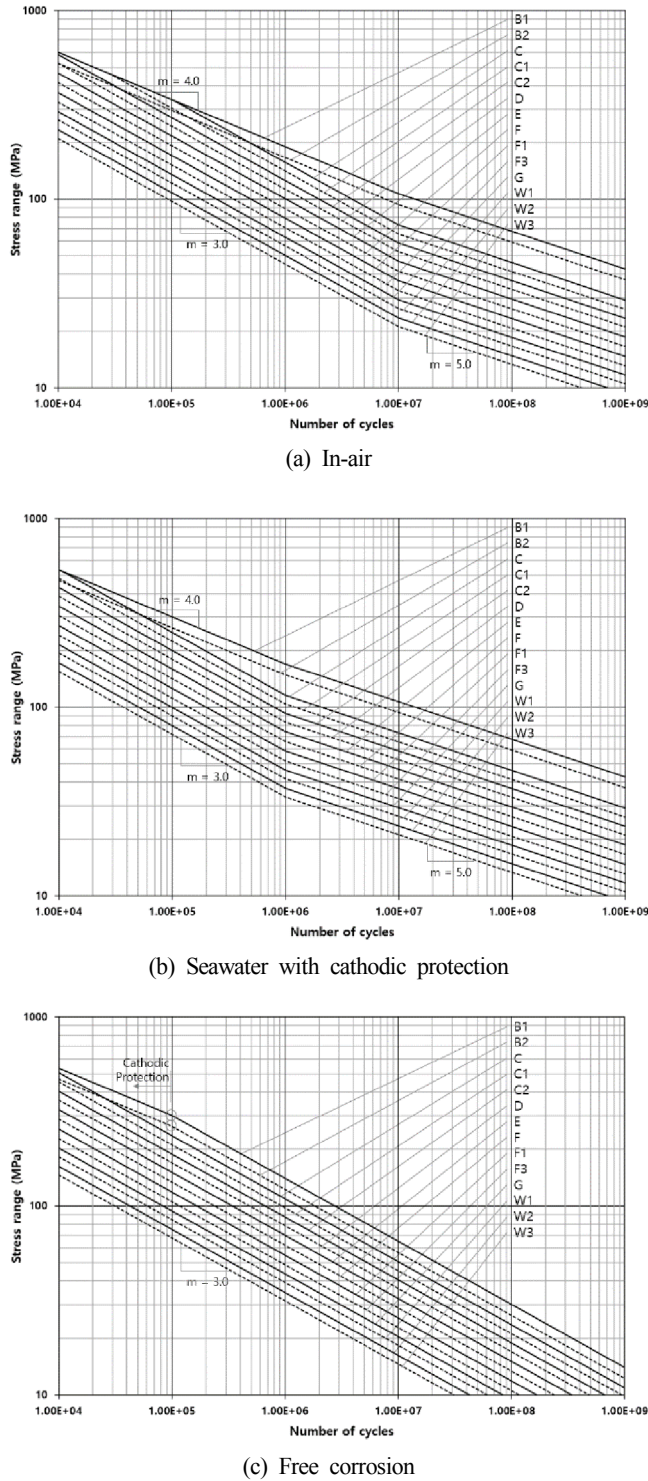
and CP environments have two slopes. In addition, each curve contains the inherent SCF. As shown in Tables 2–3, the slope of the basic design S-N curve for the IA environment changes at 10 million cycles, but that for the CP environment varies at 1 million cycles. The intercept of the first slope for the CP environment is smaller than that for the IA environment.

The basic design S-N curve for the FC environment has a single slope. The single slope was assumed because the fatigue limit was ignored due to the stress corrosion effect. The basic design S-N curve for the FC environment does not include the inherent SCF. The SCF, which is strongly dependent on the structural shape, was not included due to the variability of the structural details under the FC environment.

Fig. 4 shows the basic design S-N curves corresponding to Tables 2–4. Because the fatigue strength of the weld joint cannot exceed that of the base metal, the C and C1 curves corresponding to the weld joints where they intersect the B1 curve are shown. In a similar principle, the C curve where it intersects the B1 curve is shown because the C curve joins the B1 curve at 10,399 cycles.

The second intercepts of the basic design S-N curves corresponding to the IA and CP environments are identical, so the basic design S-N





**Fig. 4** Basic design S-N curves by DNV GL

curves over 10 million cycles coincide with each other, as shown in Fig. 4(a) and (b). On the other hand, there is an apparent difference in the fatigue strengths at less than 10 million cycles between the IA and CP environments. The fatigue strength in the FC environment is considerably lower than that in the CP environment. On the other hand, the fatigue strengths of the B1 and B2 curves for less than 98,401 cycles in the FC environment are greater than those in the CP environment.

#### 4.2 Basic Design S-N Curves of ABS

The basic design S-N curves of ABS are similar to those of DNV GL, but the SDCs of ABS are simpler. The SDCs for non-tubular joints defined by ABS are B, C, D, E, F, F2, G, and W, while DNV GL RP-C203 has 14 SDCs. Let  $N_Q$  be the number of cycles to fatigue failure. The basic design S-N curves corresponding to the cases where the number of failure cycles are smaller and larger than  $N_Q$  are expressed as Eqs. (7) and (8), respectively.

ABS provides the basic design S-N curves according to the environmental conditions and SDCs, but the advice for selecting the type of stress is unclear, which is similar to DNV GL. ABS recommends the E curve be used as the basic design S-N curve for hot-spot stress applications.

$$\log N = \log A - m \cdot \log S = \log A_1 - 2 \cdot \log \sigma - m \cdot \log S \quad (7)$$

$$\log N = \log C - r \cdot \log S = \log C_1 - 2 \cdot \log \sigma - r \cdot \log S \quad (8)$$

**Table 5** Constants of basic design S-N curves in the IA environment by ABS

SDC	$N \leq 10^7$		$N > 10^7$		Fatigue limit at $10^7$ cycles	$\log \sigma$
	$m$	$\log A$	$r$	$\log C$		
B	4.0	15.004	6.0	19.009	100.2	0.1821
C	3.5	13.626	5.5	17.413	78.2	0.2041
D	3.0	12.182	5.0	15.636	53.4	0.2095
E	3.0	12.017	5.0	15.362	47.0	0.2509
F	3.0	11.799	5.0	14.999	39.8	0.2183
F2	3.0	11.633	5.0	14.723	35.0	0.2279
G	3.0	11.398	5.0	14.330	29.2	0.1793
W	3.0	11.197	5.0	14.009	25.2	0.1846

**Table 6** Constants of basic design S-N curves in the CP environment by ABS

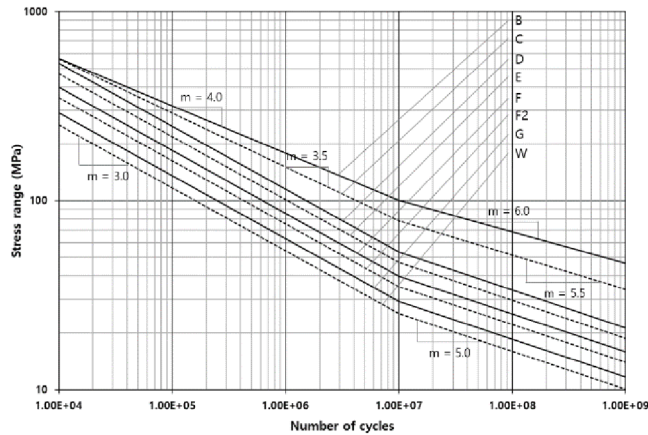
SDC	$N \leq 10^7$		$N > 10^7$		Fatigue limit at $10^7$ cycles	$\log \sigma$
	$m$	$\log A$	$r$	$\log C$		
B	4.0	14.606	6.0	19.009	158.5	-
C	3.5	13.228	5.5	17.413	123.7	-
D	3.0	11.784	5.0	15.636	84.4	-
E	3.0	11.619	5.0	15.362	74.4	-
F	3.0	11.401	5.0	14.999	62.9	-
F2	3.0	11.236	5.0	14.723	55.4	-
G	3.0	11.000	5.0	14.330	46.2	-
W	3.0	10.806	5.0	14.009	39.8	-

**Table 7** Constants of basic design S-N curves for the FC environment by ABS

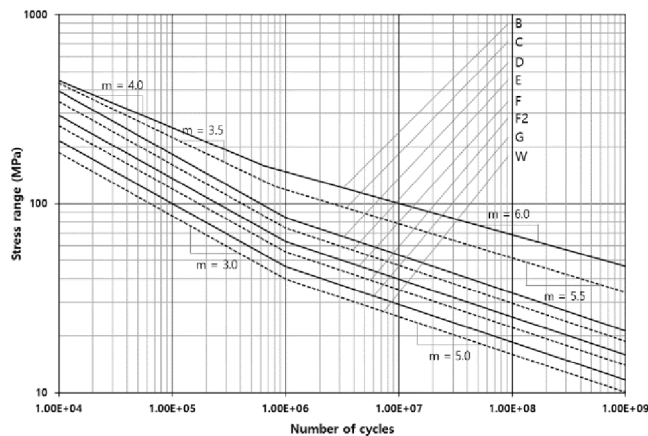
SDC	$m$	$\log A$	$\log \sigma$	SDC	$m$	$\log A$	$\log \sigma$
B	4.0	14.528	-	F	3.0	11.322	-
C	3.5	13.149	-	F2	3.0	11.155	-
D	3.0	11.705	-	G	3.0	10.921	-
E	3.0	11.540	-	W	3.0	10.727	-



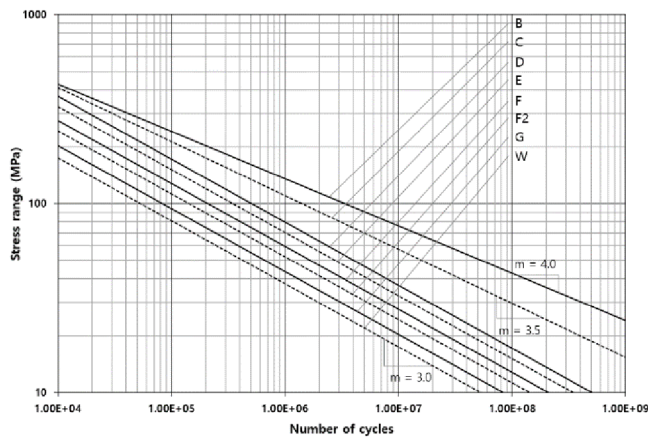
Tables 5–7 and Fig. 5(a)–(c) present the material constants required for the basic design S-N curves corresponding to the IA, CP, and FC environments, respectively. The basic design S-N curves in the IA and CP environments are doubly sloped. As shown in Tables 5–6 and Fig. 5(a)–(b), the curve slopes in the IA environment change at 10 million cycles, but two curves in the CP environment intersect at approximately 1 million cycles (to be exact 1,010,000 cycles), excluding the B and C curves.



(a) In-air



(b) Seawater with cathodic protection



(c) Free corrosion

**Fig. 5** Basic design S-N curves by ABS

Comparing ABS and DNV GL, the standard deviation of  $\log N$  in DNV GL, which is denoted as  $s_{\log N}$ , is constant regardless of the SDCs, but those in ABS,  $\log \sigma$ , vary with the SDCs, which were copied from Almar-Næss (1985) and BS.

#### 4.3 Basic Design S-N Curves of BS

The basic design S-N curve of BS is expressed as the slope ( $m$ ) and intercept ( $\log C_d$ ), as shown in Eq. (9). Table 8 lists the  $d$  value according to the probability of failure. For example, if the probability of failure is 2.3%;  $d$  equals 2.0 and  $C_d$  corresponding to this  $d$  becomes  $C_2$ .

$$\log N = \log C_d - m \cdot \log S_r = \log C_0 - d \cdot SD - m \cdot \log S_r \quad (9)$$

**Table 8** Nominal probability factors

Probability of failure (%)	$d$
50	0.0
31	0.5
16	1.0
2.3	2.0
0.14	3.0

For the relative comparison between the codes,  $d$  was assumed to equal 2.0 for the BS S-N curves. Tables 9–11 list the material constants for the three environments (the IA, CP, and FC). In Table 9,  $S_{OC}$  is the fatigue limit at 10 million cycles except for the S1 and S2 grades. Therefore, the IA environment S-N curves show an infinite life after 10 million cycles. BS also presents the S1 and S2 grades under shear stress conditions. S1 is used if fatigue cracking occurs in the weld toes, while the S2 is used for weld throats.

Table 10 lists the material constants of the S-N curves under the CP environment, which was more complicated than those by the other codes. The three fatigue strength points ( $S_{rt}$ ,  $S_{OC}$ , and  $S_{OV}$ ) are the slope change points, where the  $S_{rt}$  is listed in Table 10. The  $S_{OC}$  and  $S_{OV}$  are the fatigue strengths corresponding to 10 million and 50 million cycles, respectively. The S-N curves in the CP and FC environments cannot be applied to the cases under shear stresses.

Table 11 presents the basic design S-N curves in the FC environment, where they have single slopes like those in DNV GL and ABS.

Fig. 6(a) shows the basic design S-N curves in the IA environment. The fatigue life at low stress or high cycles in ships or offshore structures under variable loadings can be calculated after the fatigue strength  $S_{OV}$  corresponding to 50 million cycles. A bilinear S-N curve can be applied to variable loading conditions because the variable stress may sometimes exceed the fatigue limit, even though the average stress is less than the fatigue limit. For example, assuming that the second slope is 5 ( $m=5$ ), the S-N curve can be obtained, as shown in Fig. 6(b).

Because the slopes of the S-N curves in the CP environment change

**Table 9** Constants of the basic design S-N curves in the IA environment by BS

SDC	$N \leq 10^7$		$N > 10^7$		Fatigue limit at $10^7$ cycles $S_{OC}$ (MPa)	$S_{OV}$ (MPa)
	$m$	$\log C$	$m$	$\log C$		
B	4.0	15.0055	$\infty$	-	100	67
C	3.5	13.6262	$\infty$	-	78	49
D	3.0	12.1818	$\infty$	-	53	31
E	3.0	12.0153	$\infty$	-	47	27
F	3.0	11.8005	$\infty$	-	40	23
F2	3.0	11.6344	$\infty$	-	35	21
G	3.0	11.3940	$\infty$	-	29	17
G2	3.0	11.2014	$\infty$	-	25	15
W1	3.0	10.9699	$\infty$	-	21	12
S1	5.0	16.3010	$\infty$	-	46 at $10^8$ cycles	46 at $10^8$ cycles
S2	5.0	15.8165	$\infty$	-	37 at $10^8$ cycles	37 at $10^8$ cycles

**Table 10** Constants of the basic design S-N curves in a seawater environment with cathodic protection by BS

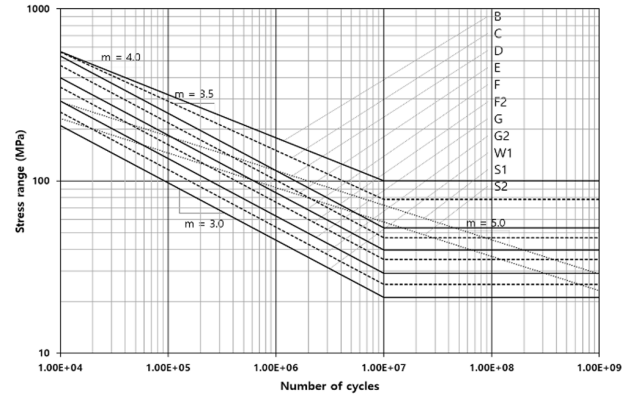
SDC	$S_r \geq S_{rt}$			$S_{rt} < S_r \leq S_{OC}$			$S_{OC} < S_r \leq S_{OV}$			$S_r < S_{OV}$		
	$S_{rt}$	$m$	$\log C_2$	$m$	$\log C_2$	$S_{OC}$	$m$	$\log C_2$	$S_{OV}$	$m$	$\log C_2$	
B	251	4.0	14.6075	5.0	17.0086	100	4.0	15.0043	67	5.0	16.8319	
C	144	3.5	13.2279	5.0	16.4654	78	3.5	13.6263	49	5.0	16.1673	
D	84	3.0	11.7839	5.0	15.6365	53	3.0	12.1818	31	5.0	15.1703	
E	74	3.0	11.6170	5.0	15.3579	47	3.0	12.0170	27	5.0	14.8927	
F	63	3.0	11.4031	5.0	15.0000	40	3.0	11.8007	23	5.0	14.5353	
F2	55	3.0	11.2355	5.0	14.7243	35	3.0	11.6345	20	5.0	14.2577	
G	46	3.0	10.9961	5.0	14.3243	29	3.0	11.3945	17	5.0	13.8573	
G2	40	3.0	10.8035	5.0	14.0043	25	3.0	11.2014	14	5.0	13.5366	
W1	33	3.0	10.5717	5.0	13.6170	21	3.0	10.9699	12	5.0	13.1492	

**Table 11** Constants of basic design S-N curves for a free corrosion environment by BS

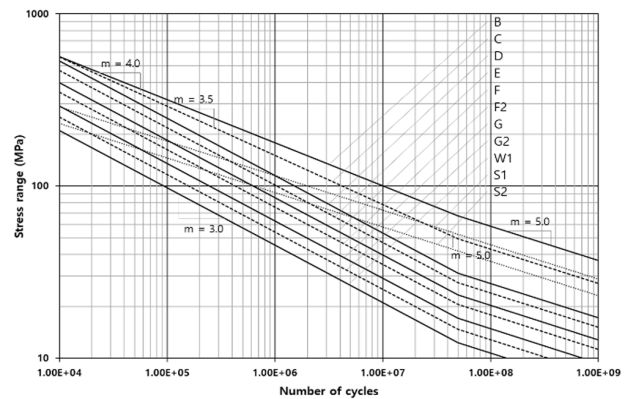
SDC	$m$	$\log C_2$	SDC	$m$	$\log C_2$
B	3.5	13.1492	G	3.0	10.9170
C	3.5	13.1492	G2	3.0	10.7243
D	3.0	11.7050	W1	3.0	10.4928
E	3.0	11.5378			
F	3.0	11.3243			
F2	3.0	11.1584			

at three fatigue strength points, each S-N curve must show a total of four lines (see Fig. 6(c)). Fig. 6(d) shows that the S-N curve in the FC environment has a single slope.

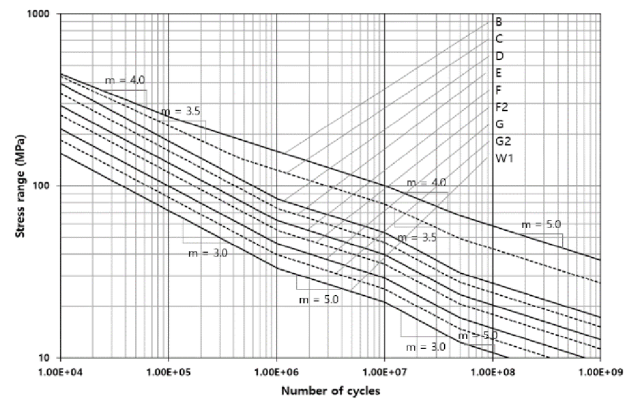
Unlike DNV GL, ABS, BS can select the basic design S-N curves by comprehensively considering the structural shape, stress component (normal and shear stresses), stress type (nominal and hot-spot stresses), and potential crack direction. In particular, the S-N curves are so well structured that an engineer can easily pick an S-N curve for structural details either subjected to nominal stress or hot-spot stress. Hence, BS is recognized as a code that can minimize human errors.



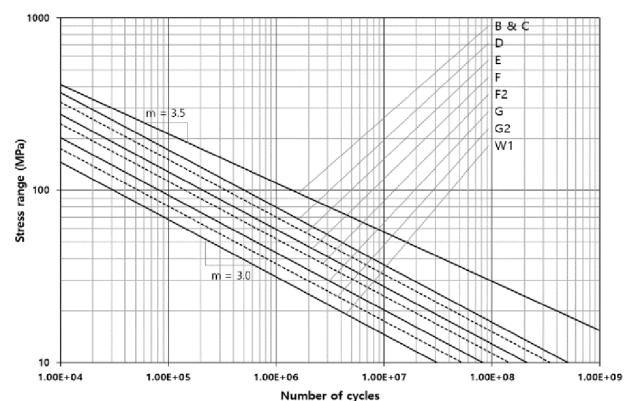
(a) In-air for standard application



(b) In-air for high cycle application



(c) Seawater with cathodic protection



(d) Free corrosion

**Fig. 6** Basic design S-N curves by BS

#### 4.4 Basic Design S-N Curves of IIW

Unlike DNV GL, ABS and BS, IIW uses the fatigue strength (FAT) at 2 million cycles and the corresponding slope to define the basic design S-N curves. The basic form of an S-N curve is expressed in Eq. (10). Eq. (12) was obtained by calculating  $C$  using equation (11) and substituting it into Eq. (10).

$$\Delta\sigma^m \cdot N = C \quad (10)$$

$$C = FAT^m \cdot 2 \times 10^6 \quad (11)$$

$$N = 2 \times 10^6 \cdot \left( \frac{\Delta\sigma}{FAT} \right)^{-m} \quad (12)$$

IIW provides the basic design S-N curves for aluminum and steel, but this paper concentrates on only the S-N curves for steel. The value of FAT determines the SDC of the basic design S-N curve provided by IIW. All basic design S-N curves can be applied to the IA condition. In the case of the CP or FC environment, it was stated that the strength level of the basic design S-N curve could be reduced by up to 70%. On the other hand, it is difficult to apply the basic design S-N curve of IIW in the case of non-IA environments.

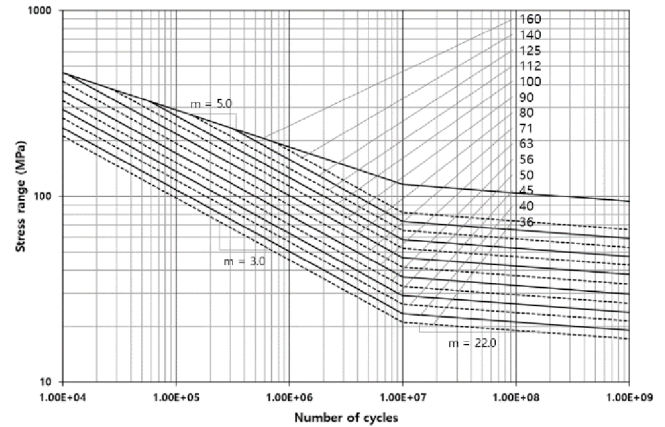
IIW provides the basic design S-N curves using nominal stress, hot-spot stress, and effective notch stress. The S-N curve by stress components was also provided. That is, thirteen and two basic design S-N curves are provided for the normal and shear stress conditions, respectively. FAT80 and FAT100 are for problems under a shear stress, while normal stress should be applied to FAT36 to FAT160.

As shown in Table 12, the basic design S-N curves over 10 million cycles for the normal stress application have either a fatigue limit, or a slope of 22.0. Fig. 7 includes the basic design S-N curves based on normal stress with the second slope  $m=22.0$ . The basic design S-N curves for the shear stress application can be considered to be single sloped because they have a fatigue limit of 100 million cycles.

IIW provides the following two approaches to construct the basic design S-N curve for the hot-spot stress application. For the first approach, among the nine structural details presented in Table 13, it is important to select a structural detail that is most similar to the welded part of the target structure. An S-N curve corresponding to the selected structural detail should then be chosen. For most of the structural details, the applicable grades are only FAT100 or FAT90, as listed in Table 13.

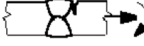
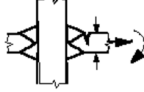

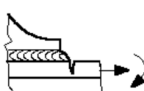

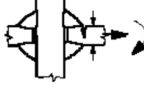
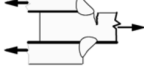
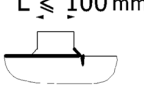
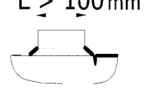
**Table 12** Constants of basic design S-N curves in the in-air environment by IIW

Under normal stress			Under shear stress		
SDC	$m$ ( $N \leq 10^7$ )	$m$ ( $N > 10^7$ )	SDC	$m$ ( $N \leq 10^8$ )	$m$ ( $N > 10^8$ )
FAT 160	5.0	$\infty$ or 22.0	FAT 100	5.0	$\infty$ or 22.0
FAT 140 or less	3.0	$\infty$ or 22.0	FAT 80	5.0	$\infty$ or 22.0



**Fig. 7** Basic design S-N curves in the in-air environment by IIW

**Table 13** Structural detail for hot-spot stress approach by IIW

Structural detail	Description	requirement	FAT
	Butt joint	As welded; NDT	100
	Cruciform or T-joint with full penetration K-butt welds	K-butt welds; No lamellar tearing	100
	Non-load-carrying fillet welds	Transverse non-load carrying attachment, not thicker than the main plate, as welded	100
	Bracket ends, ends of longitudinal stiffeners	Fillet welds welded around or not, as welded	100
	Cover plate ends and similar joints	As welded	100
	Cruciform joints with load-carrying fillet welds	Fillet welds, as welded	90
	Lap joint with load-carrying fillet welds	Fillet welds; As welded	90
	Short attachment	Fillet or full penetration weld; As welded	100
	Long attachment	Fillet or full penetration weld; As welded	90

The second method is to construct a new basic design S-N curve after revising FAT through finite element analysis. The following gives a summary of the process.

- Out of the 83 SDCs in the IIW code, select a reference structure detail, which should be most similar to the target.

- Derive two hot-spot stresses through finite element analyses for two structural details:  $\sigma_{hs,ref}$  and  $\sigma_{hs,assess}$  corresponding to the reference structural detail and target one.



- Derive a new FAT ( $FAT_{assess}$ ) based on the ratio of the hot-spot stresses using Eq. (13).

-To construct a new basic design S-N curve using the  $FAT_{assess}$ .

$$FAT_{assess} = \frac{\sigma_{hs,ref}}{\sigma_{hs,assess}} \cdot FAT_{ref} \quad (13)$$

The SDC should be FAT225 for effective notch stress applications. A basic design S-N curve can be constructed using a single slope ( $m=3.0$ ).

#### 4.5 Basic Design S-N Curves of EC3.

EC3 provides the basic design S-N curves for steel. All curves can be applied to an IA environment and cannot be used in the CP or FC environment.

In the same way as the SCD by IIW, EC3 refers to the fatigue strength corresponding to 2 million cycles as  $\Delta\sigma_C$ . EC3 determines the SDC based on  $\Delta\sigma_C$ . For intervals less than 5 million cycles, the slope is 3.0. The fatigue strength at 5 million cycles is defined as  $\Delta\sigma_D$ . The slope from 5 million cycles to 100 million cycles is 5.0. The fatigue strength at 100 million cycles is defined as  $\Delta\sigma_L$ , which is the fatigue limit.

In summary, Eq. (14) with  $m=3.0$  and Eq. (15) with  $m=5.0$  can be used for  $N_R \leq 5 \times 10^6$  and  $5 \times 10^6 < N_R \leq 1 \times 10^8$ , respectively. Fig. 8 presents the schematics of Eqs. (14) and (15).

$$N_R = 2 \times 10^6 \cdot \left( \frac{\Delta\sigma_R}{\Delta\sigma_C} \right)^{-m} \quad (14)$$

$$N_R = 5 \times 10^6 \cdot \left( \frac{\Delta\sigma_R}{\Delta\sigma_D} \right)^{-m} \quad (15)$$

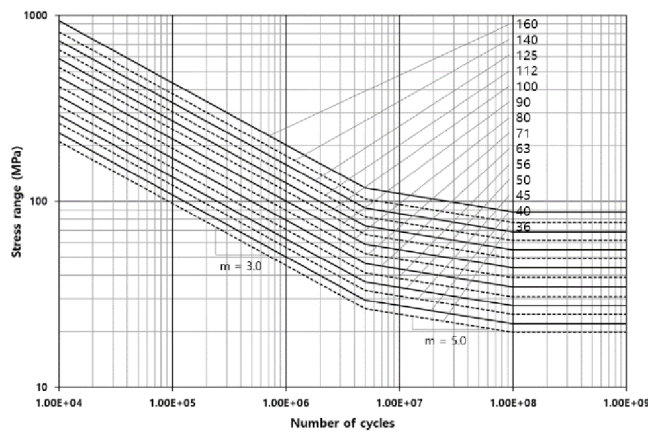


Fig. 8 Basic design S-N curves in in-air environment by IIW

## 5. Comparison between Codes

### 5.1 Comparison of Nominal SDCs

The nominal grades in the IA environment are divided into two groups because some codes do not provide S-N curves in the CP or FC

Table 14 Comparison of nominal SDCs

BS family	IIW family	BS family	IIW family
B1	FAT160	F	FAT71
B2	FAT140	F1	FAT63
C	FAT125	F3	FAT56
C1	FAT112	G	FAT50
C2	FAT100	W1	FAT45
D	FAT90	W2	FAT40
E	FAT80	W3	FAT36

environment, as listed in Table 14. Here, the BS family includes DNV GL, ABS, and BS, while the IIW family refers to IIW and EC3.

Although the 14 SDCs are classified in the same group, some SDCs are used only in specific codes. Hence, Table 14 cannot be a perfect comparison table.

### 5.2 Comparison of the Probabilities of Failure

As previously explained, DNV GL and ABS use two standard deviations, so the probability of failure of the basic design S-N curves is 2.3%. If  $d = 2.0$ , the S-N curves of BS also have the same probability of failure as DNV GL and ABS. On the other hand, IIW and EC3 provide the S-N curves with a 5% probability of failure (refer to Table 15).

Table 15 Comparison of the probabilities of failure

Code	Probability of failure (%)	Remark
DNV GL	2.3	
ABS	2.3	Not shown in updated code
BS	2.3	Selectable
IIW	5.0	
EC3	5.0	

### 5.3 Comparison of the S-N Curves

The S-N curves in the IA environment were compared because the S-N curves of some codes cannot be used in the CP or FC environment. The S-N curves of the D-, E-, and F grades were compared. Fig. 9 presents the S-N curves corresponding to the mean, +2 standard deviations, and -2 standard deviations as thick solid lines, thin dotted lines, and thick dotted lines, respectively.

#### 5.3.1 Grade E or FAT80

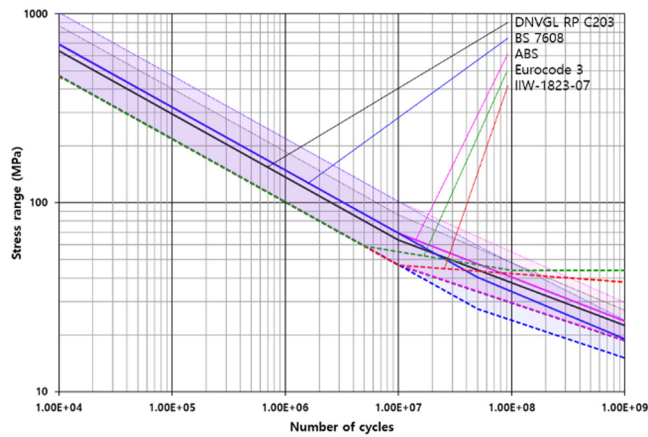
The E grade of the BS family and the FAT80 grade of the IIW family are equivalent to each other; Fig. 9(a) shows the S-N curves for the grades. The E grade mean curves by ABS and BS are the same up to 10 million cycles. Up to the same life, the mean curves by DNV GL were lower than those by ABS and BS. Therefore, the average S-N curves of DNV GL were the most conservative for 10 million cycles among the E grade curves belonging to the BS family. The mean S-N curve by BS was the most conservative for the long life of over 10 million cycles.

The basic design S-N curves (-2 standard deviation curves) of the

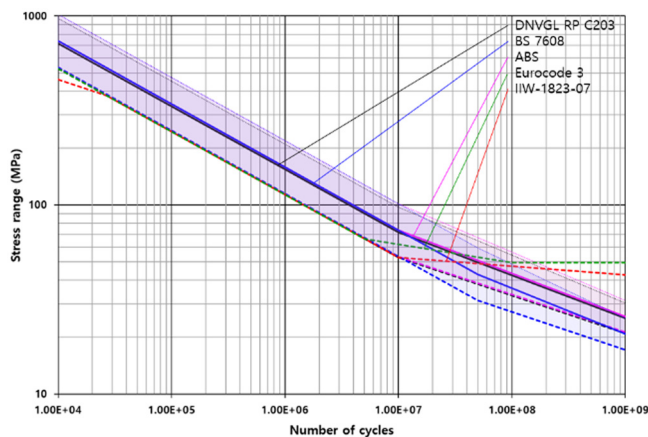
BS family coincide until 5 million cycles. The BS curve is the most conservative after 10 million cycles, while the basic design S-N curves by DNV GL and ABS are the second most conservative. The EC3 curve is most optimistic after 10 million cycles.

### 5.3.2 Grade D or FAT90

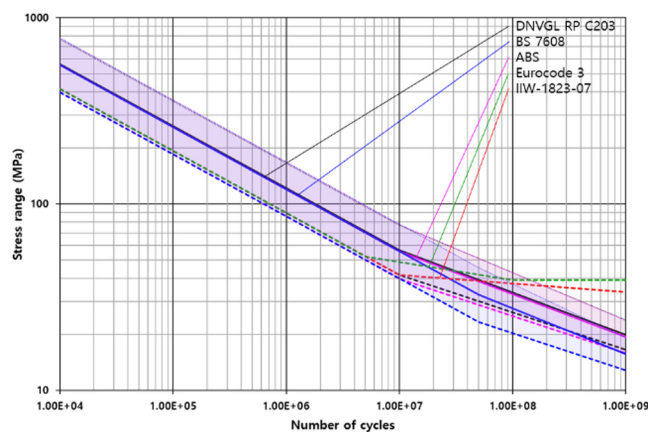
The grade D of the BS family and the FAT90 of the IIW family are equivalent. Fig. 9(b) presents the S-N curves in the IA environment.



(a) Class E



(b) Class D



(c) Class F

**Fig. 9** Comparison of various S-N curves in IA environment

The mean S-N curves by the five codes are similar up to 10 million cycles. If it exceeds 10 million cycles, the mean S-N curve by BS is the most conservative. As with the grade E, the three basic design S-N plots by the BS family were identical for up to 5 million cycles. Above 10 million cycles, the BS basic design curve was the most conservative.

### 5.3.3 Grade F or FAT71

The grade F of the BS family is equivalent to the FAT71 of the IIW family. Fig. 9(c) shows the IA environment S-N curves. The trend of the F grade curves by the codes was similar to that in the D grade curves.

## 6. Conclusions

This paper analyzed the characteristics of the S-N curves according to various industry standards and codes to provide guidelines for applying the appropriate codes when designing ships and offshore structures. The S-N curves of the five codes (DNV GL, ABS, BS, IIW, and EC3) were analyzed and compared for the non-tubular members made from steels.

Before the code-by-code comparison, the notations and symbols were summarized into a single table by each code to minimize confusion.

Unless stated otherwise, the S-N curves presented in most codes were based on the nominal stress. On the other hand, because the hot-spot stress has been used mainly in the design of offshore structures, it is important to select a basic design S-N curve for a hot-spot stress application problem code by code. In addition, a method of evaluating hot-spot stresses was introduced.

DNV GL, ABS, and BS define an S-N curve with an intercept and slope, while IIW and EC3 describe it with a fatigue strength at 2 million cycles and a slope. An examination of the probability of failure for each code, DNV GL, ABS and BS used a basic design S-N curve based on a failure probability of 2.3% and those corresponding to a 5% failure probability by IIW and EC3.

The material constants of the basic design S-N curves presented in each code were arranged in a table so that the reader can easily use them. The corresponding S-N curves are provided graphically so that a design engineer can apply them without needing to read the complex codes fully.

The nominal grades by the BS family (DNV GL, ABS, and BS) and IIW family (IIW and EC3) were tabulated to enable a relative comparison. In addition, the mean and basic S-N curves by the five codes were compared for the E, D, and F grades. Overall, the BS presented the most conservative basic design S-N curves.

Part 1 of this paper compared the basic design S-N curves. Part 2 discussed various factors influencing the basic design S-N curves. Nevertheless, because this paper targeted the non-tubular steel members, it will be necessary to deal with tubular members in future studies.



### Conflict of interest

No potential conflict of interest relevant to this article was reported.

### Funding

This work was supported by Korea Environment Industry & Technology Institute (KEITI) through Industrial Facilities & Infrastructure Research Program, funded by Korea Ministry of Environment (MOE) (146836).

### References

- American Bureau of Shipping (ABS). (2003). Guide for Fatigue Assessment of Offshore Structures (updated March 2018). Houston, USA: ABS.
- Almar-Næss, A. (1985). Fatigue Handbook. Trondheim Norway: Tapir.
- British Standard Institution (BSI). (2015). Guide to Fatigue Design and Assessment of Steel Products. London UK: BSI.
- British Standard Institution (BSI). (2005). Eurocode 3: Design of Steel Structures Part 1-9 Fatigue. London UK: BSI.
- Det Norske Veritas (DNV). (2014). Classification Notes No. 30.7 Fatigue Assessment of Ship Structures: DNV.
- DNV GL (2018). DNVGL-CG-0129 Fatigue Assessment of Ship Structures: DNVGL.
- DNV GL (2016). DNVGL-RP-C203 Fatigue Design of Offshore Steel Structures: DNVGL.
- International Institute of Welding (IIW). (2008). IIW-1823-07 Recommendations for Fatigue Design of Welded Joints and Components: IIW.
- Lee, J.M., Seo, J.K., Kim, M.H., Shin, S.B., Han, M.S., Park, J.S., Mahendran, M. (2010). Comparison of Hot Spot Stress Evaluation Methods for Welded Structures. International Journal of Naval Architecture and Ocean Engineering, 2(4), 200–210.

### Author ORCIDs

Author name	ORCID
Im, Sungwoo	0000-0001-6792-1953
Choung, Joonmo	0000-0003-1407-9031

# Instructions for Authors

## General information

To submit a manuscript to the Journal of Ocean Engineering and Technology (JOET), it is advised to first carefully read the aims and the scope section of this journal, as it provides information on the editorial policy and the category of papers it accepts. Unlike many regular journals, JOET usually has no lag in acceptance of a manuscript and its publication. Authors that find a match with the aims and the scope of JOET are encouraged to submit as we publish works from all over the world. JOET adheres completely to guidelines and best practices published by professional organizations, including Principles of Transparency and Best Practice in Scholarly Publishing (joint statement by COPE, DOAJ, WAME, and OASPA (<http://doaj.org/bestpractice>) if otherwise not described below. As such, JOET would like to keep the principles and policies of those professional organizations during editing and the publication process.

## Research and publication ethics

Details on publication ethics are found in <http://joet.org/authors/ethics.php>. For the policies on research and publication ethics not stated in the Instructions, Guidelines on Good Publication (<http://publicationethics.org/>) can be applied.

## Requirement for membership

One of the authors who submits a paper or papers should be member of the Korean Society of Ocean Engineers (KSOE), except a case that editorial board provides special admission of submission.

## Publication type

Article types include scholarly monographs (original research articles), technical articles (technical reports and data), and review articles. The paper should have not been submitted to other academic journal. When part or whole of a manuscript was already published to conference papers, research reports, and dissertations, then the corresponding author should note it clearly in the manuscript.

## Copyright

After published to JOET, the copyright of manuscripts should belong to KSOE. A transfer of copyright (publishing agreement) form can be found in submission website (<http://www.joet.org>).

## Manuscript submission

Manuscript should be submitted through the on-line submission website (<http://www.joet.org>). The date that manuscript was received through on-line website is the official date of receipt. Other correspondences can be sent by an email to the Editor in Chief or secretariat. The manuscript must be accompanied by a signed statement that it has been neither published nor currently submitted for publication elsewhere. The manuscript should be written in English or Korean. Ensure that online submission are in a standard word processing format. Corresponding author must write the manuscript using the JOET template provided in Hangul or MS Word format. Ensure that graphics are high-resolution.

Be sure all necessary files have been uploaded/ attached.

## Authors' checklist

Please refer to "Authors' Checklist" for details.

## Article structure

Manuscript must be edited in the following order: (1) Title, (2) Authors' names and affiliations, (3) Keywords, (4) Abstract, (5) Nomenclature (optional), (6) Introduction, (7) Main body (analyses, tests, results, and discussions), (8) Conclusions, (9) Conflict of interest (optional), (10) Funding (optional), (11) Acknowledgements (optional), (12) References, (13) Appendices (optional), (14) Author's ORCIDs.

## Abstract

A concise and factual abstract is required. The abstract should state briefly the background, purpose and methods of the research, the principal results and conclusions. An abstract should be written in around 300 words. References are not cited in abstract whenever possible. Also, non-standard or uncommon abbreviations should be avoided, but if essential they must be defined at their first mention in the abstract itself.

## Keywords

Immediately after the abstract, provide a maximum of 5 or 6 keywords.

## Unit

Use the international system units(SI). If other units are mentioned, please give their equivalent in SI.

## Equations

All mathematical equations should be clearly printed/typed using well accepted explanation. Superscripts and subscripts should be typed clearly above or below the base line. Equation numbers should be given in Arabic numerals enclosed in parentheses on the right-hand margin.

## Tables

Tables should be numbered consecutively with Arabic numerals. Each table should be fully titled. All tables should be referred to in the texts.

## Figures

Figures should be numbered consecutively with Arabic numerals. Each figure should be fully titled. All figures should be referred to in the texts. All the illustrations should be of high quality meeting with the publishing requirement with legible symbols and legends.

## Conflict of interest

It should be disclosed here according to the statement in the Research and publication ethics regardless of existence of conflict of interest. If the authors have nothing to disclose, please state: "No potential

conflict of interest relevant to this article was reported.”

### Funding

Funding to the research should be provided here. Providing a FundRef ID is recommended including the name of the funding agency, country and if available, the number of the grant provided by the funding agency. If the funding agency does not have a FundRef ID, please ask that agency to contact the FundRef registry (e-mail: fundref.registry@crossref.org). Additional detailed policy of FundRef description is available from <http://www.crossref.org/fundref/>. Example of a funding description is as follows:

The study is supported by the Inha University research fund (FundRef ID: 10.13039/501100002632), and the Korea Health Personnel Licensing Examination Institute research fund (FundRef ID: 10.13039/501100003647).

### Acknowledgments

Any persons that contributed to the study or the manuscript, but not meeting the requirements of an authorship could be placed here. For mentioning any persons or any organizations in this section, there should be a written permission from them.

### References in text

References in texts follow the APA style. Authors can also see how references appear in manuscript text through the ‘Template’.

### Reference list

Reference list follows the APA style. Authors can see how references should be given in reference section through the ‘Template’.

### Appendices

The appendix is an optional section that can contain details and data supplemental to the main text. If there is more than an appendix, they should be identified as A, B, C, etc. Formulae and equations in appendices should be given separate numbering: Eq. (A1), Eq. (A2), etc.; in a subsequent appendix, Eq. (B1) and so on. Similarly for tables and figures: Table A1; Fig. A1, etc.

### ORCID (Open Researcher and Contributor ID)

All authors are recommended to provide an ORCID. To obtain an ORCID, authors should register in the ORCID web site: <http://orcid.org>. Registration is free to every researcher in the world. Example of ORCID description is as follows:

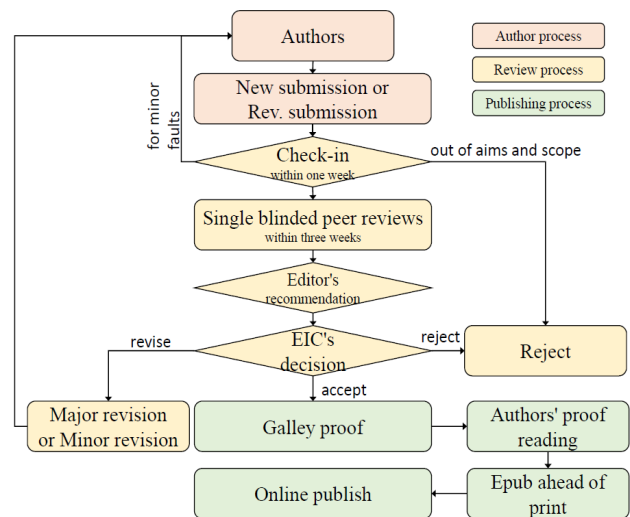
Joonmo Choung: <https://orcid.org/0000-0003-1407-9031>

### Peer review and publication process

The peer review process can be broadly summarized into three groups: author process, review process, and publishing process for accepted submissions. General scheme is presented in Figure 1.

#### Check-in process for review

If the manuscript does not fit the aims and scope of the Journal or does not adhere to the Instructions to Authors, it may be rejected immediately after receipt and without a review. Before reviewing, all submitted manuscripts are inspected by Similarity Check powered by iThenticate (<https://www.crossref.org/services/similarity-check/>), a plagiarism-screening tool. If a too high degree of similarity score is found, the Editorial Board will do a more profound content screening.



**Figure 1** Flow chart of the peer review and publication process of JOET

The criterion for similarity rate for further screening is usually 15%; however, rather than the similarity rate, the Editorial Board focuses on cases where specific sentences or phrases are similar. The settings for Similarity Check screening are as follows: It excludes quotes, bibliography, small matches of 6 words, small sources of 1%, and the Methods section.

#### Number of reviewers

Reviewers will be selected from the list of reviewers. Manuscripts are then peer reviewed by at least 2 experts in the corresponding field, usually by 2.

**Peer review process and the author response to the reviewer comments**  
JOET adopts single blind review, which means that the authors do not know the identity of the reviews. All papers, including those invited by the Editor, are subject to peer review.

The review period is 4 weeks. Usually the first decision is made within a week after completion of the review. The Editorial Board's decision after the review will be one of followings: Accept, Minor revision, Major revision, or Rejection. The Editorial Board may request the authors to revise the manuscript according to the reviewers' comments. If there are any requests for revision of the manuscript by the reviewers, the authors should do their best to revise the manuscript. If the reviewer's opinion is not acceptable or is believed to misinterpret the data, the author should reasonably indicate that. After revising the manuscript, the author should upload the revised files with a separate response sheet to each item of the reviewer's commentary. The author's revisions should be completed within 3 months after the request. If it is not received by the due date, the Editorial Board will notify the author. To extend the revision period beyond 3 months, the author should negotiate that with the Editorial Board. The manuscript review process can be provided for up two rounds. If the authors wish further review, the Editorial Board may consider it. The Editorial Board will make a final decision on the approval of the submitted manuscript for publication and can request any further corrections, revisions, and deletions of the article text if necessary. Statistical editing is also performed if the data requires professional statistical review by a statistician.

### *Processing after acceptance*

If the manuscript is finally accepted, the galley proof will be sent to the corresponding author after professional manuscript editing and English proofreading. Proofreading should be performed for any misspellings or errors by the authors. Proofreading manuscript for publication is provided to the corresponding author, and the corresponding author must review the proofreading manuscript. Corresponding authors are responsible for the content of the proofreading manuscript and any errors. After final proofreading, the manuscript may appear at the journal homepage as an article in press with a unique DOI number for rapid communication. All published articles will be replaced by the replacement XML file and a final PDF.

### *Feedback after publication*

If the authors or readers find any errors, or contents that should be revised, it can be requested from the Editorial Board. The Editorial Board may consider erratum, corrigendum or a retraction. If there are any revisions to the article, there will be a CrossMark description to announce the final draft. If there is a reader's opinion on the published article with the form of Letter to the editor, it will be forwarded to the authors. The authors can reply to the reader's letter. Letter to the editor and the author's reply may be also published.

### *How the journal handle complaints and appeals*

The policy of JOET is primarily aimed at protecting the authors, reviewers, editors, and the publisher of the journal. If not described below, the process of handling complaints and appeals follows the guidelines of the Committee of Publication Ethics available from: <https://publicationethics.org/appeals>

#### *- Who complains or makes an appeal?*

Submitters, authors, reviewers, and readers may register complaints and appeals in a variety of cases as follows: falsification, fabrication, plagiarism, duplicate publication, authorship dispute, conflict of interest, ethical treatment of animals, informed consent, bias or unfair/inappropriate competitive acts, copyright, stolen data, defamation, and legal problem. If any individuals or institutions want to inform the cases, they can send a letter via the contact page on

our website: <https://www.joet.org/about/contact.php>. For the complaints or appeals, concrete data with answers to all factual questions (who, when, where, what, how, why) should be provided.

#### *- Who is responsible to resolve and handle complaints and appeals?*

The Editorial Board or Editorial Office is responsible for them. A legal consultant or ethics editor may be able to help with the decision making.

#### *- What may be the consequence of remedy?*

It depends on the type or degree of misconduct. The consequence of resolution will follow the guidelines of the Committee of Publication Ethics (COPE).

### **Article processing charge**

#### *Payment due*

Article processing charge (APC) covers the range of publishing services JOET provides. This includes provision of online tools for editors and authors, article production and hosting, and customer services. Upon editorial acceptance of an article for the regular review service and upon submission of an article for the fast review service, the corresponding author will be notified that payment is due.

#### *APC*

The APC up to 6 pages is ₩200,000 (or \$200) and ₩550,000 (or \$550) for the regular and fast review services, respectively. An extra APC of \$50 per page is charged for papers longer than 6 pages. No taxes are included in this charge. For the fast review service, an advance fee of ₩250,000 (\$250) should be paid on submission.

#### *Payment methods*

*Credit card payment* can be made online using a secure payment form as soon as the manuscript has been editorially accepted. We will send a receipt by email once payment has been processed. Please note that payment by credit card carries a surcharge of 10% of the total APC.

*Invoice payment* is due within 7 days of the manuscript receiving editorial acceptance. Receipts are available on request.



## Title of Article

Firstname Lastname<sup>1</sup>, Firstname Lastname<sup>2</sup> and Firstname Lastname<sup>3</sup>

<sup>1</sup>Professor, Department of OO, OO School, OO University, Busan, Korea

<sup>2</sup>Graduate Student, Department of OO, OO University, Seoul, Korea

<sup>3</sup>Senior Researcher, Department of OO, OO Engineering, Corp., Seoul, Korea

**KEY WORDS:** Lumped mass line model, Explicit method, Steel lazy wave riser (provide a maximum of 5 or 6 keywords.)

**ABSTRACT:** A concise and factual abstract is required. The abstract should state briefly the background, purpose and methods of the research, the principal results and conclusions. An abstract should be written in around 300 words. References are not cited in abstract whenever possible. Also, non-standard or uncommon abbreviations should be avoided, but if essential they must be defined at their first mention in the abstract itself.

## Nomenclature (Optional)

$ITOC$	Increment of total operating cost (\$/yr)
$LHV$	Lower heating value (kJ/kg)
$P_w$	Power (kW)
$T$	Temperature (K)
$V$	Volume (m <sup>3</sup> )
$\rho$	Density (kg/m <sup>3</sup> )

## 1. Introduction

The introduction should briefly place the study in a broad context and highlight why it is important. It should define the purpose of the work and its significance. The current state of the research field should be reviewed carefully and key publications cited. Please highlight controversial and diverging hypotheses when necessary. Finally, briefly mention the main aim of the work and highlight the principal conclusions. As far as possible, please keep the introduction comprehensible to scientists outside your particular field of research.

## 2. General Information for Authors

### 2.1 Research and Publication Ethics

Authorship should be limited to those who have made a significant contribution to the conception, design, execution, or interpretation of the reported study. All those who have made significant contributions should be listed as co-authors. Where there are others who have participated in certain substantive aspects of the research project, they should be acknowledged or listed as contributors.

The corresponding author should ensure that all appropriate co-authors and no inappropriate co-authors are included on the paper, and that all co-authors have seen and approved the final version of the paper and have agreed to its submission for publication.

Details on publication ethics are found in the journal's website (<http://joet.org/authors/ethics.php>). For the policies on research and publication

Received 00 February 2100, revised 00 October 2100, accepted 00 October 2100

Corresponding author Firstname Lastname: +82-51-759-0656, e-mail@e-mail.com

It is a recommended paper from the proceedings of 2019 spring symposium of the Korea Marine Robot Technology (KMRTS).

© 2100, The Korean Society of Ocean Engineers

This is an open access article distributed under the terms of the creative commons attribution non-commercial license (<http://creativecommons.org/licenses/by-nc/4.0>) which permits unrestricted non-commercial use, distribution, and reproduction in any medium, provided the original work is properly cited.



ethics not stated in the Instructions, Guidelines on Good Publication (<http://publicationethics.org/>) can be applied.

## 2.2 Requirement for Membership

One of the authors who submits a paper or papers should be member of The Korea Society of Ocean Engineers (KSOE), except a case that editorial board provides special admission of submission.

## 2.3 Publication Type

Article types include scholarly monographs (original research articles), technical articles (technical reports and data), and review articles. The paper should have not been submitted to other academic journal. When part or whole of a manuscript was already published to conference papers, research reports, and dissertations, then the corresponding author should note it clearly in the manuscript.

Example: It is noted that this paper is revised edition based on proceedings of KAOST 2100 in Jeju.

## 2.4 Copyright

After published to JOET, the copyright of manuscripts should belong to KSOE. A transfer of copyright (publishing agreement) form can be found in submission website (<http://www.joet.org>).

## 2.5 Manuscript Submission

Manuscript should be submitted through the on-line submission website (<http://www.joet.org>). The date that manuscript was received through on-line website is the official date of receipt. Other correspondences can be sent by an email to the Editor in Chief or secretariat. The manuscript must be accompanied by a signed statement that it has been neither published nor currently submitted for publication elsewhere. The manuscript should be written in English or Korean. Ensure that online submission are in a standard word processing format. Corresponding author must write the manuscript using the JOET template provided in Hangul or MS Word format. Ensure that graphics are high-resolution. Be sure all necessary files have been uploaded/ attached.

### 2.5.1 Author's checklist

Author's checklist and Transfer of copyright can be found in submission homepage (<http://www.joet.org>).

## 3. Manuscript

Manuscript must be edited in the following order: (1) Title, (2) Authors' names and affiliations, (3) Keywords, (4) Abstract, (5) Nomenclature (optional), (6) Introduction, (7) Main body (analyses, tests, results, and discussions), (8) Conclusions, (9) Conflict of interest (optional), (10) Funding (optional), (11) Acknowledgements (optional), (12) References, (13) Appendices (optional), (14) Author's ORCIDs.

### 3.1 Unit

Use the international system units(SI). If other units are mentioned, please give their equivalent in SI.

### 3.2 Equations

All mathematical equations should be clearly printed/typed using well accepted explanation. Superscripts and subscripts should be typed clearly above or below the base line. Equation numbers should be given in Arabic numerals enclosed in parentheses on the right-hand margin. The parameters used in equation must be defined. They should be cited in the text as, for example, Eq. (1), or Eqs. (1)–(3).

$$G_{GEV}(x; \mu, \sigma, \xi) = \begin{cases} \exp[-(1 + \xi(x - \mu)/\sigma)^{-1/\xi}] & \xi \neq 0 \\ \exp[-\exp(-(x - \mu)/\sigma)] & \xi = 0 \end{cases} \quad (1)$$

in which  $\mu$ ,  $\sigma$ , and  $\xi$  represent the location (“Shift” in figures), scale, and shape parameters, respectively.

### 3.3 Tables

Tables should be numbered consecutively with Arabic numerals. Each table should be typed on a separate sheet of paper and be fully titled. All tables should be referred to in the texts.

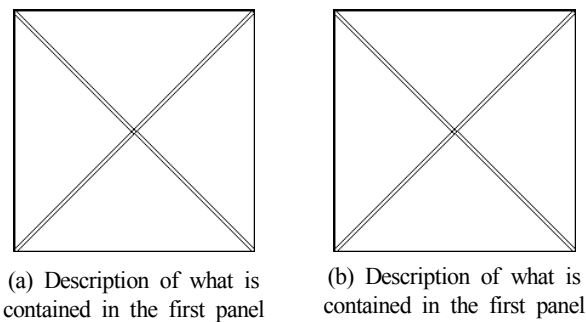
**Table 1** Tables should be placed in the main text near to the first time they are cited

Item	Buoyancy riser
Segment length <sup>1)</sup> (m)	370
Outer diameter (m)	1.137
Inner diameter (m)	0.406
Dry weight (kg/m)	697
Bending rigidity (N·m <sup>2</sup> )	1.66E8
Axial stiffness (N)	7.098E9
Inner flow density (kg·m <sup>3</sup> )	881
Seabed stiffness (N/m/m <sup>2</sup> )	6,000

<sup>1)</sup>Tables may have a footer.

### 3.4 Figures

Figures should be numbered consecutively with Arabic numerals. Each figure should be fully titled. All the illustrations should be of high quality meeting with the publishing requirement with legible symbols and legends. All figures should be referred to in the texts. They should be referred to in the text as, for example, Fig. 1, or Figs. 1–3.



**Fig. 1** Schemes follow the same formatting. If there are multiple panels, they should be listed as: (a) Description of what is contained in the first panel; (b) Description of what is contained in the second panel. Figures should be placed in the main text near to the first time they are cited

### 3.5 How to Describe the References in Main Texts

All references should be listed at the end of the manuscripts, arranged in order of Alphabet. References in texts follow the American Psychological Association (APA) style. The exemplary form of listed references is as follows:

Single author: (Kim, 1998) or Kim (1998)

Two authors: (Kim and Lee, 2000) or Kim and Lee (2000)

Three or more authors: (Kim et al., 1997) or Kim et al. (1997)

Two or more papers: (Lee, 1995a; Lee, 1995b; Ryu et al., 1998)

Year unknown: (Kim, n.d.) or Kim (n.d.)

## 4. Results

This section may be divided by subheadings. It should provide a concise and precise description of the experimental results, their interpretation as well as the experimental conclusions that can be drawn. Tables and figures are recommended to present the results more rapidly and easily. Do not duplicate the content of a table or a figure with in the Results section. Briefly describe the core results related to the conclusion in the text when data are provided in tables or in figures. Supplementary results can be placed in the Appendix.

## 5. Discussion

Authors should discuss the results and how they can be interpreted in perspective of previous studies and of the working hypotheses. The findings and their implications should be discussed in the broadest context possible. Future research directions may also be highlighted

## 6. Conclusions

This section can be added to the manuscript.

### Conflict of Interest (Optional)

It should be disclosed here according to the statement in the Research and publication ethics regardless of existence of conflict of interest. If the authors have nothing to disclose, please state: “No potential conflict of interest relevant to this article was reported.”

### Funding (Optional)

Please add: “This research was funded by Name of Funder, grant number XXX” and “The OOO was funded by XXX”. Check carefully that the details given are accurate and use the standard spelling of funding agency names at <https://search.crossref.org/funding>

### Acknowledgments (Optional)

In this section you can acknowledge any support given which is not covered by the author contribution or funding sections. This may include administrative and technical support, or donations in kind (e.g., materials used for experiments). For mentioning any persons or any organizations in this section, there should be a written permission from them.

## References

- Journal name should not be abbreviated.
- A private report with limited access or download availability can not be a reference.
- Include the digital object identifier DOI or URL for all references where available.
- Reference list follows the American Psychological Association (APA) style.

#### Referring to journal publications:

- Author, A.A., Author, B.B., & Author, C.C. (Year). Title of Article. Journal Title, vol(no), pp-pp. <https://doi.org/xx.xxxx/xxxxxx>
- Author, A.A., Author, B.B., Author, C.C. (accepted; in press). Title of Article. Title of Periodical. Retrieved from <http://xx.xxx/x.pdf>
- Lee, T.K., Kim, T.W., Rim, C.W., & Kim, S.C. (2013). A Study on Calculation of Local Ice Pressures for ARAON Based on Data Measured at Arctic Sea. Journal of Ocean Engineering and Technology, 27(5), 88–92. <https://doi.org/10.5574/KSOE.2013.27.5.088>
- Lee, T.K., Kim, T.W., Rim, C.W., & Kim, S.C. (accepted; in press). A Study on Calculation of Local Ice Pressures for ARAON Based on Data Measured at Arctic Sea. Journal of Ocean Engineering and Technology, Retrieved from <http://xxx.xxx/xxx.pdf>

#### Referring to conference proceedings:

- Author, A.A., Author, B.B., & Author, C.C. (Year). Title of Article. Proceeding Title, City, Country, pp-pp. <https://doi.org/xx.xxxx>
- Aoki, S., Liu, H., & Sawaragi, T. (1994). Wave Transformation and Wave Forces on Submerged Vertical Membrane. Proceedings of International Symposium Waves - Physical and Numerical Modeling, Vancouver, Canada, 1287–1296.
- Tsukamoto, C.L., Lee, W., Yuh, J., Choi, S.K., & Lorentz, J. (1997). Comparison Study on Advanced Thruster Control of Underwater Robots. Proceedings of International Conference on Robotics and Automation, 1845–1850. <https://doi.org/110.1109/ROBOT.1997.619056>

#### Referring to books:

- Author, A.A. (Year). Title of Book (xx ed.). Location: Publisher.
- Strunk, W., & White, E.B. (2000). The Elements of Style (4<sup>th</sup> ed.). New York, USA: Longman.
- Schlichting, H. (1968). Boundary Layer Theory (6<sup>th</sup> ed.). New York, USA: McGraw-Hill.

#### Referring to theses or dissertations:

- Author, A.A. (Year). Title of Doctoral Dissertation or Master’s thesis (Doctoral Dissertation or Master’s thesis). Name of Institution, City, Country.
- Giovanni, I. (1998). Modelling and Identification of Underwater Robotic Systems (Ph.D. Thesis). University of Genova, Genova, Italy.

## Referring to technical reports, rules, or guidelines:

Author, A.A. (Year). Title of report (Reprot No. xxx), Location: Publisher.

Likhomanov, V. (2010). Full-Scale Ice Trials of the Korean Research Icebreaker ARAON. Daejeon, Korea: Arctic and Antarctic Research Institute (AARI).

ABS. (2011). Guide for Ice Loads Monitoring Systems. Houston, USA: American Bureau of Shipping.

Lloyd's Register. (2011). FDA ICE Fatigue Induced by Ice Loading, ShipRight Design and construction - Fatigue Design Assesment. London, United Kingdom: Lloyd's Register.

Larson, M., & Kraus, N.C. (1989). SBEACH: Numerical Model for Simulating Storm-Induced Beach Change - Report 1 Empirical Foundation and Model Development (Technicla Report CERC-89-9). Coastal Engineering research center Vicksburg Ms.

## Referring to patents:

Righsholder, A.A. (Year). Title of Patent. Patent number, Patent office with country.

Dawoo Shipbulding & Maringe Engineering (DSME). (2013). Distance Length Standardization Method for Preventing Interference at the time of Uploading Cell Guide of Container Ship. Unexamined Patent Publication 1020130044635, Korean Interllectual Property Office.

## Referring to websites:

Righsholder, A.A. (Year). Title of webpage. Retrieved Month Year from <http://xxxx>

International Association of Classification Societies (IACS). (2010a). Common Structural Rules for Bulk Carriers. Retrieved July 2010 from <http://www.iacs-data.org.uk>

US Congressional Hearing. (2009). Strategic Importance of the Arctic in Us Policy. Retrieved June 2019 from <https://fas.org/irp/arctic.pdf>

Dawoo Shipbulding & Maringe Engineering (DSME). (2013). Distance Length Standardization Method for Preventing Interference at the time of Uploading Cell Guide of Container Ship. Retrieved June 2019 from <https://patentimages.storage.pdfs/792.pdf>

## Referring to software:

Righsholder, A.A. (Year). Title of Software. Downloaded Month Year from <http://xxxx>

## Standard

Organization. (Year). Title of the standard in italics [Translated title – if applicable] (Standard No.). Retrieved from <https://...>

International Organization for Standardization. (2005). Industrial sewing machines: Safety requirements for sewing machines, units and systems (ISO Standard No. 10821). Retrieved from <http://www.standard.no/no/Nettbutikk/produktkatalogen/Produktpresentasjon/?ProductID=113554>

## Translation

Author, A. A. (Year of publication). Title of work: Capital letter also for subtitle (T. Translator, Trans.). Location: Publisher. (Original work published YEAR). DOI

Ura, T., & Takakawa, S. (2015). All about Submersibles (W.S. Kim, D.S. Kim, Y.H. Choi, C.H. Park, J.S. Park, P.M. Lee, H.S. Jung, Trans.). Korea: CIR. (Original Work Published in 1994, Japan: Seizan-Shoten Publishing)

in text: (Ura and Takakawa, 1994/2015)

## Referring to some exceptional cases:

- when authors are missing, institution can replace authors

National Oceanic and Atmospheric Administration (NOAA). (2015). Deep-ocean Assessment and Reporting of Tsunamis (DART). Retrieved December 2019 from <https://nctr.pmel.noaa.gov/Dart/>

- when dates or years are missing, it is replaced with "n.d."

National Oceanic and Atmospheric Administration (NOAA). (n.d.). Deep-ocean Assessment and Reporting of Tsunamis (DART).

- when more then seven authors, first 6 authors ... last author.

Yeu, T., Choi, H.T., Lee, Y., Chae, J., Lee, Y., Kim, S.S., ... Lee, T.H. (2019). Development of Robot Platform for Autonomous Underwater Intervention. Journal of Ocean Engineering and Technology, 33(2), 168-177. <https://doi.org/10.26748/KSOE.2019.021>

## Appendix (Optional)

The appendix is an optional section that can contain details and data supplemental to the main text. For example, explanations of experimental details that would disrupt the flow of the main text, but nonetheless remain crucial to understanding and reproducing the research shown; figures of replicates for experiments of which representative data is shown in the main text can be added here if brief, or as Supplementary data. Mathematical proofs of results not central to the paper can be added as an appendix.

All appendix sections must be cited in the main text. In the appendixes, Figures, Tables, etc. should be labeled starting with 'A', e.g., Fig. A1, Fig. A2, etc.

Examples:

<https://doi.org/10.26748/KSOE.2019.022>

<https://doi.org/10.26748/KSOE.2018.4.32.2.095>

## Author ORCIDs

All authors are recommended to provide an ORCID. To obtain an ORCID, authors should register in the ORCID web site: <http://orcid.org>. Registration is free to every researcher in the world. Example of ORCID description is as follows:

Author name	ORCID
So, Hee	0000-0000-000-00X
Park, Hye-Il	0000-0000-000-00X
Yoo, All	0000-0000-000-00X
Jung, Jewerly	0000-0000-000-00X



# Authors' Checklist

The following list will be useful during the final checking of a manuscript prior to sending it to the journal for review. Please submit this checklist to the KSOE when you submit your article.

## < Checklist for manuscript preparation >

- ☐ I checked my manuscript has been 'spell-checked' and 'grammar-checked'.
- ☐ One author has been designated as the corresponding author with contact details such as
  - E-mail address
  - Phone numbers
- ☐ I checked abstract 1) stated briefly the purpose of the research, the principal results and major conclusions, 2) was written in around 300 words, and 3) did not contain references (but if essential, then cite the author(s) and year(s)).
- ☐ I provided 5 or 6 keywords.
- ☐ I checked color figures were clearly marked as being intended for color reproduction on the Web and in print, or to be reproduced in color on the Web and in black-and-white in print.
- ☐ I checked all table and figure numbered consecutively in accordance with their appearance in the text.
- ☐ I checked abbreviations were defined at their first mention there and used with consistency throughout the article.
- ☐ I checked all references mentioned in the Reference list were cited in the text, and vice versa according to the APA style.
- ☐ I checked I used the international system units (SI) or SI-equivalent engineering units.

## < Authorship checklist >

JOET considers individuals who meet all of the following criteria to be authors:

- ☐ Made a significant intellectual contribution to the theoretical development, system or experimental design, prototype development, and/or the analysis and interpretation of data associated with the work contained in the article.
- ☐ Contributed to drafting the article or reviewing and/or revising it for intellectual content.
- ☐ Approved the final version of the article as accepted for publication, including references.

## < Checklist for publication ethics >

- ☐ I checked the work described has not been published previously (except in the form of an abstract or as a part of a published lecture or academic thesis).
- ☐ I checked when the work described has been published previously in other proceedings without copyright, it has clearly noted in the text.
- ☐ I checked permission has been obtained for use of copyrighted material from other sources including the Web.
- ☐ I have processed Plagiarism Prevention Check through reliable web sites such as [www.kci.go.kr](http://www.kci.go.kr), <http://www.ithenticate.com/>, or <https://www.copykiller.org/> for my submission.
- ☐ I agree that final decision for my final manuscript can be changed according to results of Plagiarism Prevention Check by JOET administrator.
- ☐ I checked one author at least is member of the Korean Society of Ocean Engineers.
- ☐ I agreed all policies related to 'Research and Publication Ethics'
- ☐ I agreed to transfer copyright to the publisher as part of a journal publishing agreement and this article will not be published elsewhere including electronically in the same form, in English or in any other language, without the written consent of the copyright-holder.
- ☐ I made a payment for reviewing of the manuscript, and I will make a payment for publication on acceptance of the article.
- ☐ I have read and agree to the terms of Authors' Checklist.

Title of article :

Date of submission : DD/MM/YYYY

Corresponding author :

signature

Email address :

※ E-mail this with your signature to [ksoehj@ksoe.or.kr](mailto:ksoehj@ksoe.or.kr)

# Publishing Agreement

## ARTICLE DETAILS

Title of article :  
Corresponding author :  
E-mail address :  
DOI : <https://doi.org/10.26748/KSOE.2XXX.XXX>

## YOUR STATUS

I am one author signing on behalf of all co-authors of the manuscript.

## ASSIGNMENT OF COPYRIGHT

I hereby assign to the Korean Society of Ocean Engineers, the copyright in the manuscript identified above and any tables, illustrations or other material submitted for publication as part of the manuscript (the "Article"). This assignment of rights means that I have granted to Korean Society of Ocean Engineers the exclusive right to publish and reproduce the Article, or any part of the Article, in print, electronic and all other media (whether now known or later developed), in any form, in all languages, throughout the world, for the full term of copyright, and the right to license others to do the same, effective when the Article is accepted for publication. This includes the right to enforce the rights granted hereunder against third parties.

## SCHOLARLY COMMUNICATION RIGHTS

I understand that no rights in patents, trademarks or other intellectual property rights are transferred to the Journal owner. As the author of the Article, I understand that I shall have: (i) the same rights to reuse the Article as those allowed to third party users of the Article under the CC-BY-NC License, as well as (ii) the right to use the Article in a subsequent compilation of my works or to extend the Article to book length form, to include the Article in a thesis or

dissertation, or otherwise to use or re-use portions or excerpts in other works, for both commercial and non-commercial purposes. Except for such uses, I understand that the assignment of copyright to the Journal owner gives the Journal owner the exclusive right to make or sub-license commercial use.

## USER RIGHTS

The publisher will apply the Creative Commons Attribution-Noncommercial Works 4.0 International License (CC-BY-NC) to the Article where it publishes the Article in the journal on its online platforms on an Open Access basis.

The CC-BY-NC license allows users to copy and distribute the Article, provided this is not done for commercial purposes and further does not permit distribution of the Article if it is changed or edited in any way, and provided the user gives appropriate credit (with a link to the formal publication through the relevant DOI), provides a link to the license, and that the licensor is not represented as endorsing the use made of the work. The full details of the license are available at <http://creativecommons.org/licenses/by-nc/4.0/legalcode>.

## REVERSION OF RIGHTS

Articles may sometimes be accepted for publication but later rejected in the publication process, even in some cases after public posting in "Articles in Press" form, in which case all rights will revert to the author.

☒ I have read and agree to the terms of the Journal Publishing Agreement.

Corresponding author:

name

signature

※ E-mail this with your signature to [ksoehj@ksoe.or.kr](mailto:ksoehj@ksoe.or.kr) (Papers will not be published unless this form is signed and returned)

# Research and Publication Ethics

Journal of Ocean Engineering and Technology (JOET) adheres to the guidelines published by professional organizations, including Committee on Publication Ethics (COPE; <https://publicationethics.org/>)

## 1. Authorship

*JOET considers individuals who meet all of the following criteria to be authors:*

- 1) Made a significant intellectual contribution to the theoretical development, system or experimental design, prototype development, and/or the analysis and interpretation of data associated with the work contained in the article.
- 2) Contributed to drafting the article or reviewing and/or revising it for intellectual content.
- 3) Approved the final version of the article as accepted for publication, including references.

Contributors who do not meet all of the above criteria may be included in the Acknowledgment section of the article. Omitting an author who contributed to your article or including a person who did not fulfill all of the above requirements is considered a breach of publishing ethics.

**Correction of authorship after publication:** JOET does not correct authorship after publication unless a mistake has been made by the editorial staff.

## 2. Originality and Duplicate Publication

All submitted manuscripts should be original and should not be in consideration by other scientific journals for publication. Any part of the accepted manuscript should not be duplicated in any other scientific journal without permission of the Editorial Board, although the figures and tables can be used freely if the original source is verified according to the Creative Commons Attribution License (CC BY-NC). It is mandatory for all authors to resolve any copyright issues when citing a figure or table from other journal that is not open access.

## 3. Conflict-of-Interest Statement

Conflict of interest exists when an author or the author's institution, reviewer, or editor has financial or personal relationships that inappropriately influence or bias his or her actions. Such relationships are also known as dual commitments, competing interests, or competing loyalties. These relationships vary from being negligible to having a great potential for influencing judgment. Not all relationships represent true conflict of interest. On the other hand, the potential for conflict of interest can exist regardless of whether an individual believes that the relationship affects his or her scientific judgment. Financial relationships such as employment, consultancies, stock ownership, honoraria, and paid expert testimony are the most easily identifiable conflicts of interest and the most likely to undermine the credibility of the journal, the authors, or of the science itself. Conflicts can occur for other reasons as well, such as personal relationships, academic competition, and intellectual passion. If there are any conflicts of interest, authors should disclose them in the manuscript. The conflicts of interest may occur during the research process as well; however, it is important to provide disclosure. If there is a disclosure, editors, reviewers, and reader can approach the manuscript after understanding the situation and the background of the completed research.

## 4. Management Procedures for the Research and Publication Misconduct

When JOET faces suspected cases of research and publication misconduct such as a redundant (duplicate) publication, plagiarism, fabricated data, changes in authorship, undisclosed conflicts of interest, an ethical problem discovered with the submitted manuscript, a reviewer who has appropriated an author's idea or data, complaints against editors, and other issues, the resolving process will follow the flowchart provided by the Committee on Publication Ethics (<http://publicationethics.org/resources/flowcharts>). The Editorial Board of JOET will discuss the suspected cases and reach a decision. JOET will not hesitate to publish

errata, corrigenda, clarifications, retractions, and apologies when needed.

## 5. Editorial Responsibilities

The Editorial Board will continuously work to monitor and safeguard publication ethics: guidelines for retracting articles; maintenance of the integrity of the academic record; preclusion of business needs from compromising intellectual and ethical standards; publishing corrections, clarifications, retractions, and apologies when needed; and excluding plagiarism and fraudulent data. The editors maintain the following responsibilities: responsibility and authority to reject and accept articles; avoiding any conflict of interest with respect to articles they reject or accept; promoting publication of corrections or retractions when errors are found; and preservation of the anonymity of reviewers.

## 6. Hazards and human or animal subjects

If the work involves chemicals, procedures or equipment that have any unusual hazards inherent in their use, the author must clearly identify these in the manuscript. If the work involves the use of animal or human subjects, the author should ensure that the manuscript contains a statement that all procedures were performed in compliance with relevant laws and institutional guidelines and that the appropriate institutional committee(s) has approved them. Authors should include a statement in the manuscript that informed consent was obtained for experimentation with human subjects. The privacy rights of human subjects must always be observed.

Ensure correct use of the terms sex (when reporting biological factors) and gender (identity, psychosocial or cultural factors), and, unless inappropriate, report the sex and/or gender of study participants, the sex of animals or cells, and describe the methods used to determine sex and gender. If the study was done involving an exclusive population, for example in only one sex, authors should justify why, except in obvious cases. Authors should define how they determined race or ethnicity and justify their relevance.

## 7. Secondary publication

It is possible to republish manuscripts if the manuscripts satisfy the conditions of secondary publication. These are:

- The authors have received approval from the Editorial Board of both journals (the editor concerned with the secondary publication must have access to the primary version).
- The priority for the primary publication is respected by a publication interval negotiated by editors of both journals and the authors.
- The paper for secondary publication is intended for a different group of readers
- The secondary version faithfully reflects the data and interpretations of the primary version.
- The secondary version informs readers, peers, and documenting agencies that the paper has been published in whole or in part elsewhere, for example, with a note that might read, "This article is based on a study first reported in the [journal title, with full reference]"
- The title of the secondary publication should indicate that it is a secondary publication (complete or abridged republication or translation) of a primary publication.

## 8. Complaints and Appeals

The process of handling complaints and appeals follows the guidelines of the COPE available from: <https://publicationethics.org/appeals>

## 9. Post-publication discussions and corrections

The post-publication discussion is available through letter to editor. If any readers have a concern on any articles published, they can submit letter to editor on the articles. If there found any errors or mistakes in the article, it can be corrected through errata, corrigenda, or retraction.



The Korean Society of Ocean Engineers